Dissertation

Advances in Mid-Infrared Dispersion Spectroscopy of Liquids and Photothermal Gas Sensing

A thesis submitted for the degree of
Doctor of Technical Sciences (Dr. techn.)
at
Technische Universität Wien
Faculty of Technical Chemistry
Institute of Chemical Technologies and Analytics

under supervision of

Univ. Prof. Dr. Bernhard Lendl

defended by

DI Stefan Lindner
Mat.Nr. 00925022

Vienna, 02.12.2022

„Habe den Mut, deinen Verstand zu gebrauchen."

Helene Maurer, frei nach Immanuel Kant

Dedicated to Christina & Flora.

Abstract

The research carried out in this PhD thesis concerns new methods of infrared spectroscopy in the liquid and gas phase.

The focus in the liquid phase is on dispersion spectroscopy of aqueous carbohydrate solutions. An External Cavity Quantum Cascade Laser (EC-QCL) is used as light source. The central optical element of the measurement setup is a Mach-Zehnder interferometer. This consists of two arms with identical optical path length, in each of which a liquid flow cell is inserted. One of them is fed with the sample solution to be tested, the other one with the used solvent. In this way, a referencing of the measured signal of the sample solution to that of the solvent is achieved and thus an intrinsic background correction is performed. The qualitative proof of functionality of the method is proven by the high spectral overlap between the recorded dispersion spectra with dispersion spectra calculated from recorded FTIR absorbance spectra using the Kramers-Kronig transformation. In order to demonstrate the suitability of the measurement setup also for quantitative analysis, solutions of three different representative carbohydrates (glucose, fructose and sucrose) were analyzed and the spectra obtained were fed into a multivariate analysis using the Partial Least Square (PLS) calculus. For all three analytes, a detection limit in the order of 0.1 gL^{-1} is reached.

In the field of the gas phase analysis, new methods for photothermal spectroscopy, in particular for Interferometric Cavity-Assisted Photothermal Spectroscopy (ICAPS) have been developed. The core of the measurement setup is a Fabry-Pérot interferometer which is characterized by its cavity transfer function (CTF). Periodic analyte excitation using a mid-IR excitation laser (Quantum Cascade Laser, QCL) causes a periodic heating of the gas leading to a modulated change of its refractive index. This change in the refractive index causes a shift of the CTF. If a second non-absorbing laser is sent through the Fabry-Pérot cavity and its wavelength is adjusted to the inflection point of the CTF, the transmitted and reflected intensities will be modulated by the frequency of analyte excitation.

However, this signal change is only large and linear in a narrow wavelength-region around the inflection point. This makes it necessary to couple the probe laser wavelength to this inflection point (Laser-Wavelength – Cavity-Resonance Locking). For the implementation of such locking procedures, different methods have been developed and their functionality demonstrated.

In particular, these Locking schemes were i) Constant Level Locking, where the ordinate value of the CTF is used as setpoint for a feedback loop that adjusts the probe laser wavelength by means of its injection current. ii) $2f$-WM Locking, where the probe laser is periodically modulated and the $2f$ amplitude of the recorded signal is used as process variable with a setpoint of zero. The condition that the 2f amplitude is zero, is characteristic for the inflection point of the underlying profile. In this sense this method is independent from the probe laser power, what is a significant advantage compared to the Constant Level Locking scheme. The third method is called iii) Stochastic Locking and employs the statistical quantity of skewness as process variable. When it is zero, this quantity also marks the inflection point of the underlying profile. It shows advantages compared to the $2f$-WM scheme like a wider suitable frequency range or very weak requirements with respect to the waveform of the applied modulation.

Furthermore, methods for noise reduction have been developed, especially for the ICAPS measurement setup. In addition to the adaptation of established electronic filtering methods for the ICAPS system, two methods for active noise suppression (balanced detection) have been

viii

developed and their functionality demonstrated.

The first one uses the signal of the integrated monitor photodiode of the probe (diode) laser as reference signal. The balancing capabilities of this method were found to be comparable with other methods published. The second method, coined as 1f Quadrature Point Readout, uses the properties of a quadrature point between sample and reference signal, that arises, if the reference signal is pre-amplified with an inverting amplifier: If a phase shift occurs in the sample path, the $1f$ amplitude of the demodulated signal increases proportionally to this phase shift, to the applied modulation amplitude and the amplification factor of the Lock-In-Amplifier.

The qualitative and quantitative demonstration of the functionality of the developed ICAPS prototype was carried out using the carbon dioxide isotopologues $^{12}CO_2$ and $^{13}CO_2$ as analytes. For these molecules detection limits of 45.6 ppm_V and 0.39ppm_V respectively and a normalized noie equivalent absorption (NNEA) value of $5.9 \cdot 10^{-6}$ cm^{-1} W Hz$^{-1/2}$ were achieved.

Kurzfassung

Die in dieser Doktorarbeit durchgeführten Forschungsarbeiten zeitigen neue Methoden der Infrarotspektroskopie in der Flüssig- und Gasphase. Der Schwerpunkt im Bereich der Flüssigphase liegt auf der Dispersionsspektroskopie wässriger Kohlenhydratlösungen. Als Lichtquelle wird ein External Cavity Quantum Cascade Laser (EC-QCL) verwendet. Zentrales optisches Element des Messaufbaus ist ein Mach-Zehnder-Interferometer. Dieses besteht aus zwei Armen mit identischer optischer Weglänge, in die jeweils eine Flusszelle eingesetzt ist. Eine davon wird mit der zu messenden Probenlösung beschickt, die andere mit dem Lösungsmittel. Auf diese Weise wird das Messsignal der Probenlösung auf das des Lösungsmittels referenziert und so eine intrinsische Untergrundkorrektur erreicht. Der qualitative Funktionsnachweis der Methode wird durch die hohe spektrale Überlappung zwischen den aufgenommenen Dispersionsspektren mit solchen Dispersionsspektren belegt, die aus aufgenommenen FTIR-Absorptionsspektren durch Kramers-Kronig-Transformation berechnet wurden. Um die Eignung des Messaufbaus auch für die quantitative Analyse zu demonstrieren, wurden Lösungen von drei verschiedenen repräsentativen Kohlenhydraten (Glucose, Fructose und Saccharose) analysiert und die erhaltenen Spektren einer multivariaten Analyse unter Verwendung des Partial-Least-Square (PLS)-Kalküls zugeführt. Für alle drei Analyten wird eine Nachweisgrenze in der Größenordnung von 0,1 gL^{-1} erreicht.

Auf dem Gebiet der Gasanalyse wurden neue Methoden zur photothermischen Spektroskopie, insbesondere zur Interferometric Cavity-Assisted Photothermal Spectroscopy (ICAPS) entwickelt. Kernstück des Messaufbaus ist ein Fabry-Pérot-Interferometer, das durch seine Cavity Transfer Funktion (CTF) gekennzeichnet ist. Die periodische Anregung des Analyten mit einem Anregungslaser im mittleren Infrarotbereich (Quantenkaskadenlaser, QCL) bewirkt eine periodische Erwärmung des Gases, was zu einer modulierten Änderung seines Brechungsindex führt. Diese Änderung des Brechungsindex bewirkt eine Phasenverschiebung der CTF. Wenn ein zweiter nicht absorbierender Laser durch die Fabry-Pérot-Cavity geschickt und seine Wellenlänge auf den Wendepunkt der CTF eingestellt wird, werden die transmittierten und reflektierten am jeweiligen Detektor gemessenen Intensitäten durch die Anregungsfrequenz des Analyten moduliert. Diese Signaländerung ist jedoch nur in einem schmalen Wellenlängenbereich um den Wendepunkt herum groß und linear. Dies macht es erforderlich, die Sondenlaserwellenlänge an diesen Wendepunkt zu koppeln (Laser-Wavelength – Cavity-Resonance Locking). Für die Implementierung einer solchen Prozedur wurden verschiedene Verfahren entwickelt und deren Funktionalität demonstriert.

Diese Locking-Schemata waren insbesondere i) Constant Level Locking, bei dem der Ordinatenwert des CTF als Sollwert für eine Rückkopplungsschleife verwendet wird, die die Probenlaserwellenlänge mittels ihres Injektionsstroms einstellt. ii) 2f-WM-Locking, bei dem der Sondenlaser periodisch moduliert und die 2f-Amplitude des aufgezeichneten Signals als Prozessvariable mit einem Sollwert von Null verwendet wird. Die Bedingung, dass die 2f-Amplitude Null ist, ist charakteristisch für den Wendepunkt des zugrunde liegenden Profils. In diesem Sinne ist dieses Verfahren unabhängig von der Sondenlaserleistung, was einen erheblichen Vorteil gegenüber dem Constant Level Locking-Schema darstellt. Die dritte Methode heißt iii) Stochastic Locking und verwendet die statistische Größe der Schiefe als Prozessvariable. Wenn diese Null ist, markiert diese Größe ebenfalls den Wendepunkt des zugrunde liegenden Profils. Stochastic Locking zeigt Vorteile gegenüber dem 2f-WM-Schema, wie einen breiteren geeigneten Frequenzbereich oder sehr schwache Anforderungen in Bezug auf die Wellenform der

angewandten Modulation.

Darüber hinaus wurden Methoden zur Rauschunterdrückung entwickelt, insbesondere für den ICAPS-Messaufbau. Neben der Anpassung etablierter elektronischer Filterverfahren für das ICAPS-System wurden zwei Verfahren zur aktiven Rauschunterdrückung (Balanced Detection) entwickelt und deren Funktionalität demonstriert. Das erste verwendet das Signal der integrierten Monitor-Photodiode des Proben-(Dioden-)Lasers als Referenzsignal. Es konnte gezeigt werden, dass die Balancing-Kapazitäten dieses Verfahrens mit denen anderer publizierter Verfahren vergleichbar sind.

Die zweite Methode, genannt 1f Quadrature Point Readout, nutzt die Eigenschaften eines Quadraturpunktes zwischen Sample- und Referenzsignal, der entsteht, wenn das Referenzsignal mit einem invertierenden Verstärker vorverstärkt wird: Tritt im Sample-Pfad eine Phasenverschiebung auf, steigt die 1f-Amplitude des demodulierten Signals proportional zu dieser Phasenverschiebung, der angelegten Modulationsamplitude und dem Verstärkungsfaktor des Lock-In-Verstärkers.

Der qualitative und quantitative Nachweis der Funktionalität des entwickelten ICAPS-Prototyps erfolgte mit den Kohlendioxid-Isotopologen $^{12}CO_2$ und $^{13}CO_2$ als Analyten. Für diese Moleküle wurden Nachweisgrenzen von 45,6 ppm_V bzw. 0,39 ppm_V und ein normalisierter noie-äquivalenter Absorptionswert (NNEA) von $5,9 \cdot 10^{-6}$ cm^{-1} W Hz$^{-1/2}$ erreicht.

Schlüsselworte: Photothermische, Dispersion-, Absorption- und Infrarot Spektroskopie ◊ Fabry-Pérot und Mach-Zehnder Interferometer ◊ Signalverarbeitung ◊ Rauschunterdrückung ◊ Balanced detection ◊ Gas- und Flüssigkeitssensorik ◊ Laser-Wellenlänge – Cavity-Transferfunktions Koppelung ◊ Modulationstechniken

Compendium

Spatium spectri infri rubri frequentias continet, ubi moleculi magne clari saltatum resonantum faciunt. Hoc spatium spectri perbonum est, spectroscopium faciendum. Usus disciplinae multiplex est et fieri potest in omnes tres statorae materiae diei profesti. Multi opera ad statum solidum prolata sunt. Dissertatio ante lectem iacens attingit potissimum applicationis in statu liquido. Cura maxima statu gasis praebens est. In spatium examinandum primum MMCCXCI cm^{-1} circumdans, oscillatii asymmetrici in directio oscillationis carbonis oxidatis locant. Cura magnus effecerant. Investigatio spectroscopii isotopi carbonis ^{12}C et ^{13}C in carbo cremato multe utiles usuum habent. Distinguendo inter carbum naturalem fossilemque exemplum est. Cura peculiaris fontibus radiorum infri rubri spectatur.

Alii methodi sicut spectroscopio infri rubri transformatio Fourieris (FTIR) utuntur fontes calorium, qui sunt sicut corpora nigra. Hic adhibentur hastae lucis. Scientia hastarum varia est. Varietas iugit a simplicibus hastis duarum partium ad hastas compositas pluribus partibus (QCL et ICL). Color proximo medium infra rubrum. QCL'ae aliter aedificantur. Pro gasos, hasta responsio distributa (DFB-QCL) adhibetur. Pro liquores enim exteriore cavitate hasta (EC-QCL) adhibetur. Omnibus technologis communis est se saepe fontes calorium multo excutere in munu aequalitaque. Hae possessiones multas facultates novas aperiunt.

Magna munus efficit ut saccharum et ova in aqua solvuntur per spectroscopium infra rubrum metiantur. Clipeus fortis aquae in hoc spatio fontes fortes necessaries facet. Alius modus substantias metiri non est. Magna aequalitas permittit technicis interferometricis utendis. Hoc praecipue valet pro metirum obsessionis ex commercio cum materia. De calculationis Fresneli sequitur effusiem et dispersionem simul fieri.

Promptitudine fortium fontium quae investigatio spectroscopica de effectus diffusionis adhuc infantulus est. Classici methodi qualia FTIR referentia adhibentur. Sed umbilicus operis in spectroscopio dispersionis est. Pro liquidos, interferometer Machi Zehnderique adhibetur. Pro gasos, hoc opus interferometro Fabrii Perotique impletur. Compositiones commodarum technicae in hac opere discutiuntur. Eventus adepti exhibentur.

Exsecutio technica praecisa omnium technologiarum maxima pars operis est. Problemata utentis cum usu spectroscopico effectorum multiformes sunt. Exempla huius modi problematum suppressio sonitus, processus signi vel instauratio communicationis electricae sunt. Connexio stabilis es quieta coloris luce cum frequentia resonantis interferometro Fabrii Perotique maxime difficilis est. Tales coniunctionis artes uti possunt diverses proprietates signi. Multis in rebus lux modulata adhibetur. Omnes praesentatae insignitaeque in hac opere sunt.

Dicti: Spectroscopia per effusio, dispersionem et ex effectibus caloris a luce ◊ Interferometro Machi Zehnderique et Fabrii Perotique ◊ Signum dispensando ◊ Suppressio sonitus ◊ Libratum inventum ◊ Mensuratio liquorum gasorumque ◊ Artes mechanicae vibrationum

Acknowledgements

First of all, I would like to thank my supervisor, Professor Dr. Bernhard Lendl, for giving me the opportunity to do my PhD in his research group. Especially, for the years of employing me as a project assistant at the TU Wien, I want to thank Bernhard!

Also, all the other great PhD-candidates and Post-Docs in Bernhard's research group, and all the co-workers from other institutes and companies I had the honor to work together with, I want to say thank you. All the inspiring discussions that hopefully all the people who took part brought forward in their research, make scientific proceeding possible.

But it's not only the scientific colleagues, who make project like a PhD possible. That's why I want to thank also the persons, who overtook all the administrative tasks in the background. Especially this is Pily Lendl, who managed to keep the overview over all ongoing projects in the research group, and Anni Satzinger, who got never tired of bringing all the post packages and the material I needed in the lab, right to my office desk.

Further I want to thank the funding institutions, that made this PhD project possible. These are especially the FFG, the Austrian society for research funding, and the Competence Center CHASE GmbH.

As important as scientific support, is the mental support coming from the family. For this, I want to thank my parents and my whole family. My biggest thanks of this kind go my soul mate and girlfriend Christina Schwarzl. She is the biggest support I could wish in all the time and she is the most wonderful mother, I can wish for our little daughter Flora Johanna – you two, you are the sun of my life!

Danksagung

Allen voran möchte ich meinem Betreuer, Professor Dr. Bernhard Lendl, für die Möglichkeit danken, die vorliegende Dissertation in seiner Forschungsgruppe durchzuführen. Dies gilt insbesondere für die der Dissertation vorangegangenen Arbeit im Rahmen meines von ihm ermöglichten Dienstverhältnisses an der TU Wien.

Auch allen meinen Kollegen, all den anderen großartigen Dissertantinnen und Dissertanten sowie Post-Docs der Forschungsgruppe und an allen anderen Instituten mit denen ich im Rahmen meiner Dissertation zusammenarbeiten durfte, gebührt mein aufrichtiger Dank an dieser Stelle. Lebhafte Diskussionen die, so hoffe ich, alle Beteiligten in ihrer wissenschaftlichen Arbeit vorangebracht haben, oft bis spät abends, oft an „Außenstandorten" der Forschungsgruppe wie diverse Lokale in der Umgebung, machen den wissenschaftlichen Fortschritt erst möglich.

Doch es sind nicht nur die wissenschaftlichen Kollegen, die ein solches Projekt wie es eine Dissertation ist, möglich machen. Daher möchte ich mich auch bei allen Personen bedanken, die all die organisatorischen Aufgaben im Hintergrund übernommen haben. Besonders hervorheben möchte ich hier Pily Lendl die das Kunststück vollbringt, zu jeder Zeit den Überblick über alle Projekte der Forschungsgruppe zu bewahren, sowie Anni Satzinger, die trotz zeitweise großer Mengen an Paketen nie müde geworden ist, mir all mein „Material" bis auf den Schreibtisch zu bringen.

Weiters möchte ich den Institutionen danken, die diese Arbeit finanziell ermöglicht haben. Dies sind insbesondere die Österreichische Forschungsförderungsgesellschaft (FFG) und das Kompetenzzentrum CHASE GmbH.

Genauso wichtig wie die wissenschaftlich-fachliche Unterstützung ist aber auch familärer Rückhalt. Für diesen haben meine Familie und insbesondere meine Eltern zu jeder Zeit gesorgt, wofür ich ihnen herzlich danken möchte. Der größte Dank an dieser Stelle gebührt allerdings meinem Lebensmenschen und Freundin Christina Schwarzl. Sie hat mir unzählige Male den Rücken frei gehalten, war mir die beste Stütze die ich mir wünschen kann und ist die wundervollste Mutter die ich mir für unsere kleine Tochter Flora Johanna wünschen kann – ihr beide seid die Sonne in meinem Leben!

Content

Introduction – Motivation - Scope

The infrared (IR) range of electromagnetic radiation is located in the wavelength range between 0.8 and 1000 µm[1]. It can be further divided into three sub-regions, called near infrared (NIR), middle infrared (MIR) and far infrared (FIR). The range is marked in Figure 0.1.
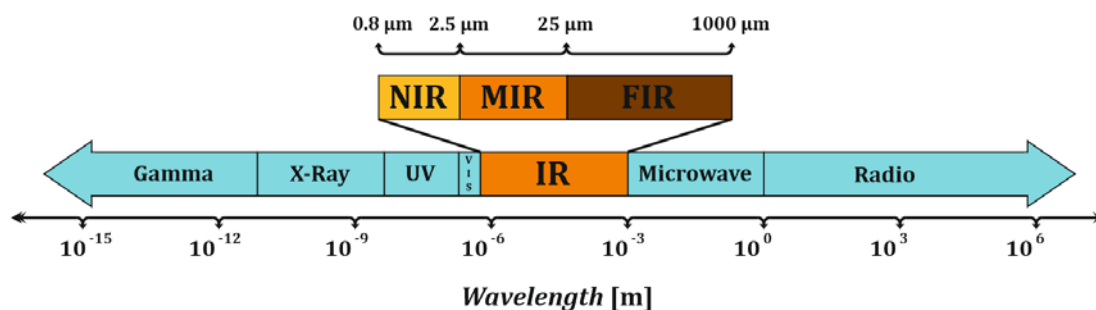
Figure 0.1: Categories of electromagnetic radiation.

In this range, the majority of molecular vibrations show their resonant frequency[2], why it is highly interesting for chemical sensing[3]. The application of IR spectroscopy ranges over all (common) states of aggregation. In this thesis, advances in two of them – Dispersion Spectroscopy of Liquids and Photothermal Gas Sensing – could be achieved.

In the field of liquid phase IR spectroscopy, advances in dispersion spectroscopy of aqueous ethanol and carbohydrate solutions could be achieved. Water itself also shows strong infrared absorption bands[4]. Some of them, around 1800 and 800 cm^{-1}, overlap with the spectral regions of interest, where carbohydrates show absorption. This leads to the problem, that the solvent of the substances of interest, already absorbs most of the light that passes the sample volume in a spectroscopic measurement. In this case, high-intensity light sources become necessary. This issue can be resolved with lasers. Solid state lasers provide a narrow emission range, but high intensity in that range[5]. In the wavelength range where the absorption bands of carbohydrates are located, External Cavity Quantum Cascade Lasers (EC-QCL's) are the sources of choice. Besides the high light intensity that can be reached with lasers, also their far bigger coherence length, compared to other sources like thermal radiation, can be beneficially used for spectroscopy. This

high coherence length allows to measure the quantity of phase shift, what leads to the field of dispersion spectroscopy. The big coherence length of lasers also enables the employment of interferometric measurement techniques[6–8]. For liquid phase dispersion spectroscopy, the Mach-Zehnder Interferometer is employed, where the phase shift generated by the targeted molecule takes place in one interferometer arm while in the other interferometer arm no phase shift occurs since only solvent is located there.

The technique, that was used in the field of photothermal gas sensing is Interferometric Cavity-Assisted Photothermal Spectroscopy (ICAPS), that was used to perform quantitative analysis of CO_2 isotopologues. This method benefits from high intensity light sources in another way than it is the case in Liquid phase dispersion spectroscopy. The principle of the photothermal effect is, that a thermal wave is generated if absorption of light takes place in a sample volume: This results in a refractive index change. The signal generated by the photothermal effect is directly proportional to the power of the light source[9], what makes lasers again to the light source of choice. In photothermal spectroscopy for gases, DFB-QCL's and ICL's were used. QCL's and even more than them ICL's are relatively new developments and represent still a very active field of research[10]. This type of semiconductor lasers are controlled via the current that is guided through the laser chip, called injection current, and the temperature of the chip. With these two parameters, the emitted wavelength can be tuned in the range of a few nm. This is enough to record gas spectra since the absorption lines of gasses, especially under reduced pressure, are very narrow[11]. In particular, the main investigated gas phase transitions in this work are the $\Sigma_u^+ \leftarrow \Sigma_g^+$ transition of $^{12}C^{16}O_2$ (00^10-00^00) at 2291.5445 cm^{-1} [12] and the $\Pi_g \leftarrow \Pi_u$ (01^11-01^10) transition of $^{13}C^{16}O_2$ at 2291.6712 cm^{-1} [13].

The main focus of this work is on technical aspects of instrumentation. Since interferometric sensing setups are highly sensitive devices in terms of environmental influence, challenges in terms of noise, sensor ruggedness and robustness occur. This is especially true for the problem of coupling a probe lasers wavelength to the inflection point of the transmission and reflection transfer function of a cavity – a core problem that arises, when an ICAPS system has to be implemented. In this field, the Laser-Wavelength – Cavity-Locking techniques, several methods were developed, tested and characterized in this thesis. An important role is taken over by the well-known $2f$ wavelength modulation technique[14]. It is used in two ways in this thesis: On the one hand it serves as signal readout technique in the ICAPS setup and on the other hand it represents the underlying principle of one of the investigated Laser-Wavelength – Cavity-Locking schemes. There, the fact is used that a 2f amplitude of zero marks the Inflection point of the underlying CTF.

Finally, signal stabilization methods are investigated and implemented in this thesis. The majority of research done in this field was the development of electronics and software that realize different noise reduction techniques that are also theoretically described in this thesis. The approaches chosen to reach the aim of effective noise reduction are of different nature. They range from single-channel signal processing techniques like frequency filtering to active noise cancelling concepts like balanced detection schemes. With that schemes, the noise of the overall sensing system can be brought down near the fundamental noise level of shot noise[8].

The $2f$-technique also served as starting point for the development of a new signal processing technique that can substitute the 2nd harmonic demodulation by the stochastic quantity of skewness. This technique shows some interesting features like the capability, to understand unwanted noise as a form of modulation, or to extend the technically useable frequency range of modulation to the fundamental limit of the *Nyquist*-barrier.

Chapter 1   Fundamentals – Theory

The thesis is divided in a theoretical and an experimental part. The theoretical part represents the majority of this thesis, therefore it is divided in two chapters. It starts with this first chapter where the physical, chemical and mathematical fundamentals are reviewed, that underly all the technological developments in the field of dispersion spectroscopy and photothermal spectroscopy.

1.1 Molecular Vibrations

Infrared spectroscopy in all its known variations and technical implementations, employs the nature of molecular vibrations to identify (qualitative analysis) and quantify (quantitative analysis) chemical substances. Together with Raman spectroscopy[15], infrared spectroscopy completes the field of vibrational spectroscopy - a highly established and still growing field of spectroscopy, from that constantly new technologies arise[7,8,16,17].

The atomic bond of two atoms in a molecule can mechanically be modelled as a mass-spring-system. The range of electromagnetic radiation, depicted in Figure 0.1, is the range, where many of those mass-spring-systems show their resonant frequency. In infrared spectroscopy, this is recognized as molecular absorption (frequency-) band: The radiation hitting the molecule acts as a driving force in this mass-spring-system. If the frequency of the radiation matches with the eigenfrequency of the mass-spring-system, resonance occurs. This leads to absorption of energy by the molecule on cost of the energy of the excitation radiation. If this loss of energy is determined as a function of the radiation wavelength, an infrared spectrum can be obtained.

An ideal mass-spring-system is a harmonic oscillator, what will be discussed in detail in the following section 1.1.1.

1.1.1 The Harmonic Oscillator

An oscillator is called harmonic, if it is swinging with a single frequency $f = 2\pi\omega$. ω is the circular frequency, defined as angle per time. The name *harmonic* comes from the field of acoustics: An acoustic oscillation with a single frequency is heard as a very "pure" and therefore "harmonic" tone. As the theory will show, this is the case, if the (spring) force F_S that acts on the mass m is proportional to the distance x from the equilibrium position of the spring with spring constant D (Hook's law):

$$F_S(t) = -D \cdot x(t) \tag{1.1}$$

F and x are time-dependent, so they are written as functions of the time t. The harmonic oscillator as a highly important model for a wide range of natural phenomena has been preoccupying physicists for centuries. In the next subsections, the two most important approaches – the classical and the quantum mechanic approach – will be discussed in detail.

1.1.1.1 Classic Approach

The aim is, to find an expression for the position function $x(t)$. Following Newton's second theorem, the force $F(t)$ can be written as $F(t) = m \cdot a$, where m is the mass and a is the acceleration of this mass. This resulting force on the mass m equals the force arising from the stretching of the spring described by equation (1.1):

$$F(t) = F_S(t) \tag{1.2}$$

The acceleration itself is nothing else than the second derivative of the position function. This leads to[18]:

$$m \cdot \frac{d^2}{dt^2} x(t) = -D \cdot x(t) \tag{1.3}$$

For simplification reasons, the quantity

$$\omega_0 = \sqrt{\frac{D}{m}} \tag{1.4}$$

is introduced. This quantity will later be found as the circular frequency of the (free) harmonic oscillator, its eigenfrequency. Further, the second time derivative of a function f is written as $\frac{d^2}{dt^2} f(t) = \partial_t^2 f = \ddot{f}$. With that, equation (1.3) simplifies to

$$\ddot{x} + \omega_0^2 \cdot x = 0 \tag{1.5}$$

what is an ordinary homogenous differential equation of second order. It is an eigenvalue problem $Ax = \lambda x$ for x with a differential operator $A = \partial_t^2$. The eigenfunction $x(t) = c \cdot e^{\lambda t}$ with the eigenvalue $\lambda \in \mathbb{C}$ and scalar constant $c \in \mathbb{C}$ leads to the characteristic equation $\lambda^2 + \omega_0^2 = 0$ with the two solutions $\lambda_{1,2} = \pm i \omega_0$. i is the complex unity.

The general (homogenous) solutions of equation (1.5) can then be found as a complex linear combination of the eigenfunctions with scalars $c_i \in \mathbb{C}, i \in \{1,2\}$, the complex amplitudes:

$$x(t) = c_1 \cdot e^{i \omega_0 t} + c_2 \cdot e^{-i \omega_0 t} \tag{1.6}$$

These solutions are complex, but only the real solutions are of interest. To find the real solutions, an additional condition for the complex amplitudes c_i has to be found.

A sum of two complex numbers, written in polar coordinates $C_i = R_i e^{i \Phi_i}$ with radii R_i and arguments Φ_i, is real, if it holds for the radii $R_1 = R_2$ and for the arguments $\Phi_1 + \Phi_2 \equiv 0 \mod \pi$: If it holds $R_1 = R_2 =: R$, the sum of C_1 and C_2 can be written as a multiple of a single exponential of e: $C_1 + C_2 = R e^{i(\Phi_1 + \Phi_2)}$. This number is real, if $\Phi_1 + \Phi_2$ is an integer multiple of π.

Writing c_i in polar coordinates with radii $r_1 = r_2 = a$ and arguments φ_i yields because of $\left[a e^{i \varphi_i} e^{\pm i \omega_0 t} = a e^{i(\varphi_i \pm \omega_0 t)} \right]$: $i(\varphi_i \pm \omega_0 t) \equiv 0 \mod \pi$. Since both of these two equations have to be fulfilled for any time t, it is finally found $\varphi_1 = -\varphi_2$ as a required condition for the arguments φ_1 and φ_2. With that, it follows, that for the complex amplitudes equation (1.7) it has to be fulfilled:

$$c_1 = c_2^* =: c = a e^{i \varphi_0} \tag{1.7}$$

It can be concluded, that for a real solution, the two complex amplitudes c_i have to be the complex conjugate to each other. With that, equation (1.6) can be written as

$$x(t) = a e^{i \varphi_0} \cdot e^{i \omega_0 t} + a e^{-i \varphi_0} \cdot e^{-i \omega_0 t} = a \left[e^{i(\omega_0 t + \varphi_0)} + e^{-i(\omega_0 t + \varphi_0)} \right] \tag{1.8}$$

With the exponential notation of sine and cosine, $\sin x = \frac{e^{ix} - e^{-ix}}{2i}$ and $\cos x = \frac{e^{ix} + e^{-ix}}{2}$, and the definition of the real amplitude $A_0 = 2a$ it can be found for the real solutions of equation (1.5):

$$x(t) = A_0 \cos(\omega_0 t + \varphi_0) \tag{1.9}$$

φ_0 is called phase of the (free) harmonic oscillator. This result can also be obtained by using

Euler's formula $e^{ix} = \cos x + i \sin x$ for equation (1.8). Then it can be found with $\hat{A} = c + c^*$ and $\hat{B} = i(c - c^*)$, which both being real constants, as real solution for equation (1.5)

$$x(t) = \hat{A} \cos(\omega_0 t) + \hat{B} \sin \omega_0 t \tag{1.10}$$

Equations (1.9) and (1.10) are equivalent and between the constants $\hat{A}, \hat{B}$ and A, φ_0 are the fixed relations $A_0 = \sqrt{\hat{A}^2 + \hat{B}^2}$ and $\tan \varphi_0 = \frac{\hat{B}}{\hat{A}}$, following from trigonometric relations.

Equation (1.5) describes a mass-spring system that is not anyhow influenced from its environment. The results that this model delivers give a good basic understanding of the nature of a harmonic oscillator, but it is incomplete: The mass m usually fulfills its oscillation in a form of fluid. This fluid slows down the movement of the mass m by fluid friction. The consequence is, that frictional force has to be added to equation (1.2):

$$F(t) = F_S(t) - F_F(t) \tag{1.11}$$

Friction in a fluid can be described as a velocity-dependent force $F_F(t)$ (Stokes friction)

$$F_F(t) = -6\pi\eta r \dot{x}(t) \tag{1.12}$$

where η is the dynamic viscosity of the fluid, a material constant, and r is the radius of the mass m, that is assumed to be a ball of finite size. With the constant $\gamma = \frac{6\pi\eta r}{2m}$, which from now on is called the damping coefficient, the influence of fluid friction adds to equation (1.5) resulting in

$$\ddot{x} + 2\gamma\dot{x} + \omega_0^2 \cdot x = 0 \tag{1.13}$$

This differential equation is still ordinary, linear, homogeneous and of second order, but has now an additional first order term. The differential operator A changes to $A = \partial_t^2 + 2\gamma\partial_t$. With the eigenfunction $x(t) = c \cdot e^{\lambda t}$ the characteristic equation $\lambda^2 + 2\gamma\lambda + \omega_0^2 = 0$ is found, which has the solutions $\lambda_{1,2} = -\gamma \pm \sqrt{\gamma^2 - \omega_0^2}$. This leads to the general solution of equation (1.13):

$$x(t) = e^{-\gamma t} \left(c_1 \cdot e^{\sqrt{\gamma^2 - \omega_0^2}\, t} + c_2 \cdot e^{-\sqrt{\gamma^2 - \omega_0^2}\, t} \right) \tag{1.14}$$

This solution is heavily dependent on the relative size of circular frequency ω_0 and the damping coefficient. In principle, three situations can be distinguished:

a) $\gamma < \omega_0$

This is the most important case, the case of a weak damping. In that case, the expression under the square root is negative, what results in a complex function. With the same mathematical thoughts as for the undamped case in equations (1.6) to (1.10), it can be found as general solution

$$x(t) = A_0\, e^{-\gamma t} \cos\left(\sqrt{\omega_0^2 - \gamma^2}\, t + \varphi_0 \right) \tag{1.15}$$

The only difference to the free harmonic oscillator is the factor $e^{-\gamma t}$, what causes an asymptotic decrease of the amplitude over time. What also is important to mention is,

that the angular frequency $\omega = \sqrt{\omega_0^2 - \gamma^2}$, the resonant frequency of the damped harmonic oscillator, is smaller than the angular frequency of the undamped harmonic oscillator, ω_0.

b) $\gamma > \omega_0$

This case, called "heavy damping", is from minor interest in this thesis and is just discussed for the sake of completeness. It results in a real exponential function as general solution. With $\alpha = \sqrt{\gamma^2 - \omega_0^2}$ and the initial boundary conditions $\dot{x}(0) = v_0$ and $x(0) = 0$ it can be found

$$x(t) = \frac{v_0}{\alpha} e^{-\gamma t} \frac{e^{\alpha t} - e^{-\alpha t}}{2} = \frac{v_0}{\alpha} e^{-\gamma t} \sinh \alpha t \tag{1.16}$$

This means, that after an initial stretch of the spring, the mass asymptotically goes back to its equilibrium position without any oscillation.

c) $\gamma = \omega_0$

Also this case, the "aperiodic borderline case", is just mentioned for the sake of completeness. It leads to degeneracy of the eigenvalues of the differential operator A, what makes a variation of constants necessary to solve the corresponding differential equation. By doing so, this results again for the initial boundary conditions $\dot{x}(0) = v_0$ and $x(0) = 0$ in the general solution

$$x(t) = A_0 \left(1 + \gamma t\right) e^{-\gamma t} \tag{1.17}$$

Taking into account that the oscillation takes place in a frictional fluid brings the model closer to reality, but there is still one further factor to be considered. Especially when discussing molecular vibrations, the behavior of the mass-spring system is of high interest, when energy is added to the system from the environment. This corresponds to an absorption process. In the model of a damped mass-spring-system from equation (1.11), this external force influencing the oscillating mass has to be added and it is found

$$F(t) = F_S(t) - F_F(t) + F_E(t) \tag{1.18}$$

The external force considered at this point is a periodic force with an angular frequency ω_E and amplitude A_0. This external force is the model for any excitation of the mass-spring system from the environment, why it's angular frequency is called ω_E and its amplitude A_E.

$$F_E(t) = F \cos \omega_E t \tag{1.19}$$

With that, equation (1.13) can be further extended and finally the differential equation for a driven damped harmonic oscillator is found as

$$\ddot{x} + 2\gamma \dot{x} + \omega_0^2 \cdot x = A_E \cos \omega_E t \tag{1.20}$$

with $A_E = \frac{F}{m}$ the excitation amplitude. This equation is again an ordinary, linear differential equation of second order, but it is inhomogeneous. This means that additionally to the homogenous solution, which is the same as it was for the damped harmonic oscillator modelled in

equation (1.13), a particulate solution has to be found. The far most important case is the oscillating case, $\gamma < \omega_0$ with its general solution represented in equation (1.15). The inhomogeneous equation (1.20) has an oscillating disturbance function, therefore the particulary solution has also to be of an oscillating form. For the general solution of equation (1.20) it follows

$$x(t) = A_I \, e^{-\gamma t} \cos\left(\sqrt{\omega_0^2 - \gamma^2} \, t + \varphi_0\right) + A_S \cos(\omega_E t + \varphi_S) \tag{1.21}$$

This equation shows an interesting result: after a long period of time, meaning $t \gg \frac{1}{\gamma}$, the amplitude of the initial oscillation, $A_I \, e^{-\gamma t}$, gets negligibly small, while the amplitude of the stationary oscillation A_S remains constant. The mass-spring-system "overtakes" the angular frequency ω_E of the excitation after that period of time - the oscillator performs a forced oscillation.

After the influence of the initial, damped oscillation has decreased significantly, the stationary term $x(t) = A_S \cos(\omega_E t + \varphi_S)$ describes the behavior of a driven damped harmonic oscillator sufficiently well. Inserting this function in the differential equation (1.20) leads to an equation that can be written as the sum of a multiple of $-\sin \omega_E t$ and a multiple of $\cos \omega_E t$ being zero. Since this equation has to be true for any time t, it follows

$$(\omega_0^2 - \omega_E^2) \sin \varphi_S + 2\gamma\omega \cos \varphi_S = 0$$
$$A_S(\omega_0^2 - \omega_E^2) \cos \varphi_S - 2A_S\gamma\omega_E \sin \varphi_S - A_E \tag{1.22}$$

From these two equations, expressions for the function describing the phase shift in the stationary condition in dependence of the excitation angular frequency,

$$\varphi_S(\omega_E) = \arctan\left(-\frac{2\gamma\omega_E}{\omega_0^2 - \omega_E^2}\right) \tag{1.23}$$

and for the function describing the amplitude in the stationary condition

$$A_S(\omega_E) = \frac{A_E}{\sqrt{\left(\omega_0^2 - \omega_E^2\right)^2 + 4\gamma^2\omega_E^2}} \tag{1.24}$$

can be found. Further, with the relations $\mathrm{Re}(A_S) = A_S \cos \omega_E$ and $\mathrm{Im}(A_S) = A_S \sin \omega_E$ the real and the imaginary part of the complex stationary amplitude can be found. These expressions can also be obtained by solving equation (1.20) in its complex form

$$\ddot{x} + 2\gamma\dot{x} + \omega_0^2 \cdot x = A_E e^{i\omega_E t} \tag{1.25}$$

By doing so, the analytical expressions

$$\mathrm{Re}(A_S(\omega_E)) = \frac{A_E(\omega_0^2 - \omega_E^2)}{(\omega_0^2 - \omega_E^2)^2 + 4\gamma^2\omega_E^2}$$
$$\mathrm{Im}(A_S(\omega_E)) = -\frac{2A_E\gamma\omega_E}{(\omega_0^2 - \omega_E^2)^2 + 4\gamma^2\omega_E^2} \tag{1.26}$$

can be found for the real and the imaginary part of the complex stationary amplitude.

The stationary amplitude expressed in equation (1.24) has a local maximum that can be found by setting the first derivative to zero. This amplitude maximum is called the resonant frequency ω_R of the driven harmonic oscillator

$$\omega_R = \sqrt{\omega_0^2 - 2\gamma^2}$$

<div align="right">(1.27)</div>

At that frequency the highest amplitude can be reached by exciting the mass-spring system with the excitation frequency ω_E. For $\gamma \ll \omega_0$, which is the most important practical case, it hardly deviates from the resonant frequency of the damped harmonic oscillator $\omega = \sqrt{\omega_0^2 - \gamma^2}$.
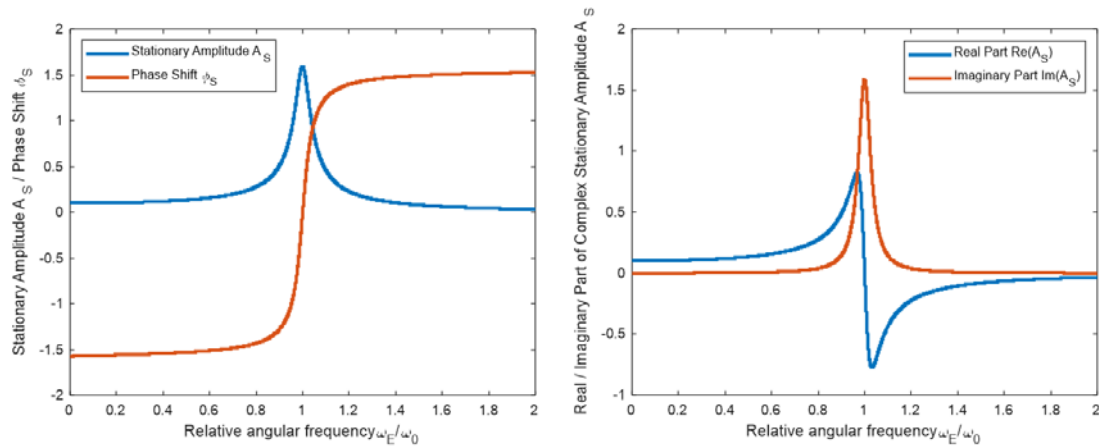
Figure 1.1: Left: Stationary amplitude and stationary phase shift from equations (1.23) and (1.24). Left: Real and imaginary part of the complex amplitude, equations (1.26).

The resonant frequency ω_R can be clearly recognized as the maximum of the stationary amplitude or the real part of the complex amplitude, or as well as the inflection point of the phase shift or the imaginary part of the complex amplitude in Figure 1.1. Further, this gives a first idea of the connection between absorption (amplitude) and dispersion (phase shift) spectroscopy, discussed in detail in section 0: Both phenomena are dependent on the frequency and their graphs show prominent spectral features around the resonant frequency. The shapes of the graphs in Figure 1.1 will be found again in that section.

1.1.1.2   Quantum Mechanic Approach

There have been observed phenomena, that could not be explained by the laws of – classic – mechanics and thermodynamics. The historically most important example is the black body radiator. This model led to the revolutionary quantum hypothesis in a few steps, which are reviewed at this point.

The starting point is a black body, for simplification reasons a cuboid, with walls of ideal conductivity. For any electromagnetic radiation inside the cuboid volume, the condition of ideal conductivity translates to a boundary condition for the radiation amplitude: it has to be zero at the walls. As a consequence, there is a restricting condition for the wavelength λ (and, because of $v = \frac{\lambda}{c}$, also for the frequency v) of possible electromagnetic radiation: there are only waves with a

wavelength λ possible, that "fit" inside the dimensions of the cuboid. Those possible waves are called "modes" and represent one possible oscillator inside the black body volume each. Figure 1.2 shows the situation for the simplified 1-dimensional case.
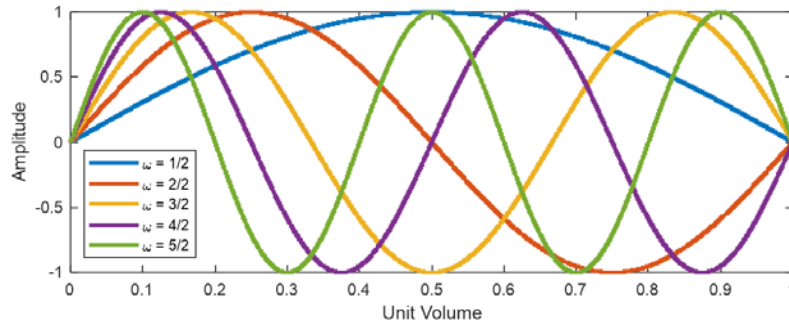

Figure 1.2: Restricting wavelength condition in a hollow body, depicted in one dimension. The first five modes are depicted

In three dimensions, the situation is the same, but due to more geometric degrees of freedom, more complex. Nevertheless, an expression for the number of modes per unit volume of the resonator and frequency interval can be found. This quantity is called the spectral mode density

$$n(v)\mathrm{d}v = \frac{8\pi v^2}{c^3}\mathrm{d}v$$

(1.28)

If this quantity is multiplied by the average energy per mode w_v in the frequency interval $\mathrm{d}v$, which is according to Boltzmann $w_v = kT$, the spectral energy density can be found as[19]

$$w(v)\mathrm{d}v = \frac{8\pi v^2}{c^3}kT\,\mathrm{d}v$$

(1.29)

with k being the Boltzmann's constant and T the temperature of the black body. Equation (1.29) is the well-known Raleigh-Jeans radiation law that describes the black body radiation by classic thermodynamics. If this description would be true for all frequencies, this would lead to the so-called "ultraviolet catastrophe": For increasing frequency, the spectral energy density would go towards infinity.

The revolutionary idea of Max Planck to resolve this issue, postulated in the beginning of the 20th century, was that the amount of energy that a single oscillator can carry, is not continuous: This is the case by using the Boltzmann model for the average energy in a frequency interval $\mathrm{d}v$, $w_v = kT$, because the temperature can have any value. Instead of that, Planck assumed that the amount of energy per mode of frequency v is an integer multiple of a smallest possible portion of energy hv. h is the Planck's constant.

Actually, the symbol Planck used for this new fundamental natural constant, h, has its origin from the way, how it was discovered: Planck found, that if the assumption of a finite, minimal amount of energy was true, a factor that he could not be explained by classical physics remained in his derivation. He called that factor a "Hilfsgröße", the German word for an arbitrary constant in that context. The logical formula symbol for that was the nowadays well-known Planck constant h.

With that assumption, the total energy of a mode of frequency v is then $\widehat{w_v} = nhv$. In the thermal equilibrium, according to the Boltzmann-equation, the probability to find n modes of frequency v

can be found by dividing the Boltzmann factor $e^{-\frac{\widehat{w_\nu}}{kT}}$ of this number of modes by the sum of the Boltzmann factors of all numbers of modes for that frequency ν:

$$p(\widehat{w_\nu}) = \frac{e^{-\frac{nh\nu}{kT}}}{\sum_{n=0}^{\infty} e^{-\frac{nh\nu}{kT}}}$$

(1.30)

The average energy per mode is then $\overline{w_\nu} = \sum_{n=0}^{\infty} p(\widehat{w_\nu}) \cdot \widehat{w_\nu}$ and multiplied with the spectral mode density from equation (1.28) this leads to the Planck law of radiation:

$$\overline{w_\nu}(\nu)\,\mathrm{d}\nu = \frac{8\pi h\nu^3}{c^3} \frac{\mathrm{d}\nu}{e^{\frac{h\nu}{kT}} - 1}$$

(1.31)

This law describes the situation in a correct way: after reaching a maximum, the spectral energy density decreases again and goes asymptotically towards zero. The consequence is, that the total energy emitted by the black body is finite – what is also found experimentally.

With the idea of discrete energy levels, the developed theory of a (classical) harmonic oscillator, made in section 1.1.1.1, can also be translated to quantum mechanics. Therefore, first the energy stored in an oscillating mass-spring system has to be considered. There are two forms of energy present in such a system: on the one hand, it is the kinetic energy

$$E_{kin} = \frac{1}{2}mv^2 = \frac{1}{2}m\dot{x}^2 = \frac{1}{2}m\left(\frac{\mathrm{d}x}{\mathrm{d}t}\right)^2$$

(1.32)

with m being the mass and v the mass' velocity. On the other hand, the potential energy. This energy, in the case of a mass-spring-system, is stored in the spring. Since the spring force $F(x)$ increases with the distance of the mass from the equilibrium position and the mechanical energy is the product of the force and the travelled distance against this force, the potential energy at the position x is

$$E_{pot} = \int_0^x F(x')\,\mathrm{d}x' = \int_0^x D \cdot x'\,\mathrm{d}x' = \frac{1}{2}Dx^2$$

(1.33)

From now on, the potential energy is just called potential $V(x)$. Analog to the classic harmonic oscillator the quantity $\omega_0 = \sqrt{\frac{D}{m}}$, the angular frequency of the free harmonic oscillator, is used. With that, the potential $V(x)$ of a free harmonic oscillator can be written as

$$V(x) = \frac{1}{2}m\omega_0^2 x^2$$

(1.34)

Further, the momentum

$$p = m \cdot v = m \cdot \dot{x}$$

(1.35)

is introduced. With that, the kinetic energy can be expressed as

$$K(p) = \frac{p^2}{2m}$$

(1.36)

The sum of the kinetic and the potential energy is, due to conservation of energy, constant over time. This leads to the following stationary equation:

$$E(x,p) = K(p) + V(x) = \frac{1}{2m} \cdot p^2 + \frac{m\omega_0^2}{2} \cdot x^2$$

<div align="right">(1.37)</div>

This is nothing else, than the (time independent) Hamilton equation. In quantum mechanics, the classical variables x and p are exchanged by the quantum mechanic operators X and P. Further, the description of the state of motion of a mass – this mass usually is a particle – by momentum and position is overtaken by the abstract wavefunction $\psi(x)$. This wavefunction describes the state of motion as a probability of presence at a given position and, if the time-dependent wavefunction is considered, also at a given time. The mathematical formalism of quantum mechanics has been developed, among others, by Louis de Broglie, Werner Heisenberg, Erwin Schrödinger and David Hilbert. A complete presentation of the whole mathematical formalism would lead too far, but the principle ideas are described at this point[20]. Continuing the ideas found during the discussion of the black body radiator in equations (1.28) to (1.31) they are the following ones:

- Additionally to the quantization of the energy $E = h\nu = h\frac{\omega}{2\pi} = \hbar\omega$, a quantization of the momentum by $p = h \cdot \frac{1}{2\pi} \cdot \frac{1}{\lambda} = \hbar k$, where k is the wave vector and $\hbar$ is the reduced Planck constant, is introduced. Together with the quantization of energy, $E = h\nu$ the formula $p = \hbar k$ describes the very fundamental idea of quantum mechanics. Both formulas together are called Einstein-de Broglie relations. They describe a today well-known paradoxon of quantum mechanics: Energy E and momentum p are typical quantities to describe the state of motion of a particle, while the wave vector k and the frequency are the fundamental quantities to describe a wave. Since with the Einstein-de Broglie relations there is found an equality, a particle and a wave has to be same. This so-called wave-particle dualism was in early times of quantum mechanics one of its biggest points of criticism, but it could later be experimentally confirmed by several historic experiments (for instance: double slit vs. light mill experiment).
- Since position x and momentum p are connected in the Hamilton equation to the energy and energy is a conservative quantity, it is a logical consequence, that if a physical quantity – in quantum mechanics: observables – can be written as a function of x, there has to be a way to express it as a function of p and vice versa. This is nothing else than a coordinate change – and the coordinate transformation that describes that change between the so-called "position space" and the "momentum space" is the Fourier transform.
- The actual state of the particle is described by the wave function $\psi(x,t)$. Its amplitude can be interpreted as the probability to find the particle at a given time in a given position. As every probability density function, there has to be a normalization, as it was also done within the discussion of the black body radiator in equation (1.30). Generally expressed, this means for the (one-dimensional, time independent) wave function nothing else than

$$\int_\Omega \psi(x) \cdot \psi^*(x) \, \mathrm{d}x = 1$$

<div align="right">(1.38)</div>

- Not every function, that fulfills the normalization criteria (1.38) has a physical meaning. They have to meet some mathematical criteria - for instance, only functions that are

defined everywhere in the carrier Ω, and that are continuous and differentiable are of physical interest. It can be found, that all the criteria that are physically required, are met by a Hilbert-space. This is a special vector space which's elements are the wave functions and where the quantum mechanic operators can be defined.

The quantum mechanic approach to the harmonic oscillator is now started at equation (1.37) and the expressions for X and P arising from the mathematical formalism are

$$X = x$$
$$P = -i\hbar\, \partial_x$$

(1.39)

By introducing that to equation (1.37) and using the fact that the total energy E is conserved and therefore a constant, and multiplying the equation by the wave function $\psi(x)$, the (stationary) Schrödinger Equation for the free harmonic oscillator is found by

$$\mathcal{H}\psi = E\psi$$

$$\left[-\frac{\hbar^2}{2m}\cdot\partial_x^2 + \frac{m\omega_0^2}{2}\cdot x^2 \right]\psi(x) = E\,\psi(x)$$

(1.40)

With $\mathcal{H}$, the expression in square brackets, being the Hamiltonian of the free harmonic oscillator. This equation (1.40) is an eigenvalue problem. The solution of this problem leads to the eigenfunctions $\psi_n(x)$ of the harmonic oscillator. With the so-called creation and annihilation operators

$$\boldsymbol{a} = \frac{1}{\sqrt{2}}(X + iP)$$
$$\boldsymbol{a}^+ = \frac{1}{\sqrt{2}}(X - iP)$$

(1.41)

The names of that operators arise from their impact on the nth eigenfunction ψ_n: They "create" ($\boldsymbol{a}^+$) or "annihilate" ($\boldsymbol{a}$) one level of energy. It can be shown that the eigenfunctions ψ_n can be found in the following recursive forms:

$$\boldsymbol{a}\,\psi_n = \sqrt{n}\,\psi_{n-1}$$
$$\boldsymbol{a}^+\psi_n = \sqrt{n+1}\,\psi_{n+1}$$

(1.42)

A formula to calculate all eigenfunctions can be found by solving these differential equations

$$\psi_n(x) = \left(\frac{m\omega_0}{\pi\hbar}\right)^{\frac{1}{4}}\cdot\frac{1}{\sqrt{2n\cdot n!}}\cdot H_n\left(\sqrt{\frac{\hbar\omega_0}{n}}\cdot x\right)\cdot e^{-\frac{1}{2}\frac{m\omega_0}{\hbar}x^2}$$

(1.43)

When the wavefunction describe a particle in a harmonic potential, the ψ_n are called eigenstates of the harmonic oscillator and follow the mathematical structure of Hermite-polynomials $H_n(\xi) = (-1)^n e^{\xi^2}\partial_\xi^n e^{-\xi^2}$. The corresponding eigenvalue to each eigenfunction is called eigenenergy (of that eigenstate). The eigenenergy of the nth eigenstate can be found as

$$E_n = \hbar\omega_0 \cdot \left(n + \frac{1}{2}\right)$$

<div align="right">(1.44)</div>

Figure 1.3 shows the eigenstates of the free harmonic oscillator for some values of n.
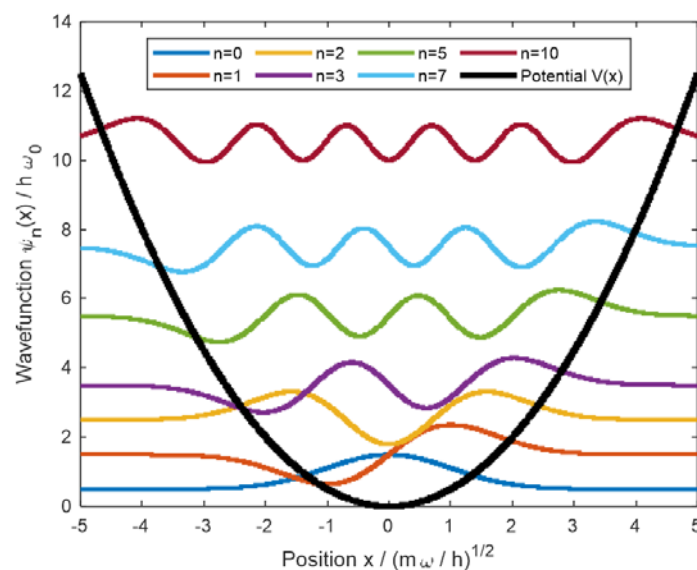
Figure 1.3: Some eigenfunctions of the harmonic oscillator with the harmonic potential $V(x)$. The (asymptotically reached) ordinate levels at the outer borders of the diagram correspond to the eigen energies.

1.1.2 Anharmonic Oscillator

The harmonic potential $V(x)$ defined in equation (1.34) is a good approximation for various types of oscillators and gives a basic understanding of the nature of vibrational modes. However, it describes the situation in a two-atom molecule only incomplete: The harmonic potential, what is therefore called harmonic approximation, is only true in the near field.
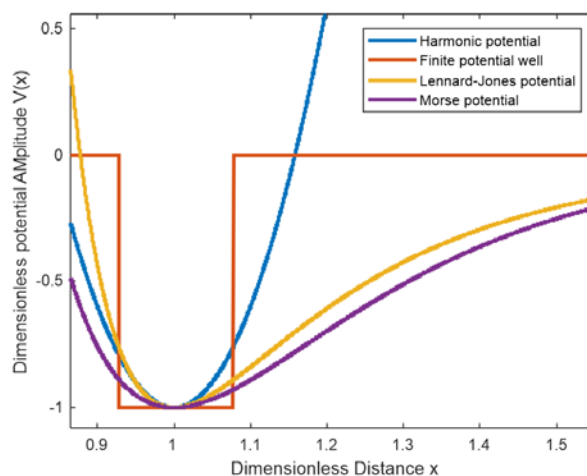
Figure 1.4: Different well-known approximations for the potential of a two-particle system

This can be understood as follows: Since the oscillator potential of a molecule is continuous and differentiable, there is a neighborhood of the equilibrium position, in that the error of the Taylor polynomial of given order can be considered small. This is especially true for the Taylor polynomial of second order – what is besides possible multiplicative constants identic with the (quadratic) potential of a free harmonic oscillator. In Figure 1.4 some other well-known potentials for different physical problems are depicted besides the harmonic potential.

The problem that arises from the fact, that the harmonic approximation only delivers sufficiently good results for the near field of the equilibrium position, can be treated by an approximation that takes asymmetric terms of the molecule potential into account: The way, how the force acting on a particle that is moved away from its equilibrium position (ground state, ψ_0) depends on the direction of this movement – it makes a difference, if the particle is moving towards or away from the equilibrium position. This makes an asymmetric potential necessary, what can not be fulfilled by a harmonic oscillator potential – an anharmonic potential needs to be found. A potential that meets this requirement better than the harmonic approximation does, was suggested by Morse[21]:

$$V_A(x) = E_0\left(1 - e^{a(x-x_0)}\right)^2$$
(1.45)

This potential behaves similar like the well-known Lennard-Jones potential for system of two particles having attracting and pushing forces in between. However, it has significant mathematical advantages compared to the Lennard-Jones-potential, when it comes to description of the state of motion of a particle in this potential.

For describing the state of motion of such a two-particle system, the theory starting from the Hamilton equation in (1.37), is used. The structure of that theory only makes an exchange of the potential $V(x)$ by the potential $V_A(x)$ necessary. With that, the stationary Schrödinger equation gets the form

$$\left[-\frac{\hbar^2}{2m}\cdot\partial_x^2 + E_0\left(1 - e^{a(x-x_0)}\right)^2\right]\psi(x) = E\,\psi(x)$$
(1.46)

This equation has the satisfying property, that analytical solutions exist for this eigenvalue problem[22]. With the Whittaker function[23] $M_{A,B}(x)$, the constant $C = \frac{\sqrt{2E_0\frac{m_1 m_2}{m_1+m_2}}}{\hbar a}$ and the eigenvalue parameter $N_n = \frac{\Gamma(n+1)\cdot\Gamma(n+1)\cdot\Gamma(2t-2n)\cdot\Gamma(2t-2n-1)}{a\cdot\Gamma(2t-n)}$, the eigenstates

$$\psi_n^A(x) = \frac{1}{\sqrt{2C}}\cdot N_n^{-\frac{1}{2}}\cdot e^{\frac{a}{2}(x-x_0)}\cdot M_{C,C-n-\frac{1}{2}}\left(\frac{1}{\sqrt{2C}}\cdot e^{\frac{a}{2}(x-x_0)}\right)$$
(1.47)

can be found. The corresponding eigenenergies are

$$E_n^A = \hbar\omega_0\cdot\left(n+\frac{1}{2}\right) - \frac{\hbar^2\omega_0^2}{4E_0}\cdot\left(n+\frac{1}{2}\right)^2$$
(1.48)

Compared to the eigenenergies of the harmonic oscillator in equation (1.44), it is noticeable, that the eigenenergy as a (discrete) function $E_n^A:\begin{cases}\mathbb{N}\to\mathbb{R}\\n\mapsto E_n^A(n)\end{cases}$ of the level n is not linear. This becomes especially clear, if the level distance ΔE_n^A is calculated:

$$\Delta E_n^A = E_{n+1}^A - E_n^A = \hbar\omega_0 - \frac{\hbar^2\omega_0^2}{2E_0}(n+1)$$

(1.49)

For the harmonic oscillator the level distance can be found by

$$\Delta E_n = E_{n+1} - E_n = \hbar\omega_0$$

(1.50)

This describes an important effect: While for the harmonic potential, the level distance is constant as a discrete function of n, this is not the case for the anharmonic (Morse-) potential. This potential causes a linear decrease of the level distance. This has two consequences: On the one hand, that means that the distance in energy level is lower for higher eigenstates, meaning that electrons on higher energy levels can be transferred between energy levels by decreasing amount of transfer energy. According to the quantization of energy by $E = \hbar\omega$, this corresponds to lower frequencies or, because of $\lambda = \frac{2\pi c}{\omega}$, to longer wavelengths for the excitation radiation. Conversely, this means that for the description of excitation by infrared radiation, an anharmonic model for the potential leads to better results than a harmonic one would do.
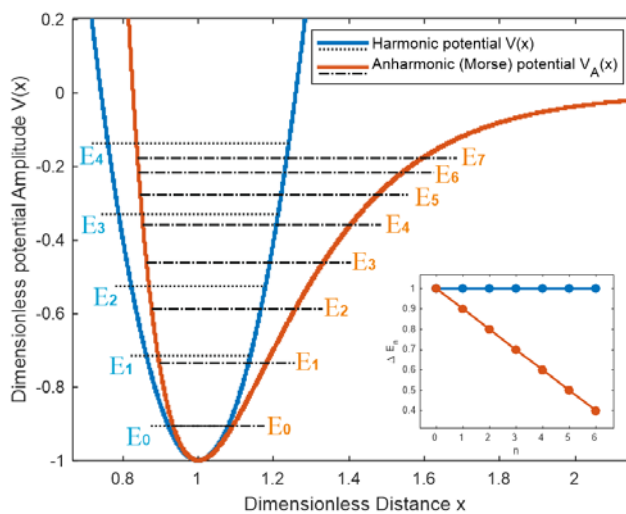
Figure 1.5: Depiction of the energy eigenvalue levels for the harmonic and the inharmonic case

On the other hand, equation (1.49) shows a weakness of this model: for very high levels, a negative level distance would be found. The critical level can be found by setting ΔE_n^A to zero, what delivers

$$n_{lim} = \frac{2E_0}{\hbar\omega_0}$$

(1.51)

This critical level n_{lim} is high enough, to get suitable results for practically relevant eigenenergies. Figure 1.5 shows a graphic depiction of the eigenenergies E_n and E_n^A of a harmonic and an anharmonic oscillator.

1.1.3 Molecular Vibrational Modes

The underlying model of molecular vibration is a three-atom molecule, or, a system of three (spheric) masses and two springs, respectively. This system shows, since it has to be considered as a quantum system, in dependency of the spring constants and the size of the masses, a manifold

of different oscillation eigenstates, as they were introduced in the last section. While the mass of an atom is given by the molar weight, the spring constant is defined by the strength of the molecular bond. With defined masses and spring constants, it follows that the oscillation cannot take place in any form. As it was described in the last section, eigenstates with corresponding eigenenergies are found. In molecular spectroscopy those eigenstates are called molecular vibrational modes. In the following subsection, those vibration modes are discussed more in detail and the specific vibrational modes of the molecules investigated in this thesis are presented. Further, a fourth quantity in addition to frequency ν, angular frequency ω and wavelength λ is introduced to describe an oscillation. In chemical spectroscopy, the wavenumber w is preferably used. It is defined as the reciprocal of the wavelength λ:

$$w = \frac{1}{\lambda} = \frac{\nu}{c} = \frac{\omega}{2\pi c}$$

<div align="right">(1.52)</div>

With c the speed of light. Most commonly the wavenumber is given in units of inverse centimeters, cm^{-1}.

1.1.3.1 Bending, stretching and rotational modes

If the system is considered from a geometric point of view, it is found, that there is limited degree of freedom for the motion of the three masses. In principle each atom has three degrees of freedom corresponding to movement in all three axes x, y and z. With that, the fundamental ways of molecular oscillation are

- **Stretching:** Translation along the direct connection of two masses
- **Rotation:** Rotation of one mass around the own axis in the perpendicular plane of the direct connection to another mass
- **Bending:** Rotation of the outer masses around the center mass

These fundamental categories can be combined, what leads to a wide variety of possible vibrational modes of a molecule. This results in a complex spectrum that is unique for every molecule. The spectrum, in its functional analytical sense, is defined as the set of eigenvalues of an operator. In spectroscopy, to this information – it would correspond to an unweighted list of all (absorption) lines of a molecule – the amplitude of the corresponding eigenstate is added, what corresponds to the line strength of that absorption line. Figure 1.6 and Table 1.1 describe different types of molecular vibration and combinations of them.

The fundamental types of molecular vibration can be combined and further categorized. The stretching vibration, for instance, can occur not only between the center and one outer atom, but also between the center atom and the second outer atom. If these two oscillations have the same frequency, they can either also share the same phase, or their phase is shifted by π. The first case is called symmetric stretching, the second one antisymmetric stretching. The same holds also for the rotation and combination of translational and rotational oscillations. Referring to Figure 1.6, the vibrational modes of a three-atom molecule can be described by the following geometric parameters:

- BA: Distance between atom B and atom A
- BC: Distance between atom B and atom C
- $\sphericalangle ABC, \alpha$: (Relative) center angle, measured from atom A via atom B to atom C
- $\sphericalangle XBA, \beta$: (Absolute) angle, measured from a fixed (x-) axis via atom B to atom A

In Table 1.1, the types of vibration are summarized and categorized by either change or constancy of the previously listed geometric parameters[24].

Description	BA	BC	α	β
Symmetric stretching	oscillating, ϕ	oscillating, ϕ	constant	constant
Antisymmetric stretching	oscillating, ϕ	oscillating, $(\phi + \pi)$	constant	constant
Rocking	constant	constant	constant	oscillating, relative to x
Bending	constant	constant	oscillating	constant
Twisting	constant	constant	constant	oscillating, relatiive to x sin(β)
Wagging	constant	constant	constant	oscillating, relative to y

Table 1.1: Summary of molecular vibration modes
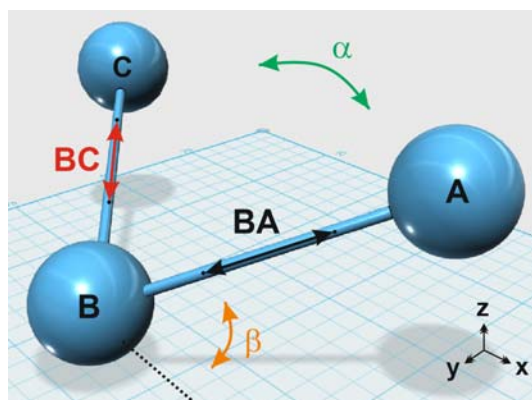
Figure 1.6: Visualization of the fundamental types of molecular vibration.

1.1.3.2   Vibrational Modes of Investigated Analytes

In the field of this thesis, mainly five molecules were investigated. In the liquid phase these were

- $C_6H_{12}O_6$, Glucose
- $C_6H_{12}O6$, Fructose
- $C_{12}H_{22}O_{11}$, Sucrose

The structures of these carbohydrates are shown in Figure 1.7.
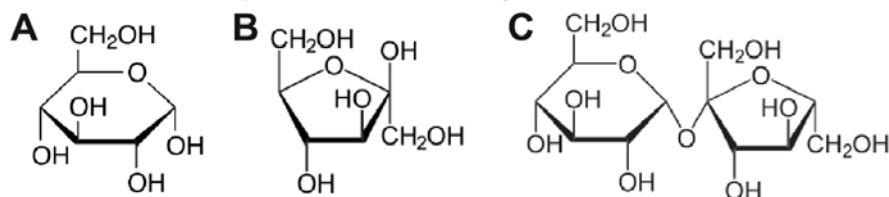
Figure 1.7: Structures of A, Glucose, B, Fructose and C, Sucrose

In the Mid-IR range, between 950 and 1200 cm^{-1} – the wavenumber range, that was investigated in this work[25] – the molecules show several characteristic transitions. The band assignment[26] is given in Table 1.2. Mixtures of these three carbohydrates in aqueous solution are an often-used model for demonstrating the capability of infrared spectroscopy for the determination of sugars (carbohydrates) in real samples solutions[27–29].

Wavenumber [cm-1]	Glucose	Fructose	Sucrose	Vibration type
1181		x		C-O stretching
1154		x		C-O stretching
1149	x			C-O stretching
1133			x	C-O stretching
1107	x			C-O ring stretching
1104		x	x	C-O ring stretching
1080		x		C-O stretching, C-C stretching, COH bending
1078	x			C-O stretching, C-C stretching, COH bending
1063		x		C-O stretching, C-C stretching, ring
1055			x	C-O stretching, C-C stretching, ring
1032	x			C-O stretching, C-C stretching, ring
1015			x	C-O stretching, C-C stretching, ring
998			x	C-O-H bending, C-O stretching

Table 1.2: Characteristic Transitions of Glucose, Fructose and Sucrose in diluted aqueous solution in the investigated wavenumber regime

In the gas phase, the investigated molecule was carbon dioxide in two different isotopologues:

- $^{12}C^{16}O_2$
- $^{13}C^{16}O_2$

For gas phase spectra, there is a highly detailed database for molecular vibrational modes available, the HITRAN[30] database. Spectral features in gas spectroscopy are much more detailed as individual rotational-vibrational transitions are spectrally resolved. Therefore, they are often called "lines" instead of "bands. Since the molecular vibration was modelled as a mass-spring-system, it gets clear, that different isotopes of the same atom, especially if the atom is relatively small like it is the case for carbon, have different oscillation eigenstates and therefore different spectral lines: according to equation (1.4), the eigenfrequency of the corresponding oscillator changes, if the mass changes. In the field of this thesis, mainly two transitions of two CO_2 isotopologues were investigated:

- The $\Sigma_u^+ \longleftarrow \Sigma_g^+$ transition of $^{12}C^{16}O_2$ (00^10-00^00) at 2291.5445 cm^{-1} [12]
- The $\Pi_g \longleftarrow \Pi_u$ transition of $^{13}C^{16}O_2$ (01^11-01^10) at 2291.6712 cm^{-1} [13]

Here, the expressions in brackets are a group-theoretic notation of the transition. Any vibrational mode can be expressed by a set of symmetry operations. From an algebraic point of view, the fundamental types of molecular vibrations, depicted in Figure 1.6, are nothing else than symmetry operations. Together with the functional composition, this set of functions build up an algebraic group.

1.2 Dispersion and Absorption

When solving the eigenvalue problem of the driven damped harmonic oscillator in section 1.1.1.1, it was found in equation (1.26), that there is a complex solution. The real and the imaginary part, found in that equation and depicted in Figure 1.1, have the same shapes which are found in theory and, also observed in experimental measurements.

Refraction is, besides reflection, scattering and diffraction, one of the fundamental phenomena that occur when an electromagnetic wave, or commonly "light", interacts with matter. Figure 1.8 depicts the situation, if all four phenomena occur at the same time, what in principle always is the case. Refraction and scattering occurs in highest strength, if the surface between material 1 and 2 has a roughness in the size of the wavelength range of the incident electromagnetic wave. In the experiments discussed in this thesis, polished, smooth surfaces were used, thus scattering from the surfaces could be neglected. Usually, the intensity of reflected and transmitted light is dependent on various parameters. It is a matter of optical properties of the material with that the electromagnetic wave interacts, as well as on polarization and angle of incidence.

The angle of refraction as well as the amplitude of the electromagnetic wave after it travelled a given distance trough material 2 is dependent from the wavelength. The effect, that the angle of refraction is dependent from the wavelength is called dispersion. The effect, that the amplitude of the electromagnetic wave is getting smaller the wider it travels through a material, is called absorption.
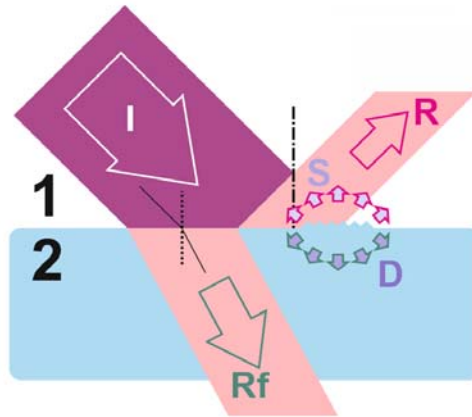
Figure 1.8: Overview over light matter interactions. Incident electromagnetic wave (I), Refraction (Rf), Reflection (R), Diffraction (D) and Scattering (S)

The main focus of this thesis is dispersion spectroscopy. Thus the spectrum of interest is the wavelength dependent real part of the complex refractive index. While absorption is best described by the Lambert-Beer law to be introduced later, dispersion is best described by the Snellius law

$$n_{1,2} = \frac{c_1}{c_2} = \frac{n_2}{n_1} = \frac{\sin \alpha_1}{\sin \alpha_2}$$

(1.53)

where n_1 and n_1 are the refractive numbers of material 1 and 2, α_1 and α_2 the angle between the materials surface and the right angle to that surface and c_1 and c_2 the speed of light in the first (1) and the second (2) material, an electromagnetic wave crosses. $n_{1,2}$ is the refractive index of the passage from material 1 to material 2.

Starting point of the discussion of the phenomena of wavelength dependent absorption and dispersion is a microscopic model that considers an electromagnetic wave and its interaction with matter.

1.2.1   Microscopic Model – Complex Refractive Index

To discuss the effect of dispersion and absorption of an electromagnetic wave in matter, the complex form of a plane electromagnetic wave[31], $E(x,t) = E_0\, e^{i(\omega t - kx)}$ is used. $E(x,t)$ is here the electromagnetic field strength of the wave with the amplitude E_0, corresponding to the amplitude A of a harmonic oscillator, discussed in section 1.1.1. The difference to the harmonic oscillator discussed there is the term $-kx$ with the wave vector k. It describes the dependency of the electromagnetic field strength of the position x – additionally to the time t. With the velocity, the wave propagates along a given direction x through a medium, the phase velocity $v_{Ph} = \frac{\omega}{k}$, $E(x,t)$ can be expressed as

$$E(x,t) = E_0\, e^{i\omega\left(t - \frac{x}{v_{Ph}}\right)} \tag{1.54}$$

While the electromagnetic wave in vacuum propagates with the speed of light c, the phase velocity is experimentally found to be reduced by a factor n, so that it holds $v_{Ph} = \frac{c}{n}$. Additionally, this factor was found to be wavelength-dependent. If the wave propagates through a medium of thickness Δx, this takes, due to the reduced velocity in that medium, an additional time

$$\Delta t = \frac{\Delta x}{v_{Ph}} - \frac{\Delta x}{c} = \frac{n\Delta x}{c} - \frac{\Delta x}{c} = (n-1)\frac{\Delta x}{c} \tag{1.55}$$

This means, that after passing the medium, the wave can be written as

$$E(x,t) = E_0\, e^{i\omega\left(t - (n-1)\frac{\Delta x}{c} - \frac{x}{c}\right)} = E_0\, e^{i\omega\left(t - \frac{x}{c}\right)} e^{-i\omega(n-1)\frac{\Delta x}{c}} =: E_0\, e^{i\omega\left(t - \frac{x}{c}\right)} e^{-i\Delta\varphi} \tag{1.56}$$

The factor $E_0\, e^{i\omega\left(t - \frac{x}{c}\right)}$ describes the wave in the form it would have at the position x, if there was not any medium along the distance Δx – it is the incident wave that has propagated to a position x after the space, where the medium of thickness Δx will be placed. The factor $e^{-i\omega(n-1)\frac{\Delta x}{c}}$ describes the influence of the medium. This influence on the incident wave is equivalent to a phase shift

$$\Delta\varphi = \omega(n-1)\frac{\Delta x}{c} \tag{1.57}$$

If the phase velocity differs not much from the speed of light, what is equivalent to a factor n of $n \approx 1$, what is fulfilled in good approximation for gasses, the phase shift $\Delta\varphi$ is near zero and the approximation

$$e^{-i\Delta\varphi} \approx 1 - i\Delta\varphi \tag{1.58}$$

can be used. With that, the expression for $E(x,t)$ from equation (1.56) can be written as

$$E(x,t) = E_0\, e^{i\omega\left(t-\frac{x}{c}\right)} - i\omega(n-1)\frac{\Delta x}{c}\, e^{i\omega\left(t-\frac{x}{c}\right)} = E_i + \sum_d E_d \tag{1.59}$$

This is a superposition of the incident wave $E_i = E_0\, e^{i\omega\left(t-\frac{x}{c}\right)}$ and the sum of the field contributions from all particles in the medium $\sum_d E_d = -i\omega(n-1)\frac{\Delta x}{c}\, e^{i\omega\left(t-\frac{x}{c}\right)}$.

If an electromagnetic wave enters a medium of thickness Δx, it interacts with charged particles – in the simplest model this is just a single electron – and forces them to perform also an oscillation. These charged particles have own electromagnetic fields that, due to the oscillation of the particles induced by the incident electromagnetic wave, generate secondary electromagnetic fields E_d. The same applies to an oscillating dipole during molecular vibration.

With this interpretation, E_d denotes the induced field of one such single oscillator. To understand the effects of absorption and dispersion, the structure of the second term, $\sum_d E_d$ has to be discussed more detailed. Therefore, the model of a driven damped harmonic oscillator in equation (1.20) is adapted:

In a first step, a single electron in the medium with charge $-\hat{e}$ oscillating relative to the atomic nucleus with a charge of $\hat{e}$, forming a simple dipole is considered. On that dipole – with fixed atomic nucleus, so that just the electron is oscillating – the incident electromagnetic field E_i is acting and the electron finds a force

$$F = -\hat{e} \cdot E_i \tag{1.60}$$

with the elementary charge $\hat{e} = 1.602 \cdot 10^{-19}\, C$ acting on it. The complex equation of motion for that electron can then be written as differential equation for the wave amplitude $a(x,t)$:

$$\ddot{a} + 2\gamma\dot{a} + \omega_0^2 a = -\hat{e}E_0\, e^{i(\omega t - kx)} \tag{1.61}$$

where the constants are defined in the same way as it was done in section 1.1.1. For simplification reasons, here a polarized wave in x-direction is considered. Analog to the solution for the driven damped harmonic oscillator, for the amplitude $a_{x=0}$ of the electromagnetic wave induced by the oscillating dipole at the position $x = 0$ it can be found

$$a_{x=0} = -\frac{\hat{e}}{m}\frac{1}{\omega_0^2 - \omega^2 + 2i\gamma\omega} E_0 e^{i\omega t} \tag{1.62}$$

$x = 0$ is the equilibrium position of the dipole and therefore the "surface" of the model medium. In order to find a real expression for the amplitude of the oscillating term $e^{i\omega t}$, $a_{x=0}$ is first multiplied by the complex conjugate of the denominator, what leads to

$$a_{x=0} = -\frac{\hat{e}}{m}\frac{\omega_0^2 - \omega^2 - 2i\gamma\omega}{(\omega_0^2 - \omega^2)^2 + 4\gamma^2\omega^2} E_0 e^{i\omega t} \tag{1.63}$$

Then, a coordinate change to polar coordinates is performed. With the real part $\mathrm{Re} = \frac{\omega_0^2 - \omega^2}{\left(\omega_0^2 - \omega^2\right)^2 + 4\gamma^2\omega^2}$, the imaginary part $\mathrm{Im} = \frac{-2\gamma\omega}{\left(\omega_0^2 - \omega^2\right)^2 + 4\gamma^2\omega^2}$ and the relation $r = \sqrt{\mathrm{Re}^2 + \mathrm{Im}^2}$ it can be found by introducing the phase $\varphi = \arctan\left(-\frac{2\gamma\omega}{\left(\omega_0^2 - \omega^2\right)}\right)$

$$a_{x=0} = -\frac{\hat{e}}{m} \cdot \frac{1}{\sqrt{(\omega_0^2 - \omega^2)^2 + 4\gamma^2\omega^2}} e^{i\varphi} \cdot E_0 e^{i\omega t}$$

(1.64)

The next step is, to discuss the dipoles contribution E_d to the total field $\sum_d E_d$ of all induced oscillating dipoles. From electrodynamics it is known, that at a position r, under an angle ξ from the x axis, far away from $x = 0$, where the electromagnetic wave traveling with the speed of light c arrives after a time $t = \frac{r}{c}$, the contribution to the total field of that given dipole, E_d, is

$$E_d(r, \xi) = -\frac{\hat{e}\omega^2 a_{x=0}}{4\pi\varepsilon_0 c^2} \cdot \frac{1}{r} \cdot \sin\xi \cdot e^{i\omega\left(t-\frac{r}{c}\right)}$$

(1.65)

with the dielectric constant ε_0. Since a position far behind the medium is considered, the angle ξ for all electrons in the medium is only negligibly smaller than 90° and it can be approximated $\sin\xi \approx 1$.

To find an expression for the total field, generated by all dipoles in the medium of thickness Δx that are excited by the incident wave E_i, the particles in that medium are assumed to be uniformly distributed. This means, that the medium can be described by a constant dipole density N, describing the number of dipoles in an infinitesimally small circular area $dA = 2\pi\varrho d\varrho$ with radius ϱ in the plane perpendicular to the polarization direction x of the incident wave. With that, the total field $\sum_d E_d$ generated by all dipoles in the medium of thickness Δx can be found by integration along ϱ of $E_d(r, \xi) \cdot N \cdot \Delta x \cdot dA$. With $r^2 = x^2 + \varrho^2$, and therefore $\varrho d\varrho = rdr$ because x is constant in the given, fixed distance far away from $x = 0$, the total field $\sum_d E_d$ has the form

$$\Sigma_d E_d = -\frac{\hat{e}\omega^2 a_{x=0} e^{i\omega t}}{4\pi\varepsilon_0 c^2} \cdot \Delta x \cdot N \cdot \int_{r=x}^{\infty} \frac{1}{r} \cdot e^{-i\omega\frac{r}{c}} \cdot 2\pi r dr$$

(1.66)

For the integral it holds $\int_{r=x}^{\infty} e^{-i\omega\frac{r}{c}} dr = \frac{ic}{\omega}\left[e^{-i\omega\frac{r}{c}}\right]_x^{\infty}$. Because the incident wave is a beam of finite diameter, the upper limit of the integral can be neglected and it is found

$$\Sigma_d E_d = \frac{i\hat{e}\omega a_{x=0} N}{2\varepsilon_0 c} \cdot \Delta x \cdot e^{i\omega\left(t-\frac{x}{c}\right)}$$

(1.67)

With the expression for $a_{x=0}$ from equation (1.63) this can be expressed as

$$\Sigma_d E_d = -i\omega \frac{\Delta x}{c} \frac{N\hat{e}^2}{2\varepsilon_0 m(\omega_0^2 - \omega^2 - 2i\gamma\omega)} \cdot E_0 e^{i\omega\left(t-\frac{x}{c}\right)}$$

(1.68)

Comparing this to equation (1.59) allows to recognize the initially introduced factor n as

$$n = 1 + \frac{N\hat{e}^2}{2\varepsilon_0 m(\omega_0^2 - \omega^2 - 2i\gamma\omega)}$$

(1.69)

When the fraction is multiplied by the complex conjugate of the denominator this leads to

$$n = 1 + \frac{N\hat{e}^2}{2\varepsilon_0 m} \cdot \frac{\omega_0^2 - \omega^2}{(\omega_0^2 - \omega^2)^2 + 4\gamma^2\omega^2} - i\frac{N\hat{e}^2}{2\varepsilon_0 m}\frac{2\omega\gamma}{(\omega_0^2 - \omega^2)^2 + 4\gamma^2\omega^2} \tag{1.70}$$

This means that the factor $n =: n_r + \kappa$ that is actually a complex factor and is called the complex refractive index, has a real and an imaginary part. The real part of n,

$$n_r(\omega) := 1 + \frac{N\hat{e}^2}{2\varepsilon_0 m} \cdot \frac{\omega_0^2 - \omega^2}{(\omega_0^2 - \omega^2)^2 + 4\gamma^2\omega^2} \tag{1.71}$$

is called coefficient of dispersion and describes the dispersive effect of the medium. The imaginary part

$$\kappa(\omega) := \frac{N\hat{e}^2}{2\varepsilon_0 m}\frac{2\omega\gamma}{(\omega_0^2 - \omega^2)^2 + 4\gamma^2\omega^2} \tag{1.72}$$

Is proportional to the coefficient of absorption. This becomes clear, when equation (1.70) is substituted to equation (1.56): The real exponential function that remains, $e^{-\omega\kappa\frac{\Delta x}{c}}$ describes an exponential decrease of the amplitude of the electromagnetic wave when passing the medium. This is nothing else than the Lambert-Beer law. With the coefficient of absorption ε, the relation

$$\varepsilon = \frac{2}{c} \cdot \omega \cdot \kappa \tag{1.73}$$

can be found.

Another important note is, that again – the situation is the same as it was described during the discussion of the driven damped harmonic oscillator – the frequency of maximum absorption, characterized by $\frac{\partial}{\partial\omega}\kappa(\omega) = 0$ can be found by

$$\omega_{\kappa_{max}} = \omega_0\sqrt{1 - \frac{\gamma^2}{3\omega_0^2}} \tag{1.74}$$

That means, that the absorption maximum does not exactly match with the eigenfrequency ω_0 of the model harmonic oscillator. Since the damping γ is very weak with $\gamma \ll \omega_0$, the difference between absorption maximum and eigenfrequency is very small.

If the expressions found in equations (1.71) are (1.72) are compared to the results found during the discussion of the damped harmonic oscillator in equation (1.26), it can be recognized that the expressions have, besides scaling factors, the same mathematical structure. The functions $n_r(\omega)$ and $\kappa(\omega)$ have, around ω_0, the same shape as it is depicted in Figure 1.1.

The shape of the $\kappa(\omega)$ function and therefore also the absorption spectrum around ω_0 has a well-known form: It has the shape of a shifted Lorentzian curve $L(x) = \frac{A}{B(x-x_0)^2+1}$. This can be understood, if equation (1.72) is considered in a neighborhood of $\omega = \omega_0$ and when it is taken into account that for the present case of weak damping $\gamma \ll \omega_0$ holds. With that and neglecting the electrodynamic prefactor, equation (1.72) can be written as

$$\kappa(\omega)_{\omega \approx \omega_0} \approx \frac{2\gamma\omega_0}{(\omega_0 - \omega)^2(\omega_0 + \omega_0)^2 + 4\gamma^2\omega_0^2} = \frac{2\gamma\omega_0}{(\omega - \omega_0)^2 \cdot 4\omega_0^2 + 4\gamma^2\omega_0^2}$$

$$= \frac{1}{2\gamma\omega_0} \cdot \frac{1}{\frac{1}{\gamma^2}(\omega - \omega_0)^2 + 1}$$

$$(1.75)$$

This is a Lorentz curve $L(\omega)$ with peak position ω_0 and the constants $A = \frac{1}{2\gamma\omega_0}$ and $B = \frac{1}{\gamma^2}$.

1.2.2   Kramers-Kronig-Transformation

The previous section has shown, that there is a strong connection between absorption and dispersion. This leads to the motivation, to see wether it is possible to calculate the absorption spectrum from a recorded dispersion spectrum and vice versa. The optical property of a sample is related to its chemical composition and can be described by its wavelength dependent complex refractive index

$$n(\omega) = n_r(\omega) + i \cdot \kappa(\omega)$$

$$(1.76)$$

Mathematically, what here is looked for is nothing else than a (invertible) transformation that converts the function $n_r(\omega)$ via the connecting function $n(\omega)$ to the function $\kappa(\omega)$. This transformation has been discovered by Hendrik Anthony Kramers[32] and Ralph Kronig[33] and is therefore is called Kramers-Kronig transformation. The transformation connects the real and the imaginary part of a special type of a complex function, a meromorphic function, by an integral equation and represents a special case from the more general Hilbert transformation. The mathematical details would lead to far and do not improve the practical understanding of this transformation and how it is used in spectroscopy. This is why the transformation is presented without derivation. It is also not proven at this point, that the function $n(\omega)$ fulfils all requirements to be a meromorphic function.

The Kramers-Kronig transformation for the real and imaginary part of the complex refractive index can be written as[34]

$$n_r(\omega) = 1 + \frac{2}{\pi} P \left[\int_0^\infty \frac{\omega'\kappa(\omega')}{\omega' - \omega} d\omega' \right]$$

$$(1.77)$$

and in the other direction

$$\kappa(\omega) = \frac{2\omega}{\pi} P \left[\int_0^\infty \frac{n_r(\omega') - 1}{\omega'^2 - \omega^2} d\omega' \right]$$

$$(1.78)$$

P here denotes the Cauchy principal value of the (complex) integral. This can be understood as follows, and is important for the numerical implementation of the Kramers-Kronig transformation in this thesis: If a complex function has a singularity in a range in that it has to be integrated, the nature of the complex numbers can be employed to work around the problem of integrating over a singularity. If the path of the integral leads through a singularity, an alternative path can be used by entering the complex plane. The situation is depicted in Figure 1.9. The alternative path for the integration is still continuous (but it is not differentiable), but is not going through the singularity of the function. This means that the integral can be evaluated. It can be shown, that in the limit of

infinitesimal small "bypass radii" ϱ, the alternative integral has the same value as the initial.

$$\int_{z_1}^{z_2} V(z)\, d\,\gamma_i(z) = \int_{z_1}^{z_2} V(z)\, d\,\gamma_a(z)$$

$$= \int_{z_1}^{z_2} V(z)\, d\,\gamma_a'(z)$$
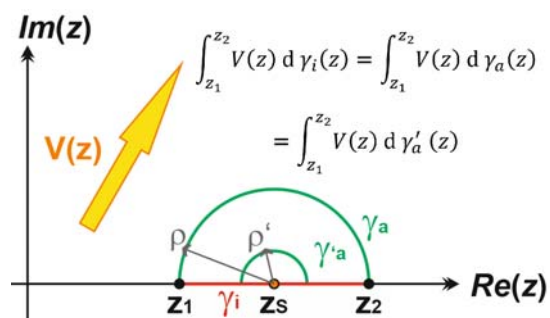
Figure 1.9: Motivation for the Cauchy principal value

For the numerical implementation of a Kramers-Kronig transformation this means, that the transformation can be implemented by discretizing the integral by a sum and leaving out the "critical" summand at the position of the singularity $[\omega_0 - \omega]_{\omega=\omega_0}$. The specific implementation of the Kramers-Kronig transformation in MATLAB, the program used for processing the data in this thesis and the connected publications, is shown in the appendix, page 187.

1.3 Spectroscopy

From a mathematical point of view, the spectrum (of an operator A) is the set[35]

$$\sigma(A) = \{\, \lambda \in \mathbb{C} : Ax = \lambda x, x \in (V, \mathbb{C}) \,\} \tag{1.79}$$

Where $(V, \mathbb{C})$ is a vector space over the complex numbers and A is an operator defined on that vector space. In the section 1.1.1.2, it was demonstrated that in quantum theory, the eigenvalues λ and the corresponding eigenvectors x describe the fundamental modes of behaviour, that a given physical property represented by the operator A – in the considered case of a particle in a harmonic potential the property would be the position of that particle – can show. All modes of behaviour can be described as a combination of those fundamental modes – expressed in terms of linear algebra, (under some additional requirements to the operator A), the set of all eigenvectors form a complete base of the underlying vector space. The corresponding eigenvalues to these eigenvectors were interpreted as the energy levels of the given "fundamental mode of behavior" and were, with the reduced Planck constant $\hbar$, connected with a specific frequency. Here, the connection to the chemical understanding of a "Spectrum" can be found:

Each of those frequencies is connected to the eigenfrequency of a given mode of oscillation, a molecule can perform (section 1.1.3.1). The set of all those frequencies – the molecules spectrum – is a complete and unique description of this molecule. From that, it can be identified among other molecules, and, by measuring not only the values of the eigenfrequencies but also the strengths of the response to those frequencies, quantified.

In analytical chemistry, a spectrum is, generally speaking, the graph of a function, that addresses a measure of response of particles in a sample to a continuously tuned incident physical quantity. In Infrared spectroscopy, this continuously tuned quantity usually is the wavenumber, measured in inverse centimetres. The measure of response investigated in this thesis is, depending on the specific method, a measure of absorption or dispersion of (Mid-) infrared laser radiation caused by induced molecular oscillations. The oscillations observed in this spectral region are molecular vibrations and molecular rotations and combinations thereof.

In some of those methods, the information about the measure of response of the particles in the sample – this will simply be called "signal" from now on – is carried by the incident laser beam with the continuously tuned wavenumber itself after passing the sample volume. Therefore, these methods are called direct methods. In the field of this thesis, all absorption spectroscopy methods that were employed and investigated can be subsumed under direct methods, but also dispersion spectroscopy in the liquid phase is realized as direct technique.

In some other methods, the signal is carried not by the incident laser beam, but is read from some different (part of the) sensor. As an example, this can be second (probe-) laser that measures transmission or reflection of a Fabry-Pérot Cavity (Interferometric cavity-assisted photothermal spectroscopy, ICAPS[8,36]) that contains the sample volume, a sensitive microphone (Photoacoustic spectroscopy[37]) or a quartz tuning fork (Quartz-enhanced photoacoustic spectroscopy, QEPAS[38]). The signal is not (directly) read from the incident laser beam, therefore those methods are called indirect techniques.

Often, an experimental setup offers the opportunity, to investigate both, direct as well as indirect spectroscopic effects. This was especially the case for the sensors that were developed in the field of this thesis.

In the following sections, that close this first theory chapter of this thesis and represents a connecting passage from the underlying, fundamental physical principles to fundamental

technology that is employed in this thesis, the basic principles of direct and indirect spectroscopy techniques are discussed. Further, in Figure 1.10 the very basic difference between direct and indirect spectroscopy techniques is depicted.
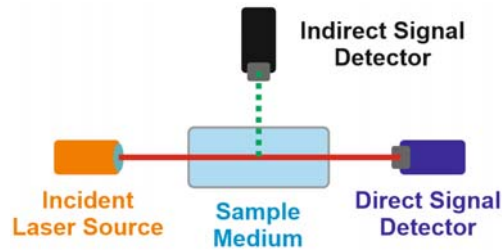

Figure 1.10: Depiction of the principal difference between direct and indirect spectroscopy

1.3.1 Direct Techniques

The direct spectroscopy techniques that were developed and employed in the field of this thesis can be divided in those detecting intensities and phase shifts, respectively. The first group of methods are called Absorption Spectroscopy methods, the second one is called Dispersion Spectroscopy methods.

In direct methods, the laser beam that is used for analyte excitation carries the measurement signal. The incident excitation laser beam is, after interacting with the analyte in a given interaction volume, detected and the detector signal is further processed and analyzed. Especially, there is no other optical signal – the detected excitation laser is – via a more or less complicated electronic and algorithmic signal transduction chain – directly converted to the sensor output signal. An example for a direct sensing method that was experimentally performed in this thesis is direct absorption 2*f*-wavelength modulation spectroscopy (2*f*-WMS), which is discussed in section 3.5.1.

1.3.1.1 Absorption Spectroscopy

The underlying principle for absorption spectroscopy is the Lambert-Beer- law. As already sketched in section 1.2.1, it is a direct consequence of the passage of an incident electromagnetic field that passes a sample medium of thickness Δx. When inserting the result for the complex refractive index in cartesian coordinates from equation (1.70) in the electromagnetic wave in its form after passing the sample medium from equation (1.56), it can be found, that the resulting powers of e can be devided in a real exponential function, describing the decay of the amplitude of the electromagnetic wave during the passage through the medium, and a complex exponential function. This complex exponential function, the oscillating term, describes the phase shift that occurs by passing the medium. This is the dispersive effect of the passage through the medium. The real exponential function that describes the absorption of the electromagnetic wave $E(x,t)$ has the form[31]

$$E_{real} = e^{-\omega\kappa\frac{\Delta x}{c}}$$

(1.80)

and by using the relationship $I = c\varepsilon_0 E^2$ between the Intensity of the light I and the electric field E of the corresponding electromagnetic wave it can be retrieved

$$I = I_0 e^{-\frac{2\omega\kappa}{c} \cdot \Delta x} \tag{1.81}$$

The coefficient $\frac{2\omega\kappa}{c} =: \varepsilon$ is called coefficient of absorption and with that, the relation

$$I = I_0 e^{-\varepsilon \cdot \Delta x} \tag{1.82}$$

is nothing else than the Lambert-Beer law.

The negative decadic logarithm of the relation between the incident intensity I_0 and the intensity I found after the passage through the medium,

$$-\log\frac{I}{I_0} =: A \tag{1.83}$$

is called absorption. It is dimensionless, or, often given the arbitrary unit "AU", called absorption units. With that, the Lambert-Beer-Law can be written as $A = \varepsilon\Delta x$. Since the particles in the sample volume is the only part of the volume that interacts with the electromagnetic wave, the number of particles that the electromagnetic wave interacts with along the travelled distance Δx through the medium, $N(x)\Delta x$ can be written instead of Δx. $N(x)$ here is the already introduced particle density along x. Dividing this expression by the Avogadro constant N_A leads to the molar particle concentration $c = \frac{N(x)}{N_A}$. With this, the linearized form of the Lambert-Beer-Law that is commonly known in Analytical Chemistry

$$A = \varepsilon_m \cdot c \cdot \Delta x \tag{1.84}$$

This shows the linear dependency of the Absorption A from the molar concentration c. The factor ε_m is called molar absorption coefficient.

Special technique: 2f-wavelength modulation (absorption) spectroscopy (2f-WMS)

In the field of modulation spectroscopy, to the continuously but slow (Hz or even mHz range) tuned wavenumber of the incident laser a fast (kHz range) sinusoidal wavelength modulation with fixed frequency f is added. Details of this approach will be discussed in section 3.5.1. The main advantage of this can be explained by theory: The (absorption) signal is now carried only in a very narrow frequency range of the total signal found by the direct signal detector. With a very narrow-band signal filter, a Lock-In-Amplifier (LIA) only that frequency component (actually, the frequency f gets doubled in a special sense, what leads to the designation "2f"-WMS) is read out. All other frequencies present in the detector signal are heavily damped. This is nothing else than a very effective, active noise suppression method that significantly improves the signal to noise ratio (SNR), what is an important figure of merit for the performance of a spectroscopic method.

1.3.1.2 Dispersion Spectroscopy

Considering equations (1.71) to (1.73) it can be derived, that the complex refractive index $n(\omega)$, introduced in section 1.2.1, is a function of the analyte concentration. To understand this, the electric susceptibility

$$\chi = \frac{P}{\varepsilon_0 E}$$

(1.85)

is introduced. With that quantity, which is a proportionality factor between the macroscopic polarization P and electric field E, scaled by the dielectric constant ε_0, the equation describing the frequency-dependence of the refractive index, contains a quantity that is dependent on the number of dipoles in a given volume, what is nothing else than a concentration[39]:

$$n_r(\omega) = \sqrt{1+\chi} = \sqrt{1 + \frac{N_A P c}{\varepsilon_0 N E}}$$

(1.86)

For liquid phase sensing, the Mach-Zehnder interferometer is used in this thesis. This optical device is presented in detail in section 2.2.1. The core of the setup consists of two mirrors and two beamsplitters, that together form a rectangular beam path. One of the mirrors is mounted on a piezo drive, that introduces a displacement $\delta(\omega)$. This displacement is introduced to compensate any phase shifts arising from dispersion that takes place in the corresponding interferometer arm. In this sense, it is a wavenumber-dependent quantity. Since the piezo drive is mounted in a 45° angle to the mirror surface, it holds the relation $d = \delta(\omega) \cdot \sqrt{2}$, where d is the optical pathlength change. As a consequence of the sequence of reflection and transmission in the two beamsplitters in this device, it can be found that the phase shift in the sample arm of a Mach-Zehnder interferometer is[25,39,40]

$$\Delta\varphi = 2\pi\omega d\Delta n = 2\pi\omega\big(\delta(\omega) \cdot \sqrt{2}\big)\Delta n$$

(1.87)

Combining those equations an equation reassambling the Lambert-Beer law from equation (1.82) can be found

$$\mathrm{n}(\omega) = \frac{2\pi N_A \omega P}{NE} cd = \varepsilon_D \cdot c \cdot d_S$$

(1.88)

which shows a linear dependence of the refractive index spectrum amplitude $n(\omega)$ from the analyte concentration c and the sample thickness d_S with a proportionality constant ε_D. In this sense, equation (1.88) represents a relation for dispersion spectroscopy that corresponds to the Lambert-Beer law in absorption spectroscopy.

1.3.2 Indirect Techniques

The energy stored in an electromagnetic wave is proportional to the square of the electromagnetic field strength. If the electromagnetic field strength decreases by absorption in a medium, as a consequence of the conservation of energy, the corresponding energy has to be deposited in the medium. This is the underlying principle of indirect spectroscopy: The deposited energy induces new effects, that can be measured. The magnitude of those can then be related to quantities that describe chemical information about the medium, like the concentration of an analyte.

The incident excitation laser beam that is used in indirect methods usually also carries chemical information about the analyte, after it has passed the interaction volume, although it is not used as the final sensor output signal. However, detecting this beam can be used as an easily implementable reference, what often is done in practical applications. Indirect methods measure

effects, that arise from the interaction of the excitation beam with the analyte. In the case of photothermal spectroscopy, this effect is the photothermal effect: The excitation beam, that gets partially absorbed in the interaction volume, causes a change in refractive index due to temperature change in the focal volume. This refractive index change is then transformed to the sensor output signal. The photothermal effect is always accompanied by another, the photoacoustic effect, that can be sensed using a pressure sensitive detector like a microphone or a tuning fork.
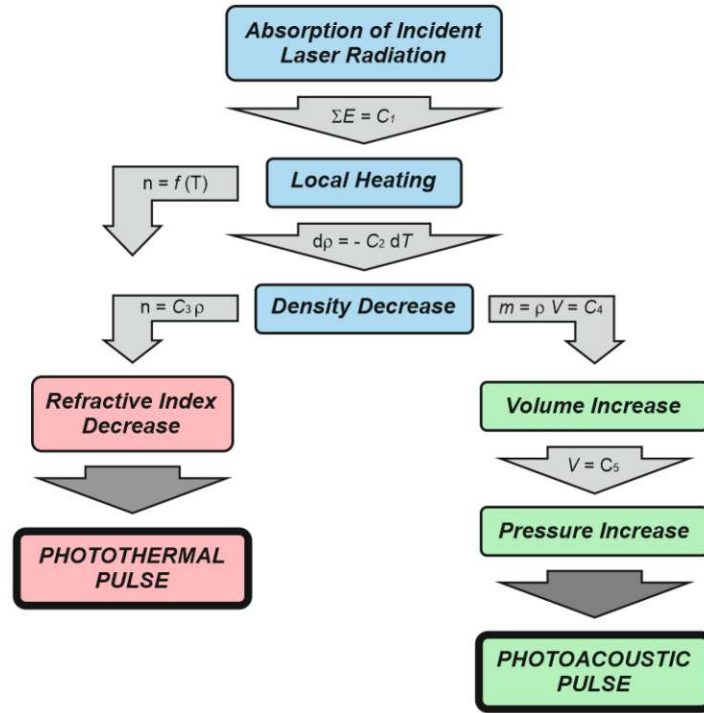

Figure 1.11: Schematic depiction of the formation of the photoacoustic and photothermal wave

The principle steps of formation of the photothermal and the photoacoustic wave are schematically depicted in Figure 1.11. The quantitative description of the photoacoustic as well as of the photothermal effect can be summarized by the strength of the indirect signal S[9]

$$S = k \cdot \frac{P \cdot \varepsilon}{\nu \cdot V_f} \tag{1.89}$$

with a proportionality constant k, the power of the incident laser P, the incident laser's modulation frequency ν, the coefficient of absorption ε and the focal volume V_f.

The theory behind those two effects is very complex, as it is obvious from the multiple steps of formation of the photothermal and photoacoustic wave sketched in Figure 1.11. A sketch of the mathematical formalism of the formation of those two waves is presented in section 1.3.2.3.

In most of the indirect techniques and especially in all indirect techniques discussed in this thesis, the incident laser light is introduced to the sample volume not by a single pulse, but is modulated by a fixed frequency ν. This has the consequence that instead of a single pulse, a wave starts to propagate – the two waves that form by the modulated incident laser are correspondingly called photothermal and photoacoustic wave. Further, the incident laser is guided through a focussing lens before entering the sample volume. The higher the energy density in the sample volume

where the incident laser passes through is, the higher the temperature change and as a consequence, the higher the amplitudes of the formed photothermal and photoacoustic wave are. The part of the sample volume, where the formation of the two waves take place is therefore called the focal volume V_f.

1.3.2.1 Photothermal Effect

This effect causes a change in refractive index: A less dense sample volume, especially if the sample is a gas, has a less dense particle density and can be imagined to get closer to vacuum, what has a refractive index of 1. The heating causes an expansion of the sample volume, causing a reduction of its density and hence also a decrease of the refractive index in the sample volume, where the initial beam passes through. Due to heat conduction, this decrease of the refractive index by heating propagates with time also into the surrounding layers of the sample medium – a (thermal) pulse starts to propagate. This pulse was induced by photons, so the effect it causes is called photothermal effect.

The change of refractive index caused by the photothermal effect can be detected – besides by the technique of Interferometric Cavity-Assisted Photothermal Spectroscopy (ICAPS), that has been investigated in this thesis and is discussed in section 3.5.1 – by a relatively wide field of various methods[41]. Some of them reach detection limits down to the ppb range.

- *Thermal lens microscope*. This method uses the effect, that the heating process due to absorption is not uniform – the highest magnitude of heating takes place along the incident laser beam. The magnitude is going down with increasing radial distance to the beam. From this, layers of continuously changing refractive index emerge forming a (photothermal) lens. This lens can also be used for sensing purposes. There are methods published, that reach suboctomole sensitivity in liquid samples[42].

- *Dual beam photothermal spectroscopy based on a Mach-Zehnder interferometer*[43]. This method employs a Mach-Zehnder interferometer to measure water in organic solvents by the photothermal effect. The photothermal wave is detected by a Helium-Neon laser that overlaps with one of the two beams of a Mach-Zehnder interferometer.

- *Mach-Zehnder interferometer based spatial gas localization*[44]. In this method, a gas sample is introduced in one arm of a Mach-Zehnder interferometer, while the other arm contains an acousto-optic modulator (AOM). The gas sample volume is excited with an excitation laser emitting at an absorbance maximum of the desired analyte gas. With this configuration, the position of the analyte gas in the sample volume can be retrieved from the frequency spectrum of the demodulated detector signal.

- *Photothermal spectroscopy in hollow-core-fibers*[45]. The inner volume of hollow-core fibers can be used to guide an excitation laser as well as a probe laser through a relatively small volume, resulting in a high interaction length.

- *Intra-cavity photothermal spectroscopy*[46]. This method describes an all-fiber configuration, that brings the advantage of potentially high ruggedness. The cavity plays here a double role: On the one hand, it is used to increase the pathlength of the excitation beam and on the other hand, it is used to read out the photothermal wave that is formed.

1.3.2.2 Photoacoustic Effect

The temperature change due to absorption causes apart from a change in refractive index, also a pressure change. Due to heat conduction, the volume decreases again. If the excitation is periodic, what is the case in photothermal and photoacoustic spectroscopy, also a pressure (acoustic) wave is formed. This is particularly the case for higher modulation frequency from the range of some tens of kHz on: Due to the sluggishness of heat conduction, the thermodynamic process is of adiabatic nature. The tone that is formed can be sensed by a suitable microphone and converted into a sensor output signal. The photoacoustic effect can be used for a wide field of technological applications:

- *Cantilever Enhanced Photoacoustic Spectroscopy (CEPAS)*[47]. CEPAS employs a cantilever that picks up the photoacoustic wave. Similar to QEPAS and also the photothermal method ICAPS, CEPAS benefits from small sample volumes. This means that a sensor miniaturisation, which is also generally advantageous in terms of technological applications of the analyzer, is even beneficial for the technique. CEPAS has also been commercialized (GASERA).
- *Integrated circuit photoacoustic sensor.* The photoacoustic wave can be detected by a miniaturized electronic microphone. This technique, registered as CMOSense® by the swiss company Sensirion allows to build hand-held devices that have a size below one cm^3 and offer a sensitivity of 50 ppm and lower, what is enough to use the analyzer for simple and cheap indoor CO_2 monitoring[48].
- *Quartz Enhanced Photoacoustic Spectroscopy (QEPAS)*[37,38,49]*.* This chemical sensing method for trace gases achieves detection limits down to the ppt range. In this method, an excitation laser is modulated in the higher kHz range – a frequency, where quartz tuning forks have their resonance frequency. The excitation laser is guided through the prongs of such a tuning fork, and the electrodes placed on the tuning fork pick up the piezoelectric voltage that is generated as soon as the tuning fork gets in resonance with the (detected) photoacoustic wave.
- *Optical microphone*[50]. When a laser's wavelength is coupled to the inflection point of the cavity transfer function of a Fabry-Pérot interferometer, a system that is highly sensitive to changes of refractive index can be established. One way of causing refractive index changes is, if the gas pressure changes. This is the case, if a sound wave is propagating through a given volume. If the previously described system is introduced in such a volume, a optical microphone can be built.

1.3.2.3 Sketch of the Mathematical Description of the Photothermal and Photoacoustic Effect

The first step in describing the formation of photoacoustic and a photothermal waves is to model the heat dissipation in a given sample volume. The sample volume is here assumed to be isotropic in terms of its heat conductivity. This leads to the heat equation[51]

$$(\partial_t - \nabla^2)\,\theta(\boldsymbol{x},t) = f(\boldsymbol{x},t) \tag{1.90}$$

with the disturbance function $f(\boldsymbol{x},t)$, which is a function of the time t and the spatial vector $\boldsymbol{x}$. Further, $\theta(\boldsymbol{x},t)$ denotes the temperature field that is looked for. $\nabla^2 = \Delta$ denotes the Laplace operator. The fundamental solution of this Partial Differential Equation (PDE) can be found as

$$\theta(\boldsymbol{x},t) = \begin{cases} (4\pi t)^{-\frac{3}{2}} e^{-\frac{|\boldsymbol{x}|^2}{4t}} & t > 0 \\ 0 & t < 0 \end{cases}$$

(1.91)

The disturbance function f describes the incident laser beam. A real laser beam with a finite diameter can be modelled best with a gauss-shaped intensity distribution. See therefore also the measured data in section 2.1.3. Further, to describe the medium in that the laser beam propagates, an absorption behaviour that follows the Lambert-Beer law from equation (1.84) is assumed. This leads to the following form of the disturbance function:

$$f(\boldsymbol{x},t) = \frac{P}{2\pi\sigma^2} e^{-\frac{1}{2\sigma^2} \cdot \frac{\langle \boldsymbol{l},\boldsymbol{n}\rangle}{\|\boldsymbol{l}\|^2}}$$

(1.92)

P denotes the laser power and σ its beam waist. $\boldsymbol{l}$ denotes the spatial unity vector of the direction of the laser beam and $\boldsymbol{n}$ the surface normal of the sample volume.

As soon as the photoacoustic wave starts to propagate, fluid dynamics in the sample medium has to be taken into account as well. This has to be done with the Navier-Stokes equations.

To get a model for the complete system, the Navier Stokes equations have to be combined with the heat equation. After using some algebraic decompositions to simplify the problem, like the Helmholtz-Hodge decomposition[52], that allows to separate a vector field into a transverse and a and conservative vector field, the following system of PDE's is found:

$$\begin{cases} \partial_t \theta + A \operatorname{div} u - B\nabla^2\theta = \dfrac{H(\boldsymbol{x},t)}{C} \\ \partial_t(p - D\theta) + E \operatorname{div} u = 0 \\ \rho\, \partial_t u + \operatorname{grad} p - \dfrac{4\eta}{3}\nabla^2 u = 0 \end{cases}$$

(1.93)

This system cannot be solved analytically. Therefore, it was numerically simulated with the software COMSOL Multiphysics[53]. In Figure 1.12 the simulation results for a laser beam that hits an isotropic material is shown. The depiction shows the (uniform) heat distribution before the laser hits the sample volume ($t = 0$) and the heat distribution after one and two seconds after switching on the laser beam.
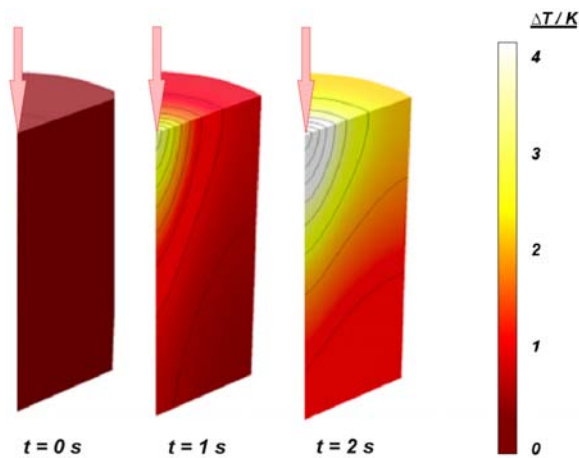
Figure 1.12: Simulation of the heat distribution in an isotropic sample volume while being hit by a laser beam (light red arrow)

1.3.2.4 Differences in Technical Properties of Photothermal and Photoacoustic Wave

As it can be recognized from theory[9], the photothermal and the photoacoustic effect always arise together. Nevertheless, both waves – the photothermal and the photoacoustic wave – have highly different physical properties, especially in terms of damping, that can technically exploited.

While the photothermal wave is heavily damped, the photoacoustic wave is weakly damped (see section 1.1.1.1). Therefore the microphone can detect sound waves, whose origin is spatially seperated from the sensor.

In photothermal spectroscopy, the photothermal wave is, because of the fact that it is heavily damped, only detectable *in loco nascendi*, in a very narrow volume around the point of origin. This point of origin usually is the focal spot of the excitation laser. This high locality of the photothermal effect can on the one hand lead to technical difficulties, since the focal spot has to be precisely adjusted. On the other hand a reference sensor, that measures the background signal, can be installed very close to the photothermal sensor. This allows the implementation of optical balanced detection sensing schemes, where the reference sensor is used to subtract the background noise in real-time.

Chapter 2   Fundamentals - Technology

In this second Chapter the fundamental technologies are presented and discussed. This includes the operating principles of all relevant hardware components used in the experimental setups. Beginning with the various types of infrared lasers that are used as light sources, the different interferometer types will be discussed as they are the optical core components of the setups. Finally it comes to one of the cores of this thesis, the technology of signal processing, where most of the developments in this thesis were achieved.

2.1 Semiconductor Lasers

One of the most basic models that can be used for the description of semiconductor devices is a particle in a quantum well. This is a potential, that has a finite, negative value in an area of finite dimension and is zero outside this area. An example is depicted in Figure 1.4, orange plot. The potential can be written as[20]

$$V(x) = \begin{cases} -V_0 & -\dfrac{a}{2} < x < \dfrac{a}{2} \\ 0 & x < -\dfrac{a}{2} \lor x > \dfrac{a}{2} \end{cases}$$

(2.94)

For an infinitely deep potential well, so for $V_0 = \infty$, the solutions for the corresponding Schrödinger equation

$$\left[-\frac{\hbar^2}{2m} \cdot \partial_x^2 + V(x) \right] \psi(x) = E\, \psi(x)$$

(2.95)

can be found by

$$E_n = \frac{n^2 \pi^2 \hbar^2}{2ma^2}$$

(2.96)

for the eigenenergies and

$$\psi_n(x) = \sqrt{\frac{2}{a}} \sin\left(\frac{n\pi x}{a} \right)$$

(2.97)

for the corresponding wavefunctions. These wavefunctions can be found by simple considerations: starting from the general solution of the differential equation in (2.95), $\psi(x) = Ae^{ikx} + Be^{-ikx}$, it has to be recognized, that inside the potential well, including the boundary, the wavefunction has to be continuous. Behind the boundaries, the wavefunction has to be zero. This leads to the requirement that at the boundaries the wavefunction as well as the wavefunction's first derivative have to be zero. These wavefunctions have the same form as the standing waves in a black body radiator, depicted in Figure 1.2.

If the potential well has a finite depth, the wavefunction is not zero behind the boundaries, rather it shows an exponential decrease. The situation is the same as it was discussed for the harmonic oscillator in section 1.1.1.2 with the result depicted in Figure 1.5: Also here, the wavefunction decreases exponentially outside the parabolic potential well.

If there is another potential well in the direction where the wave function propagates and the "wall" that separates that two wells is small compared to the length, within that the wavefuinction amplitude decreases, the wavefunction amplitude is not zero in the next potential well. This is nothing else than the tunneling effect.

Real semiconductors, that are more or less perfect crystals, can be described by a potential consisting of two components. The first one is a Coulomb potential that describes the electric field and therefore the interaction between charges. The second one arises from the spatially well-defined lattice of such semiconductor crystals – the potential it is a periodic, three dimensional cascade of potential wells, called lattice potential.

In general, there are no analytical solutions for the Schrödinger equation with such complicated potentials. A very successful numerical approach whose development is still ongoing is the dynamical mean field theory (DMFT)[54]. This approach can be used to model the field that arises

from a combination of given semiconductor layers, as it is done for Quantum Cascade Laser simulation before they can be fabricated.

2.1.1   Underlying Principles

In the field of this thesis, infrared lasers of different types are used as sources of infrared radiation. To understand the principle of infrared solid state lasers, the light generating process, the photo effect, and the principle of a laser has to be understood.

2.1.1.1   Photoeffect

The underlying effect for light generation by semiconductors is the photo effect, discovered by Hertz, Hallwachs and Lenard[55]: It was observed, that a metal plane that carried a negative charge, was losing that charge over time, if ultra violet light was shined on it. This meant, that electrons must have been leaving the metal plate. Lenard found out, that the energy of the electrons depend not on the intensity of the light – higher intensity lead to more emitted electrons but not to electrons of higher energy – but on the frequency of the incident light. The correct theoretical description was found by A. Einstein[56]: The energy of the incident photons, $h\nu$, equals the kinetic energy of the electron $h\nu$ and the work function eU.

$$E = h\nu + eU$$

<div align="right">(2.98)</div>

This effect can also be reversed: An electron of specific energy can cause the emission of a photon with a frequency corresponding to equation (2.98). In the introduction to this section and also in the section dealing with the harmonic oscillator, it was found that the energy of an electron in a given potential – and semiconductor crystal lattice provides such a potential for the electron – cannot have any value, but just discrete values (see equations (1.44), (2.96)). As a consequence and because of equation (2.98) the frequency values of the emitted photons can also have only discrete values. This is a huge difference to "classic" light sources like the glowing filament in a light bulb or, especially for infrared radiation, the globar. These sources are based on heat radiation, following the Maxwell-Boltzmann distribution – its emission spectrum is continuous.

2.1.1.2   Semiconductors – n and p Type Conductors

Semiconductors consist of a perfect crystal of mostly silicon or germanium. These elements have four valence electrons, what means that all electrons are used to form the chemical bonds between the atoms in a crystal lattice. As a consequence there are no free electrons in the lattice. If the crystal is doped with atoms that either have three (p-conductors, *p*ositive) or five (n-conductors, *n*egative) valence electrons, this lattice gets disturbed: in n-semiconductors, there is an overflow of electrons, while in p-semiconductors there is a lack of these. A missing electron is called a hole. The combination of a p- and a n-conductor leads to a diode, what is the fundamental component of modern logical electronics. Under some circumstances, that are not discussed in detail because that would lead too far, the (reversible) recombination of an electron and a hole can release the energy causing the emission of a photon by the (inverse) photo effect.

2.1.1.3   Laser

The word laser is an acronym for **L**ight **A**mplification by **S**timulated **E**mission of **R**adiation, that in principle already explains how that device works: A light wave, gets amplified (by self-interference

along a given direction) because more light (of the same wavelength) is generated in the volume, where the initial light wave travels. This additional light has to emerge in the volume itself without introducing any obstacle in the way of travelling for the initial light wave. This requirement can be fulfilled by light emission in a material, that is transparent for the emitted wavelength. Since the energy for this emission has to come from somewhere else to form a stable process, spontaneous emission is not enough and stimulated emission is required. Figure 2.1 shows a principal sketch of a laser.
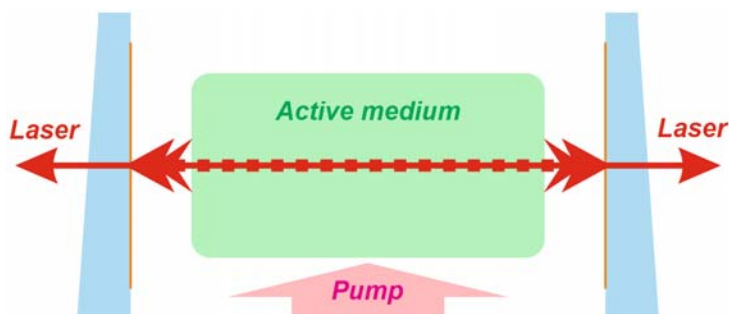

Figure 2.1: General principle of a laser

One of the most important properties of the laser radiation, compared to classical light sources, is the far higher coherence length. The coherence length is the length, in that an emitted electromagnetic wave has a stable phase. Common light sources such as blackbody emitters, usually have coherence lengths in the range of a few multiples of the wavelength. Contrary to that, lasers have coherence lengths up to macroscopic scales, some lasers even shown coherence lengths in the km range. This long coherence lengths makes technical exploitation of interference effects possible, which is highly relevant for the techniques that have been investigated and developed within this thesis.

Another big difference of a laser compared to classical thermic emitters is the far narrower spectral power density compared to a thermal emitter. While the spectrum of a thermal emitter covers several orders of magnitude of wavenumbers, a laser has a spectral with below 1 cm^{-1} (see Figure 3.16).

Further, the emitted radiation of a laser is polarized – another property, a thermal emitter does not have. This can be technically important (selection of the correct optical fibers in a fiber based experimental setup, orientation of beamsplitters). Also, it allows to use components, whose operation principle is based on polarized light, like an optical circulator. Finally, it is to be mentioned that there are spectroscopic methods based on the polarized nature of the employed light source, like Vibrational Circular Dichroism Spectroscopy[57].

2.1.2   NIR Diode Laser

In the simplest form of a semiconductor laser, the diode laser, the lattice of has a two-sided role: On the one hand, it provides the pump source because of the photo effect that takes place due to the change of the electron between different energy levels. On the other hand, the macroscopic surface of the semiconductor crystals act as resonator mirrors for the emerging laser wave. Due to the crystal nature of the semiconductor, these surfaces also follow the crystal lattice and therefor offer a very flat surface of high optical quality.

In this thesis, a NIR diode laser was used in the experimental setups developed for gas sensing.

Their operation principles are explained in the following subsections.

2.1.2.1   Distributed Feedback (DFB) Laser

The idea of a distributed feedback laser is, that the active medium has a periodic structure with alternating regions of different refractive index[58]. This means, that in the direction of propagation, the laser beam sees a one-dimensional grating that acts as a Fabry-Pérot filter and has the effect of an additional wavelength selection: As the depiction in Figure 2.1 shows, a basic laser – for a semiconductor (diode) laser, the active medium is the junction area between the p- and the n-conductor - forms a Fabry-Pérot interferometer. As it will be discussed in section 2.2.2, in a Fabry-Pérot interferometer, not only one frequency, but also other frequencies get amplified. These so-called "sidemodes" can lead to problems like dispersion effects in optical fibers. To avoid the unwanted effects coming from sidemodes, they are suppressed by the previously mentioned periodic structure of alternating refractive index.

The wavelength-selecting property of the one-dimensional grating is in principle defined by two quantities:

- The thickness of the elements of the periodic structure. Since the structure is macroscopic and therefore has finite size, it is affected by heat expansion of the material. On the one hand, this means that in order to stabilize one specific wavelength, a very precise temperature control has to be implemented. On the other hand, it means, that if the temperature of the grating is changed by purpose, the wavelength the DFB-laser emits can be tuned at least in a narrow range.

- The current, that is flowing through the active zone of the laser (injection current). Higher injection current leads also to increased heating but also to a higher charge density in the active zone and therefore in the Fabry-Pérot filter structure. This varying charge density leads to varying refractive indices of the elements of the structure, what also has influence on the wavelength that is emitted. The tuning by injection current leads to a second effect besides the wavelength change, that has to be taken into account: The change of the amount of electrons that pass the active zone and therefore the filter structure, leads also to a change in the emitted laser power.

Both tuning capabilities are very crucial for the applications that have been developed in this thesis. Also the different time scales of the two ways to tune the laser have been exploited: While the temperature tuning can just be performed on a relatively large time scale (nm per second range), but therefore in a wavelength range of around 10 nm compared to just below 1 nm for the injection current tuning. However, injection current tuning can be performed very fast, even below nm per ms range.

2.1.2.2   Fiber Coupling

Fiber-based optical setups are advantageous compared to those using free space optics, because they are far easier to align and there are more degrees of freedom how to arrange optical components in an experimental setup. Also, fiber-based setups are potentially more robust, because of these reasons.

Optical fibers have been developed for telecom applications, especially for wavelengths in the NIR range. Optical fibers in the NIR range show significantly better performance than in MIR. In this thesis, fibers based on a solid core are used, where the effect of total reflection is employed: If a

laser beam (or any other electromagnetic wave) is guided from a medium of refractive index n to a medium of refractive index m and it holds $m < n$, then the angle of the incident beam to the surface normal, α, is smaller than the angle of the refracted beam to the surface normal, β. The consequence is, that there is an angle α_T of the incident laser, so that the refracted beam is parallel to the surface between the materials with refractive index n and m. This angle is called angle of total reflection: If α is increased beyond α_T, the beam is not entering the medium of refractive index m at all (besides the so-called evanescent field: The corresponding electromagnetic field has a finite, exponentially decreasing amplitude in the medium of refractive index m). It gets totally reflected back into the material of refractive index n. The situation is depicted in Figure 2.2. The angle of total reflection can be calculated by

$$\alpha_T = \arcsin\left(\frac{m}{n}\right)$$

<div align="right">(2.99)</div>

what follows directly from the Snellius law in equation (1.53).

The effect of total reflection can be used for guiding a laser beam in a thin optical fiber: An optical fiber consists of a core fiber of refractive index n that is surrounded by another material that has a refractive index m (cladding), again holding $m < n$. Figure 2.2 shows what is going on: due to multiple total reflection, the laser beam follows the fiber and can be guided as technically required.

If a fiber entrance is placed right after the active area of a (DFB) laser diode, the laser emits all the light into the fiber. The technical challenge here is, to get the emitted laser light into the fiber with losses that are as small as possible. Although these losses cannot be brought down to zero, this technology is highly beneficial: There are many optical components commercially available that allow to set up an experiment just by plugging one (fiber coupled) component after the other. Thus, the time consuming step of optical alignment of the different components is omitted. As a last note, it is important to not mix up fiber coupled lasers with fiber lasers: while for fiber coupled lasers the fiber is just the way to guide the laser light, whereas a fiber lasers the fiber is an active component of the laser itself: It is used as external resonator, so the laser is formed by the light emitting semiconductor chip and the resonance formed in the fiber.
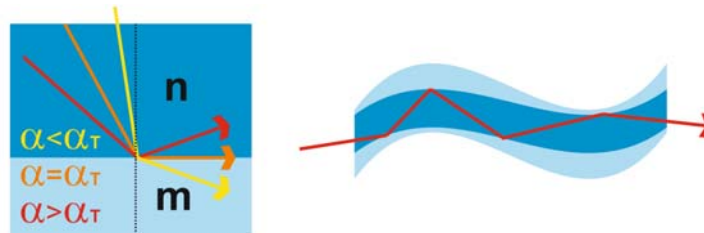

Figure 2.2: Left: principle of total reflection. Right: Total reflection in a fiber.

2.1.3 Quantum Cascade Laser (QCL)

The quantum cascade laser (QCL), a relatively young technology of semiconductor lasers, was first demonstrated by Faist et. al. in 1994[59]. The fundamental principle, how the laser light is generated, is fundamentally different from the mechanism that takes place in a diode laser: While the diode laser uses electron-hole recombination in the semiconductor lattice to gain the energy for photon emission, a QCL uses bandgap transitions inside the conduction band of the

semiconductor. In particular, these are inter subband transitions, so electron transitions between the subbands of the semiconductor.

This can be reached by a specific design of the laser substrate: The band structure, that is first computationally designed, is reconstructed by a specific sequence of layers of different semiconductor materials such as GaAs, AlGaAs or InGaSb. These materials have different band gaps that allow, if combined to a macroscopic structure, to build up complicated band structures. Some of these layers have a thickness just nanometers.

The technology, how such sequences of very thin layers can be manufactured is molecular beam epitaxy (MBE). The principle is, on a molecular scale, similar to extrusion-based 3D printing: The substrate, that is placed in a high vacuum chamber, is exposed to a molecular beam that has the desired composition. In that way, on the surface of the substrate a very well-defined crystal consisting of the molecules/atoms of the molecular beam is formed in nearly any desired thickness. This process is repeated multiple times with different molecular beam compositions.

The typical band structure of the conduction band are periodic potential wells of decreasing depth, as depicted in Figure 2.3. This forms a quantum cascade, that gives the laser its name. In every step of the cascade, a photon is emitted.
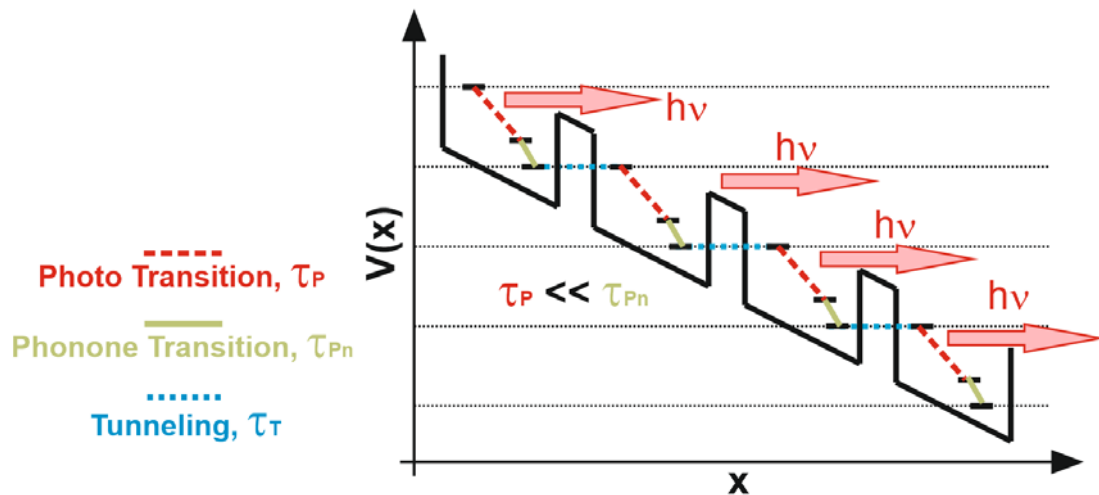

Figure 2.3: Typical local band structure inside a QCL material with three types of electron activity: The tunneling through the potential wells is much faster than the (laser) transition, what causes a population inversion.

The typical wavelength of this type of semiconductor lasers is in the range of a 3 to 15 microns and in the THz range – a wavelength range, that is hardly covered by other semiconductor laser technologies, except the interband cascade lasers (ICL's, available up to around 7 microns), that will be introduced in the next section.

In this wavelength range most molecules exhibit fundamental vibrational and ro-vibrational transitions leading to strong absorption bands. Soon, the potential of these light sources for chemical sensing was recognized[60]: All the general advantages of infrared lasers compared to thermal light sources, discussed in section 2.1.1.3 hold also for this type of laser. Together with the chemically highly interesting wavenumber range, this leads to a high potential for improving chemical sensing methods. One example is infrared absorption spectroscopy: The problem of the limited spectral power density that thermal sources offer can be worked around if a QCL is used instead, what leads to complete new application possibilities[61].
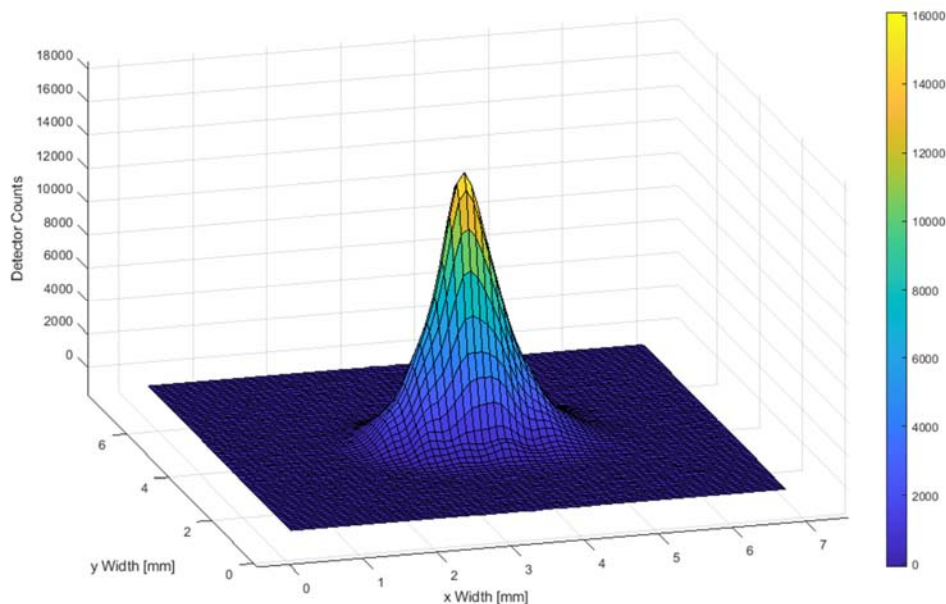
Figure 2.4: Measured intensity distribution of the HHL (high heat load) housed QCL by Alpes Lasers, emitting at a wavenumber of 2291.5 cm^{-1}, where a couple of absorption bands of $^{12}CO_2$ and $^{13}CO_2$ are located.

The excitation laser beam used in the experimental ICAPS setup developed in this thesis (see section 3.5.1), has been checked for proper focusing. The laser beam is expected to show Gaussian shape, what could be experimentally confirm with a PYROCAM infrared camera, as shown in Figure 2.4. Further, the beam diameter, what is defined as the full width of half maximum (FWHM) of the intensity profile, after focusing was found to be 0.8 mm.

2.1.3.1 Distributed Feedback Quantum Cascade Laser (DFB-QCL)

With the DFB technology, the emitted wavelength of an QCL can be stabilized and also tuned over a narrow range by changing the temperature of the QCL chip or the injection current. Both, the temperature and the injection current are connected to each other by the ohmic heat that is produced as soon as current is flowing through the laser chip. For DFB-based QCLs (and also for DFB based laser diodes) this tuning capabilities are typically in the range of a few nm, or expressed in terms of wavenumbers, a few cm^{-1}.

This tuning range is enough to cover a few multiples of the typical width of infrared absorption bands of small molecule gasses like carbon, sulphur or nitrogen oxides. Several recently developed chemical spectroscopy methods are based on that type of lasers[62,63], and also the research in gas phase spectroscopy performed in this thesis is based on such devices.

For liquid phase samples, the tuning range a DFB-QCL offers is usually not enough to achieve the required selectivity when measuring an analyte in a complex matrix due to broad, overlapping absorption bands often present in liquid samples.

2.1.3.2   External Cavity Quantum Cascade Laser (EC-QCL)

The tuning range of a QCL can be increased by using an external cavity. This leads to the technology of EC-QCL's[64]: Contrary to DFB-QCL's the active region of the laser has no one-dimensional grating. Additionally, one facet of the gain medium has an anti-reflection coating. The initial laser light is then guided to a – mechanically turnable – macroscopic grating. The angle, the grating encloses with the direction of propagation of the initial laser light defines, which wavelength is redirected to the gain medium to be amplified and emitted at the other side of the laser chip. With that, tuning ranges of a few hundreds of wavenumbers can be reached[65]. That tuning range is enough for sensing liquid samples including aqueous solutions. Figure 2.5 shows a principal sketch of an EC-QCL.
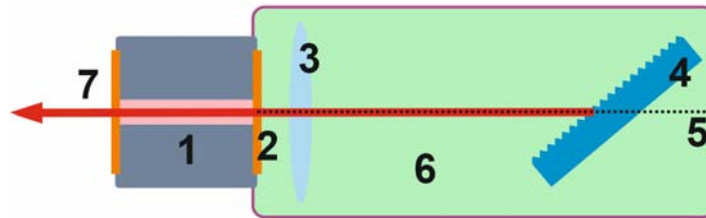

Figure 2.5: Principle of an EC-QCL: 1..Substrate (grey) with active region (pink), 2..Anti reflection coating, 3...Collimation lens, 4..Grating, 5..Optical axis, 6...External cavity housing, 7..Laser output

2.1.3.3   QCL Arrays and Ring Cavity Surface Emitting QCL

Another way to extend the wavelength range of QCLs is to combine the beams of more than one DFB-QCL. This can be reached by different optical solutions that are based on semitransparent mirrors (beamsplitters)[66] or by QCL arrays, where more than one QCL is located on one laser chip. The emitted light of this array is then focussed and collimated to one beam containing multiple wavenumbers[67].

A very elegant way to combine more than one QCL is the relatively young field of vertically emitting QCLs. This approach leads to the idea of ring cavity surface emitting QCLs[10,68]: The active region of the QCLs (emitting at different wavenumbers) are shaped in the form of concentric circles. With that, a concentric beam is obtained, that can be focussed. The resulting focal spot contains all wavenumbers of the QCL's. A principal sketch is given in Figure 2.6.
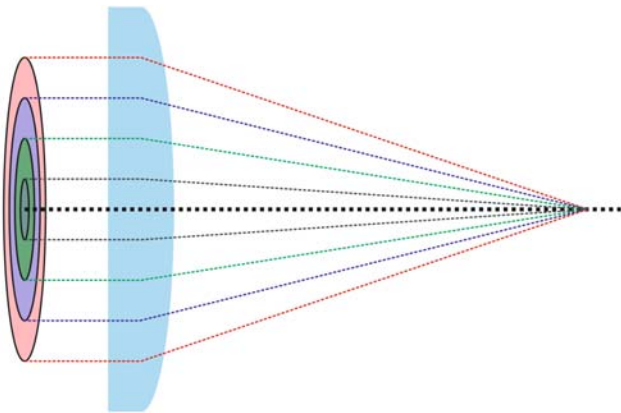

Figure 2.6: Principle of Ring cavity surface emitting QCL's

2.1.4 Interband cascade Laser (ICL)

It is possible to construct semiconductor materials with a band structure that allows transitions between the valence band and the conductivity band of two different semiconductors. These transitions are called inter band transitions. It has been shown, that these transitions can be employed for band structure engineering[69] and the construction of a new type of lasers, the interband cascade lasers (ICLs). The approach to use two different materials makes the fabrication process more complicated but opens up more degrees of freedom in band structure engineering. Especially, smaller energy level differences compared to semiconductor lasers that consist of just one material get accessible. With that smaller transition energy, lasers of longer wavelengths can be fabricated.

The emission wavelengths that can be reached by these devices are located between 3 and 7 microns. ICLs are, from their structures and operation principles point of view similar to QCLs. From the spectroscopic application's point of view, there are two major differences to QCLs – on the one hand, the output power of ICLs is at the current state of the art limited to the single digit mW range, while QCLs offer output power ranges of up to some hundreds of mW. On the other hand, ICLs have a significantly lower power consumption, what makes them highly interesting for the construction of portable sensors or other applications, where low energy consumption is required. Since the research on the ICL technology is a very young field, it is to expect, that the range of output power and wavelengths, where ICLs are available can be further extended in the future.

2.2 Interferometry

The optical core devices of all sensing techniques that have been investigated during this thesis, are interferometers of various design. The most important of them are described in the following subsections: While the Mach-Zehnder-Interferometer represents the core of the liquid phase sensor setup that was investigated in this thesis, this role is overtaken by the Fabry-Pérot interferometer in gas phase spectroscopy.

In the following sections, the starting point again is an electromagnetic wave

$$E_I = A_I e^{-(\omega t - kx)} \tag{2.100}$$

That wave is interacting with beam splitters and mirrors leading to either reflection or transmission. For simplification reasons and because of the fact, that the used optical elements in the experimental setups are optimized for the wavelength range they are employed for, it is assumed, that there are no other effects, especially no absorption, besides reflection and transmission. Due to conservation of energy, this means that the process that is going on at a given mirror or beam splitter surface, can be described by two dimensionless factors R and T. They represent the fraction of reflected and transmitted Intensity and because of the assumptions previously made, they hold

$$R + T = 1 \tag{2.101}$$

Further, the relation between the amplitude of the electromagnetic wave A and the measured Intensity I, which is a measure of energy, has to be reviewed at this point. The relation between these two quantities can be found, as it was discussed in Chapter 1, by

$$I = A \cdot A^* = |A|^2 \tag{2.102}$$

With equations (2.101) and (2.102), the reflected (A_R) and the transmitted (A_T) fraction of an incident (A_I) beam that hits, as an example, a beam splitter can be written as

$$A_R = \sqrt{R}\, A_I$$
$$A_T = \sqrt{T}\, A_I = \sqrt{1-R}\, A_I \tag{2.103}$$

If multiple reflections or transmissions take place, this formalism can be employed iteratively: A beam that, as an example, gets reflected and then transmitted (under the condition, that the initiating optical component is of the same type) has the amplitude $A_{RT} = \sqrt{RT}\, A_I = \sqrt{R(1-R)}\, A_I$. These relations will be used in the following sections.

Another important relation is the translation of an introduced increase of the length a beam travels, Δs, in a phase shift $\Delta\varphi$ of the wave. Since a whole spatial period of the wave has the length λ, the wavelength, a change of travel length Δs can be expressed as a multiple of the wavelength. In angular coordinates, in which also the phase of the wave is measured, a whole period corresponds to an angle of 2π. If these two facts are combined, the relation

$$\Delta\varphi_g = \frac{2\pi}{\lambda}\Delta s \tag{2.104}$$

can be found. Mathematically, this is nothing else than a coordinate change from spatial to angular coordinates.

A change of travel length Δs can also be introduced, if the beam is travelling in media with different refractive indices. This optical pathlength can be understood if a layer parallel plate of thickness d is considered, that is hit by a laser beam under an angle of α to the surface normal, as depicted in Figure 2.7.

The first step is to find the refracted angle β. If the plate has a refractive index of n and the surrounding medium a refractive index of 1, this can be done by using the Snellius law from equation (1.53). With that, β can be found by

$$\sin \beta = \frac{\sin \alpha}{n} \tag{2.105}$$

The next step is to calculate the opposite leg of the rectangular triangle that is defined by β, the surface normal and the refracted beam. The doubled length of this value is marked as thick grey line in Figure 2.7. If the length of that line is denoted as $2x$, it is found

$$\tan \beta = \frac{x}{d} \tag{2.106}$$

$2x$ is the length of the hypothenuse of another rectangular triangle. The leg parallel to the reflected beam has the length δ, the travelling distance of the reflected beam. The smaller one of the two non-rectangular angles can be found as $\frac{\pi}{2} - \alpha$. With that it is found $\cos\left(\frac{\pi}{2} - \alpha\right) = \frac{\delta}{2x}$. The cosine on the left side is equal to $\sin \alpha$, what becomes clear from the trigonometric summation theorems. This leads, together with equation (2.106), to $\frac{\delta \cos \beta}{2d \sin \beta} = \sin \alpha$, and for δ it is found

$$\delta = \frac{2d \sin \beta \sin \alpha}{\cos \beta} \tag{2.107}$$
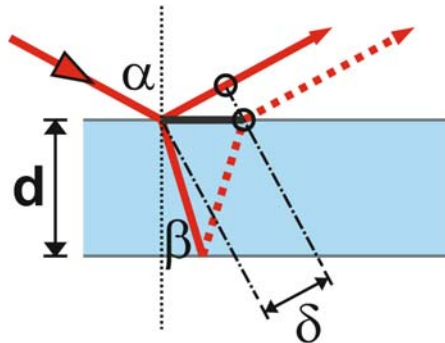

Figure 2.7: Sketch for the derivation of the optical pathlength.

The path length of the refracted beam Δ, that has to be multiplied with the refractive index n to get the optical pathlength, can be found by two times the hypothenuse of the triangle with angle β and legs $\frac{x}{2}$ and d by

$$\Delta = \frac{2nd}{\cos \beta} \tag{2.108}$$

the optical pathlength difference, that is caused by refraction is then

$$\Delta s_O = \Delta - \delta \tag{2.109}$$

and by combination of equations (2.105), (2.107), (2.108) and (2.109) it can be found

$$\Delta s_O = 2d\sqrt{n^2 - \sin^2 \alpha} \tag{2.110}$$

If the angle of incidence α is small, this can be approximated by $\Delta s_O = 2nd$, what corresponds to an additional pathway by refraction of

$$\Delta s_O = nd \tag{2.111}$$

for a one-way-travel through the plate of thickness d.

2.2.1 Mach-Zehnder Interferometer

A Mach-Zehnder interferometer consists of two beam splitters and two mirrors and is depicted in Figure 2.8. The incident laser beam gets divided into two beams, that are recombined at a second beam splitter. In the part of the interferometer where the beam is separated in two beams (these two parts of the overall beam path are called "arms" of the interferometer), materials of different refractive indices can be located. Exactly this is the underlying principle of Mach-Zehnder dispersion spectroscopy (see section 3.3), where significant contributions could be achieved within this thesis.

One of the technical challenges in setting up a sensing device that is based on a Mach-Zehnder interferometer is the fact that the entire beam path of the interferometer has to be aligned to a plane: Only if the beam path is perfectly planar, the interferometer works. In experimental practice this means that many degrees of freedom that mutually influence each other have to be brought under control: both mirrors and both beam splitters have to be mounted on a three-axis stage, resulting in 12 degrees of freedom for the alignment.
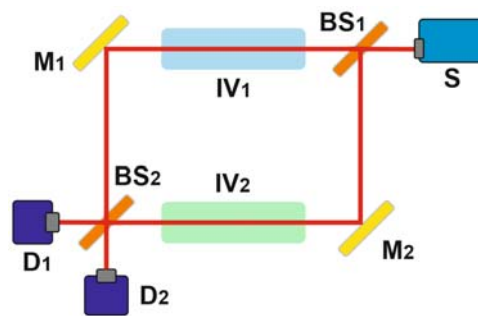

Figure 2.8: Sketch of a Mach-Zehnder interferometer: S..Source, M..Mirror, BS..Beam splitter, D..Detector, IV..Interaction Volume

2.2.1.1 Phase-sensitive Quadrature Point Readout

The principle of Mach-Zehnder dispersion spectroscopy lies in the fact, that the recombined beams, the two detectors see, are – exact alignment and equal refractive index in both arms preconditioned – shifted in phase by π. This can be understood by a simple consideration:
Transmission through an - infinitely thin - material surface causes besides an infinitely small and

therefore negligible decrease of the amplitude by absorption no change to the electromagnetic wave, especially no phase shift. This is different when it comes to reflection: Due to the fact, that the electromagnetic field has to be continuous, the reflection surface has to act as a nodal plane for the incident and exiting wave (similar to the situation in a hollow body resonator, depicted in Figure 1.2). This means, that a reflection causes a phase shift of π.

If the sketch of a Mach-Zehnder interferometer in Figure 2.8 is considered with that knowledge and the beam path is followed from the source (arrow in the right corner next to beam splitter BS 1) to

- Detector D1, two paths can be identified
  - via transmission through BS1, reflection at M1 and reflection at BS2. So, there are two reflections – the total phase shift is $2\pi \equiv 0 \bmod 2\pi$.
  - via reflection at BS1, reflection at M2 and transmission through BS2. There are again two reflections, resulting in a total phase shift of $2\pi \equiv 0 \bmod 2\pi$.
- Detector D2, again two paths can be identified
  - via transmission through BS1, reflection at M1 and transmission through BS2. The total phase shift is $\pi \equiv \pi \bmod 2\pi$
  - via reflection at BS1, reflection at M2 and reflection at BS2. The total phase shift is $3\pi \equiv \pi \bmod 2\pi$

This list of possible beam path is taxative. From that, it follows that the difference in phase of the waves seen at detector D1 (even numbers of reflections) and detector D2 (uneven numbers of reflections) is always π.

This phase difference of π between the detectors is just present if the interferometer is perfectly aligned and especially, if the refractive index is equal in the interaction volumes IV1 and IV2. "Perfect alignment" means, that there is no additional, unwanted pathway Δs, that would translate to a phase shift according to equation (2.104). This phase shift is called geometric phase shift $\Delta\varphi_g$. A difference in refractive index, $\Delta n = n(IV1) - n(IV2)$, leads also to a phase shift. This (optical) phase shift can be found as $\Delta\varphi_O = \frac{2\pi}{\lambda}\Delta n \cdot d$, where d is the length, the wave travels in the media with a refractive index difference Δn. The product $\Delta n \cdot d$ is the additional optical pathlength from equation (2.108).
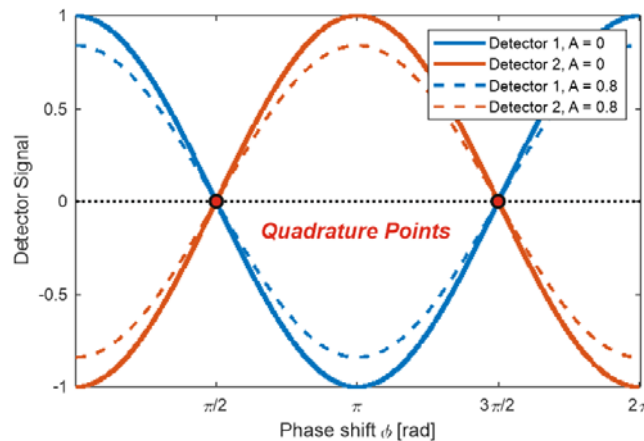

Figure 2.9: Quadrature points of a Mach-Zehnder Interferometer

The underlying principle of Mach-Zehnder-dispersion spectroscopy is the technical implementation of these two contributions to the total phase shift $\Delta\varphi = \Delta\varphi_g + \Delta\varphi_o$ for sensing purposes: While the geometric phase shift is used for locking the system to a total phase shift of $\Delta\varphi = \frac{\pi}{2}$ (this operating point is called quadrature point, see Figure 2.9), the optical phase shift, that can be read as the negative geometric phase shift that has to be applied to lock the system to the quadrature point, carries the chemical information of refractive index difference. Technical details are discussed in the experimental chapter in section 3.3.

2.2.2   Fabry-Pérot Interferometer

The Fabry-Pérot interferometer, that is often just called cavity or etalon, consists of two semi-transparent mirrors, that have a well-defined distance to each other. A sketch is given in Figure 2.10. The Fabry-Pérot interferometer can be understood as the small angle limit of a multiple reflection between two parallel mirrors (see Figure 2.10, left side). In this way, the transfer function of a Fabry-Pérot interferometer – the cavity transfer function, that was one of the core objects where research was performed in this thesis – can be derived.

In a Fabry-Pérot interferometer, there is always a reflected as well as a transmitted beam. The derivation of the transfer function follows the same ideas for both, the reflected and the transmitted beam. This is also true for many other properties of the Fabry-Pérot interferometer. The transmitted and the reflected fraction of the total intensity always sum up to one, what means that the transmitted fraction can be calculated from the corresponding reflected fraction by

$$\frac{\psi_{Trans}}{\psi_{Total}} = 1 - \frac{\psi_{Ref}}{\psi_{Total}}$$

(2.112)

For that reason, for the rest of this and the following chapters, if not stated differently, any statement that contains the term "transmitted" is true in the sense of equation (2.112) as well for a statement where this term is replaced by "reflected" and vice versa.
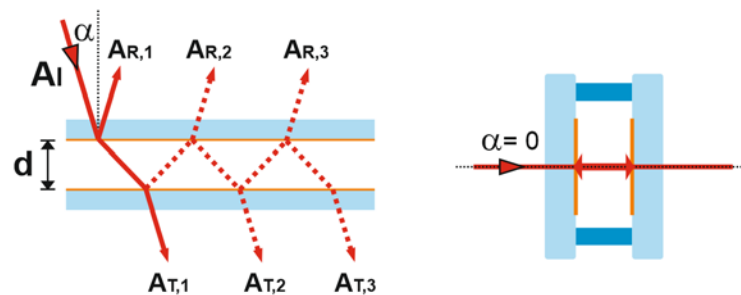

Figure 2.10: Sketch of the beam path between two plates (left) with the Fabry-Pérot interferometer as limit case for $\alpha \to 0$ (right)

To derive the Cavity Transfer Function (CTF), it is recognized, that for small values of the angle α in Figure 2.10, the amplitudes $A_{R,j}$ or all secondary reflected waves (depicted up to $j = 3$) the waves are spatially so close to each other, that they overlap and interfere[31]. The secondary reflected waves can also be written in the form of the incident wave, represented in equation (2.100). There are just two changes with increasing j: if the n-th secondary wave is considered,

according to equation (2.103), the coefficient of reflection R has to be multiplied n times. Further, the pathway the wave travels increases with increasing j. This affects the optical pathlength from equation (2.110) and with that, because of the relation between pathlength and phase shift given in equation (2.104), also the phase of the corresponding wave. From this, it follows that the interfered reflected wave can be written as the following series:

$$E_{Ref} = \sum_{j=1}^{n} A_j e^{i(j-1)\Delta\varphi} = A_0\sqrt{R}\left[1 - (1-R)e^{i\Delta\varphi}\right] \cdot \sum_{j=1}^{n} R^j e^{ij\Delta\varphi}$$

(2.113)

This is a geometric series $\sum_k a_0 q^k$ with $q < \xi \in \mathbb{R} < 1$. If a sequence of such parallel plates with angles of incidence $\alpha_{k,k\in\mathbb{N}}$ is considered that fulfils

$$\lim_{k\to\infty} \alpha_k = 0$$

(2.114)

and the reflected beams are still considered in a finite spatial interval left to the point of incidence, it follows, that the number of reflections n goes towards infinity. This means that the geometric series in equation (2.113) becomes an infinite geometric series, for that it holds $\sum_{k=1}^{\infty} a_0 q^k = a_0 \frac{1}{1-q}$. For the series of secondary reflected electromagnetic waves this means

$$E_{Ref} = A_0\sqrt{R}\frac{1 - e^{i\Delta\varphi}}{1 - R e^{i\Delta\varphi}}$$

(2.115)

For the intensity of that wave it follows according to equation (2.102) and with $\cos x = \frac{e^{ix}+e^{-ix}}{2}$

$$I_{Ref} = I_0 R \frac{2 - 2\cos\Delta\varphi}{1 + R^2 - 2R\cos\Delta\varphi}$$

(2.116)

With the relation $1 - \cos x = 2\sin^2\frac{x}{2}$ this can be written as

$$I_{Ref} = I_0 \frac{(1-R)^2}{(1-R)^2 + 4R \cdot \sin^2\frac{\Delta\varphi}{2}}$$

(2.117)

By introducing the reflectivity finesse F

$$F = \frac{4R}{(1-R)^2}$$

(2.118)

it can finally be obtained

$$I_{Ref} = I_0 \frac{F\sin^2\frac{\Delta\varphi}{2}}{1 + F\sin^2\frac{\Delta\varphi}{2}}$$

(2.119)

and, with an analogue consideration of the transmitted beams $A_{T,j}$ in Figure 2.10

$$I_{Trans} = I_0 \frac{1}{1 + F\sin^2\frac{\Delta\varphi}{2}}$$

(2.120)

The last two equations are called the Airy formulas and, in this thesis, due to the technical employment of these relations, Cavity Transfer Function(s). They have the mathematical form of a Lorentzian profile $L(x) = \frac{1}{1+x^2}$ (with $x = \sqrt{F}\sin\frac{\Delta\varphi}{2}$). Figure 2.11 shows the shape of cavity transfer functions of different finesse F.
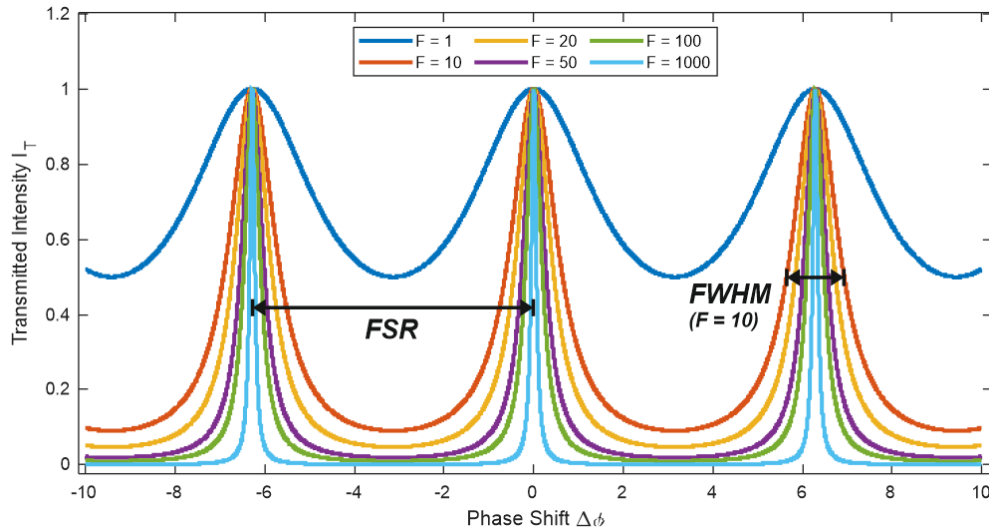
Figure 2.11: (Transmission) Airy functions, equation (2.120) resulting from different values of the Finesse F with the free spectral range and the full with of half maximum (FWHM)

2.2.2.1   Form Parameters of a Fabry-Pérot Interferometer

The finesse F is the main form parameter of the cavity transfer function. From Figure 2.11, it can be seen, that also the parameters, ε, the full width of half maximum (FWHM) of one transmission maximum and δ, the free spectral range (FSR) can be used to describe the form of the CTF. Actually, both of these parameters can be expressed as function of the Finesse F, what points out the interpretation of the finesse as universal form parameter.

It can easily be found, that for ε it holds, by simply setting $I_T = \frac{1}{2} I_0$

$$\varepsilon = 4 \arcsin \sqrt{\frac{1}{F}} \approx \frac{4}{\sqrt{F}}$$

(2.121)

The approximation is true for high values of F, for them it holds $\arcsin(x) \approx x$.

To find an expression for δ, it is recognized that for a FPI, where the angle of incidence α is zero, the phase shift $\Delta\varphi$ simplifies to

$$\Delta\varphi = 4\pi \cdot \frac{1}{\lambda} \cdot n \cdot d$$

(2.122)

From equation (2.120) it can be seen, that the maxima of I_T are reached, where the sine is zero. Using equation (2.122), it can be seen that this is the case at values for λ of $\lambda = \frac{2nd}{k}$ for any integer value $k \in \mathbb{N}$. The free spectral range (FSR) in terms of wavelength can then be expressed as the difference of two neighboured maxima:

$$\delta = \frac{2nd}{k} - \frac{2nd}{k+1} = \frac{2nd}{k(k+1)}$$

(2.123)

With the frequency

$$\nu = \frac{c}{\lambda} \tag{2.124}$$

δ can be written independent from k as

$$\delta_\nu = \frac{c}{2nd} \tag{2.125}$$

Also ε can be expressed in the frequency domain by combination of equations (2.118), (2.120), (2.122) and (2.124), where this new variable ε_ν can be found to be

$$\varepsilon_\nu = \frac{c}{2nd} \frac{1-R}{\pi\sqrt{R}} \tag{2.126}$$

With the frequency domain δ_ν and ε_ν, the Lorentzian finesse F^* can be defined as

$$F^* = \frac{\delta_\nu}{\varepsilon_\nu} = \frac{\pi\sqrt{R}}{1-R} \tag{2.127}$$

This value is connected to the reflectivity finesse by

$$F^* = \frac{\pi}{2}\sqrt{F} \tag{2.128}$$

As can be seen by equations (2.118) and (2.127), δ_ν and ε_ν can be used to experimentally determine the Lorentzian finesse F^*.

2.2.2.2 Fabry-Pérot Cavity as Transducer in Photothermal Spectroscopy

The purpose, for that a Fabry-Pérot cavity is used in this thesis is, to enhance a (wavelength modulated, see section 2.4.2) signal that the incident laser beam carries. If the finesse is sufficiently high, the slope of the cavity transfer function is higher than 1 in the linear range of the Lorentzian peaks. The highest slope of the CTF it found in the CTF inflection point. If the DC component of a modulated signal is stabilized at that wavelength (laser-wavelength cavity-resonance locking, see section 3.4), the amplitude of the transmitted (reflected) wave gets amplified. The CTF phase not only change due to the applied modulation. Also the change of parameters like the refractive index of the medium inside the cavity – the photothermal signal – causes a phase shift of the CTF. The principal concept is depicted in Figure 2.12.
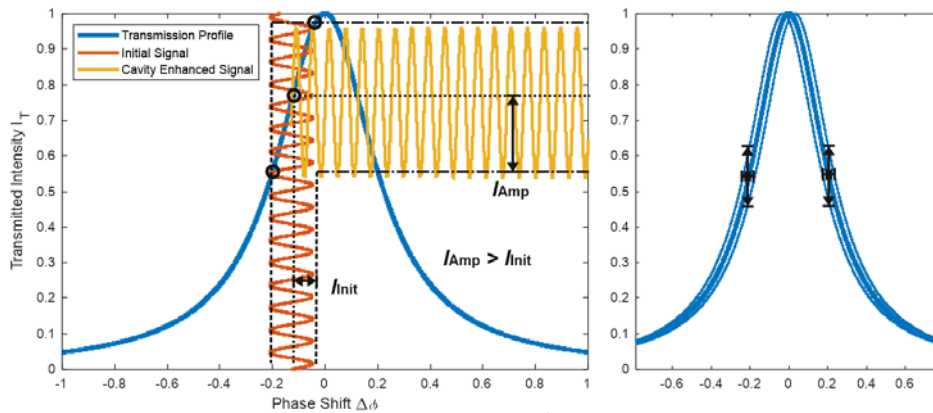

Figure 2.12: Left: Principle of cavity enhancement of modulated signals, Right: Enhancement of a phase-dependent signal by CTF phase change.

It has to be mentioned, that Figure 2.12 shows an idealized situation: The shape of the amplified signal follows the (local) shape of the transmission profile. This means that the amplified signal is just a pure sine, if the transmission function would be perfectly linear in the corresponding range. For a non-linear underlying profile, as it is the case even in theory for the Lorentzian, the amplified sine is more or less distorted, a fact that causes unwanted contributions to the signal. However, if the modulation amplitude is small compared to the FWHM of the cavity profile, what is usually fulfilled in the studied applications, the deviation from linearity and therefore the distortion of the amplified signal is negligibly small.

With that knowledge, it is obvious that the critical quantity for modulated signals is the relation of the modulation amplitude and the FWHM of the underlying signal. Because of its high importance in modulation spectroscopy it has an own designation, the modulation index m_i

$$m_i = \frac{I_{PP}}{FWHM} = \frac{A_{mod}}{HWHM}$$

(2.129)

Where I_{PP} denotes the peak-to-peak intensity and $A_{mod} = \frac{1}{2} I_{pp}$ the modulation amplitude of the initial signal and $HWHM = \frac{1}{2} FWHM$ the so-called half width of half maximum of the underlying transmission profile. Further technical details of modulation will be discussed in section 2.4.2.

2.3   Detector Technology

In this section, the most important detector technologies that have been employed in this thesis are introduced. The detectors were just used as ready-to-operate devices and no research was performed in the field of detector technology. Therefore, just the operating principles are reviewed[70,71].

Two types of infrared detectors have been used: On the one hand, photothermal detectors like the pyroelectric detector, on the other hand, detectors based on the inverse photoeffect like the Mercury-Cadmium Telluride (MCT-) detector and the Indium Gallium Arsenide (InGaAs-) detector. Table 2.3 gives an overview of the most important properties and features of the detector types used in this thesis.

Property	Pyroelectric Detector	MCT Detector	InGaAs Detector
Wavelength Range	2 to 14 µm	1 to 15 µm	0.8 to 1.8 µm
Detection Bandwidth	< 1kHz	200 MHz	10 MHz
Cooling required	No	Yes	Yes
Price level	low	high	medium
Manufacturer	Infra Tec	VIGO Photonics	Thorlabs
Size	small	medium	medium
Detectivity	$3.0 \cdot 10^8$ cm Hz$^{-1/2}$ W^{-1}	$1.0 \cdot 10^{10}$ cm Hz$^{-1/2}$ W^{-1}	$1.6 \cdot 10^9$ cm Hz$^{-1/2}$ W^{-1}
Typical Temperature	20°C	- 80°C	20°C

Table 2.3: Overview of the core properties of employed detectors

2.3.1   Photothermal Detectors

The most important thermoelectric detector is a pyroelectric detector. Pyroelectricity is a microscopic effect, that is caused by the lattice of some crystals. The effect is comparable to the piezoelectric effect: While piezoelectricity describes the conversion between electric and kinetic energy without influencing the thermal energy in a crystal, pyroelectricity describes the conversion between thermal and electric energy without influencing the kinetic energy[72].

To show pyroelectric activity, the crystal needs to have intrinsic polarization due to its crystal structure – the crystal has to be asymmetric. This means that the unity cell of such crystals is a dipole. If temperature changes, also the crystal lattice changes its form due to microscopic heat expansion. These changes can lead to two different types of motion, causing two sub-types of the pyroelectric effect:

1. *Uniform heat expansion.* The crystal expands uniformly, what causes a change in the charge to volume ratio and therefore a change of the charge that occurs at the polarized facets of the pyroelectric crystal.
2. *Change of the crystal lattice structure due to heat.* Higher temperature of the crystal means that the atoms have a higher vibrational energy. This can cause a change of the crystal structure that has the consequence – since the initial unity cell is asymmetric and therefore polarized – that the polarization amplitude changes. This leads to a change of the macroscopic charge of the crystal.

Both effects have in common, that the macroscopic charge at the corresponding crystal facets changes. They deliver two contributions to the entire pyroelectric effect. If an electrode is mounted on the facets of the crystal, an electric signal that is proportional to the temperature change is generated and can be measured after electronic amplification (Voltage Buffer, see

3.1.3.2).

In the field of this thesis, pyroelectric detectors from Infra-Tec, Dresden, Germany were used. In these detectors Lithiumtantalate ($LiTaO_3$) is used as pyroelectric crystal. In this material, the type 2 pyroelectric effect described before, is stronger than the type 1 effect: The change of the crystal lattice contributes more to the overall pyroelectric effect than uniform heat expansion. To further increase the signal amplitude of the detector, the crystal is covered with a black coating that increases the absorption of infrared radiation.

Pyroelectric detectors have the advantage, that they are relatively cheap and easy to handle. One disadvantage is, that the detection bandwidth is very limited – for the pyroelectric detectors, a modulation frequency up to 1 kHz can be applied. This limitation is caused by two effects:

- On the one hand, the pyroelectric effect is caused by heat change of a macroscopic body, the crystal. Due to the crystal's finite size, there is a finite time that it takes from light absorption to complete heat dissipation in the active region of the sensor.
- On the other hand, the voltage that is generated by the pyroelectric effect, is highly sensitive to unavoidable leakage current in the electronics – The voltages that can be reached by the pyroelectric effect can be very high (kV range), but the current is, especially due to the small size of the crystal, very small (nanoampere range).

Another material, that shows pyroelectric behavior and that has to be mentioned at this point due to its high technical relevance, is Deuterated L-alanine-doped triglycine sulphate (DLATGS). With that material, that is more expensive than $LiTaO_3$, pyroelectric detectors of higher sensitivity can be built. An important application of these detectors are routine-grade FTIR instruments, because of their higher robustness together with reduced price and operator-friendliness: For research grade FTIR instruments, MCT detectors are used, that are more sensitive, but require liquid nitrogen cooling.

2.3.2   Photoelectric Detectors – MCT and InGaAs

Both, the Mercury-Cadmium Telluride (MCT) as well as the Indium-Gallium Arsenide (InGaAs) detectors operate on the principle of photoelectricity. It is the inverse of the photo effect that is the underlying principle of semiconductor lasers.

The theoretical background to the photo effect is the same as for photoelectricity and is reviewed in section 2.1. The mechanism of photon generation in semiconductor lasers is reversed in photoelectric detectors: A photon that has an energy (and therefore: a frequency, according to equation (2.98)) that is larger than the band gap energy can excite an electron from the valence to the conduction band of the semiconductor. The detectable frequencies of a photoelectric detector are thus dependent on the band structure of the underlying semiconductor material.

For the wavelength ranges that were employed in this thesis, two types of photoelectric detectors were employed. The main difference between these two detector types, that also gives them their names, is the semiconductor material on that they are based.

- *Indium-Gallium Arsenide (InGaAs) detector.* This detector material is optimized for a wavelength of 1550 nm, a wavelength that is frequently used in telecommunication applications. In the experimental setups that have been developed, a 1550 nm laser was used as probe laser to read out the photothermal signal generated in a Fabry-Pérot cavity. The laser is described in detail in section 3.2.3.2. InGaAs detectors can be operated at

room temperature, but show – as the majority of infrared detectors, because the dark current is reduced at low temperatures – better performance if they are cooled. This can be done by an integrated thermoelectric cooler. The InGaAs detector that was used in the setup, is the Thorlabs PDA 10-CS model. It is an amplified photodetector operating at room temperature, that has an integrated, adjustable transimpedance amplifier with variable gain.

- *Mercury-Cadmium-Telluride (MCT) detectors*. This material offers a very broad wavelength range in which it shows high detectivity (generated signal per incident power per unit bandwidth and square root unit detector surface). The detectivity and speed is, with the temperature parameters that were used in this thesis (see Table 2.3), higher than the values that can be reached with an InGaAs detector or a pyroelectric detector. Because of the broad wavelength range that detector type can be used when a wide range of different wavelengths need to be detected. MCT detectors are often used in research applications of FTIR spectroscopy. A disadvantage is, that MCT detectors need to be cooled – to reach full performance down to the temperature of liquid nitrogen.

  The MCT detector used in the developed setups of this thesis is cooled by multiple stage thermoelectrical coolers. With that technique, temperatures of around -80 °C can be reached. The consequence is, that due to effective heat dissipations, the detector by VIGO Photonics needs to be actively cooled by a fan. This represents a significant source of noise in the sensing system.

The most important properties of both detector types are compared to each other and to the properties of pyroelectric detectors in Table 2.3.

For the sake of completeness, another type of detector that has not been used in this thesis, but that points out the principle of inversion of a known effect like the photoelectric affect and the photo effect, is shortly introduced: The Quantum Cascade Detector (QCD) inverts the working principle of a Quantum Cascade Laser. There have been recent developments in this field and promising results concerning the performance of these detectors have been demonstrated[73–75].

2.4   Signal Processing

While in the last chapter the hardware components such as laser sources, transducers and detectors were introduced, this chapter describes the overall signal transduction chain in a generic way. The signal constitution and transduction is an important part of this thesis. The raw signal measured by the infrared detectors described before, have to be processed to extract the chemical information that is looked for. This happens in several steps, that are visualized in Figure 2.13.
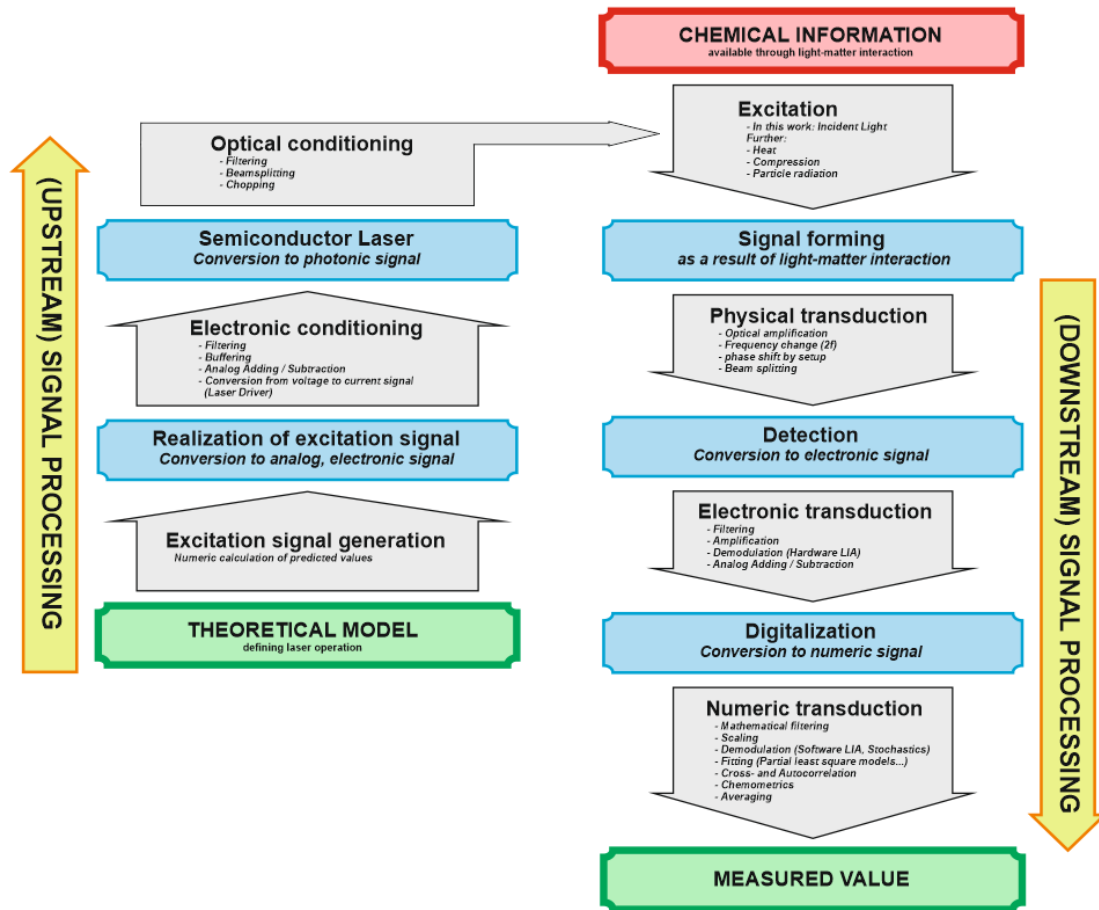

Figure 2.13: Signal transduction chain

The signal transduction chain shown in Figure 2.13 shows the most important steps in a very general way and is complete for the case of photothermal gas sensing by ICAPS. For the other methods investigated in this thesis some steps are to be understood in a different way:

- For direct absorption spectroscopy in gases (2*f*-WMS, see section 3.5.3) the excitation is the process of absorption itself. The signal is formed by the reduction of the intensity of the incident laser itself.
- For indirect photothermal spectroscopy in gases (ICAPS, see section 3.5.1) the excitation is also the process of absorption, but the signal is formed in more steps: First, heating of the sampe gas takes place. This results, together with the heating itself, in a change in refractive index, what further leads to a phase shift of the incident probe laser beam. The

signal transduction chain from detection to the measured value is done by the probe laser signal, while the excitation laser beam is dumped after the light-matter interaction. Additionally, the way from the theoretical model to the photonic signal, the laser, has to be gone twice – for the excitation- as well as for the probe laser.

- For Mach-Zehnder interferometer based liquid phase dispersion spectroscopy (see section 3.3), an example for direct spectroscopy, the excitation is represented by the phase shift of the excitation laser beam due to diffraction. As a consequence and as the form of signal forming in this method, this causes a change of the intensity arriving at the two detectors – the normalized differential signal is not zero anymore.

After detection of the laser beam, located in the middle blue box of the right column in Figure 2.13, the electronic transduction takes place. Due to its very practical and experimental nature, the majority of this link of the transduction chain will be discussed in section 3.1, where the electronics that have been developed are introduced.

After the analog electronic signal is digitalized – this is a very critical step that will be discussed in section 2.4.1 – the algorithmic transduction, where all the signal processing takes place, leads to the final output signal. Signal processing contributes a lot to the overall sensor performance. Suitable detection technology and a carefully designed signal transduction chain are crucial to get a raw signal that carries all the relevant information about the analyte. One of the biggest challenges that has to be dealt with when setting up an analyzer is noise: Unwanted contributions to the raw signal that may come from very different sources. These noise sources are of different origin and include also environmental factors. Proper implementation of signal processing, in the step of electronic transduction as well as in the step of algorithmic transduction can reduce the noise contribution to the signal by several orders of magnitude. An optimized signal processing also includes measures to amplify the wanted signal which can be attributed to the analyte.

One of the most important terms in this context is the Signal-to-Noise ratio (SNR). It can be defined in a generalized way as

$$SNR = \frac{Analyte\ Signal\ Amplitude}{Noise\ Amplitude} = \frac{Amplitude\ of\ wanted\ signal\ contributions}{Amplitude\ of\ unwanted\ signal\ contributions} \tag{2.130}$$

2.4.1 Signal Digitalization

The numeric transduction part of the signal transduction chain is, due to data set sizes of up to several millions of double-precision numbers, computationally very intense. These tasks cannot be fulfilled without a computer – what makes digitalization of the analog signals necessary.

In this thesis, this task was overtaken solely by commercially available and LabView compatible devices of National Instruments Corporation, headquartered in Austin, Texas. In particular, these devices were

- NI 9263: Digital to Analog converter (DAC), -10 to +10 V in 16 Bit resolution, 100 kSamples per second sampling speed
- NI 9239: Analog to Digital converter (ADC), -10 to +10 V in 24 Bit resolution, 50 kSamples per second sampling speed

For further details refer to the user manuals of these devices.

Digitalization of signals is a highly complex field of electronics[76]. The underlying problem is, that

an analog signal that has – theoretically, when neglecting the quantized nature of voltage due to single electrons – infinite resolution, upon digitalization it is converted in a signal, that has finite resolution on the amplitude as well as on the time axis. The digitalization process has to be done without loss of information.

The very intuitive problem that results from the different nature of analog and digital signals is, that values have to be rounded in order to bin them. This is true for the time axis (sampling speed) as well as for the signal axis (resolution). Figure 2.14 shows this problem by the example of a Lorentzian peak with given FWHM: The black curve represents the analog signal. The effect of limited sampling speed and signal resolution can be clearly seen:

- Left: Sampling speed limitation - If the function is sampled with a given time step width $\delta \approx \frac{FWHM}{2}$, the peak cannot be satisfyingly resolved – all values in the grey area between the lower (blue) and upper (orange) limit could be argued to be in some sense the "correct" value. If it holds $\delta \ll \frac{FWHM}{2}$, the uncertainty gets negligibly small, but often it is the case, that a measurement has to be performed close to the sampling speed limit of the employed Analog to Digital converter.
- Right: Same is true on the signal axis if there is a finite resolution of σ: Again, an uncertainty of the measured signal is the consequence of the limited signal resolution.

Both effects lead to a natural source of uncertainty by digitalization (digitalization error). The Nyquist-Shannon Sampling Theorem, that usually is formulated in the frequency domain, defines a limiting condition for the sampling frequency that is required to sample/digitalize an analog signal of given frequency. The same is true on the signal axis – here, the Nyquist-Shannon theorem defines correspondingly a limiting condition for the signal resolution.
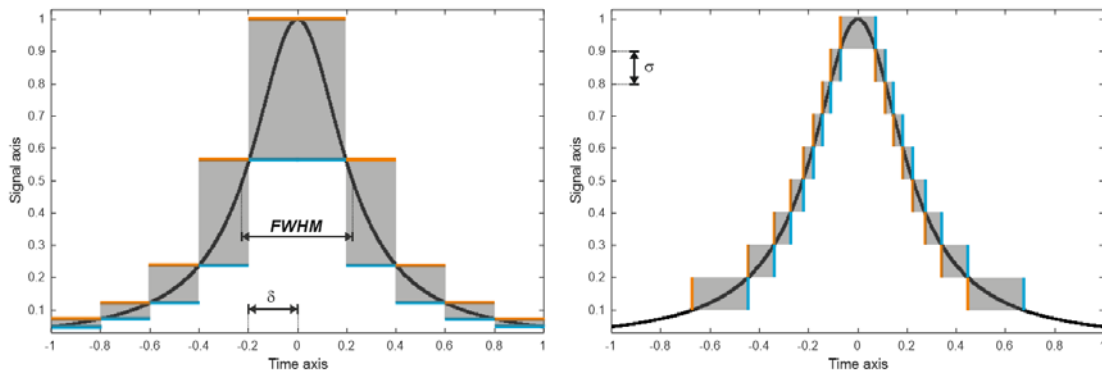

Figure 2.14: The problem of sampling

2.4.1.1   Nyquist-Shannon Sampling Theorem

A review of the complete theory of sampling would lead too far, but a simple way to get to the main result of the Nyquist-Shannon Sampling theorem is the following[77]: Sampling a signal $S(t)$ that is a function of the time t can be modelled by multiplication of a sum of equidistant Dirac distributions, a so-called Dirac comb $C(t) = \sum_n D(t - t_n)$. For the values of t_n it holds

$$t_{n+1} - t_n = \delta \tag{2.131}$$

what is equivalent to

$$t_n = t_0 + n\delta \tag{2.132}$$

with a starting time t_0. Now, the Fourier transform of the sampled signal $\hat{S}(t) = S(t) \cdot C(t)$ is considered and it is used that the Fourier transform of a product is the convolution of the Fourier transform of the single factors:

$$\mathcal{F}(\hat{S})(\omega) = \mathcal{F}(S \cdot C)(\omega) = \mathcal{F}(S)(\omega) * \mathcal{F}\left(\sum_n D(t - (t_0 + n\delta))\right)(\omega) \tag{2.133}$$

Because of the periodicity of the Dirac comb it follows, that $\mathcal{F}(\hat{S})(\omega)$ is periodic with a period of $\frac{2\pi}{\delta}$ in the frequency domain. Because of the definition for the convolution of two periodic functions f and g

$$f * g(t) = \frac{1}{T} \int_{t_0}^{t_0+T} f(\tau) \cdot g(t - \tau) \, d\tau \tag{2.134}$$

where T denotes the longer one of the periods of f and g, it follows, that the smaller one of the periods of f and g, must not exceed the half of the bigger one – otherwise, there would be a time τ, where both functions f and g contribute to the integral. The consequence would be, that the transformation could not be resolved anymore, or in other words, the information of the unsampled signal $S(t)$ could not be reconstructed anymore by the inverse Fourier transform. This leads to the Nyquist-Shannon condition

$$\frac{1}{\delta} = f_{Spl} > 2 f_{Sig}^{max} \tag{2.135}$$

with f_{Spl} the sampling frequency and f_{Sig}^{max} the biggest occurring frequency in the unsampled signal: The sampling frequency has to be bigger as the doubled value of the highest frequency that occurs in the unsampled signal. The frequency $\frac{f_{Spl}}{2}$ therefore is called the Nyquist barrier.

For data which are composed only by frequencies far above zero, the generalized Nyquist-Shannon condition can be found by

$$f_{Spl} > 2\left(f_{Sig}^{max} - f_{Sig}^{min}\right) = 2b \tag{2.136}$$

The limiting value then is not the highest occurring frequency but the bandwidth b of the unsampled signal. For signals with components near to constant values, it holds the approximation $f_{Sig}^{min} = 0$ and equation (2.136) turns into equation (2.135).

In Figure 2.15 the situation is depicted graphically. The same result can be found by any other function argument instead of the time t – especially for space or voltage being the function argument.
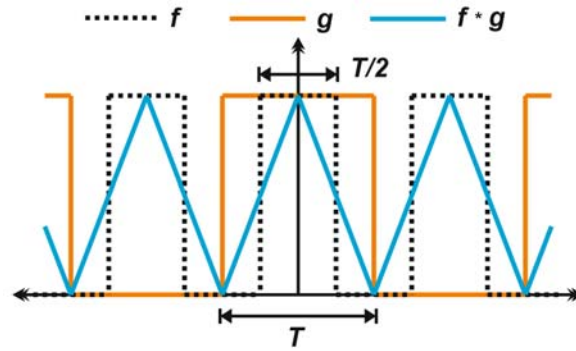
Figure 2.15: Sketch to the Nyquist-Shannon Sampling Theorem

2.4.2 Modulation

Most of the techniques developed in this thesis are based on signal modulation methods. The idea is, to add a periodic function, usually of small amplitude, to the excitation signal[78]:

$$S_e(t) = S_e^0(t) + M(t)$$

(2.137)

with $M(t + \tau) = M(t)$. The frequency $f_{mod} := \frac{1}{\tau}$ is called modulation frequency. The consequence is that the chemical information which has to be measured is then stored in exactly this frequency (or, in a real sensing system: in a narrow frequency band around this frequency) and its integer multiples, the so-called higher harmonics of that frequency.

This means, that the raw signal can be band-pass filtered having a very narrow frequency band. This has two beneficial effects: The wanted parts of the signal remain, while the unwanted frequencies can be efficiently filtered out. In practical applications, this task is overtaken by a Lock-In-Amplifier that acts as a band pass filter with adjustable, very narrow pass band.

Modulating an incident signal usually has major effects on the output signal. If there is a nonlinear link in the signal transduction chain, the waveform of the modulation is changed. This is due to the fact, that the transfer function of the corresponding signal transduction chain link is convoluted with the waveform function of the modulation. The case of a nonlinear transduction is the normal case. This is also true for a Fabry-Pérot cavity used for signal enhancement, as it is the case in ICAPS. The nonlinear transfer function in this case are the Airy functions. It is obvious, that the required modulation amplitude and the width of any spectral features that have to be measured is somehow connected. As it was discussed in section 2.2.2.2, the critical quantity is the relation between modulation amplitude and width of the spectral feature that has to be measured. This leads to the highly important quantity of the modulation index m_i, defined in equation (2.129).

2.4.2.1 2f-Wavelength Modulation

2f-Wavelength Modulation (2f-WM) is a relatively young, but already well-established technique in gas spectroscopy[14]. In this thesis, it is used in two different ways. For both of them, a modulated (laser) light source is shined on a transducer. This transducer has to be understood in a very general way: It can be a component of the signal transduction chain, as it is the case for cavity-enhancement techniques, but it can also be the process of signal forming itself, as it is the case for absorption spectroscopy around an absorption peak of a sample molecule:

- 2f-WM as a spectroscopic readout technique: The technique can be employed for signal detection in absorption spectroscopy. For that purpose, the incident laser light is modulated and the detected signal is demodulated at the second harmonic of the initial modulation frequency. The result is the 2f-amplitude as a function of the center wavelength of the incident laser light. This function is called the 2f-spectrum and contains qualitative (peak position) and quantitative (peak area, approximated by peak height) information of the measured analyte. In particular, the methods in this field were direct absorption 2f-WMS and ICAPS, where also a 2f-WMS readout is used.

- 2f-WM as the underlying principle for coupling a laser's wavelength to the inflection point of a Fabry-Pérot interferometer's cavity transfer function (CTF): The same principle of using a modulated light source and measuring the second harmonic of the detected signal can be used to detect and stabilize the lasers wavelength to the inflection point of a Fabry-Pérot interferometer's CTF. This technique is called 2f-WM locking and is discussed in section 3.4.5. Having available a reliable and stable locking method is crucial for the performance of an ICAPS sensor, as it is pointed out in section 3.5.1.

To understand this behaviour, a modulation signal $m(t)$ is considered that is periodic with a period τ. If this signal is passed through a transducer whose transfer function $T(x)$ has a peak at a given point x_0, and that peak is significantly broader than the amplitude of the modulation, the signal gets in some sense reflected in the transfer function peak: Mathematically, the effect of the transfer function to the modulation can be described by a composition of the modulation and the transfer function

$$m_T(t) = T \circ m\,(t)$$

(2.138)

where $m_T(t)$ denotes the transduced modulation. If now x_0 is a peak of the transfer function, this means that due to the periodicity of m and the fact that the sign of the slope changes at the peak of a function, $m_T(t)$ follows locally the form of the peak of the transfer function with a period of $\frac{\tau}{2}$. This corresponds to a doubling of the modulation frequency $f_{mod} = \frac{1}{\tau}$.
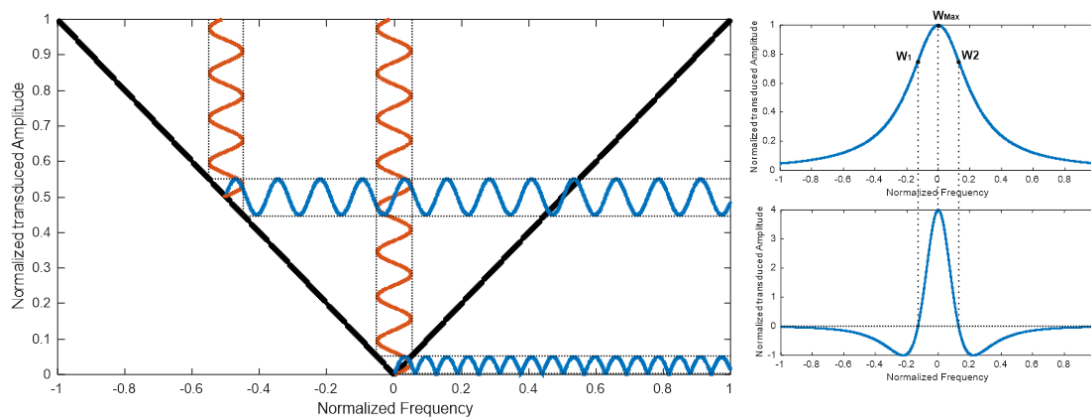

Figure 2.16: Left: Frequency doubling of a sinusoidal modulation at the peak of the absolute value function as transfer function. Right: Lorentzian peak and its 2f-amplitude with maximum (Max) and inflection points (M$_{1,2}$) marked.

As a very simple example, as transfer function the absolute value function can be chosen: A sine function of low amplitude, composed with that transfer function at a position away from the peak, leaves the sine function unchanged. If the sine function is composed with the transfer function at the peak, the sine gets transformed to the absolute sine function – this function has a period twice of the initial sine function. An exact mathematical description can be gained by local Fourier decomposition of $m_T(t)$. This leads to very bulky and technical expressions that qualitatively do not provide more information than the graphical depiction in the left part of Figure 2.16.
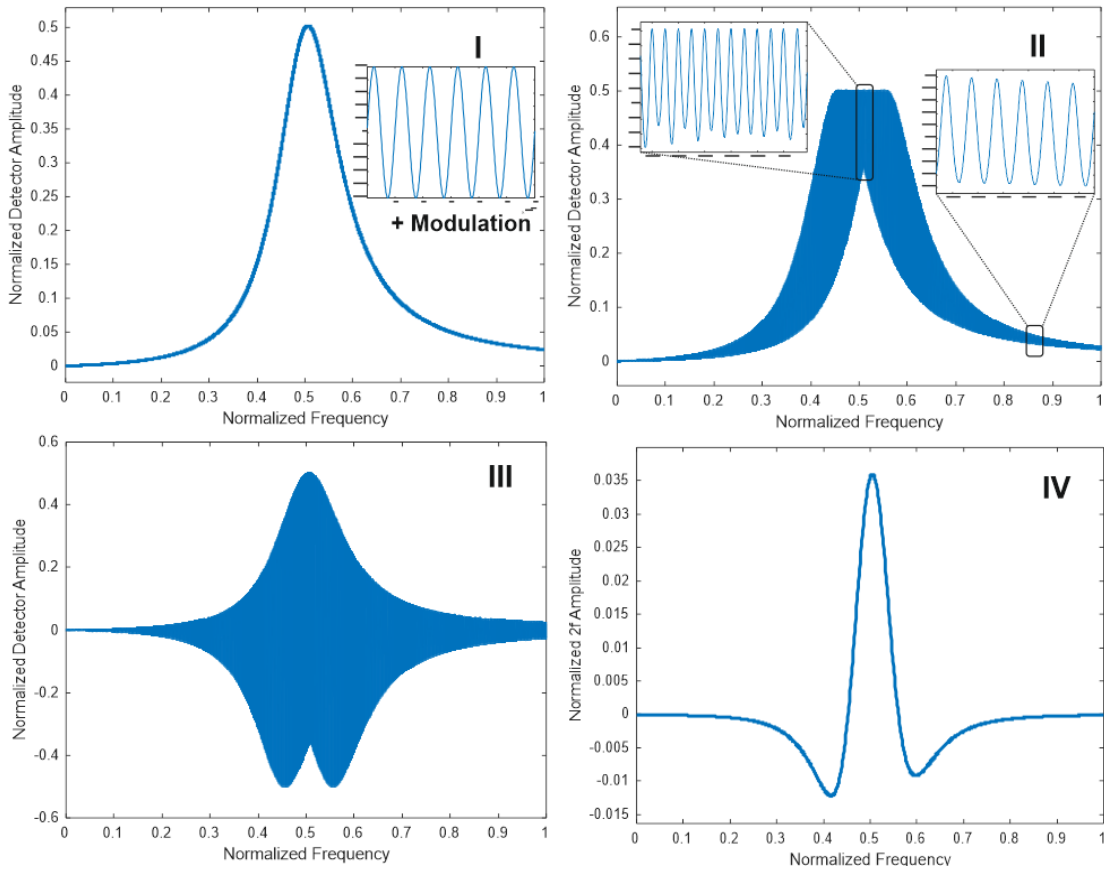

Figure 2.17: Frequency doubling of modulation at CTF peak and typical 2*f* pattern after demodulation for different modulation indices. I..Unmodulated CTF profile and modulation signal to apply, II..Modulated CTF profile with zoom-in at the peak (doubled frequency) and off the peak (no recognizable contributions of doubled frequency), III...Modulated CTF profile multiplied with reference signal of double frequency, IV..Same as III, after Low-pass filter being applied

As already mentioned, a Fabry-Pérot cavity has a Lorentzian shaped transfer function. The transfer function and the amplitude of it's 2*f*-signal with a given modulation amplitude is depicted in Figure 2.16, right side: The peak position of both functions corresponds to each other and the inflection point of the transfer function corresponds to the zero crossing of the 2*f*-amplitude. This is true for modulation amplitudes that are significantly smaller than the width of the underlying Lorentzian peak. For higher amplitudes, there is a broadening effect that is discussed in section 3.5.2.

A good approximation of the overall system that was used for laser-cavity locking purposes in this thesis, consisting of a diode probe laser with (nearly) linear injection current vs. output power

characteristics, is a sum of a Lorentzian and a linear function. With that, the transmitted intensity of a semiconductor laser with linearly increased injection current that is guided through a Fabry-Pérot cavity can be modelled. Figure 2.17 shows the signal transformation beginning with the detector response of an unmodulated laser (I). The small graph shows the modulation function – a sine with an amplitude smaller than the FWHM of the transfer function peak. (II) shows the detector response of a modulated laser.

All the information about the transfer function is now stored in the signal of frequency $2f_{mod}$ – The amplitude of that part of the signal is maximum at the peak of the transfer function. In the region where the transfer function is close to linearity, what is the case in a neighbourhood of the inflection points of the transfer function, there is no $2f_{mod}$ contribution to the signal. Further, the sign of the curvature changes in the inflection point – that has the consequence, that the amplitude of the $2f_{mod}$ contribution changes its sign; the $2f_{mod}$ function has a zero crossing at the inflection point of the transfer function. This property is the underlying principle of the 2f-WM laser-wavelength cavity-resonance locking scheme that is introduced in section 3.4.5.

To retrieve the amplitude of the $2f_{mod}$ contribution, the raw detector signal has to be multiplied by a sine (or rectangular signal) of the desired frequency, namely $2f_{mod}$ – the so-called reference signal. The result is depicted in graph (III). After that, this intermediate signal is band-pass filtered with a narrow passband around $2f_{mod}$. This task is fulfilled by a Lock-In-Amplifier (LIA) and is called demodulation at the second harmonic of the modulation frequency. The operating principle of a LIA is briefly reviewed in section 3.2.1. If the $2f_{mod}$ amplitude in the detector signal is plotted against the frequency axis, graph (IV) in Figure 2.17 is retrieved. This is the well-known 2f-pattern.

It can be recognized that the result of this process (Figure 2.17, IV) is an asymmetric pattern, compared to the symmetric pattern of Figure 2.16, right part. This asymmetry is a consequence of the combination of a Lorentzian and a linear function, what was used (see Figure 2.17, I) to model the cavity transfer function of the Fabry-Pérot cavity in combination with the linear dependence of the probe laser output power from the laser injection current.

All the theory that has been discussed up to now, is based on the restriction, that the modulation amplitude is small compared to the FWHM (modulation index, see equation (2.129)) of the transfer function peak. An increase of the modulation index has the effect, that on the one hand the amplitude of the 2f signal is increasing to a finite maximum, but also, that the 2f pattern is broadening. This broadening is problematic as the zero crossing no longer corresponds to the inflection point of the CTF. This is of relevance for laser-wavelength cavity-resonance locking and further details to that topic are discussed in section 3.5.2.

2.4.2.2 Determination of the Modulation Index

For the modulation index m_i, according to equation (2.129), the HWHM of the cavity transfer function (CTF) and the modulation amplitude, both in same argument units have to be known. For accuracy reasons, this information is ideally gained by an accurate measurement. Therefore, the detector response is measured while the laser injection current is constantly increased (injection current ramp). x_{HMWM} is determined by measuring the detector output signal and the probe laser current monitor signal around the CTF peak. After subtraction of the laser power characteristics (see section 3.2.3.2), the FWHM and with that the HWHM can be read at half maximum height of the peak. For the probe laser and the Fabry-Pérot cavity used in experiments to this thesis, x_{HWHM} was found to be 4.78 mA, corresponding to 58 pm considering the current tuning parameters of the employd diode laser.

The modulation amplitude a_m (of a sinusoidal modulation signal) is determined by measuring the the injection current monitor signal of the laser driver for at least a few hundreds of modulation periods. The modulation amplitude a_m can be calculated from the root mean square (RMS) of this dataset, a_{RMS}, by

$$a_m = a_{RMS} \cdot \sqrt{2}$$

(2.139)

This can be easily found by integrating the squared sine function over a whole period divided by this period.

2.4.2.3   Stochastic Method

The idea of this method is to find an alternative way to demodulate a modulated detector signal (graph (II) in Figure 2.17). This has technical reasons:

The lock-in-amplification is a well-established technique but suitable LIA's of sufficient performance are bulky and very expensive. Theoretically, the whole process of lock-in-amplification could be shifted to the stage of numeric transduction by using a software-based LIA. This approach was also investigated (see section 3.2.1.2), but still some technical inconveniences remain. As an example, also for the software-based LIA a physical reference channel is needed. The problem is the high sensitivity of a Lock-In-Amplifier to the phase shift between signal and reference signal: The multiplication of the raw signal with the reference sine or cosine is a projection on the real (called "X") and imaginary ("Y") axis of the signal. The information is carried, in principle, on both coordinates. By adjusting the phase shift between signal and reference signal one of the two directions of projection can be brought to zero and the whole information is carried on one axis.

Usually, once adjusted, the phase should be stable, but in practical measurements it turns out that this is – at least on large time scales – not the case.

Another problem is, that the proper determination of the X and Y value of a demodulated signal requires proper sampling of the waveform. If the waveform is not "clean" enough in the sense that it includes unwanted frequency components additionally to the wanted one, this results in a low-quality reference signal. This pushes, practically, the limit in sampling rate far below the theoretical limit, the Nyquist barrier.

A quantity that was found to offer an alternative to 2f-WM for locking the probe laser to the inflection point of the CTF is the 3rd moment of a measured distribution, the skewness[79].

If a modulated signal is measured for a given period of time and the skewness of this dataset is calculated, a function can be generated that

- Is zero at the inflection points of the transducer's transfer function
- Is additionally zero at the peak position of the transfer function
- Is not phase-dependent
- Is not limited to sinusoidal modulation waveforms
- Can be used for signal processing purposes right up to the limit of the Nyquist barrier

Details of this technique are presented in one of the publications that were performed within this thesis and that can be found as full-text in the appendix (Lindner et.al: *Theory, implementation and characterization of low-frequency Laser wavelength – Cavity resonance Locking Schemes for Cavity-enhanced spectroscopy*) so that here the idea is here just briefly reviewed.

The skewness of a dataset is defined as

$$\gamma = E\left(\left(\frac{X - \mu}{\sigma}\right)^3\right)$$

<div align="right">(2.140)</div>

where E is the expectation value, X is a stochastic variable, μ is the mean and σ the standard deviation.
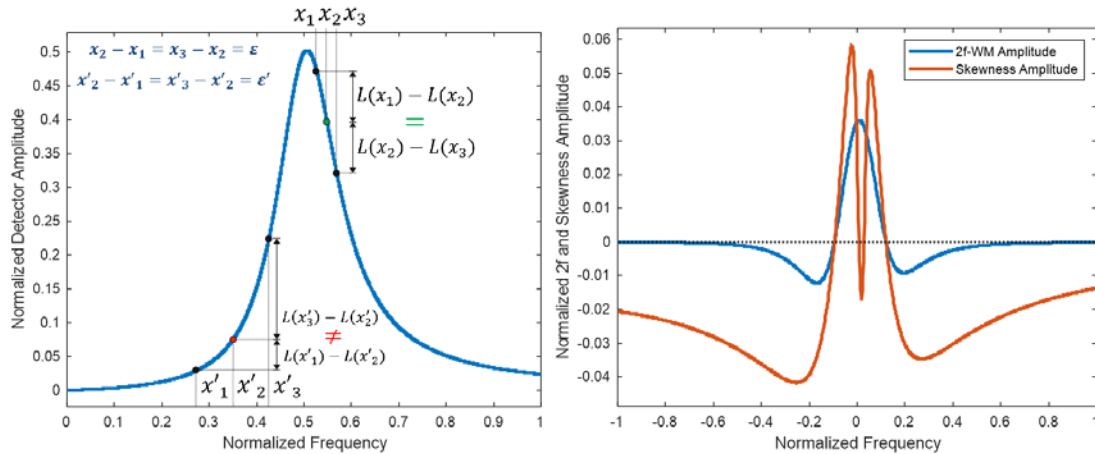

Figure 2.18: Left: Principle of skewness used as a measure of symmetry. Right: Demodulation of Graph II of Figure 2.17 by the skewness (orange) in direct comparison to the $2f$ amplitude

The property, that a skewness value of zero corresponds to the inflection point and as well to the peak value of a function, is very intuitive: An "unskew" section of a function is, in common understanding, connected with symmetry. Exactly this is the case: The skewness can be understood as a mathematical quantification of symmetry. The situation is depicted in Figure 2.18, left. On the left side, the result of demodulation by skewness is shown: Instead of demodulation by a LIA, the modulated detector raw signal described in section 2.4.2.1 is demodulated by applying the skewness operator.

2.4.3   Noise Suppression

As already mentioned in the beginning of this section (equation (2.130)), the suppression of noise is one side of improving the SNR. Since it turned out during the work in this thesis that the achievable increase of signal amplitude, especially in ICAPS, was very limited, the focus was put on the suppression of noise. The results of this research are published in Lindner et.al: *Noise suppression and 1f-Quadrature Point readout technique for cavity-enhanced optical dispersion spectroscopy* and are shortly reviewed in the following subsections.

2.4.3.1   Electronic Filtering

Since all signals are brought to the electronic domain after detection (see Figure 2.13), the logical first step is, to apply electronic filtering. The technique is highly established[80] and can, in principle, described by the circuitries depicted in Figure 2.19. A high-pass and a low-pass filter is the technical realisation of a Heaviside function in the frequency domain

$$H: \mathbb{R} \to (0,1) \cap \mathbb{N} \qquad H: x \mapsto \begin{cases} 0 & x < x_c \\ 1 & x \geq x_c \end{cases}$$

(2.141)

for the signal. All frequencies up to (low-pass, $H(-x)$) or from a specific frequency x_c on (high-pass, $H(x)$) can pass the filter, all others are stopped, respectively attenuated. x_c is called the cut-off-frequency and is defined by

$$x_c = \frac{1}{2\pi RC}$$

(2.142)

Where R denotes the resistance of the resistor in Figure 2.19 and C the capacitance of the capacitor.
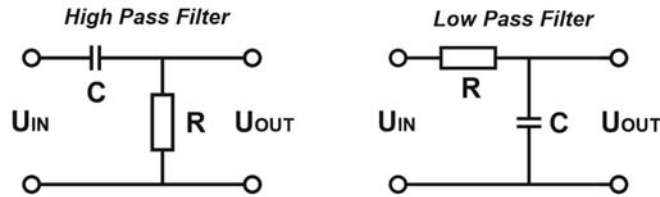

Figure 2.19: Electronic high- and low-pass filters

Low- and high-pass filters can be combined. Depending on the exact values of the cut-off-frequencies of high-pass and low-pass filter, x_c^{HP} and x_c^{LP}, they can be combined:

- $x_c^{HP} < x_c^{LP}$ leads to a band-pass-filter
- $x_c^{HP} > x_c^{LP}$ leads to a band-stop filter. If $x_c^{HP} - x_c^{LP}$ is low, the filter is called Notch-filter

A real filter does not represent an ideal Heaviside function. First, the frequencies that are supposed to be stopped (the values where the Heaviside function is zero) are actually not completely stopped but just attenuated. The attenuation is measured in dB, a logarithmic scale

$$[dB] = -20 \log_{10} \frac{A}{A_0}$$

(2.143)

Where A and A_0 denote the signal amplitude after and before the filter.

Second, the attenuation occurs not on a singular frequency, but just increases (low-pass) or decreased (high-pass) from the cut-off frequency on. The rate of this, in terms of attenuation per distance from the cut-off frequency can be increased if several filters of the same characteristics are combined in a cascade of filters. The number of such cascaded filters is called the order of the filter. It can be found, that the attenuation of a real filter is $20n$ dB per frequency octave, where n is the order of the filter. To describe the characteristics of a filter, often the depiction of attenuation vs. frequency is used. This logarithmic diagram is called Bode-diagram[81].

The filters that were designed and in-house manufactured during this thesis are described in section 3.1.1.

2.4.3.2   Balanced Detection

The idea of balanced detection is, although its technical realisation is highly complex, relatively simple: A real, measured signal consists of the (pure) signal itself and noise. If, besides the measured signal (signal path), also the noise is known from a separate measurement (reference

path) as a function of the time (or more generalized: of the same variable), the pure signal can be retrieved by simply subtracting the noise from the measured signal. The idea is depicted in Figure 2.20.

The technical implementation of this concept is not so straight-forward since several effects have to be considered. Generally speaking, the signal- and the reference path have to experience exactly the same transduction. If this is not the case, the noise in the reference path that should measure only noise has another phase or amplitude than the noise that is also carried in the signal path. Then, the subtraction does not lead to noise cancellation, but can even add more noise.
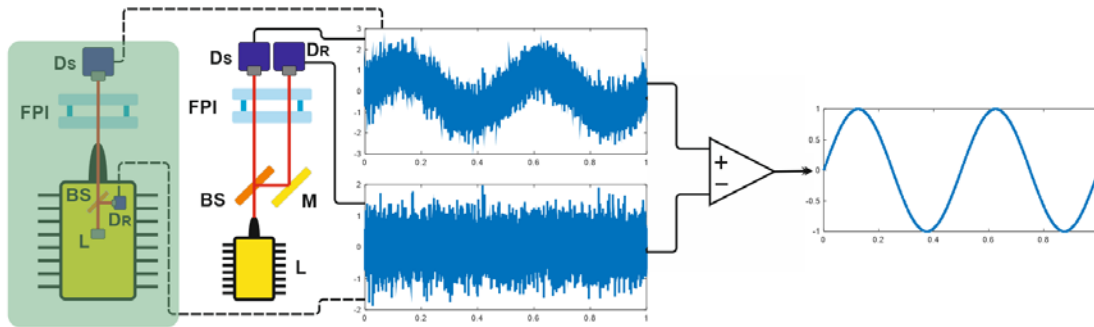

Figure 2.20: Principle of Balanced Detection: L..Laser, BS..Beam Splitter, M..Mirror, FPI..Fabry-Pérot Interferometer, D_R..Reference Detector, D_S..Signal Detector. For optical balancing (setup on white background), all components are part of the optical setup (free space optics). For Electronic Balancing and 1f-Quadrature Point Readout Balanced Detection, (Green Background) these components are not needed and the integrated monitor photodiode of the probe laser is read out instead of the reference detector signal.

2.4.3.3   Electronic Balanced Detection

Balanced detection techniques have been developed in many different applications[8,16,82]. In this thesis, balanced detection has been developed for Interferometric Cavity-Assisted Photothermal Spectroscopy (ICAPS). The aim was a reduction of complexity compared to optical balancing such as reported in[8]. For that purpose, the second optical path (reference path) was substituted by a read-out of the internal monitor photodiode of the probe laser. In that way, noise contributions from the probe laser in terms of intensity noise, but not the optical contributions from the cavity amplifying the frequency noise of the laser as well as acoustic noise could be balanced out. It could be demonstrated that the achievable noise, suppression is relatively close to the suppression capability of optical balancing, while the system complexity could be drastically reduced[83].

2.4.3.4   1f Quadrature Point Readout Balanced Detection (1f-QBD)

When implementing a balanced detection scheme that is based on the internal monitor photodiode of the readout-laser as described before, it is crucial that signal- and reference path are exactly in phase – the phase difference has to be 0.

The 1f-Quadrature point readout technique is published as well in Lindner et.al: *Noise suppression and 1f-Quadrature Point readout technique for cavity-enhanced optical dispersion spectroscopy*. The full-text of this publication can be found in the appendix and is shortly reviewed at this point. The idea here is, to establish a phase difference of π instead of zero in an *ex situ nascendi* sense. That means, that the reference and the signal path are pre-amplified with different sign. This

leads to the situation, that quadrature points are arising that give the method its name.

After aligning the signal amplitudes of the monitor photodiode and the detector photodiode, instead of a subtraction of signal and reference path as it is done in electronic balancing, a summation is performed. This leads also to a cancellation of the noise due to the opposite sign of signal and reference path. Additionally, if the signal path is slightly phase-shifted by the analyte, this has the consequence that the sum signal is not zero anymore but gets periodic with the same frequency the excitation uses as modulation frequency. If the sum signal is now demodulated at the first harmonic by a LIA, the system is highly sensitive to phase shifts in the signal path and the phase shift can be measured.
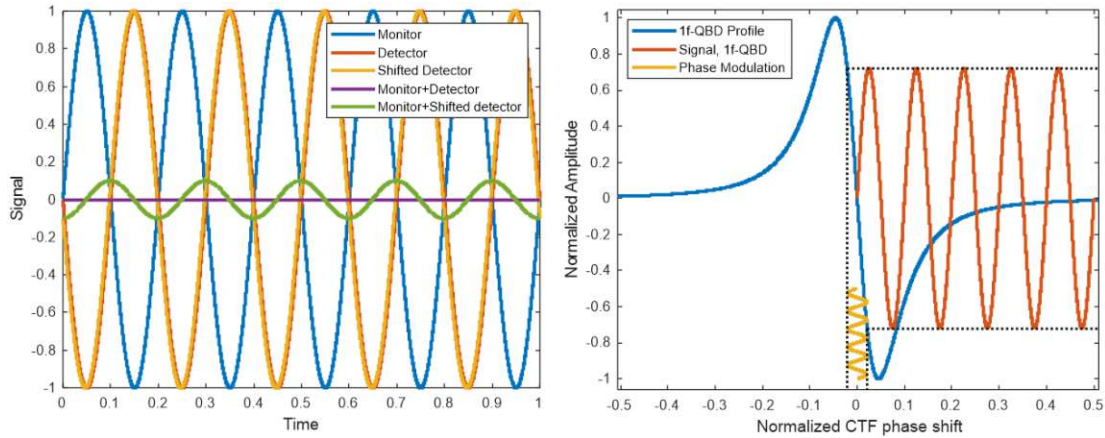

Figure 2.21: Principle of 1f-Quadrature point readout. Left: Depiction of the effect on the 1f amplitude of the sum signal (green) if the detector signal is phase shifted. Right: Signal enhancement effect of the 1f demodulation

Figure 2.21 shows the principle of the 1f-Quadrature point readout technique: On the left side, the signal generation due to a slight phase shift is visualized: The monitor photodiode (blue) has fixed phase – on that diode, no light-matter interaction takes place. Before a dispersing analyte is applied to the interaction volume the detector photodiode has a phase shift of π (orange) and the sum of detector and monitor photodiode is constantly zero (purple). If a phase shift due to analyte dispersion in the light-matter interaction volume between the mirrors of the Fabry-Pérot cavity (see Figure 2.20) takes place, the sum signal (green) shows significant oscillation with the same frequency the laser is modulated. For this effect even very little phase shift is enough – in the example shown in Figure 2.20, the phase shift is just 1.5% of the oscillation period, what is from similar magnitude as it was observed in Mach-Zehnder interferometer based liquid sensing (see section 3.3) causing an amplitude of more than 10% of the modulation amplitude.

If the sum signal is demodulated at the 1st harmonic, the blue transfer function on the right side of Figure 2.21 function is obtained. It is the amplitude of the 1st harmonic – if the detector signal is phase shifted in positive time direction, the 1f amplitude goes down in the negative range. If it is shifted in the negative time direction, the 1f amplitude goes in positive direction. Any change of the phase difference, depicted as a yellow sine, is amplified by the slope of that transfer function (orange signal).

Chapter 3   Experimental Details and Developments

In this third chapter of the thesis, technical and experimental details and the actually implemented technology that has been developed is presented. Major state-of-the-art technology that was intensively used and/or has been a crucial part of the entire experimental setups is reviewed and aspects of special interest are pointed out.

3.1 Circuitry Developed and Used

In-house developed electronics played an important role in the practical work of this thesis. The underlying principles of the implemented circuitry are all well known[80]. However, due to the fact that they are crucial for the functionality and the performance of the developed sensing setups, they are presented and briefly described at this point. Further, knowing that a filter, an amplifier or other well-known electronic devices are used, is far not enough to be able to reproduce a system. It is the knowledge about exact values of the implemented passive components (resistors and capacitors) or the specific model of the integrated circuits (operational amplifier) that specifies the characteristics of any circuitry and is therefore crucial for the understanding of the role of that circuitry in the sensing system.

3.1.1 Filters

The principal circuitry of an electronic filter is depicted in Figure 2.19. However, the depicted filters are passive filters. This means, that they represent a load. This can be problematic: Some devices in the electronic system are limited in the current they can provide. The digital-analog converter (DAC) as an example that has been briefly described in section 2.4.1, is limited to a maximum output current of 5 mA. If the load connected to the DAC is higher, the voltage output is not correct anymore.

For that reason, so-called active filters are used. The core device of this circuitries is a low-noise operational amplifier (OPA). In the developed circuits in this thesis, the OPA 227 and its two- and four channel versions (OPA2227, OPA 4227) by Texas Instruments were employed. This OPA shows very low noise (3nV Hz$^{-1/2}$) and is able to be operated both in high frequency ranges and in DC. The OPA, as an active device, always needs a supply voltage. For the OPA 227, 12V from a linear power supply (Thorlabs) was used. Following the datasheet, damping capacitors of 100 and 1000 nF each parallel to the positive and the negative power supply were applied.

Further, high- and low-pass filters are combined to band-pass and band-stop filters – as depicted in Figure 3.1. The entire circuitry implemented in the sensing system is given in the appendix.
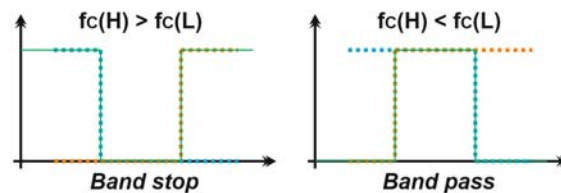

Figure 3.1: Combination of a High-pass (orange) and a Low-pass filter (blue) to a Band-stop or Band-pass filter (green)

3.1.1.1 Low-Pass-Filter

In Figure 2.19, it can be recognized that the filters are nothing else than (complex) voltage deviders[80]. The complex resistance (impedance) of an ohmic resistor is equal to the real resistance: $Z_R = R$. The impedance of a capacitor can be found by

$$Z_C = \frac{1}{i\omega C}$$

(3.144)

where i is the imaginary unity and C is the capacitance of the capacitor. Since the impedance of a

capacitor is dependent on the angular frequency ω, the consequence is a frequency-dependent voltage divider. The logarithmic depiction of this dependence, is the Bode-diagram, introduced in section 2.4.3.1. The Bode diagram has two asymptotes – one parallel to the frequency axis, the other one asymptotic to the flank of the Bode diagram. The frequency value of the intersection of these two asymptotes is called the cut-off-frequency, that can be calculated from equation (2.143).

First order filters would show a far too low edge steepness for the desired application in the spectroscopic sensing system. For that reason, higher order (in particular: fourth order) filters were implemented. For active filters, it is possible to combine two filter stages to a second order filter, as depicted in Figure 3.2. Consequently, two of those second order filters were combined to a filter of fourth order (see appendix).
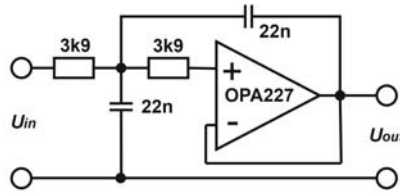

Figure 3.2: Active second order Low-Pass filter, $f_C = 1.85$ kHz

3.1.1.2   High-Pass-Filter

For realizing a High-pass filter, the same underlying principles apply as for the Low-pass filter described before. Basically, just resistors and capacitors are exchanged. The circuitry of the second order active filter that was implemented, is depicted in Figure 3.3.
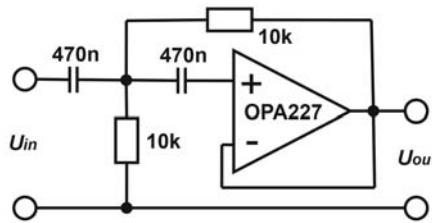

Figure 3.3: Active second order High-Pass filter$f_C = 34$ Hz

3.1.1.3   Bode-Diagrams of In-House-Built Filters

The entire filter board that has been developed, was tested before it was applied to the sensing system. The obtained Bode diagram is depicted in Figure 3.4. There were three input and four output channels that are described in Table 3.4.

Channel	Input	Output	Type	Cut-off frequencies	Order	Description
1	EL DAQ	EL DRV	Low Pass	1.85 kHz	4	Anti-aliasing filter for excitation laser driver
2	PL DAQ	PL DRV	Low Pass + Band Stop	10.2 kHz, 15.9 Hz + 1.29 kHz	4	Anti-aliasing filter for probe laser driver and Band-stop for ICAPS modulation frequency range
3	DET	LOCK	Low-Pass	10.2 kHz	2	Anti-aliasing filter for analog-digital converter
4	DET	ICAPS	Low Pass + Band Pass	10.2 kHz, 1.75 kHz, 34 Hz	4	Anti-aliasing filter for analog-digital converter and Band-pass for ICAPS modulation frequency range

Table 3.4: Implemented filter channels on the main filter board in the sensing system
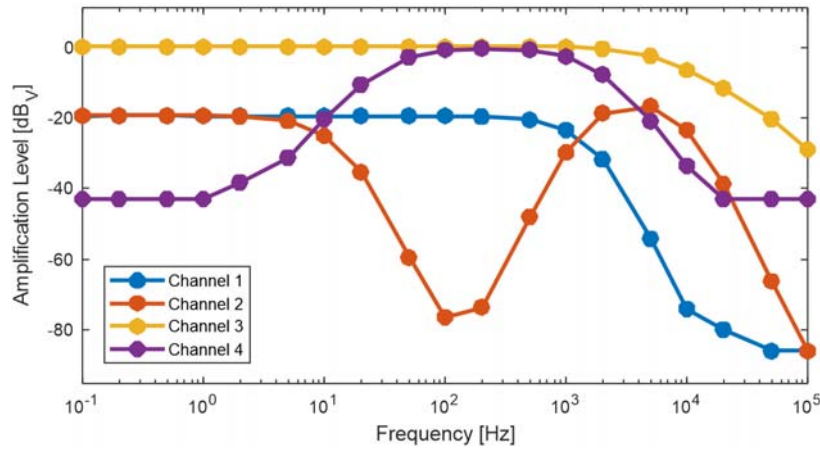
Figure 3.4: Measured Bode-Diagrams of the in-house-built filter stage. The channel numbers refer to Table 3.4

3.1.1.4   Noise Suppression Capabilities

As the nature of electronic filters predicts (see Bode diagrams, Figure 3.4), the filtering capabilities are heavily dependent on the frequency range: the farer away from the cut-off frequency, the higher the noise suppression capabilities are. The in-house developed filters reach a maximum suppression performance of -30 dB Hz-1/2[83]. For details, it is referred to the manuscript in Lindner et.al: *Noise suppression and 1f-Quadrature Point readout technique for cavity-enhanced optical dispersion spectroscopy*, that can be found in full-text in the appendix of this thesis.

3.1.2   Phase Shifter (All-Pass-Filter)

Application of filters lead also to a phase shift of the transmitted frequencies in addition to intensity reduction of those frequencies covered by the stop band. This is due to the complex nature of the capacitor impedance. The phase shift of a single capacitor can be calculated by

$$\Delta\varphi = \pm\arctan(\omega RC)$$

<div align="right">(3.145)</div>

Where the expression with positive sign represents the phase shift of a high-pass filter and the negative sign the phase shift of a low-pass filter.
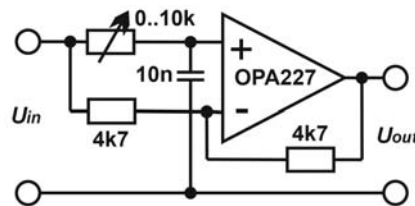

Figure 3.5: Active first order All-Pass filter, used as (adjustable) phase shifter

This effect can be used to build up a device that does shift the input signals phase: If the cut-off frequencies of a Low-pass and a High-pass filter overlap, filter characteristics can be obtained, that show no attenuation at all. This is, with corresponding choice of the values of R and C, not true for the phase shift – it remains different from zero. Since a filter of this kind does not

attenuate the signal at any frequency, it has a pass band of infinite width and is therefore called All-pass filter. Figure 3.5 shows the circuitry of the implemented first order All-pass filter.

3.1.3   Amplifiers

The majority of the signals in the sensing system are voltage signals – measured signals as well as control signals. Often, the signal level at the output of a device does not match with the required input signal level of the next device. In this case, the signal level has to be adapted. Further, signals that are not in the voltage domain have to be translated to voltage.

3.1.3.1   Transimpedance Amplifier

A transimpedance amplifier (TIA) is used to convert a current signal into a voltage signal. Such a device is needed to read out a photodiode: the photodiode generates, according to the theory reviewed in the last chapter, a photo current. This current is very small (nano- to microampere range) and needs to be converted to a voltage signal with as low influence on that small current as possible. For this purpose, the property of an operational amplifier having infinitely high input impedance, is exploited. Effectively, the TIA acts as a resistor, what leads to its name. The conversion factor for the input current to the output voltage is the value of the resistor R:

$$U = -I \cdot R$$

<div align="right">(3.146)</div>

The circuitry is depicted in Figure 3.6. For the monitor photodiode of the probe laser in the sensing system, a fixed resistor of $1\text{k}\Omega$ was used in serial connection with two variable resistors of $0..10\text{k}\Omega$ and $0..100\text{k}\Omega$ resistance.
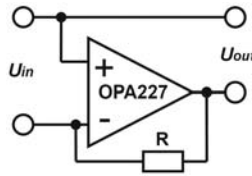

Figure 3.6: Transimpedance amplifier for photodiodes

3.1.3.2   Buffer

Often, the maximum current output of a device is too low in order to drive the following device. This is because the following device has a too low input impedance. This problem can be avoided, if a buffer is used in between. Again, the high input impedance of an OPA is employed. The voltage at the input is reproduced 1:1 at the output of the OPA. The specific circuitry is depicted in Figure 3.7.
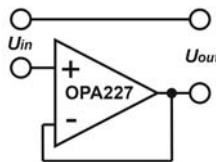

Figure 3.7: Voltage buffer

3.1.3.3   Gain

A gain changes the voltage amplitude of a signal. This can be done in two directions: If the voltage amplitude has to reduced, a voltage divider in combination with a buffer can be used. For an increase of the voltage amplitude, the voltage divider has to be applied to the feedback side of an OPA. Figure 3.8 shows on the left side an active voltage gain that reduces the voltage amplitude and on the right side an amplifying voltage gain.
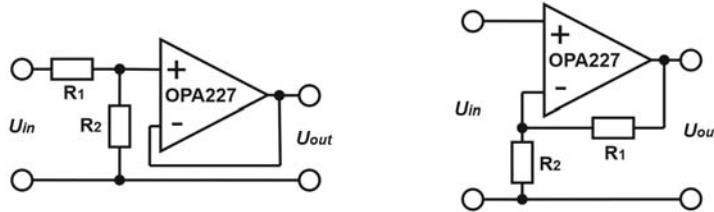

Figure 3.8: Left: Gain with amplification factor below 1, Right: Gain with amplification factor above 1

3.1.4   Adder and Subtractor

An OPA can also be used to add and subtract signals. The active adder, depicted in Figure 3.9 is the direct connection of two inputs that is then buffered by the OPA. The active adder utilizes the fact, that an OPA has an inverting as well as a non-inverting input – the minuend is connected to the non-inverting input while the subtrahend is connected to the inverting input. Additionally, the sum as well as the difference can be weighed by resistors.
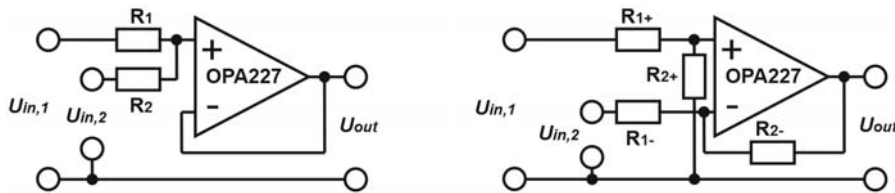

Figure 3.9: Active adder (left) and subtractor (right)

3.1.5   Reference Source – RC Oscillator

For some applications like lock-in-amplification, a stable, one-frequency signal is needed. Whenever signals are generated digitally, the sampling frequency is anyhow present in the analog output signal of the digital-analog converter. A step-free, continuous signal has to be formed in an analog way.

This can be done by a RC-oscillator. A capacitor is charged by a voltage source. Via a resistor, the capacitor then is discharged again. The arising oscillation is then stabilized by an OPA. The oscillation frequency is defined by the resistor and the capacitor and can be calculated by

$$\omega = \frac{1}{RC}$$

(3.147)

Figure 3.10 shows the circuitry of a RC-oscillator with an adjustable frequency between 1 and 10 kHz. (Wien-Robinson oscillator, US patent US2268872A, William R. Hewlett) This oscillator was used in the sensing system as reference source and for probe laser modulation.
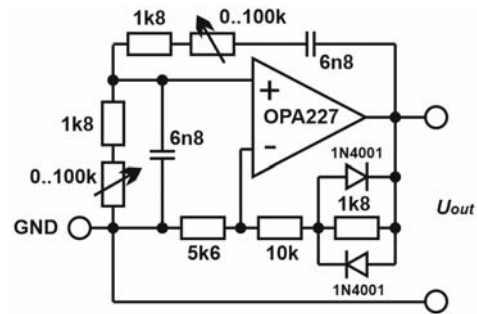

Figure 3.10: Buffered RC-oscillator

3.2 Table Top Devices

There were many instruments used in the sensing system, that are commercially available. In this section, the most important of them are briefly reviewed in terms of their functionality.

3.2.1 Lock-In-Amplifier

A Lock-In-Amplifier (LIA) effectively is a very narrow band pass filter with an additional integrator, that is phase-selective[84].

The operation as a narrow-band pass filter is widely employed in modulation spectroscopy. Especially, the fact that low frequency contributions to a signal are heavily damped leads to a significant improvement in signal-to-noise ratio. This is especially the case because of the $1/f$ - noise. This noise contribution is primarily caused by the noise caused by the finite resistance of electronic components: The $1/f$ - noise decreases with increasing frequency. If low frequencies can be filtered out, the $1/f$ - noise contribution to the total noise is accordingly low.

The property of phase-selectivity can lead to problems because in a real sensing system even small differences in phase impair the quality of long term measurements.

3.2.1.1 Operation Principle

The operation principle of a LIA can be described by cross-correlation of the signal and a reference signal, that is a sinusoidal signal of constant amplitude that has exactly the frequency, at that the measurement has to be performed. After the signals have been aligned in phase by a phase shifter, they are multiplied and afterwards low-pass-filtered, what is equivalent to an integration. The integration time has to be at least one period of the reference signal or expressed in the frequency domain, $\frac{1}{f}$, where f is the reference frequency. The output signal then is proportional to the average amplitude of the frequency band of the input signal that is located in a narrow neighborhood of the targeted frequency. Usually, this frequency is the modulation frequency of the input signal or multiples of it. Because of that rectifying effect – instead of the entire oscillation, the average amplitude of the frequency of interest is output – and the fact, that the output signal is dependent on the phase difference between signal and reference, a LIA is also called phase-sensitive rectifier. Figure 3.11 shows a principal sketch of a LIA – the input filter, marked in green, can be beneficial for preconditioning of the signal, but it is not mandatory. The other components are crucial for its functionality.
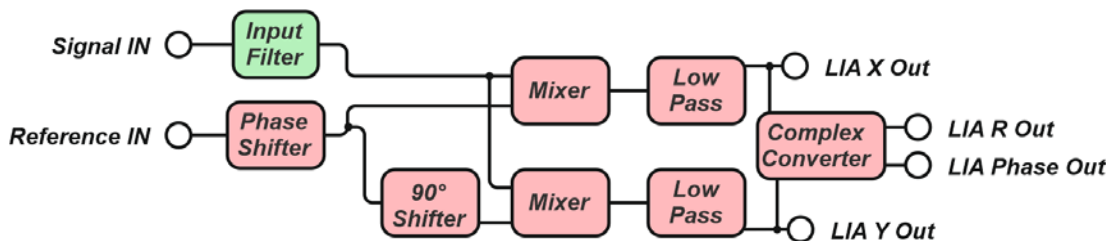

Figure 3.11: Principal sketch of signal transduction in a Lock-In amplifier.

3.2.1.2   LabView Based LIA

Table-Top LIA instruments with research grade performance such as the SRS 860 instrument by Stanford Research Systems that was employed in the field of this thesis, are bulky devices. There are also small LIA models available on the market, but an even more elegant approach is to digitally implement a LIA. Since all the instrument control of the developed sensing systems is performed in LabView, a graphical programming language by National Instruments Inc. A LIA was implemented on that platform. The core pieces of code (virtual instruments, VI's) were taken from a LabView user community open-source project that aimed at the development of a LabView- based LIA. The code was adapted to embed it in the overall LabView control software of the sensing system and is given in the appendix.

The performance of the LabView based LIA was compared to the SRS 860 by a 2f-WMS direct absorption spectroscopy (see section) measurement. The result is depicted in Figure 3.12.
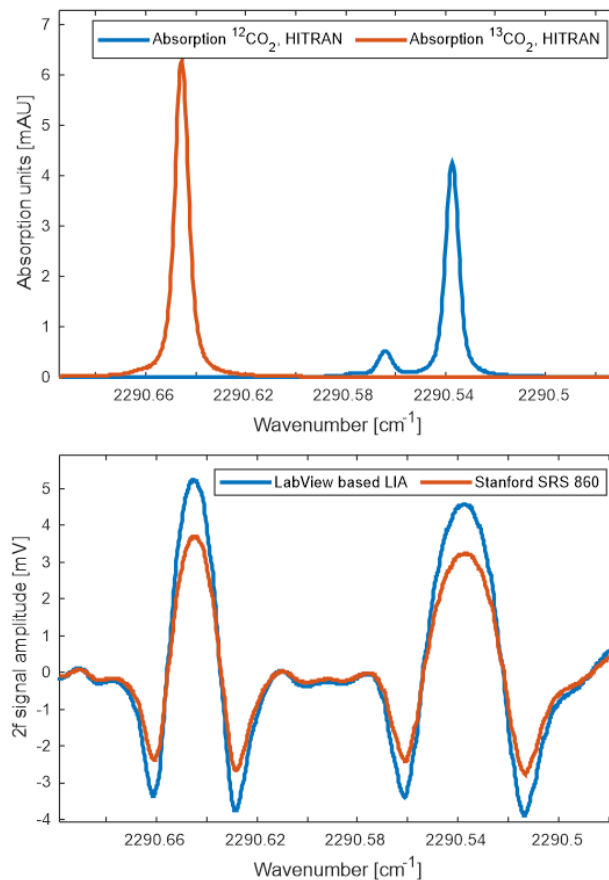
Figure 3.12: Comparison of the performance of a table-top LIA and the LabView-based LIA. Parameters: 1 second integration time, 18 dB Low-pass filter, 10 mV sensitivity.

3.2.1.3   Phase-independent Noise Expression

A problem that can arise in some applications is that the output of a LIA is dependent on the reference phase. This is the case when noise of a system, that employs a LIA has to be characterized, as the phase assignment is unwanted because noise contributions with any phase are from interest. For that purpose, the following consideration was made within the work for this thesis:

A technical problem arising from the phase-dependent nature of a signal processed by a LIA is the fact that the noise level seen on the X and the Y channel is dependent on the phase between the signal and the reference. Since the signal is, when considering noise, often almost zero, its phase is often unknown what would make a measurement of both, X and Y, necessary in order to measure all noise contributions.

If the signal is near zero, this technical increase in measurement complexity can be avoided by a simple mathematical consideration that employs just the R channel of the LIA.

First, the combined variance of the noise of X and Y channel is defined as the mean of the single variance values. This combined standard deviation can then be written as

$$\sigma_{XY} := \sqrt{\frac{1}{2}(V_X + V_Y)}$$

(3.148)

By use of the definition of the variance and the circumstance, that during a noise measurement the mean of as well the X and the Y component is zero over time, with $X_i^2 + Y_i^2 = R_i^2$ the approximation

$$\sigma_{XY} = \frac{1}{\sqrt{2}}\sqrt{\frac{1}{n}\sum_i (X_i - \bar{X})^2 + \frac{1}{n}\sum_i (Y_i - \bar{Y})^2} \cong \frac{1}{\sqrt{2}}\sqrt{\frac{1}{n}\sum_i R_i^2}$$

(3.149)

can be found. This expression is equivalent to $\frac{1}{\sqrt{2}}\sqrt{\mu_{(R-0)^2}}$, where μ expresses the mean. Finally, with Steiner's theorem it is found

$$\sigma_{XY} = \frac{1}{\sqrt{2}}\sqrt{\sigma_R^2 + \mu_R^2}$$

(3.150)

With that expression, the combined noise on both, the X and the Y component, can be described – without the need of simultaneous measurement of both quantities X and Y.

3.2.2 Spectrum Analyzer

A spectrum analyzer can be understood as a multiple-frequency LIA – the reference frequency is swept over the desired frequency range with a given speed. In this way, the frequency distribution in this range can be measured in terms of the power density function[85,86]. Since only specific frequencies such as the modulation frequency of a laser and its integer multiples are expected, this frequency spectrum delivers valuable information about the frequency distribution of the noise that is carried by the signal. Once an unexpected or unwanted frequency is detected, this often allows conclusions about the source of the noise and how it could be mitigated.

In principle, the task a spectrum analyzer overtakes, can also be fulfilled by the Fast Fourier Transformation (FFT) – this is a powerful mathematical algorithm to calculate the frequency spectrum out of sufficiently fast sampled data. However, a spectrum analyzer delivers, due to its measurement principle, far more detailed and resolved information.

The instrument that was used in this thesis was a FSV4 Signal Analyzer by Rohde&Schwarz.

3.2.3   Lasers

Different semiconductor lasers are core devices of the developed sensing systems. While the theory of lasers is presented in section 2.1, here the experimental characterizations in terms of wavelength- and power spectrum of the employed lasers are presented.

3.2.3.1   DFB-QCL from Alpes Lasers

The Alpes Lasers HHL-packaged DFB-QCL (serial number: HHL-678), that emits around 2291.5 cm^{-1} that was used as excitation laser for ICAPS and direct absorption 2f-WMS, has been driven by a Koheron QCL100 quantum cascade laser driver. Power-spectra were measured using a gentec-eo Solo 2 laser power meter. Wavenumber spectra were recorded on a Bruker Vertex 80v Fourier-Transform-Infrared Spectrometer. The results are depicted in Figure 3.13.
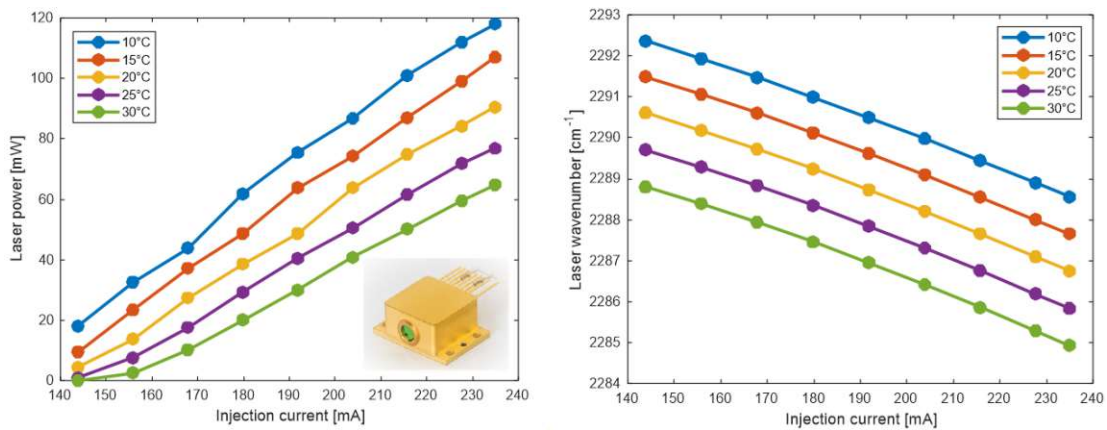
Figure 3.13: Power- and wavelength spectra of the implemented QCL

3.2.3.2   Fiber-coupled Telecom Laser from Emcore

The Emcore 1550nm fiber coupled butterfly-packaged telecom laser (model 1782B-NM-050-34-FC-PM), that was used as probe laser for the Fabry-Pérot cavity, was driven by a Koheron CTL101-B400 butterfly laser driver. The characteristic spectra were recorded with the same devices as it was done for the DFB-QCL (section 3.2.3.1). The results are depicted in Figure 3.14.

Figure 3.14: Power- and wavelength spectra of the implemented NIR laser

This laser has also an integrated monitor photodiode with an output of 100 to 2500 µA. Corresponding to this value, a transimpedance amplifier (TIA) was designed in-house to be able to read it out in real time. The designed TIA is described in section 3.1.3.1.

3.2.4 Fourier-Transform-Infrared (FTIR) Spectrometer

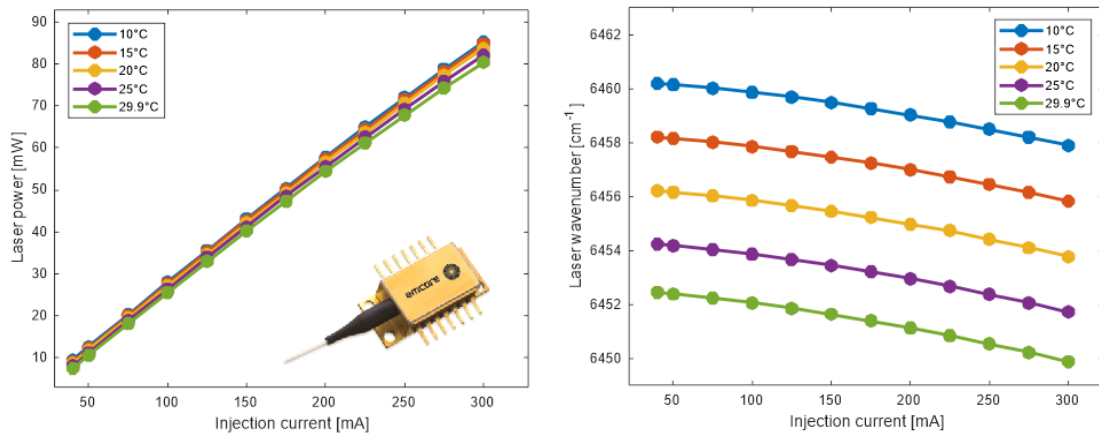Fourier-Transform-Infrared spectroscopy is one of the most important techniques of infrared spectroscopy and serves as a well-established reference method[87]. In the field of this thesis, a Bruker Vertex 80v instrument was employed to characterize lasers (see section 3.2.3) and to gain reference spectra for sugars to compare them to the results that were obtained by the Mach-Zehnder dispersion spectroscopy setup (section 3.3)[25].

A detailed description of this technique would lead too far, but the principal sketch of a FTIR-spectrometer is depicted in Figure 3.15.

The core of the instrument is a Michelson-Morley interferometer. The raw data measured by the detector (that is often a liquid nitrogen cooled MCT detector), the interferogram, is then Fourier-transformed by FFT to get the infrared spectrum, what gives the method its name.
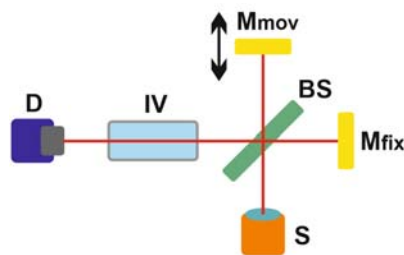
Figure 3.15: Principal sketch of a Fourier-Transform-Infrared Spectrometer (FTIR): S..Source, Mfix..fixed Mirror, Mmov..movable Mirror, BS..Beam splitter, IV..Interaction volume, D..Detector

3.2.4.1 Measurement of Reference Spectra

For measuring laser spectra, the resolution capabilities of the Bruker Vertex 80V FTIR spectrometer had to be pushed to the limit of 0.07 cm^{-1}. Figure 3.16 shows exemplary FTIR emission spectra of the QCL and the NIR probe laser employed in the ICAPS setup and of the EC-QCL used in the Mach-Zehnder interferometer based dispersion spectroscopy setup for liquids, including the full width of half maximum (FWHM) of each emission peak. At this point it is to mention, that the experimentally found FWHM of the DFB lasers is very close to the resolution limit of the FTIR. From the laser's datasheets it is known, that the laser line width of the DFB lasers is significantly below 0.01 cm^{-1}. This is narrower than the FTIR resolution limit, with the consequence that the measured spectra are not accurate. Contrary to that, the laser line of the EC-QCL with a line width of around 1 cm^{-1} is able to be resolved by the FTIR instrument.
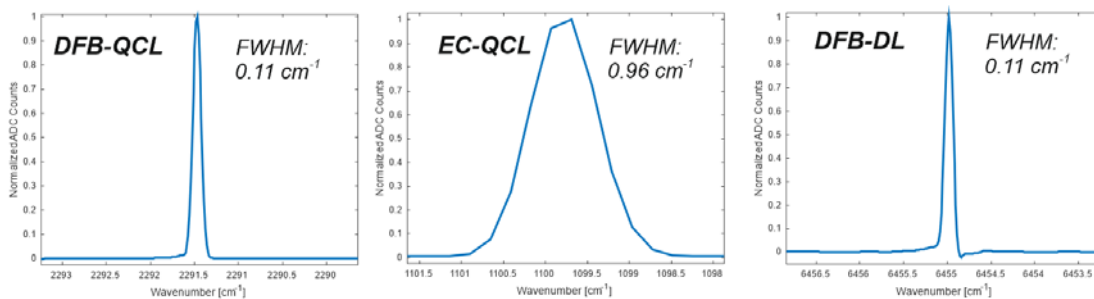
Figure 3.16: Exemplary spectra of the output of the employed DFB-QCL (left), EC-QCL (middle) and NIR laser (right), measured by a Bruker Vertex 80V FTIR spectrometer

Figure 3.17 shows FTIR spectra of the analytes measured in this thesis:

- In the first row, the FTIR spectrum of the CO_2 reference gas (50 mm length, wedged and tilted MgF_2 windows, 40 Torr, 50% CO_2, wavelength references) cell that was used in the ICAPS system is shown. On the left side, the whole range where the investigated absorption lines are located is presented. On the right side, the green marked range is given in detail.
- In the second line, FTIR spectra of ethanol and glucose is given.

If the analyte spectra from Figure 3.17 are compared to the laser emission spectra given in Figure 3.16, it can be recognized that the broad emission line of the EC-QCL, that was used to perform liquid phase spectroscopy with ethanol and glucose solutions as analytes, corresponds to the broad spectral features of ethanol and glucose. The narrow DFB-QCL emission line corresponds to the narrow gas absorption lines of CO_2. Second is the spectrum of ethanol and the last one is the spectrum of glucose.
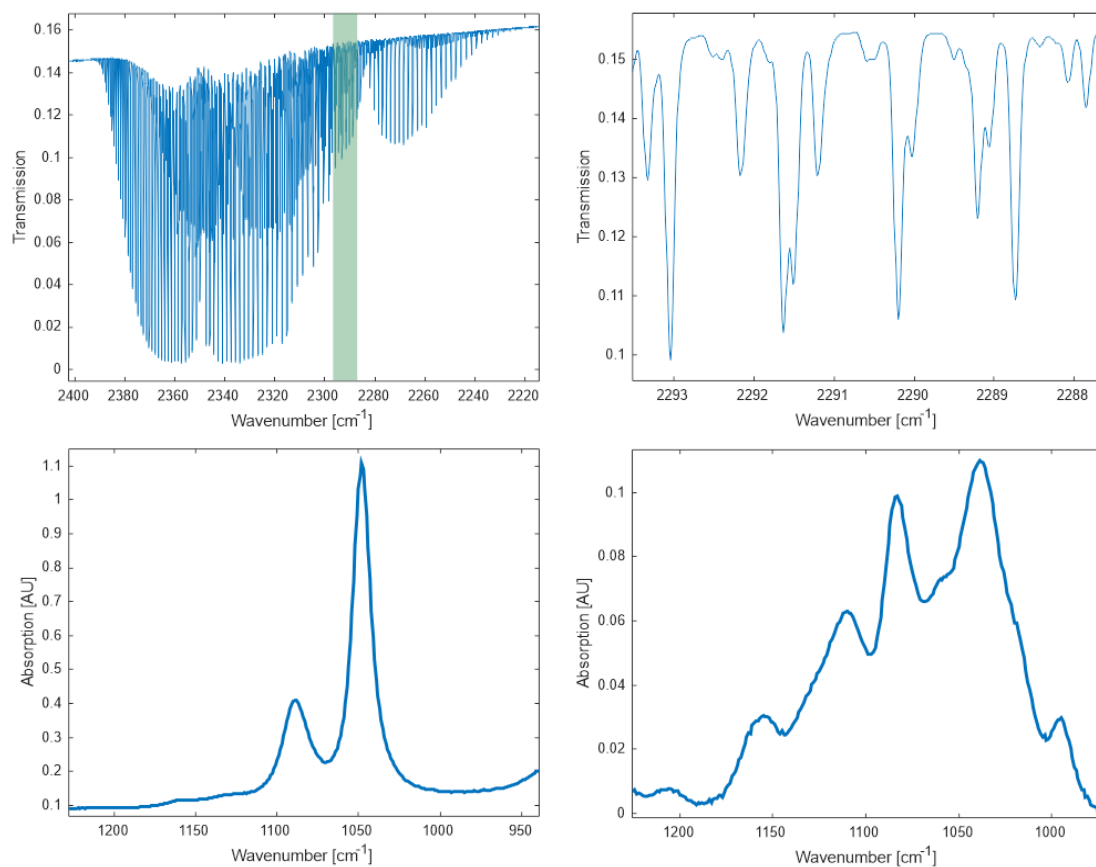
Figure 3.17: First line: FTIR-Spectrum of the CO_2 reference cell, used in the ICAPS setup, measured by a Bruker Vertex 80V FTIR spectrometer in two different wavenumber ranges. The marked range in the left spectrum that is shown in the right spectrum is the range, the DFB-QCL that was used in the ICAPS and $2f$-WMS setups covers. Second line: FTIR Spectra of ethanol (left) and glucose (right) in the wavenumber range covered by the employed EC-QCL.

3.3 Dispersion Spectroscopy of Liquids

3.3.1 Setup of the Mach-Zehnder Interferometer

The Mach-Zehnder interferometer (MZI), that is the core optical device for the technology developed in the field of dispersion spectroscopy of liquids, was introduced in section 2.2.1 and is depicted in Figure 2.8. In this thesis, the Mach-Zehnder interferometer was used to perform dispersion spectroscopy in the liquid phase[25,88]. Figure 3.18 shows the sketch and a picture of the Mach-Zehnder interferometer developed in this thesis.
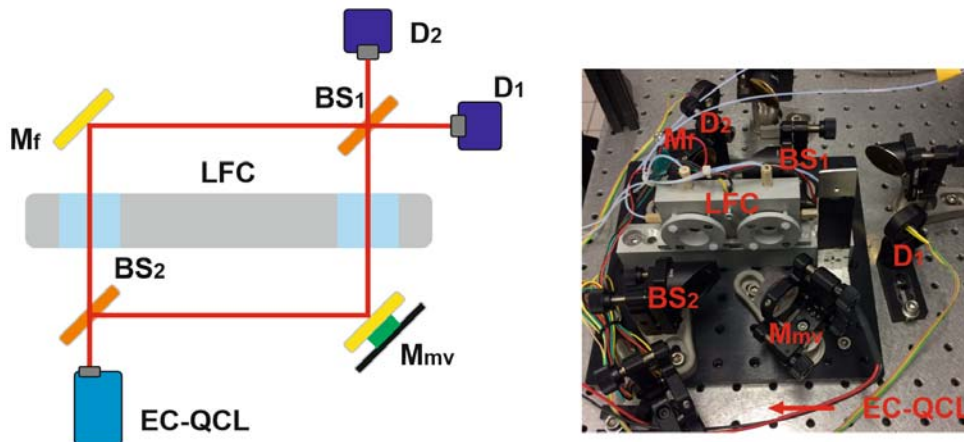
Figure 3.18: Left: Sketch of Mach-Zehnder Dispersion Spectroscopy Setup: EC-QCL..External cavity Quantum Cascade Laser Daylight solutions, BS..Beam Splitter, Mf..Fixed Mirror, Mmv..Movable Mirror (mounted on Piezo actuator, green), D..Detectors, LFC..Liquid Flowcell; Right: Photograph of the realized Setup

To understand the sensing capabilities of this setup it has to be analyzed which intensity arrives at the detectors D1 and D2. Both beams pass the (double) liquid flow cell, where a liquid sample of 50 µm thickness is located between barium fluoride windows. One beam passes the flow cell filled with solvent (reference) with an absorption of A_0, the other beam the flow cell filled with the analyte dissolved in the solvent (sample) with an absorption of $\hat{A} = A_0 + A$.

Assuming an initial laser intensity of I_0, the intensity that reaches the detector can be calculated by

$$I = I_0 \cdot C_1 \cdot C_2 \cdot 10^{\hat{A}}$$

(3.151)

where $C_1, C_2 \in \{R, T\}$ are either reflection or transmission coefficients, depending on the beam path and what is happening at the beam splitters BS1 and BS2. For example, for the part of the lower beam path in Figure 3.18 detected by detector D1, it holds $C_1 = R$ and $C_2 = T$. $\hat{A}$ is the total absorption, the corresponding beam is experiencing. Depending on where the sample and where the solvent is located, it either holds $\hat{A} = A_0$ or $\hat{A} = A_0 + A$.

The total detected intensity of one detector can be found by

$$I = I_a + I_b + 2\sqrt{I_a I_b}\cos\Delta\varphi \tag{3.152}$$

with $\Delta\varphi = \frac{2\pi}{\lambda}(\Delta l + d\Delta n)$, where Δl denotes the difference in path length, Δn the difference in refractive index, $d = 50\mu m$ the effective flow cell thickness and λ the wavelength of the laser. As already mentioned in section 2.2.1, additionally to that, there is a phase difference of π between upper and lower path of the MZI, what leads to the dependence of I from the phase depicted in Figure 2.9.

The chemical information can be extracted from the differential signal of both detectors. Applying equations (3.151) and (3.152) for all beams depicted in Figure 3.18, leads to

$$\Delta I = \frac{I_{D1} - I_{D2}}{I_{D1} + I_{D2}} = \frac{\cos(\Delta\varphi)}{\frac{1}{2}\left(10^{\frac{A}{2}} + 10^{-\frac{A}{2}}\right)} \tag{3.153}$$

At the quadrature point, it holds $\Delta l = \frac{\lambda}{4}$, as it can be recognized from Figure 2.9. With that, equation (3.153) simplifies to

$$\Delta I = \frac{2\sin\left(\frac{2\pi d}{\lambda}\Delta n\right)}{10^{\frac{A}{2}} + 10^{-\frac{A}{2}}} \tag{3.154}$$

what can be further simplified by use of the approximation $\sin x \approx x$ for small values of x and the fact that the absorption is very small. This leads to

$$\Delta I \approx \frac{2\pi d}{\lambda}\Delta n \tag{3.155}$$

For more details, the reader is referred to the publication "Lindner et.al.: "*External Cavity Quantum Cascade Laser-Based Mid-Infrared Dispersion Spectroscopy for Qualitative and Quantitative Analysis of Liquid-Phase Samples*" that can be found as full-text in the appendix.

3.3.1.1 Operation of the MZI - Moving Piezo Method

This method is the intuitive and physically correct one: In order to keep the system at its highest possible sensitivity and linearity, the optical pathway in the lower arm of the Mach-Zehnder interferometer in Figure 3.18 is constantly corrected by a movement of one mirror placed on a piezo actuator. Due to the geometry of the setup and due to the fact that the optical pathway is the geometric pathway weighed by the refractive index n of the medium, a travelled pathway dx_{Piezo} translates to a change of the optical pathway dx_{opt} by

$$dx_{opt} = dx_{Piezo} \cdot n \cdot \sqrt{2} \tag{3.156}$$

The constant correction of the optical pathway is realized by a feedback loop: The differential detector signal is measured and fed to a PID controller with zero as setpoint, that controls the piezo voltage. This voltage is proportional to the travelled pathway dx_{Piezo}. This piezo voltage is the sensor output signal that can then be translated to a refractive index value of the medium by calibration of the sensor with a substance of known refractive index.

The Moving Piezo Method has the advantage, that the sensor output signal – the piezo voltage –

is physically connected to the sensed quantity, the refractive index. The refractive index is proportional to the change in optical pathlength, that itself is proportional to the piezo voltage. However, this method has the technical disadvantage that the setup contains, with the movable mirror mounted on the piezo actuator, a moving part. Such parts are disadvantageous in terms of sensor ruggedness − if the sensor is used in the field, moving parts can be problem or at least potentially introduce a lot of noise to the system.

3.3.1.2   Operation of the MZI - Fixed Piezo Method

For the reason given above, a method was developed, that does not need any moving parts. This can be achieved by fixing the moveable mirror in the equilibrium position (the quadrature point) and then start the measurement. The range of the sensor is then limited to a phase shift of maximum $\pm\frac{\pi}{2}$, because the detector signal would get ambiguous if the phase shift exceeds this value. However, a possible phase shift of $\pm\frac{\pi}{2}$ is enough for the investigated sensing applications.

The idea of the Fixed Piezo Method is to use the raw differential detector signal $D_1(\varphi) - D_2(\varphi)$ as the sensor output signal. As mentioned before and as it can be visually recognized from Figure 2.9, this value is also proportional to the phase shift within the neighbourhood of a quadrature point.

3.3.1.3   Range Extension by Sine-Line-Extrapolation

The measurement range of the Fixed Piezo Method can be extended, if the measured detector signals are used to calculate the corresponding extrapolated value of the linear approximation around the quadrature point. The situation is depicted in Figure 3.19.
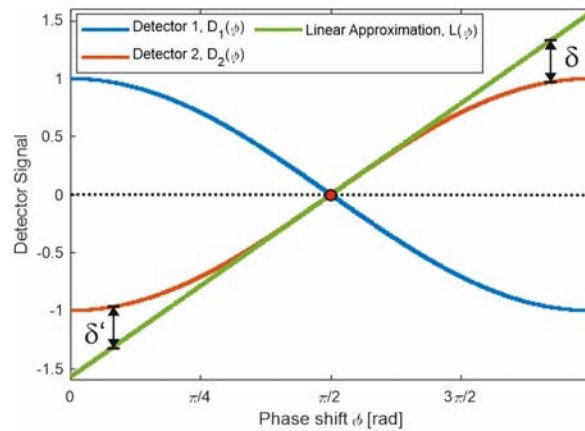
Figure 3.19: Sine-Line extrapolation for fixed piezo method

The detector amplitudes $D_1(\varphi)$ and $D_2(\varphi)$ are known from the measurement. With those two values, the correction value δ to extrapolate the value of the linear Approximation $L(\varphi)$ can be calculated by

$$\delta(\varphi) = \frac{D_1(\varphi)-D_2(\varphi)}{2} - \frac{\pi}{2} + \arccos\left(\frac{D_1(\varphi)-D_2(\varphi)}{2}\right) \tag{3.157}$$

This value can then be added to the differential detector signal $D_1(\varphi) - D_2(\varphi)$ to get the extrapolated linear approximation $\hat{L}(\varphi)$ by

$$\hat{L}(\varphi) = D_1(\varphi) - D_2(\varphi) + \delta(\varphi) \tag{3.158}$$

The transformation described by equation (3.157) is implemented in the MATLAB function `sinlincorr`, presented in the appendix.

3.3.2 Liquid Sensing

Finally, the sensing capabilities of the developed sensor is demonstrated. The Mach-Zehnder Dispersion Spectroscopy setup can also be used for absorption spectroscopy – for that purpose, the beam going through the flow cell carrying the pure solvent has to be blocked. With that, the interferometer properties are lost and the setup works as a direct absorption spectrometer.

3.3.2.1 Dispersion Spectra of Ethanol

First, qualitative spectra are acquired to demonstrate the functionality for absorption as well as for dispersion spectroscopy. For that purpose, an isolated (double) absorption peak of ethanol located between 1100 and 1025 cm^{-1} is investigated. Figure 3.20 shows the results: The absorption measurement by the Mach Zehnder setup overlaps very well with a reference spectrum recorded with a Bruker Vertex 80v FTIR spectrometer.
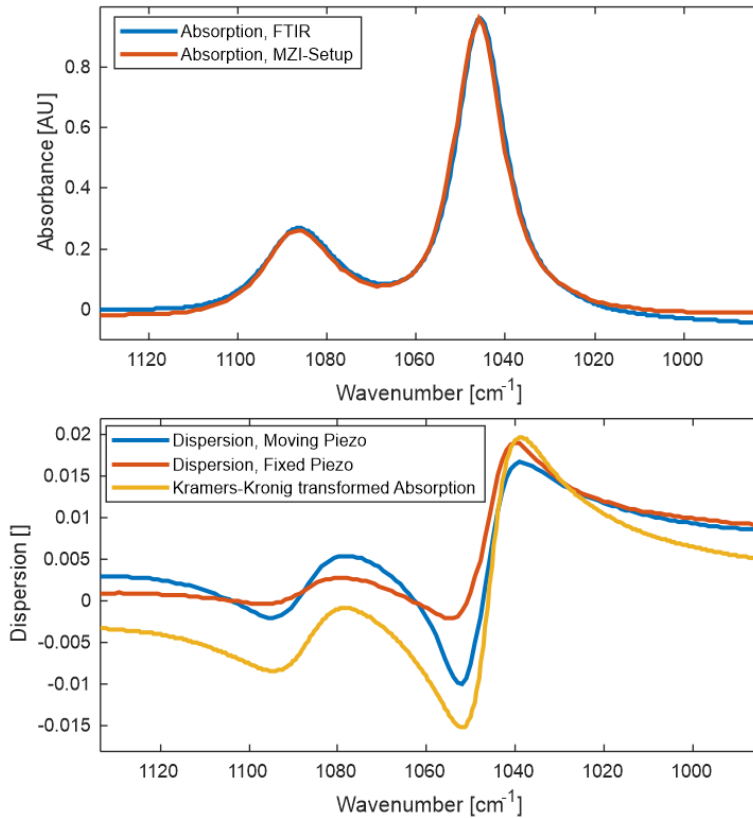

Figure 3.20: Above: absorption spectra of ethanol, measured by FTIR and MZI-setup. Down: Dispersion spectra of ethanol measured by Moving Piezo and Fixed Piezo Method and Kramers-Kronig-transformed absorption spectrum.

The dispersion spectra recorded by moving and fixed piezo method differ more from each other, but also match to the dispersion spectrum calculated from the recorded absorption spectrum using the Kramers-Kronig-Transformation: As it was described in section 1.2.2, it can also be seen that the absorption peak corresponds to the inflection point of the dispersion spectrum pattern.

3.3.2.2 Quantitative Multivariate Analysis of Ternary Sugar Solutions Using Dispersion Spectroscopy

In order to demonstrate the functionality of the setup also for complex analytes, a multivariate quantitative analysis of a ternary mixture of glucose, fructose and sucrose in the concentration range from 1 to 10 gL^{-1} was performed. The spectra of different mixtures were analysed by a partial least square (PLS) analysis. The results are summarized in Table 3.5. RMSEC denotes the root mean square of calibration in g L^{-1}, RMSECV the root mean square of cross validation[25].

Parameter	Fructose	Glucose	Sucrose
Spectral region [cm^{-1}]	958 to 1209	917 to 1180	917 to 1185
RMSEC, Absorption [g L^{-1}]	0.05	0.04	0.04
RMSEC, Dispersion [g L^{-1}]	0.11	0.09	0.06
RMSECV, Absorption [g L^{-1}]	0.07	0.05	0.05
RMSECV, Dispersion [g L^{-1}]	0.22	0.17	0.08

Table 3.5: Summary of PLS analysis of multivariate sugar analysis by the Mach-Zehnder Dispersion spectroscopy setup.

The obtained results show for the first time the successful application of dispersion spectroscopy in the mid-IR range for quantitative analysis.

3.4 Laser-Cavity-Locking Techniques

3.4.1 Purpose of Laser-Cavity-Locking

The technology developed and presented in the following sections is crucial for the operation of cavity enhanced techniques (see section 2.2.2.2). It is required for stable long-term operation in ICAPS based gas sensing and for achieving constant measurement sensitivity (see 3.5.1.).

The cavity transfer function (CTF) of a Fabry-Pérot cavity as used in ICAPS is, among other variables, a function of the probe laser's wavelength and has a Lorentzian shape. The slope of this function is a fundamental parameter of the systems sensitivity. The wavelength yielding the highest sensitivity therefore corresponds to the CTF's inflection point (see Figure 2.12).

To keep the system at this highest sensitivity, the probe laser emission wavelength has to be stabilized at the inflection point of the CTF.

This becomes clear, if equations (2.120) and (2.122) are considered: The phase $\Delta\varphi$ of the CTF is – among other parameters – dependent on

- The wavelength λ of the probe laser
- The refractive index of the medium between the mirrors of the Fabry-Pérot cavity which itself is dependent on
    - The chemical composition of the medium
    - Temperature and pressure of the medium
- Geometric parameters of the Fabry-Pérot cavity and the incident laser beam, being the mirror distance d and the angle of incidence θ.

From a technical point of view, these parameters can be classified into three categories, namely

- The parameter carrying the wanted chemical information. This is the heat induced (specific) refractive index change of the medium as a consequence of analyte excitation
- The parameter that allows to actively control the CTF phase. This is the laser wavelength, or more specific, the injection current that defines the laser wavelength (for constant laser temperature, see the principle of the DFB technology, section 2.1.2.1)
- All other parameters, which if changed due to any reasons, cause unwanted drifts of the CTF phase.

The parameters that cause unwanted drifts can shift the CTF so far, that the enhancement by the cavity is reduced or completely lost. This makes techniques necessary, which allow to stabilize the CTF phase at the CTF's inflection point. These techniques are called Laser-Wavelength – Cavity-Resonance Locking techniques and are reviewed in the following sections. At this point, it is also referred to the manuscript Lindner et. al.: *Theory, implementation and characterisation of Laser wavelength – Cavity locking Schemes for Cavity-enhanced spectroscopy*, that can be found in full-text in the appendix.

The reasons, why parameters can change, that cause unwanted drifts of the CTF phase, can be various. Some examples are[89]:

- Pressure fluctuations in the measurement cell ($\Delta n \cong 3 \cdot 10^{-4}\ kPa^{-1}$)

- Temperature fluctuations of the analyte gas ($\Delta n \cong 10^{-6} \ K^{-1}$)
- Analyte matrix composition fluctuations (Humidity: $\Delta n \cong 10^{-7} \ [\% \ r.H.]^{-1}$)
- Heat expansion of the cavity and its housing (see section 3.4.3.1)
- Changes in the optical properties of the cavity due to aging or chemical/mechanical damage. The parameter that can change is the finesse (see section 2.2.2)

For a better understanding of the effects influencing the CTF phase, Figure 3.21 shows a photograph of the cavity employed in the ICAPS system developed in this thesis. All relevant components that the following sections refer to are marked.
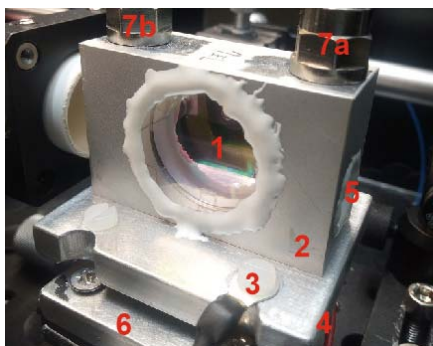

Figure 3.21: Photograph of the cavity employed in the ICAPS system developed in this thesis. 1..Cavity, 2..Cavity housing, 3..NTC temperature sensor for the cavity housing, 4..(power cable of) the Peltier element between cavity housing and heat sink, 5..Excitation laser window, 6..Mounting plate and heat sink, 7..Gas in- and outlet

3.4.2   General Considerations about Locking Techniques

Generally, when a cavity-enhanced sensing system, such as ICAPS, is activated, the probe laser's wavelength does not automatically correspond to a CTF inflection point – the cavity is unlocked. The first step therefore is to perform a wavelength scan (at given cavity temperature) by sweeping the probe laser injection current to locate the CTF inflection point.

Since the wavelength of the probe laser is dependent on the injection current as well as on the cavity and housing temperature (see Figure 3.14), the CTF peak is located at different injection current values for different cavity and housing temperatures. Figure 3.22 shows such scans for different cavity temperatures. From the recording, also the strong power dependence on the laser injection current can be seen.

After the CTF inflection point is located in terms of injection current, the laser-wavelength cavity-resonance locking algorithm (LC-lock) is activated to adjust the laser wavelength to a value, that corresponds to the CTF inflection point. The technical implementation of such algorithms can be performed by employing different principles – some of them were found by the research performed within this thesis[79]. All of these locking schemes have in common, that the variables λ_0, d and θ are adjusted in order to tune the CTF phase shift $\Delta\varphi$. The relation between these variables is nothing else than the expression for the CTF, given in equation (3.163).

For a stable LC-lock, the locking procedure has, on the one hand, to be very fast to be able to react to sudden changes of the CTF phase. On the other hand, it has to be able to tune $\Delta\varphi$ in a range, that is wide enough to access any wavelength/detector level point within one CTF period. This means that at least one cavity FSR has to be covered.
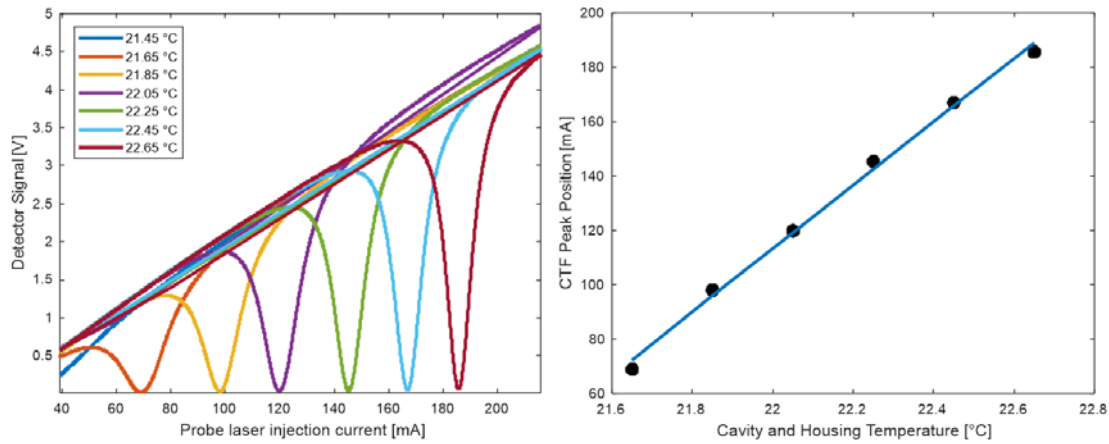
Figure 3.22: CTF peaks for different cavity and housing temperatures

Those two requirements are met by two functionally and technically separated operating domains of the LC-lock:

- A fast tuning of λ_0 in a limited range by adjusting the probe laser injection current. This is limited in speed only by the edge steepness of the laser driver. On the other hand, it covers only a narrow tuning range of around 60% of the cavity FSR. This is a consequence of the probe laser characteristics, given in Figure 3.14. λ_0 could also be changed by laser chip temperature tuning, but this would lead to technical problems in terms of dynamic stabilization of the temperature of an object that shows changing heat dissipation. For this reason, the laser chip temperature is kept constant.
- Tuning of d and θ by micro-deformation due to cavity temperature adjustment is very slow due to the fact that thermal effects are employed and the cavity as well as its aluminum housing have a relatively high heat capacity. The tuning capability is therefor far higher than the one by injection current adjustment. It was found that one FSR can be covered by a temperature variation of $\pm$ 2.5 K.

The tuning speed by cavity temperature change is limited by a system-immanent maximum temperature change speed of the cavity of approximately 0.1 Ksec^{-1}. Higher temperature change rates would be possible, but this results in longer resettlement times for the TEC controller. In this thesis, a meerstetter TEC-1091 was employed.

The maximum tuning speed for the injection current was found to be actually limited by just $4.5 \cdot 10^5$ nm sec^{-1}, what corresponds to the maximum sampling frequency of the used DAQ device. This limit is reduced to approximately 10 nm sec^{-1}, because for high levels of output signal changes, the voltage resolution of the employed DAQ device is reduced. With a speed below 10 nm sec^{-1} the resolution can be kept on a level, that the sinusoidal modulation waveform of the probe laser stays undeformed.

3.4.3 Wide-Range Tuning by Temperature

As described above, the CTF phase can be tuned by changing the temperature of the cavity itself. This causes micro-deformation of the cavity and thus affects the geometric cavity parameters d and θ. This micro-deformation is caused by the effect of heat expansion of the cavity and housing material (aluminum).

To express d and θ as a function of the cavity temperature analytically is not straight forward. Although the underlying principle – heat expansion of the cavity and its housing – is clear, its effect on the gas cell geometry is not easy to predict by a closed mathematical expression. Principally, there are two effects thinkable, that can affect d and θ:

- The mirror distance d increases, if the material expands in perpendicular direction to the cavity mirror planes.
- If this expansion is not uniform the expansion is anisotropic and the cavity mirrors will be tilted. This is equivalent to a change of the angle of incidence θ. The Peltier element of the gas cell's thermoelectric cooler (TEC) can only be attached on a fixed side of the cavity housing. In combination with the fact, that the housing has a finite size, it follows that the temperature distribution is not uniform over the housing body. This means, that it has to be expected that temperature change of the cavity and its housing results in angular deformations – and as a consequence in a change of the angle of incidence θ.

Principally trigonometric expressions for d and θ as a function of the cavity temperature could be found. Since those functions would strongly depend on the unknown exact temperature distribution in the gas cell, the cavity-temperature dependence of the CTF phase was determined experimentally. The result is shown in Figure 3.22. A linear dependence of the CTF phase from cavity temperature with a slope of 116.5 mA K^{-1} was found. This indicates, that the main contribution to the change of temperature distribution is indeed a uniform linear expansion, especially in perpendicular direction to the mirror planes. Expressed in terms of laser wavelength, that is dependent from the laser injection current by 0.00223 nm mA^{-1}, the temperature dependency can also be described by a slope of 0.26 nm K^{-1}.

3.4.3.1 Numeric Discussion of Heat Expansion Effects

In order to get a better understanding for the effect of temperature change to the cavity, the change of d and θ for a temperature change of 1 K is discussed: To compensate a shift of λ_0 of 0.26 nm, what is the measured change of the CTF peak position (see above) in terms of wavelength caused by a cavity temperature change of 1 K, it requires an increase of d of Δd = 167 nm:

$$\frac{4\pi}{\lambda_0 + 0.26 \text{ nm}} n(d + \Delta d) = \frac{4\pi}{\lambda_0} nd$$

(3.159)

with $\lambda_0 = 1550$ nm and $d = 1mm$ and a constant angle of incidence of 0° with $\cos 0° = 1$. This value is higher than the heat expansion of aluminum (23nm per °C at 20°C)[90], of which the cell is made of. To discuss the effect of temperature change to the angle of incidence θ, it is assumed, that the CTF phase change is caused only by the angle of incidence. It was found, that for a 0.26 nm change of λ_0, the change of θ has to be

$$\Delta\theta = \cos^{-1}\left(\frac{1550}{1550.26}\right) = 1°$$

(3.160)

This value is much higher, than one-sided heat expansion of the cavity (since it is cooled from the bottom) can explain: From a simple trigonometric consideration we get for this:

$$\sin^{-1}\left(\frac{23}{1mm\cdot 10^6}\right) = 4.7''$$

(3.161)

Also this discrepancy shows, that the effect of CTF peak change by cavity temperature change is not solely caused by change of the angle of incidence. However, (in a small enough temperature range) the dependency of the CTF phase from the cavity temperature could be found to be in first order approximation linear (see Figure 3.22).

3.4.4 Constant Level Locking

The constant level locking scheme is the most intuitive of all developed LC-locking schemes. It measures the CTF peak profile, stores the ordinate value of the CTF inflection point (detector signal) and uses that value as a setpoint for a feedback loop that adjusts the probe laser injection current to keep the CTF phase at a value that corresponds to the stored ordinate value.

This scheme has one big disadvantage: the ordinate value of the CTF inflection point is not constant due to the probe laser power characteristics (Figure 3.14): If the CTF phase drifts due to any environmental changes like the pressure between the mirrors of the cavity, the feedback loop corrects this by changing the probe laser wavelength via injection current tuning. The time constant of this feedback loop (in the case of the developed ICAPS system: 10 ms) has to be bigger than the period of the excitation laser modulation (ICAPS: 9 ms). But, changing the injection current leads also to a change in the emitted probe laser power what shifts the CTF inflection point ordinate value to higher values – the stored setpoint is not correct anymore.
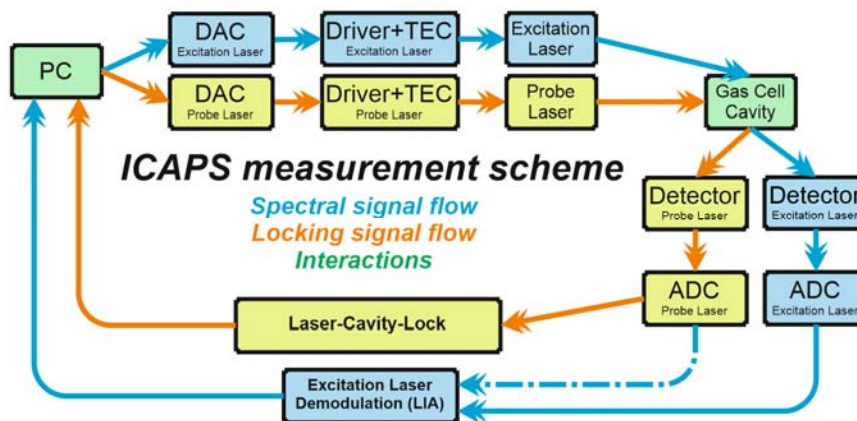
Figure 3.23: Sketch of the Laser-Cavity-locking feedback loop inside an ICAPS signal flow.

This problem can be mitigated in principle, if the dependency of the CTF inflection point from the probe laser injection current is known. However, the problem, that the setpoint is gained just from a calibration of a relatively volatile system, remains.

Because of its simplicity and because it was applied in former published ICAPS systems[8,36], the

Constant Level Locking Scheme is used as a benchmark for other LC-locking schemes that have been developed[79]. Figure 3.23 shows a schematic depiction of the feedback loop of a LC-locking scheme as part of the ICAPS signal flow.

3.4.5   2f-WM-Locking

As already described, the CTF of the Fabry-Pérot cavity has a Lorentzian shape. If the probe laser is modulated with small modulation amplitudes (an amplitude, significantly smaller than the FWHM of the CTF peak), it is known from the theory of 2f-WM spectroscopy (section 2.4.2.1) that in an inflection point of the CTF, the 2f-amplitude is zero. This fact can be employed to implement a feed-back loop with the 2f amplitude as process variable and zero as setpoint.

The most important difference to the previously introduced Constant Level Locking scheme is, that no periodic recalibration of the setpoint is needed – the condition that the 2f amplitude is zero if the wavelength of the CTF inflection point is met, is in this sense universal. There are deviations from this behaviour, especially with increasing modulation amplitude as it can be recognized from Figure 3.32 and Figure 3.31. However, since the purpose of LC-locking is to keep the probe laser wavelength in a range that corresponds to the centre of the linear range of the underlying CTF, minor deviations from the inflection point can be neglected.

For more details, it is referred to the publication "Lindner et. al.: *Theory, implementation and characterization of low-frequency Laser wavelength- Cavity resonance Locking schemes for cavity-enhanced spectroscopy* at this point, that could be achieved within the research done in this thesis.

3.4.6   Stochastic Locking

The idea of a LC-locking scheme, that does not need periodic recalibration, was further developed with the stochastic locking scheme. As it was described in section 2.4.2.3, the skewness, or third moment of the detected probe laser intensity values in a given period of time, also gets zero in the wavelength of the probe laser that corresponds to the inflection point of the underlying CTF.

The skewness amplitude has, in comparison with the 2f-amplitude the advantage that it is not dependent on the phase difference between the signal and a reference signal that is needed for 2f-demodulation. This can be understood by a simple stochastic argument: If the period of the modulation sine is far lower than the period of time for that the skewness is calculated the empirical density distribution of the measured values gets more and more independent from the phase of the modulation sine. The situation is depicted in Figure 3.24. The independency from the phase is an advantage of the stochastic LC-scheme compared to the 2f LC-scheme.
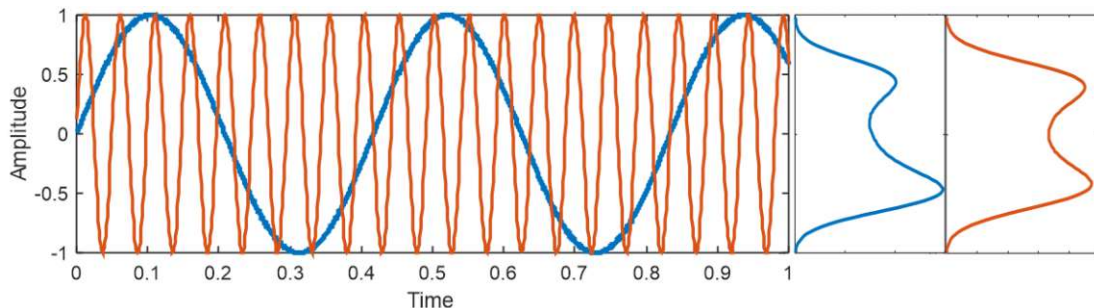

Figure 3.24: Effect of different modulation frequencies to empirical density distribution symmetry

Another interesting feature of using the skewness for Laser-Cavity-locking is that the waveform of the probe laser modulation does not need to be sinusoidal. Again, the argument is a stochastic one: It is crucial for the method that the probe laser wavelength values are symmetrically distributed around a centre value – for any wavelength value with a distance $\Delta\lambda$ to the centre value, there has to be present another wavelength value with distance $-\Delta\lambda$ to the centre value in the time period for that the skewness of the probe laser detector is calculated.

For a (high frequency) sinusoidal modulation, this symmetry requirement is fulfilled as it can be recognized from Figure 3.24. However, this symmetry requirement is also fulfilled, as an example, for a sawtooth modulation or even for gaussian noise. Figure 3.25 shows the influence of different modulation waveforms to the skewness function in a neighbourhood of the CTF peak.

Further, the modulation frequency can be pushed close to the Nyquist limit, if stochastic LC-Locking is used. It is even beneficial to use high frequencies, as it is shown in Figure 3.24. For the $2f$ Laser-Cavity-locking scheme, however the detector signal has to be sampled with sufficient resolution, what results in a reduction of the maximum modulation frequency far below the Nyquist limit. This is not the case, if the skewness is used as process variable and the only limit is the Nyquist limit of the used digitalization unit.
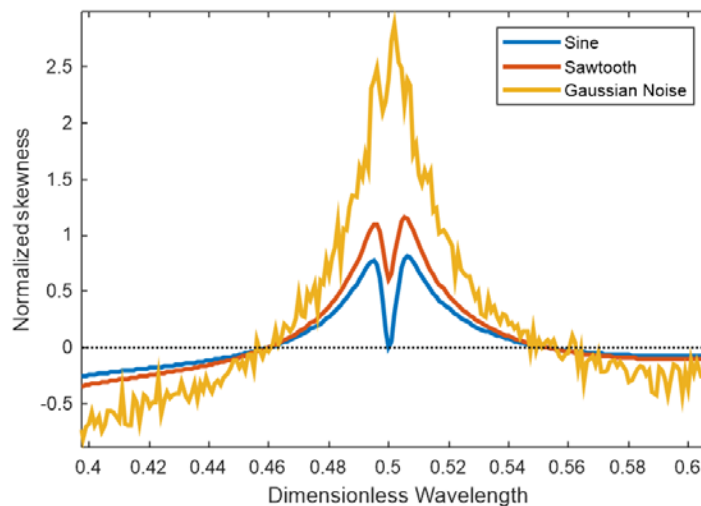
Figure 3.25: Effect of different waveforms to the Skewness function

For more details, again the reader is referred to the publication "Lindner et. al.: *Theory, implementation and characterization of low-frequency Laser wavelength- Cavity resonance Locking schemes for cavity-enhanced spectroscopy* that can be found in full-text in the appendix.

3.4.7   Time-discrete Locking

In early stages of developing LC-locking schemes, also two time-discrete schemes have been investigated. That means, that a time period, during with the LC-locking takes place – the locking period – is followed by a time period, during with the probe laser parameters are kept constant – the measurement period. In these periods, the spectroscopic measurement takes place. The measurement period is followed by the next locking period and so on.

The idea was, that since in the measurement periods the probe laser is not anyhow disturbed due to active locking, a very low noise level was expected in these periods.

It turned out, that the change between measurement and locking period introduced so much noise, that these schemes are not practicable. Especially if a modulation is needed for the spectroscopic measurement, the time-discrete detector signal is problematic for the Lock-In-amplification.

For the sake of completeness, the two time-discrete LC-locking schemes that have been developed, are briefly reviewed.

3.4.7.1   Scanning Scheme

The timeline of the probe laser detector signal during this LC-locking scheme is depicted in Figure 3.26: In the locking period, that has a typical duration in the range of 1 to 3 seconds, an injection current scan in the neighborhood of the CTF peak is performed. After that, a Lorentzian fit is calculated, that is then used to calculate the injection current value that corresponds to the CTF inflection point. This injection current value is then fixed for the following measurement period (depending on the duration of one spectral acquisition – for ICAPS, this is typically in the range of 1 to 5 minutes). The timeline of the method is depicted in Figure 3.26. Measurement periods are marked orange, locking periods blue.
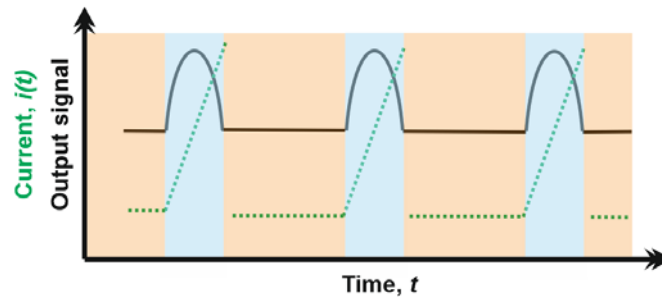
Figure 3.26: Schematic sketch of the Scanning LC-Locking scheme. Blue: Locking periods, Orange: Measurement periods

3.4.7.2   Differential Scheme

A big problem of the scanning scheme was the discontinuous change between a scan and a period of constant injection current. One approach to resolve this problem was, to make the scan as fast as possible – if the scan is fast enough, the scan should be in some sense adiabatic: it is faster than the reaction time of the system to the impact of the scan.

The idea of the differential LC-locking scheme was to substitute the scan by a three-point-measurement: the detector response of the last measurement period is compared to the detector response, if the laser is driven with an injection current close above and close below the injection current of the last measurement period. From these three pairs of values, a symmetry parameter is calculated – the slope left and right from the last injection current value has to be equal, if the last injection current value corresponds to the CTF inflection point.

The situation is depicted in Figure 3.27. With use of the depicted variables, the process variable dS can be calculated by

$$dS = s - \frac{S \cdot c}{C}$$

(3.162)

While the measurement period is in the same range as it was for the scanning scheme (1 to 5 minutes), the locking periods can be brought down to the sub-ms range.

It has to be mentioned, that this scheme is strongly connected to the idea of the stochastic locking scheme: equal slope on the left and the right side of an initial point corresponds to symmetry in that point (see Figure 2.18, left)
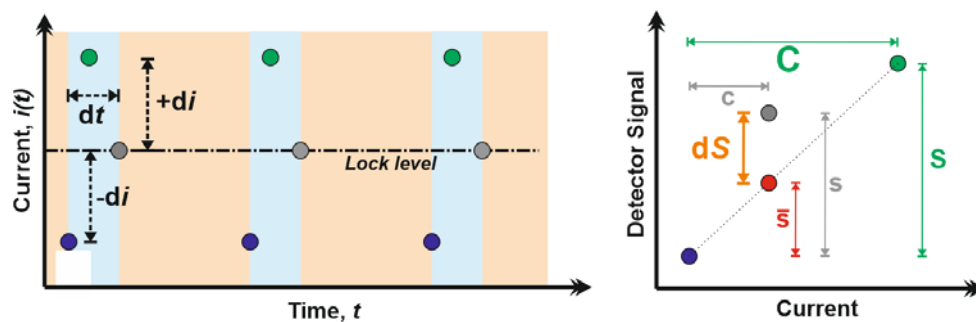

Figure 3.27: Schematic sketch of the Differential LC-Locking scheme. Blue: Locking periods, Orange: Measurement periods

3.5   Spectroscopy in Gas Phase

The main focus in this thesis was on indirect sensing, especially in the field of photothermal spectroscopy, but also some work in the field of direct absorption spectroscopy was performed.

3.5.1   Interferometric Cavity-Assisted Photothermal Spectroscopy (ICAPS)

The principle of ICAPS was first introduced in 1981 by Campillo et. al.[91] and further developed and coined as ICAPS by Waclawek et. al. from 2016 on[8,36,82]. It is an indirect sensing method that employs a Fabry-Pérot cavity and a probe laser to read out minimal changes in refractive index that are caused by the photothermal effect, an excitation laser has on an analyte gas. As excitation laser, a mid-IR laser – mostly in this thesis it is a QCL – is used. The probe laser has the requirement to be very frequency-stable, but has no requirements regarding the wavelength besides the condition, that the wavelength of the probe laser has to be in a range where neither the analyte nor the matrix gas show significant absorption. These requirements are well fulfilled by NIR telecom lasers. These lasers are highly optimized for their centre frequency in terms of stability since they are industrially used in telecommunication systems. The centre frequency of the probe laser that was employed in this thesis is located at 1550 nm. The characterisation of that laser is given in section 3.2.3.2.

3.5.1.1   Setup and Principle

A typical ICAPS setup is depicted in Figure 3.28. The probe laser beam is guided via an optical circulator perpendicular to the mirrors of a Fabry-Pérot cavity. The excitation laser beam is guided parallel to the mirrors and intersects the probe laser beam. Both beams are focussed to the point of intersection. At this point, the photothermal effect is largest and the refractive index change can be sensed: The cavity transfer function (CTF) enhances the amplitude of phase shift, as it is depicted in Figure 2.12.

It is to be mentioned at this point, that the ICAPS setup depicted in Figure 3.28 can also be used to perform direct absorption 2f-WMS spectroscopic measurements (see section 3.5.3): The Fabry-Pèrot cavity is then used as gas flow cell and the absorption signal is detected with the Mid-IR detector ED.

The theory of cavity enhancement was developed in section 2.2.2.2. The practically most important results are the dependency of the (transmission) CTF amplitude from the phase shift $\Delta\varphi$:

$$CTF^{Trans} = \frac{1}{1 - \left(\frac{2F}{\pi}\right)^2 \sin^2 \frac{\Delta\varphi}{2}}$$

(3.163)

and further, the dependency of the phase shift from the refractive index n, the geometric parameters of cavity mirror distance d and angle of incidence θ, and the probe laser wavelength λ:

$$\Delta\varphi = \frac{4\pi}{\lambda_0} nd \cos\theta$$

(3.164)

While the function $\Delta\varphi(n)|_{\lambda,d,\theta=const.}$ is the origin of the ICAPS signal, the function $\Delta\varphi(\lambda,d,\theta)|_{n=const.}$ is responsible for the fact, that a laser wavelength – cavity resonance (LC-) locking scheme has to be implemented. Details of that schemes are discussed in section 3.4. They

are crucial for the operation of an ICAPS based sensor with constant sensitivity and highest possible long-term-stability.
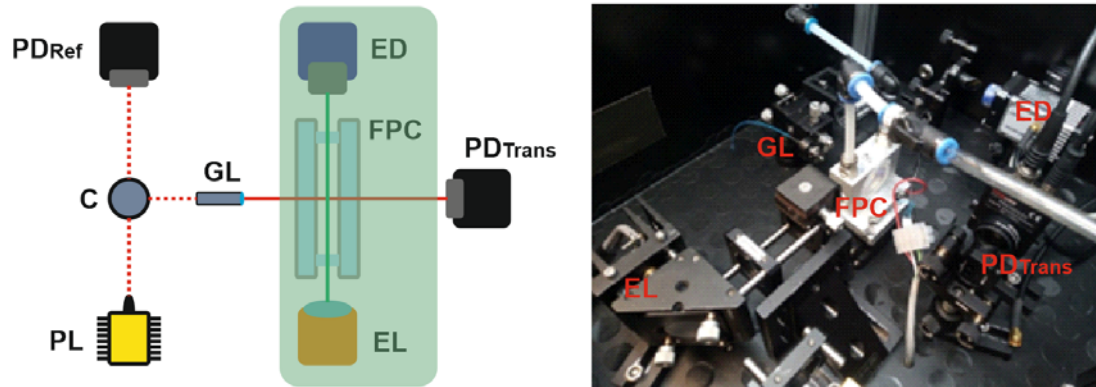

Figure 3.28: Left: Principal sketch of an ICAPS setup in reflection and transmission mode: PL..Probe Laser, EL..Excitation Laser, C..Optical Circulator, GL..GRIN Collimation Lens, FPC..Fabry-Pérot Cavity, ED..Excitation Laser Dectector (optinal, for Direct Absorption 2*f*-WMS), PDRef..Probe Laser Detector, Reflection, PDTrans..Probe Laser Detector, Transmission. The transparent green part of the setup can also be used as Direct Absorption 2*f*-WMS setup. Right: Photograph of the optical compartment of the realized ICAPS setup. The components that are not marked, are placed under the base plate of the setup, where the electronic compartment of the analyzer is located.

3.5.1.2 Reflection vs. Transmission Mode ICAPS

Because of the use of the optical circulator in the ICAPS setup not only the transmitted beam but also the reflected beam of the cavity can be read out. The CTF of the reflected and the one of the transmitted beam holds, as it was theoretically described in section 2.2.2.2

$$CTF^{Trans} + CTF^{Ref} = 1 \tag{3.165}$$

This means, that the reflected and the transmitted beam carry the same information.

The use of the reflected beam brings several technical advantages: Due to the fact, that fibre optics are used, the beam alignment and especially the coupling of the probe laser into the cavity is much easier than it is in free-space-optics. This also leads to higher robustness compared to a free-space optics setup.

Further, the space behind the cavity is not needed since the transmitted beam can be dumped. This allows a compactification of the sensor. For this reason, the ICAPS setup in this thesis was mainly used in reflection mode. Figure 3.29 shows on the left side measured data of a transmission (blue) and reflection (orange) CTF. The sum of both is in good approximation equal to the output power characteristics of the probe laser (linear line, yellow). The sum is not exactly linear, especially not at the CTF peak. On the right side, a wavelength scan over the transmission CTF is performed in parallel to a measurement of the monitor photodiode response. Since the laser is optically isolated, it is expected, that the CTF follows its usual Lorentzian shape while the monitor photodiode just shows a linear increase due to the power increase with increasing injection current. Actually, this was found to be not the case – at the CTF peak, there is a negative peak in the monitor photodiode response. This can be explained by back-coupling and interference effects that lead to a partial cancellation of the laser light.
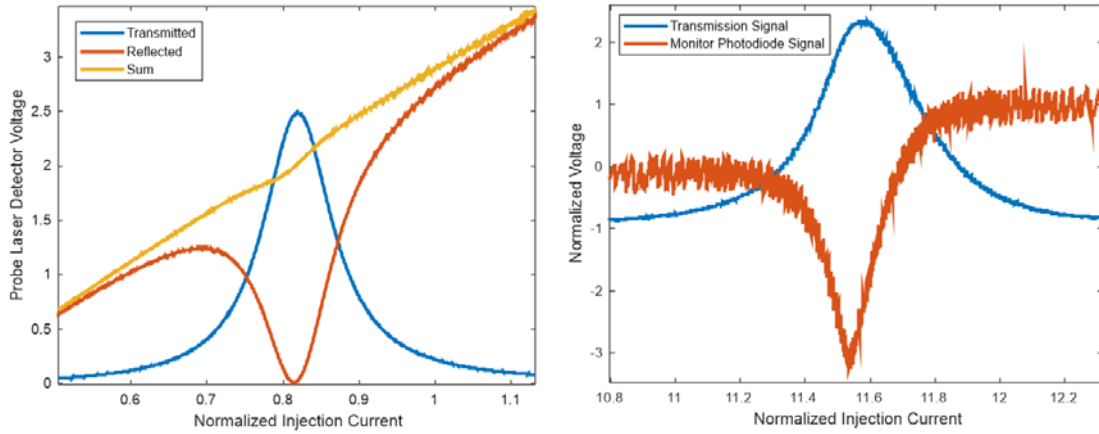
Figure 3.29: Left: Detector intensity of reflected and transmitted probe laser beam, Right: Parallel measurement of transmission CTF and monitor photodiode response

3.5.1.3   Carbon Dioxide Isotope sensing

As a showcase, carbon dioxide in a wavenumber regime between 2291 and 2292 cm-1 was sensed with the developed ICAPS system. Figure 3.30 shows a typical ICAPS spectrum. A limit of detection of 0.39 ppm for $^{13}CO_2$ and 45.6 ppm for $^{12}CO_2$, corresponding to a normalized noise equivalent absorption (NNEA) of $5.9 \cdot 10^{-6}$ cm^{-1} W Hz$^{-1/2}$ could be achieved. For the ICAPS demodulation a time constant of 3 seconds and a 24 dB filter was used, resulting in a system bandwidth of 26 mHz. The QCL was modulated by a sinusoidal modulation signal of 1.2 mA modulation depth, or expressed in wavenumbers, of 0.048cm^{-1}. This corresponds to a modulation index of 0.5.
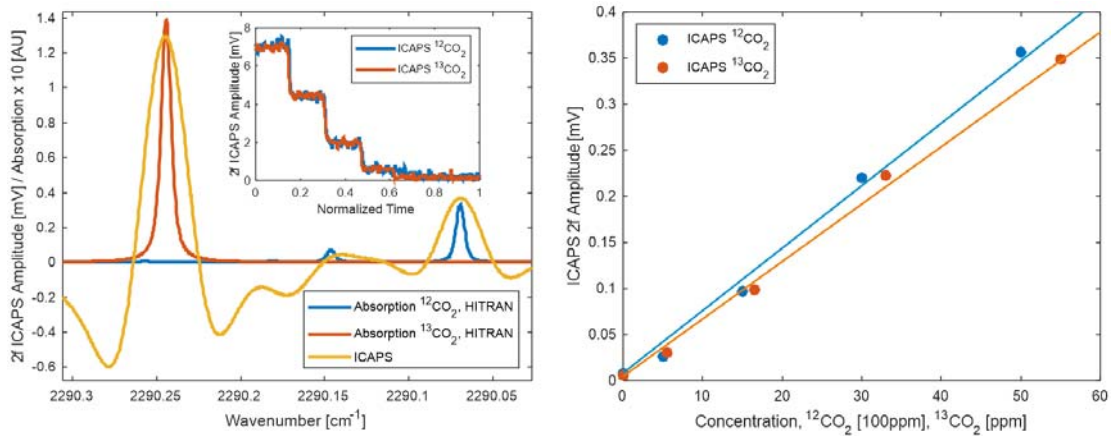
Figure 3.30: Acquired ICAPS Spectra of $^{12}CO_2$ and $^{13}CO_2$ in direct comparison to HITRAN database spectra of these molecules

3.5.2 2*f* and Skewness Peak Broadening

The 2*f*-WMS peak width is not only dependent on molecular parameters such as the absorption strength, but also on operational parameters of the sensing system such as the modulation depth, or, more specific, the relation of the modulation depth and the absorption peak width. This quantity is called the modulation index, defined in equation (2.129). It can be observed that the width of the 2*f*-WMS peak is increasing with increasing modulation index[92]. Further, also the 2*f*-WMS peak height is increasing with increasing modulation index but shows a maximum.
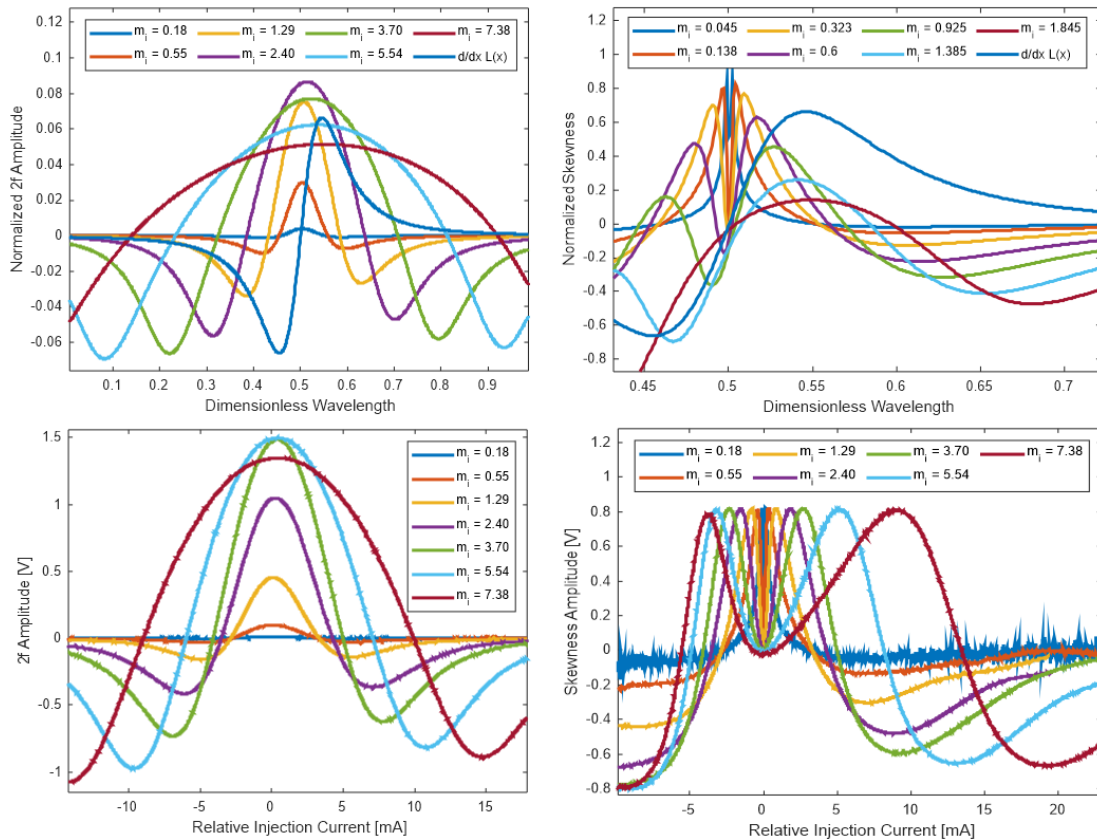
Figure 3.31: Simulated (up) and measured (down) data of 2*f*-WMS (left) and skewness (right) peak broadening

The effect can be understood empirically, when considering an absorption peak and a modulated excitation signal. As it is known from section 2.4.2.1, the frequency doubling takes place at the peak of the absorption, at a given wavelength λ_0. If the (wavelength) modulation index is now increased, the interval $(\lambda_{min}, \lambda_{max})$ of wavelength values that are covered by the modulation is increased. This leads to the effect, that even if the offset of the modulation (the center of this interval) is away from λ_0, it still holds $\lambda_0 \in (\lambda_{min}, \lambda_{max})$ – the 2*f*-contribution to the signal is found in a wider range around the absorption wavelength λ_0. Further, due to the increased modulation amplitude, also the amplitude of the doubled frequency signal is increased. On the other hand, there is an averaging effect becoming stronger with increasing modulation index: In the interval of increased length $\lambda_{max} - \lambda_{min}$, there is an increasing part, where the 2*f*-contribution to the signal is near zero. The combination of these effects lead to the observable effect, that the 2f peak is, with increasing modulation index, increasing in height and width and, after reaching a maximum height, further increasing in width while the height is decreasing again.

The same empirical understanding holds for the dependence of the skewness peak from the modulation index.

In Figure 3.31, the situation is depicted for simulated (up) and measured (down) data of the $2f$-WM signal of a Fabry-Pérot cavity. Here, the underlying "absorption" peak is caused by the structure of the cavity transfer function.

3.5.3 $2f$-Wavelength Modulation Direct Absorption Spectroscopy ($2f$-WMS)

The principle of $2f$-WMS was described in section 2.4.2.1. In direct absorption spectroscopy, the signal is formed by absorption of the incident laser light. This effect follows the Lambert-Beer law, described in equation (1.84). Direct absorption $2f$-WMS combines both principles: The frequency doubling, described in Figure 2.16, arises from the form of the absorption peak: as soon as the offset value of the modulation signal reaches the absorption maximum, the $2f$-component of the light transmitted through an absorption cell reaches its maximum.

Accordingly, the zero crossing of the $2f$-component marks the inflection point of the absorption peak. At this point it is to be mentioned, that the inflection point distance, a measure for the peak width, is heavily dependent on the sample gas pressure: It increases with increasing pressure[93,94].

In practical applications, the way, the excitation beam travels through the interaction volume – the absorption length – is set as long as possible. With modern multi-pass gas cells, absorption lengths in the order of hundred meters can be reached[63].

In this work, direct absorption $2f$-WMS was employed as a test method before implementing the indirect methods: If in an indirect spectroscopy setup the excitation beam is detected and demodulated, a direct absorption $2f$-WMS signal can be measured.

Figure 3.32, left part, shows direct absorption $2f$-WMS spectra of a dilution series of CO_2 in nitrogen. The excitation laser in this experiment was an ICL that emits at a very strong absorption line of CO_2 at 2360.11 cm^{-1}. Because of that, the linear (Lambert-Beer-) range of the concentration vs. $2f$-WMS peak height function is exceeded, as can be seen in the right part of Figure 3.32. It can be recognised, that even at very high absorption, the typical form of the $2f$-WMS peak is kept and, besides the reduced height, not somehow distorted.
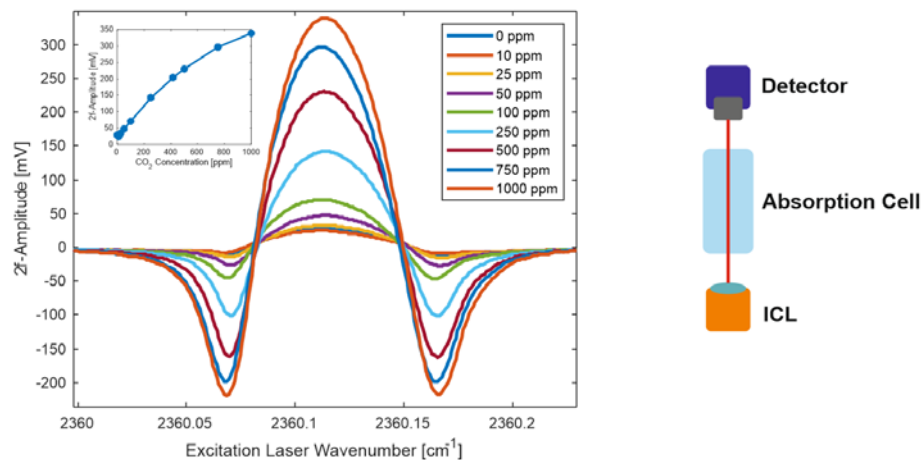
Figure 3.32: $2f$-WM absorption spectroscopy setup (right) and typical $2f$-WMS spectra with calibration line (left)

Chapter 4   Summary and Outlook

In this last short chapter, all results achieved in this thesis are reviewed. Conclusions of the work are made, cross-connections pointed out and summarized. Furthermore, the achievements and encountered problems discussed in detail, including a presentation of possible explanation for these problems. Finally, the potential of the achieved results for future developments is discussed and an outlook is given, where further research in the field of this thesis could be directed.

4.1 Summary

First, the results achieved during the work in this thesis are summarized and results as well as encountered problems are pointed out.

4.1.1 Summary of Results

The most noticeable achievements of this thesis are in the field of measurement technique and signal processing technology.

- **Dispersion spectroscopy of liquids**. A Mach-Zehnder interferometer based dispersion spectroscopy setup was developed and investigated in detail. Two types of a feedback loops for stabilizing the interferometer's quadrature point (See section 3.3.1) were developed. These types of feedback-loops were

  - *Moving Piezo Method*. The phase shift that occurs in the sample arm of the Mach-Zehnder interferometer due to the dispersion of the sample, is compensated by physically increasing or decreasing the pathlength, the laser has to travel in that arm. In other words, to keep the optical pathway constant, the geometric pathway is adapted by actively controlling the voltage of a piezo crystal, the mirror of the corresponding interferometer arm is mounted on. Due to the geometry of the Mach-Zehnder interferometer, a change of x in the piezo crystal travelling direction, causes a change of $x\sqrt{2}$ in the beam pathway. With that, a change in the optical pathway caused by dispersion in the sample cell can be compensated by a change of the geometric pathway of the corresponding interferometer arm. In that way, the system can be kept at the interferometers quadrature point and a feedback-loop can be implemented.

  - *Fixed Piezo Method*.[25] Moving parts in an optical setup are a source of noise and uncertainty. Because of that, a way to avoid the movement of the piezo crystal that is crucial for the "Moving Piezo Method", was looked for. This would allow a complete replacement of the piezo crystal, what would significantly reduce complexity of the setup. The development achieved in this thesis was the so-called "Fixed Piezo Method". The idea is, that the differential detector signal shows a well-defined behavior also away from the quadrature point. This behavior is expected also from theory and is strictly sinusoidal. The principle of the Fixed Piezo Method is to find a sinusoidal model for the behavior of the differential detector signal around the quadrature point and then use this model to mathematically correct the measured detector signal if the system is not in the interferometers quadrature point. With this method, comparable results as found with the moving piezo method could be achieved, while the (physical) complexity of the setup could be reduced.

o *Experimental results on sensing ethanol and sugars in aqueous solution.*

- Realization of a Mach-Zehnder interferometer based setup for dispersion spectroscopy of liquid samples

- Using ethanol as test analyte dispersion spectra were measured that matched dispersion spectra calculated from recorded absorption spectra by Kramers-Kronig transformation

- Quantitative dispersion spectroscopy

  ✓ RMSEC of 0.22 g L^{-1} for Fructose

  ✓ RMSEC of 0.17 g L^{-1} for Glucose

  ✓ RMSEC of 0.08 g L^{-1} for Sucrose

- Quantitative absorption spectroscopy

  ✓ Root mean square error of calibration (RMSEC) of 0.07 g L^{-1} for Fructose

  ✓ RMSEC of 0.05 g L^{-1} for Glucose

  ✓ RMSEC of 0.05 g L^{-1} for Sucrose

- **Interferometric Cavity-Assisted Photothermal Spectroscopy (ICAPS)**. In Fabry-Pérot cavity-based sensing systems like ICAPS it is crucial for the stability and sensitivity, that the wavelength of the probe laser corresponds to an inflection point of the periodic cavity transfer function at any time of the measurement. For that purpose, feedback loop algorithms with different process variables were investigated.

  o *Constant Level Scheme*. This scheme is very intuitive and has already been successfully applied in earlier ICAPS setups[8,36]. The absolute detector DC level of the probe laser beam is measured. The position of the cavity transfer function inflection point is known from a wavelength (injection current) scan. The detector DC value of this position is then used as setpoint for the feedback loop. While low complexity of this scheme is a clear advantage, the scheme shows – at least for a diode laser, that had clearly inconstant injection current vs. power characteristics – a significant disadvantage: since the inflection point can shift over time due to a manifold of reasons, a periodic recalibration of the setpoint in the form of a new wavelength (injection current) scan is necessary to keep the system in a correct condition. This scan would interrupt the measurement and, due to different heat dissipation at different injection current values, heavily affect long-term temperature stability, what itself is a strong source of noise. Nevertheless, due to its low complexity, this scheme is serving as a benchmark for the other schemes that have been developed.

  o *2f-Wavelength Modulation Scheme*. This scheme is based on the fact, that the second harmonic amplitude of a modulated probe lasers signal that's wavelength is tuned over a resonance peak of a Fabry-Pérot cavity, shows a zero crossing at the inflection point of the cavity transfer function. This condition is just dependent on the modulation depth of the probe laser wavelength, and not on

the DC level of the probe laser detector. Further, the dependence from the modulation depth is negligible for low modulation depths – and could even be compensated by a simple algorithm for higher modulation depths. This allows the implementation of a locking scheme that does not need to be constantly recalibrated, since the inflection point of the cavity transfer function is approached directly with the condition of the $2f$-amplitude being zero.

o *Stochastic Scheme*. The central principle of this scheme is that if the signal of a modulated probe laser that is tuned over the resonance profile of a Fabry-Pérot cavity is measured for a given period of time, the third moment (skewness) of the measured detector values also allows the identification of the inflection point of the cavity transfer function (Section 3.4.6). At the inflection point, the skewness shows, similar to the $2f$ amplitude, a zero crossing. While the probe laser modulation for the $2f$-wavelength modulation scheme is limited in terms of the waveform (to sinusoidal modulation) and the frequency (to a multiple of the Nyquist barrier since a sinusoidal curve has to be sampled), the stochastic scheme is more universal. The waveform just has to meet some symmetry requirements and the frequency can be pushed right to the Nyquist barrier, what is the half maximum sampling frequency of the digital-analog converter that is used in the system.

o *Sensing Carbon dioxide isotopologues with Interferometric Cavity-Assisted Photothermal Spectroscopy (ICAPS)*

- Realization of a ICAPS setup for gas sensing

- Clearly distinguishable ICAPS peaks of $^{13}CO_2$ and $^{12}CO_2$

- Normalized noise equivalent absorption (NNEA) of the developed ICAPS system determined to be $5.9 \cdot 10^{-6}\,cm^{-1}\,W\,Hz^{-1/2}$

- Limit of detection (LOD) of the developed ICAPS system determined by

  ✓ $45.6\,ppm_V$ for $^{12}CO_2$

  ✓ $0.39\,ppm_V$ for $^{13}CO_2$

- Implementation of a software based Lock-In-Amplifier that meets the requirements of a $2f$-wavelength modulation based laser-wavelength cavity resonance locking scheme. The software solution shows comparable results to a state-of-the-art table-top Lock-In-Amplifier.

- Implementation and successful testing and application of a custom, compact electronic board for ICAPS including all electronic filters developed for efficient noise reduction.

- **Noise suppression for cavity-based spectroscopy**. The signal-to-noise ratio is one of the most important figures of merit for a chemical sensing system. Since the increase of the signal level is principally limited, especially by the maximum available laser power (see equation (1.89)), the reduction of noise level offers more potential to improve (increase) the signal-to-noise ratio. In addition to filter circuitry also two active noise suppression methods were developed within this thesis.

  o Development of electronic filters. Electronic filters for noise suppression could be successfully built, tested and implemented in the ICAPS system. The theoretical filter parameters match with the measured Bode-diagrams.

  o *Electronic Balanced Detection.* The idea of electronic balanced detection is to perform the balancing by reading the monitor photodiode of the probe laser and using this signal as a reference. This is far less complex than a complete optical balancing system, which requires the implementation, alignment, and equilibration of a second probe laser beam. On the other hand, the electronic balancing system is not capable of suppressing noise coming from the cavity itself. However, it was found that the intensity noise contributions coming from the laser itself and the control electronics – what can be suppressed by electronic balanced detection – sum up to the biggest part of the overall noise level. As a result, the electronic balancing approach delivers comparable results to optical balancing.

  o *1f-Quadrature Point Balanced Detection.* The principle of this balancing technique is a phase shift of π between the monitor and the detector photodiode. With this phase shift, a quadrature point between the monitor and the detector signal is formed. Demodulating the differential signal at the first harmonic leads to a signal that is balanced, band-pass filtered and amplified at the same time. The technique also shows comparable performance to optical balancing. Besides that, the technique offers high potential in the sense that there are still parameters that can be optimized to further improve its performance.

4.1.2   Encountered Problems

There were also problems that have been encountered during the work on this thesis. The most important to be mentioned here are

- **Long-term instability and baseline drift of the Mach-Zehnder dispersion spectrometer**. While the spectrum-to-spectrum reproducibility of the achieved dispersion spectra measured by the Mach-Zehnder dispersion spectrometer was on a level in the range of the noise, there were long-term drifts that could not be avoided. The mechanism that was expected to be responsible at least for the biggest contribution to this behavior was that during one measurement the temperature of the entire setup changes due to any environmental influences. Due to heat expansion of aluminum, what most of the parts of the setup consist of, one degree Celsius of temperature change is enough to cause geometric dimension changes in the range of the wavelength of the laser. It was expected, that by a reduction of the overall size of the Mach Zehnder interferometer and by an active temperature stabilization in the form of a water-cooled breadboard on which the entire setup is mounted, this unwanted effect is able to be reduced. This expectation was actually found to be correct by some continuing work by Dabrowska et. al.[88]

- **Time discrete laser-wavelength cavity-resonance locking**. There were two further Laser-wavelength Cavity-resonance locking schemes investigated, that turned out to show not the expected performance. Both of them have in common, that they are time-discrete, what means that a period of sensing (measurement period) and a period of sensor recalibration (locking period) constantly alternates. The effect, that was expected to be the most challenging part of the implementation, in the end turned out to introduce too much noise to the system: Due to the highly inconstant laser power vs. injection current characteristics of the diode laser that was employed as probe laser, the abrupt change of injection current at the beginning and the end of the recalibration period led to temperature instabilities of the laser. These instabilities could not be taken under control at a level that would have allowed low-noise performance of the sensor in the sensing period.

- **ICAPS Signal generation**. The procedure of finding the intersection of the probe laser and the excitation laser beam in the ICAPS system was far more challenging than expected. It is expected from theory of simple beam geometry, that the spatial range of the intersection – the focal spots of two invisible laser beams have to be matched in a volume that cannot be directly accessed, for instance with an infrared camera, because it is located in the center of a vacuumized gas cell – is extremely small in all three dimensions of space. However, although it is an expected problem, it has been already solved in earlier work. Nevertheless, despite of putting much effort to this crucial step, the ICAPS signal of earlier setups could not be reached and it was not fully understood, what exactly was the reason for that. The singular position of the intersection point is expected to be one main reason, but it is also possible that there are others, that have so far not been discovered.

- **Autocorrelation of ICAPS Signals**. One approach, to compensate the very low ICAPS signal levels was, to make use of its periodicity, not only concerning the modulation of the excitation laser (what is employed for the implementation of a $2f$ wavelength modulation detection scheme), but also of the (mHz range) injection current offset ramp. The underlying, simplified idea of autocorrelation, what can be used as a powerful data post processing algorithm, is that periodic proportions of the signal are amplified while nonperiodic proportions are suppressed. Some promising results could be achieved (see appendix), but due to the fact that the mechanism was not fully understood, this approach was not further investigated and other noise suppression techniques were developed.

4.2 Outlook

One of the most important goals when doing research on novel chemical sensing technologies is to become capable of detecting smaller and smaller amounts and concentrations of the target analyte. In any sensing system the target analyte generates, via a specified chain of transduction, a signal that is somehow correlated to the target analyte amount or concentration. Since other effects possibly can always trigger any link in that chain of transduction there is always also a given level of noise at the sensor signal output. In this very principal model, the "quality" of the sensor – that is aimed to be improved by the research that is performed – can be described by the ratio of these two quantities – the ratio of the signal level to the noise level, the signal-to-noise ratio, SNR. In a real-world sensor there are of course other important measures such as sensor robustness, accuracy or long-term-stability, but the SNR is indeed an important figure of merit to describe the performance of a sensing setup.

From this simple model, it follows that in principle there are two approaches that theoretically lead to an increase (improvement) of the SNR:

- Increase of the signal level
- Decrease of the noise level

The main focus of this thesis has been put on the second approach, the decrease of the noise level. The highlights achieved in this field have been summarized in the last section.

Noise has a very deep and basic influence to any sensing technique. The way, how noise emerges and what the sources of noise are present, is very specific to the sensing system that is investigated. Also, the origin of the single contributions to total noise of a sensor can be found in many different areas. The presence of any type of noise and strategies to keep its level as low as possible, on the other hand, is a technical challenge that has to be dealt with in any sensing techniques. From this point of view, the results that have been achieved in this thesis may be applied not only to improve cavity-based infrared spectroscopy sensing techniques and especially the ICAPS technique, but also in other fields.

Measuring the skewness of the detector signal in a given period of time allows not only the identification of the inflection point of an underlying profile, but also the identification of peak maxima and minima, where the condition of a skewness of zero is also fulfilled. Despite so far technical application has been found for this feature may still be used in future applications. For instance, it would be thinkable to lock the laser wavelength to a cavity resonance by making use of the inflection point identification feature, to read information about the finesse of the cavity (related to the width of the centre peak of skewness), and to gain information about the peak maximum from the skewness function.

The detection principle of ICAPS could theoretically be extended to liquid phase sensing. For that purpose, the probe laser beam and the excitation laser beam would have to be aligned to one axis – and not perpendicular to each other. Sensing liquids with this technique and as well the different optical setup that is necessary for it leads to a manifold of new challenges. Starting with the identification of a suitable mirror material and coating – it has to be highly reflective for the probe laser and transparent for the excitation laser – over the problem of chemical stability of the coating material in the expected solvents. A technical implementation of liquid phase ICAPS – coined LIQUICAPS – would be highly challenging. On the other hand, due to the promising performance of gas phase ICAPS, the application of this technique to the liquid phase could be of interest. A principal sketch of this technique is depicted in Figure 4.1.

The electronic balancing technique and especially the 1*f*-Quadrature point balancing technique, where a proof of principle could be demonstrated in this thesis, would also have high potential for further development. It could further improve the ICAPS detection scheme while the setup is simplified at the same time. This potentially also increases robustness of the sensor. Together with software-based lock-in-amplification, a compact and robust ICAPS based gas sensor could be realized in the near future.
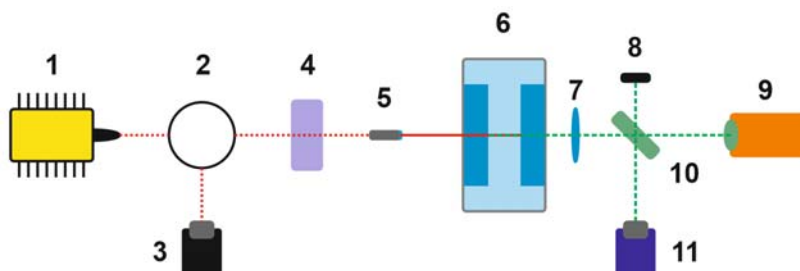

Figure 4.1: Principal LIQUICAPS setup. 1…Probe Laser, 2…Circulator, 3…Probe Laser Detector, 4…Filter, 5…Collimation and Focusing Lens, 6…Flow Cell with Fabry-Pérot Cavity, 7…Focusing Lens, 8…Beam Block, 9…Excitation Laser, 10…Beam Splitter, 11…Excitation Laser Detector

The text of this thesis started with the theory that is the basis for all further developments. To close the cycle, or, actually to make a cycle out of it, the last words of this thesis should also be dedicated to theory – and even deeper thoughts.

The origin of noise is from very fundamental nature – exactness is something that does not exist by theory. Coming back to quantum mechanics, where an effect was found that describes this fact in a very elegant way. It was found by Werner Heisenberg, when he discovered his famous uncertainty principle: An exact determination of the momentum of a particle would lead to the circumstance, that the position of this particle is completely undefined. The price of an exact measurement of one quantity would be the total loss of information about a different one.

Kurt Gödel went even one step further, when he discovered his theorems of incompleteness. They tell us in principle, that a logical system – such as mathematics and subsequently also physics – can never be fully proven from the axioms that system is based on.

In this sense, the solution to any scientific problem can just be an approximation of the truth, that only nature itself can know. As scientists it is our natural effort – and taking serious our responsibility we carry for mankind, it also is our duty – to ask nature the correct questions. It does not matter, if we ask that questions in the form of experiments or in the form of theoretical thoughts – even if there is a more or less big chance, that the answer we get is not like we would wish it to be: We never should lose the courage to ask all questions we have, in any way we think they make sense. Nature will not judge us, independent of how ridiculous a question seems to be when it comes to our mind the first time. The opposite is the case: History often prooved, that a question seen to be highly ridiculous by our social and professional environment, turned out to be the basis of a great idea. We just have to never stop daring to ask those questions:

Habe den Mut, deinen Verstand zu gebrauchen.

Bibliography

1. Meschede, D. *Gerthsen Physik*. *Gerthsen Physik* (Springer Berlin Heidelberg, 2006). doi:10.1007/3-540-29973-4

2. Landau, L. D. & Lifshitz, E. M. *Mechanics*. **1**, (Elsevier, 1976).

3. Griffiths, P. R. *Fourier transform infrared spectrometry*. *Science* **222**, (Wiley VCH, 1983).

4. Coker, D., Reimers, J. & Watts, R. The Infrared Absorption Spectrum of Water. *Aust. J. Phys.* **35**, (1982).

5. Slivken, S. & Razeghi, M. High Power Mid-Infrared Quantum Cascade Lasers Grown on GaAs. 0–5 (2022).

6. Kozma, P., Kehl, F., Ehrentreich-Förster, E., Stamm, C. & Bier, F. F. Integrated planar optical waveguide interferometer biosensors: A comparative review. *Biosensors and Bioelectronics* (2014). doi:10.1016/j.bios.2014.02.049

7. Sieger, M., Balluff, F., Wang, X., Kim, S. S., Leidner, L., Gauglitz, G. & Mizaikoff, B. On-chip integrated mid-infrared GaAs/AlGaAs mach-zehnder interferometer. *Analytical Chemistry* (2013). doi:10.1021/ac302551s

8. Waclawek, J. P., Moser, H. & Lendl, B. Balanced-detection interferometric cavity-assisted photothermal spectroscopy employing an all-fiber-coupled probe laser configuration. *Opt. Express* **29**, 7794 (2021).

9. Bialkowski, S. E. *Photothermal Spectroscopy Methods for Chemical Analysis*. (1995).

10. Knötig, H., Hinkov, B., Weih, R., Höfling, S., Koeth, J. & Strasser, G. Continuous-wave operation of vertically emitting ring interband cascade lasers at room temperature. *Appl. Phys. Lett.* **116**, (2020).

11. Gharib-Nezhad, E., Heays, A. N., Bechtel, H. A. & Lyons, J. R. H2-induced pressure broadening and pressure shift in the P-branch of the v3 band of CH4 from 300 to 655 K. *J. Quant. Spectrosc. Radiat. Transf.* **239**, (2019).

12. Baldacci, A., Devi, M., Narahari Rao, K., Chen, D.-W. & Fridovich, B. Absorption Spectrum of Carbon Dioxide at 4.3 µm. *J. Mol. Spectrosc.* **70**, 143–159 (1978).

13. Baldacci, A., Linden, L., Devi, M., Narahari Rao, K. & Fridovich, B. Interpretation of the 13C16O2 Spectrum at 4.4 µm. **72**, 135–142 (1978).

14. Schilt, S. & Thévenaz, L. Wavelength modulation photoacoustic spectroscopy: Theoretical description and experimental results. *Infrared Phys. Technol.* **48**, 154–162 (2006).

15. Koningstein, J. A. *Introduction to the Theory of the Raman Effect*. *Introduction to the Theory of the Raman Effect* (1972). doi:10.1007/978-94-010-2901-8

16. Akhgar, C. K., Ramer, G., Żbik, M., Trajnerowicz, A., Pawluczyk, J., Schwaighofer, A. & Lendl, B. The Next Generation of IR Spectroscopy: EC-QCL-Based Mid-IR Transmission Spectroscopy of Proteins with Balanced Detection. *Anal. Chem.* **92**, (2020).

17. dos Santos, A. C. V.D., Lendl, B. & Ramer, G. Systematic analysis and nanoscale chemical imaging of polymers using photothermal-induced resonance (AFM-IR) infrared spectroscopy. *Polym. Test.* **106**, 107443 (2022).

18. Demtröder, W. Experimentalphysik 1 (Mechanik und Wärme). *Exp. 1* (2008).

19. Demtröder, W. *Experimentalphysik 3, Atome, Moleküle, Festkörper*. *Springer Lehrbuch* **3**, (2010).

20. Cohen-Tannoudji, C., Diu, B. & Laloë, F. *Mécanique Quantique - Tome 1*. *Mécanique Quantique - Tome 1* (2020). doi:10.1051/978-2-7598-2288-1

21. Demtröder, W. Molekülphysik Theoretische Grundlagen und experimentelle Methoden, 2.Auflage. *Oldenbourg Verlag München* (2012).

22. Geenawalt, E. M. & Dickinson, A. S. On the use of Morse eigenfunctions for the variational calculation of bound states of diatomic molecules. *J. Mol. Spectrosc.* **30**, 427–436 (1969).

23. Sneddon, I. N. L. J. Slater, Confluent Hypergeometric Functions (Cambridge University Press, 1960), 247 pp., 65s. *Proc. Edinburgh Math. Soc.* **12**, (1961).

24. Fadini, A. Spektroskopie: Schwingungsspektroskopie. Eine Einfrung. Von J. Weidlein, U. Müller und D. Dehnicke. Georg Thieme Verlag, Stuttgart 982. X, 226 S., 226 Abb., 45 Tab., geb. DM 49.80. . *Nachrichten aus Chemie, Tech. und Lab.* **30**, (1982).

25. Lindner, S., Hayden, J., Schwaighofer, A., Wolflehner, T., Kristament, C., González-Cabrera, M., Zlabinger, S. & Lendl, B. External Cavity Quantum Cascade Laser-Based Mid-Infrared Dispersion Spectroscopy for Qualitative and Quantitative Analysis of Liquid-Phase Samples. *Appl. Spectrosc.* **74**, 452–459 (2020).

26. Kačuráková, M. & Mathlouthi, M. FTIR and laser-Raman spectra of oligosaccharides in water: Characterization of the glycosidic bond. *Carbohydr. Res.* (1996). doi:10.1016/0008-6215(95)00412-2

27. Leopold, L. F., Leopold, N., Diehl, H. A. & Socaciu, C. Quantification of carbohydrates in fruit juices using FTIR spectroscopy and multivariate analysis. *Spectroscopy* (2011). doi:10.1016/j.enbuild.2016.03.026

28. Cadet, F., Robert, C. & Offmann, B. Simultaneous determination of sugars by multivariate analysis applied to mid-infrared spectra of biological samples. *Appl. Spectrosc.* (1997). doi:10.1366/0003702971940224

29. Duarte, I. F., Barros, A., Delgadillo, I., Almeida, C. & Gil, A. M. Application of FTIR spectroscopy for the quantification of sugars in mango juice as a function of ripening. *J. Agric. Food Chem.* (2002). doi:10.1021/jf011575y

30. Gordon, I. E., Rothman, L. S., Hargreaves, R. J., Hashemi, R., Karlovets, E. V., Skinner, F. M., Conway, E. K., Hill, C., Kochanov, R. V., Tan, Y., Wcisło, P., Finenko, A. A., Nelson, K., Bernath, P. F., Birk, M., Boudon, V., Campargue, A., Chance, K. V., Coustenis, A., *et al.* The HITRAN2020 molecular spectroscopic database. *J. Quant. Spectrosc. Radiat. Transf.* **277**, (2022).

31. Demtröder, W. *Experimentalphysik 2 (Elektrizität und Optik). Springer-Verlag Berlin Heidelberg* (2013).

32. Kramers, H. A. La diffusion de la lumière par les atomes. *Atti Cong. Intern. Fis.* **2**, (1927).

33. de L. Kronig, R. On the Theory of Dispersion of X-Rays. *J. Opt. Soc. Am.* **12**, (1926).

34. Ramer, G. & Lendl, B. Attenuated Total Reflection Fourier Transform Infrared Spectroscopy. *Encycl. Anal. Chem.* (2013). doi:10.1002/9780470027318.a9287

35. Werner, D. Funktionalanalysis. in (2009). doi:10.1007/978-3-540-79696-1_5

36. Waclawek, J. P., Bauer, V. C., Moser, H. & Lendl, B. 2f-wavelength modulation Fabry-Perot photothermal interferometry. *Opt. Express* (2016). doi:10.1364/OE.24.028958

37. Pinto, D., Moser, H., Waclawek, J. P., Dello Russo, S., Patimisco, P., Spagnolo, V. & Lendl, B. Parts-per-billion detection of carbon monoxide: A comparison between quartz-enhanced photoacoustic and photothermal spectroscopy. *Photoacoustics* **22**, (2021).

38. Spagnolo, V., Kosterev, A. A., Dong, L., Lewicki, R. & Tittel, F. K. NO trace gas sensor based on quartz-enhanced photoacoustic spectroscopy and external cavity quantum cascade laser. *Appl. Phys. B Lasers Opt.* **100**, 125–130 (2010).

39. Dabrowska, A., Lindner, S., Schwaighofer, A. & Lendl, B. Mid-IR dispersion spectroscopy – A new avenue for liquid phase analysis. *Spectrochim. Acta Part A Mol. Biomol. Spectrosc.* **286**, 122014 (2023).

40. Hayden, J., Hugger, S., Fuchs, F. & Lendl, B. A quantum cascade laser-based Mach–Zehnder interferometer for chemical sensing employing molecular absorption and dispersion. *Appl. Phys. B Lasers Opt.* **124**, 1–9 (2018).

41. Krzempek, K. A review of photothermal detection techniques for gas sensing applications. *Appl. Sci.* **9**, (2019).

42. Tokeshi, M., Uchida, M., Hibara, A., Sawada, T. & Kitamori, T. Determination of subyoctomole amounts of nonfluorescent molecules using a thermal lens microscope: Subsingle-molecule determination. *Anal. Chem.* **73**, (2001).

43. Ricchiuti, G., Dabrowska, A., Pinto, D., Ramer, G. & Lendl, B. Dual-beam photothermal spectroscopy employing a Mach-Zehnder interferometer and an external cavity quantum cascade laser for detection of water traces in organic solvents. *Anal. Chem.* (2022).

doi:10.1021/acs.analchem.2c03303

44. Krzempek, K., Dudzik, G., Abramski, K., Wysocki, G., Jaworski, P. & Nikodem, M. Heterodyne interferometric signal retrieval in photoacoustic spectroscopy. *Opt. Express* **26**, (2018).

45. Jin, W., Cao, Y., Yang, F. & Ho, H. L. Ultra-sensitive all-fibre photothermal spectroscopy with large dynamic range. *Nat. Commun.* **6**, (2015).

46. Zhao, Y., Jin, W., Lin, Y., Yang, F. & Ho, H. L. All-fiber gas sensor with intracavity photothermal spectroscopy. *Opt. Lett.* **43**, (2018).

47. Kauppinen, J., Koskinen, V. & Huuskonen, M. Extreme sensitivity in photoacoustics by using optical cantilever-type microphone. in *Forum Acusticum Budapest 2005: 4th European Congress on Acustics* (2005).

48. Mayer, F. CMOS based sensors: From a sample to real products. *Proc. IEEE Int. Conf. Micro Electro Mech. Syst.* 1–5 (2008). doi:10.1109/MEMSYS.2008.4443578

49. Ma, Y., He, Y., Tong, Y., Yu, X. & Tittel, F. K. Quartz-tuning-fork enhanced photothermal spectroscopy for ultra-high sensitive trace gas detection. *Opt. Express* **26**, 32103 (2018).

50. Fischer, B. Optical microphone hears ultrasound. *Nat. Photonics* **10**, 356–358 (2016).

51. Evans, L. C. *Partial Differential Equations (Graduate Studies in Mathematics, Vol. 19). Instructor* (2009).

52. Bhatia, H., Norgard, G., Pascucci, V. & Bremer, P. T. The Helmholtz-Hodge decomposition - A survey. *IEEE Transactions on Visualization and Computer Graphics* **19**, (2013).

53. Vajdi, M., Sadegh Moghanlou, F., Sharifianjazi, F., Shahedi Asl, M. & Shokouhimehr, M. A review on the Comsol Multiphysics studies of heat transfer in advanced ceramics. *J. Compos. Compd.* **2**, (2020).

54. Jaderberg, B., Agarwal, A., Leonhardt, K., Kiffner, M. & Jaksch, D. Minimum hardware requirements for hybrid quantum-classical DMFT. *Quantum Sci. Technol.* **5**, (2020).

55. Reboul, G. L'effet Hertz-Hallwachs et l'absorption de la lumière. *Le Radium* **9**, (1912).

56. Einstein, A. Über einen die Erzeugung und Verwandlung des Lichtes betreffenden heuristischen Gesichtspunkt. *Ann. Phys.* **322**, (1905).

57. Hermann, D. R., Ramer, G., Kitzler-Zeiler, M. & Lendl, B. Quantum Cascade Laser-Based Vibrational Circular Dichroism Augmented by a Balanced Detection Scheme. *Anal. Chem.* **94**, 10384–10390 (2022).

58. Pourdavoud, N., Mayer, A., Buchmüller, M., Brinkmann, K., Häger, T., Hu, T., Heiderhoff, R., Shutsko, I., Görrn, P., Chen, Y., Scheer, H. C. & Riedl, T. Distributed Feedback Lasers Based on MAPbBr3. *Adv. Mater. Technol.* **3**, (2018).

59. Faist, J., Capasso, F., Sivco, D. L., Sirtori, C., Hutchinson, A. L. & Cho, A. Y. Quantum Cascade Laser. *Science (80-.).* **264**, 553–556 (1994).

60. Lendl, B., Frank, J., Schindler, R., Müller, A., Beck, M. & Faist, J. Mid-infrared quantum cascade lasers for flow injection analysis. *Anal. Chem.* (2000). doi:10.1021/ac990833b

61. Schwaighofer, A., Montemurro, M., Freitag, S., Kristament, C., Culzoni, M. J. & Lendl, B. Beyond FT-IR Spectroscopy: EC-QCL based mid-IR Transmission Spectroscopy of Proteins in the Amide I and Amide II Region. *Anal. Chem.* (2018). doi:10.1021/acs.analchem.8b01632

62. Moser, H., Pölz, W., Waclawek, J. P., Ofner, J. & Lendl, B. Implementation of a quantum cascade laser-based gas sensor prototype for sub-ppmv H2S measurements in a petrochemical process gas stream. *Anal. Bioanal. Chem.* **409**, (2017).

63. Genner, A., Martín-mateos, P., Moser, H. & Lendl, B. A quantum cascade laser-based multi-gas sensor for ambient air monitoring. *Sensors (Switzerland)* **20**, (2020).

64. Maulini, R., Beck, M., Faist, J. & Gini, E. Broadband tuning of external cavity bound-to-continuum quantum-cascade lasers. *Appl. Phys. Lett.* **84**, (2004).

65. Weida, M. J., Arnone, D. & Day, T. Tunable QC laser opens up mid-IR sensing applications. *Laser Focus World* **42**, (2006).

66. Brandstetter, M., Genner, A., Anic, K. & Lendl, B. Tunable external cavity quantum cascade laser for the simultaneous determination of glucose and lactate in aqueous phase. in *Analyst* (2010). doi:10.1039/c0an00532k

67. Fedeli, J. M., Labeye, P., Marchant, A., Lartigue, O., Fournier, M. & Hartmann, J. M. Mid-Infrared Platforms for Chemical Sensing. *IEEE Int. Conf. Gr. IV Photonics GFP* **2018**-**Augus**, 135–136 (2018).

68. Knötig, H., Hinkov, B., Weih, R., Schwarz, B., Lindner, S., Waclawek, J. P., Lendl, B., Höfling, S., Koeth, J. & Strasser, G. Vertically emitting ring interband cascade lasers. in (2021). doi:10.1117/12.2577764

69. Yang, R. Q. Infrared laser based on intersubband transitions in quantum wells. *Superlattices Microstruct.* **17**, (1995).

70. Razeghi, M. Current status and future trends of infrared detectors. *Opto-Electronics Review* **1998**, (1998).

71. Vm, E. & Cm, E. Advanced Features of InfraTec Pyroelectric Detectors Advanced Features of InfraTec Pyroelectric Detectors. *Current* **2**, (2003).

72. Lanagan, M. T. Review of: "CERAMIC MATERIALS FOR ELECTRONICS: PROPERTIES AND APPLICATIONS" Edited by Relva C. Buchanan 1986, Published by Marcel Dekker, Inc., 270 Madison Avenue, New York, New York 10016, $79.75 (U.S. and Canada), $95.50 (All other countries). *Mater. Manuf. Process.* **4**, (1989).

73. Dabrowska, A., David, M., Freitag, S., Andrews, A. M., Strasser, G., Hinkov, B., Schwaighofer, A. & Lendl, B. Broadband laser-based mid-infrared spectroscopy employing a quantum cascade detector for milk protein analysis. *Sensors Actuators B Chem.* **350**, (2022).

74. Jollivet, A., Hinkov, B., Pirotta, S., Hoang, H., Derelle, S., Jaeck, J., Tchernycheva, M., Colombelli, R., Bousseksou, A., Hugues, M., Le Biavan, N., Tamayo-Arriola, J., Montes Bajo, M., Rigutti, L., Hierro, A., Strasser, G., Chauveau, J. M. & Julien, F. H. Short infrared wavelength quantum cascade detectors based on m-plane ZnO/ZnMgO quantum wells. *Appl. Phys. Lett.* **113**, (2018).

75. Dabrowska, A., David, M., Schwaighofer, A., Hinkov, B., Harrer, A., Strasser, G. & Lendl, B. Towards Broadband Mid-Infrared Fully Integrated Protein Sensor employing a Quantum Cascade Laser and Quantum Cascade Detector. in *2021 Conference on Lasers and Electro-Optics Europe and European Quantum Electronics Conference, CLEO/Europe-EQEC 2021* (2021). doi:10.1109/CLEO/Europe-EQEC52157.2021.9542319

76. Fricke, K. *Digitaltechnik*. *Digitaltechnik* (2021). doi:10.1007/978-3-658-32537-4

77. Görne, T. Tontechnik. in *Tontechnik* (2014). doi:10.3139/9783446441491.fm

78. Kudrawiec, R. & Misiewicz, J. Optical Modulation Spectroscopy. in *Springer Series in Materials Science* **150**, (2012).

79. Lindner, S., Pinto, D., Moser, H., Waclawek, J. P. & Lendl, B. Theory, implementation and characterization of low-frequency Laser wavelength – Cavity resonance Locking Schemes for Cavity-enhanced spectroscopy. *[ready for submission]* (2022).

80. Tietze, U. & Schenk, C. *Halbleiter-Schaltungstechnik*. *Halbleiter-Schaltungstechnik* (1971). doi:10.1007/978-3-662-11943-3

81. Bavafa-Toosi, Y. Bode diagram. in *Introduction to Linear Control Systems* (2019). doi:10.1016/b978-0-12-812748-3.00007-0

82. Waclawek, J. P., Kristament, C., Moser, H. & Lendl, B. Balanced-detection interferometric cavity- assisted photothermal spectroscopy. *Opt. Express* **27**, (2019).

83. Lindner, S., Pinto, D., Moser, H., Waclawek, J. P. & Lendl, B. Noise suppression and 1f - Quadrature Point signal readout technique for cavity-enhanced spectroscopy. *[ready for submission]* (2022).

84. Lock-in Amplifiers. *Am. J. Phys.* **32**, (1964).

85. Thumm, M., Wiesbeck, W. & Kern, S. *Hochfrequenzmesstechnik*. *Hochfrequenzmesstechnik* (2008). doi:10.1007/978-3-663-01599-4

86. Strauß, F. Hochfrequenzmesstechnik. in *Grundkurs Hochfrequenztechnik* (2017). doi:10.1007/978-3-658-18163-5_7

87. Griffiths, P. R. & De Haseth, J. A. *Fourier Transform Infrared Spectrometry: Second Edition*. *Fourier Transform Infrared Spectrometry: Second Edition* (2006). doi:10.1002/047010631X

88. Dabrowska, A., Schwaighofer, A., Lindner, S. & Lendl, B. Mid-IR refractive index sensor for detecting proteins employing an external cavity quantum cascade laser-based Mach-Zehnder interferometer. *Opt. Express* **28**, 36632 (2020).

89. Owens, J. C. Optical Refractive Index of Air: Dependence on Pressure, Temperature and Composition. *Appl. Opt.* (1967). doi:10.1364/ao.6.000051

90. Wilson, A. J. C. The thermal expansion of aluminium from 0° to 650°C. *Proc. Phys. Soc.* (1941). doi:10.1088/0959-5309/53/3/305

91. Campillo, A. J., Davis, C. C. & Lin, H. Fabry – Perot photothermal trace detection. *Appl. Phys. Lett.* **41**, 327 (1982).

92. Li, H., Rieker, G. B., Liu, X., Jeffries, J. B. & Hanson, R. K. Extension of wavelength-modulation spectroscopy to large modulation depth for diode laser absorption measurements in high-pressure gases. *Appl. Opt.* **45**, (2006).

93. Devi, V. M., Benner, D. C., Gamache, R. R., Tran, H., Smith, M. A. H. & Sams, R. L. Multispectrum analysis of air-broadened spectra in the v3 Q branch of 12CH4. *J. Quant. Spectrosc. Radiat. Transf.* **206**, (2018).

94. Nizkorodov, S. A., Sander, S. P. & Brown, L. R. Temperature and pressure dependence of high-resolution air-broadened absorption cross sections of NO 2 (415-525 nm). *J. Phys. Chem. A* **108**, (2004).

95. Goldfischer, L. I. Autocorrelation Function and Power Spectral Density of Laser-Produced Speckle Patterns. *J. Opt. Soc. Am.* **55**, 247 (1965).

96. Adler, D. C., Ko, T. H., Herz, P. R. & Fujimoto, J. G. Optical coherence tomography contrast enhancement using spectroscopic analysis with spectral autocorrelation. *Opt. Express* **12**, 5487 (2004).

97. Benea-Chelmus, I. C., Rösch, M., Scalari, G., Beck, M. & Faist, J. Intensity autocorrelation measurements of frequency combs in the terahertz range. *Phys. Rev. A* **96**, 1–8 (2017).

98. Engel, V. The calculation of autocorrelation functions for spectroscopy. *Chem. Phys. Lett.* **189**, 76–78 (1992).

99. Werle, P. Accuracy and precision of laser spectrometers for trace gas sensing in the presence of optical fringes and atmospheric turbulence. *Appl. Phys. B Lasers Opt.* **102**, 313–329 (2011).

100. Serio, C., Lubrano, A. M., Romano, F. & Shimoda, H. Cloud detection over sea surface by use of autocorrelation functions of upwelling infrared spectra in the 800–900-cm^-1 window region. *Appl. Opt.* **39**, 3565 (2000).

101. Xu, X. G., Konorov, S. O., Hepburn, J. W. & Milner, V. Noise autocorrelation spectroscopy with coherent Raman scattering. *Nat. Phys.* **4**, 125–129 (2008).

102. Box, G. E. P., Jenkins, G. M. & Reinsel, G. C. *Time series analysis: Forecasting and control: Fourth edition*. *Time Series Analysis: Forecasting and Control: Fourth Edition* (2013). doi:10.1002/9781118619193

Appendix

A. Scientific Papers

On the following pages, the achieved scientific papers in this thesis are presented in full-text. These papers are:

1. Stefan Lindner, Jakob Hayden, Andreas Schwaighofer, Tobias Wolflehner, Christian Kristament, María Gonzáles-Cabrera, Stefan Zlabinger and Bernhard Lendl: *External Cavity Quantum Cascade Laser-Based Mid-Infrared Dispersion Spectroscopy for Qualitative and Quantitative Analysis of Liquid-Phase Samples*, Appl. Spectrosc. **74** (4) 452-459 (2020)

2. Stefan Lindner, Davide Pinto, Harald Moser, Johannes P. Waclawek and Bernhard Lendl: *Theory, implementation and characterization of low-frequency Laser-Cavity-Locking schemes for Interferometric Cavity-Assisted Photothermal Spectroscopy (ICAPS)*, Ready for submission

3. Stefan Lindner, Davide Pinto, Harald Moser, Johannes P. Waclawek and Bernhard Lendl: *Noise suppression and 1f - Quadrature point signal readout technique for cavity-enhanced spectroscopy*, Ready for submission

Further, there were contributions to several other scientific papers delivered.

1. <u>Davide Pinto</u>, Johannes P. Waclawek, Stefan Lindner, Harald Moser, Giovanna Ricchiuti and Bernhard Lendl: *Wavelength Modulated Diode Probe Laser for an Interferometric Cavity-Assisted Photothermal Spectroscopy Gas Sensor*, SSRN Electronic Journal (2022), doi:10.2139/ssrn.4210238
2. <u>Alicja Dabrowska</u>, Andreas Schwaighofer, Stefan Lindner, and Bernhard Lendl: *Mid-IR refractive index sensor for detecting proteins employing an external cavity quantum cascade laser-based Mach-Zehnder interferometer*, Optics Express, **28** (24) 36632-36642 (2020)
3. <u>Alicja Dabrowska</u>, Stefan Lindner, Andreas Schwaighofer, and Bernhard Lendl: *Mid-IR dispersion spectroscopy – A new Avenue for liquid phase analysis*, Spectrochimica Acta Part A: Molecular and Biomolecular Spectroscopy (2023), doi: 10.1016/j.saa.2022.122014
4. <u>Hedwig Knötig</u>, Borislav Hinkov, Robert Weih, Benedikt Schwarz, Stefan Lindner, Johannes P. Waclawek, Bernhard Lendl, Sven Höfling, Johannes Koeth and Gottfried Strasser: *Vertically emitting ring interband cascade lasers*, Proc. SPIE 11705, Novel In-Plane Semiconductor Lasers XX, 1170517 (5 March 2021)

The contributions to these publications were in detail:

1.	Discussing ideas about the mathematical background of the observed effects. Practical collaboration in the laboratory. Discussion of the interpretation of raw signals. Reviewing the theoretical part of the manuscript.
2.	Practical collaboration in the laboratory.
3.	Working on the theory section of the paper. Contributions to the mathematical formalism. Reviewing the theoretical part of the manuscript.
4.	Discussion of possible applications of the laser for chemical sensing.

External Cavity Quantum Cascade Laser-Based Mid-Infrared Dispersion Spectroscopy for Qualitative and Quantitative Analysis of Liquid-Phase Samples

Stefan Lindner[1] , Jakob Hayden[1], Andreas Schwaighofer[1],
Tobias Wolflehner[1], Christian Kristament[1],
María González-Cabrera[2], Stefan Zlabinger[1],
and Bernhard Lendl[1]

Abstract

Acquisition of classical absorption spectra of liquids in the mid-IR range with quantum cascade lasers (QCLs) is often limited in sensitivity by noise from the laser source. Alternatively, measurement of molecular dispersion (i.e., refractive index) spectra poses an experimental approach that is immune to intensity fluctuations and further offers a direct relationship between the recorded signal and the sample concentration. In this work, we present an external cavity quantum cascade laser (EC-QCL) based Mach–Zehnder interferometer setup to determine dispersion spectra of liquid samples. We present two approaches for acquisition of refractive index spectra and compare the qualitative experimental results. Furthermore, the performance for quantitative analysis is evaluated. Finally, multivariate analysis of a spectrally complex mixture comprising three different sugars is performed. The obtained figures of merit by partial least squares (PLS) regression modelling compare well with standard absorption spectroscopy, demonstrating the potential of the introduced dispersion spectroscopic method for quantitative chemical analysis.

Introduction

In the mid-infrared (mid-IR) region (400–4000 cm^{-1}) organic molecules possess their strongest rotational–vibrational transitions, thus offering highly discriminatory information inherently allowing molecule specific detection. Currently, the most widespread type of mid-IR spectroscopy for routine quantitative and qualitative analysis is absorption spectroscopy in the form of Fourier transform IR (FT-IR) spectroscopy because of its versatility and simplicity. In absorption spectroscopy, attenuation of the radiation intensity caused by an absorption process is measured. This relies on detecting small signal changes due to absorption of the analyte on top of a large background, i.e., the total light intensity arriving at the detector. General drawbacks of absorption spectroscopy arise from a direct impact of the intensity noise on the measured absorption signal and possible dynamic range limitations due to eventual nonlinearities of the detectors used.[1–3] For thermal light sources employed in FT-IR spectroscopy, these intensity fluctuations can usually be neglected; however, their low emission power constitutes a disadvantage for many applications.

More than two decades ago, the first quantum cascade lasers (QCLs) were introduced as a high-intensity light

[1]Institute of Chemical Technologies and Analytics, Technische Universität Wien, Getreidemarkt, Vienna, Austria
[2]Department of Physical and Analytical Chemistry, Universidad de Jaén, Campus Las Lagunillas, Jaén, Spain

Corresponding author:
Bernhard Lendl, Technische Universität Wien, Getreidemarkt 9, Wien 1060, Austria.
Email: Bernhard.lendl@tuwien.ac.at

source for the mid-IR region. QCLs provide polarized and coherent light with spectral power densities several orders of magnitude higher than thermal light sources.[4,5] For liquid-phase applications, the high available emission power was the first of these unique characteristics that was exploited to implement direct absorption setups. The high laser intensities allowed to increase optical paths of transmission measurements compared to FT-IR spectroscopy,[6] particularly after emergence of external cavity (EC)-QCLs that provide spectral tuning ranges of several hundred wavenumbers.[7–9] However, recently reported EC-QCL-based systems offer increased ruggedness compared to FT-IR spectroscopy at only slightly better signal-to-noise ratios (SNR)[10] owing to the high noise levels introduced by the laser light sources.

Very recently, an EC-QCL was combined with a Mach–Zehnder interferometer (MZI) for proof-of-principle measurements of broadband dispersion (refractive index) spectra in the mid-IR spectral region.[11] In dispersion spectroscopy, the phase shift of the radiation due to passing through a sample is measured. Dispersion and absorption are caused by the same process, thus the same spectral information about the sample can be retrieved by determining either of the two properties. Approaches to measuring molecular dispersion using QCLs were reported for applications in the gas phase using chirped laser dispersion spectroscopy (CLaDS),[12] and recently also using a new variant entitled heterodyne phase sensitive dispersion spectroscopy (HPSDS). Measuring anomalous dispersion at a molecular resonance rather than its absorption yields the advantage of independence of signals from laser power and a linear relationship between dispersion signals and sample concentration, even for optically thick samples.[13] Particularly the former aspect holds promise for applications of QCLs that emit with comparably high intensity noise.

In this work, we present an EC-QCL based MZI setup for acquisition of broadband refractive index spectra. MZIs are well known for refractive index sensing at single wavelengths from biosensing applications in wavelength regions from the visible to the mid-IR,[14–16] but their application to broad band mid-IR dispersion spectroscopy is yet pending. In the presented approach, the MZI is operated at an optical phase difference of $\frac{\pi}{2}$ to record phase shifts at highest sensitivity induced by the sample and reference placed inside the interferometer arms. We present two approaches for acquisition of refractive index spectra. One method employs active compensation of the sample-induced phase shift using a mirror mounted on a piezo actuator, whereas the second method requires no moving parts. Whereas the first method (moving-piezo method) appears to be more accurate from a metrological point of view, the second method (fixed-piezo method) entails the advantage of being more rugged as no moving parts are involved. After comparison and discussion of the qualitative experimental results, the performance of the latter

approach for quantitative analysis is evaluated. Finally, multivariate analysis of a mixture of three different sugars is performed to demonstrate the capability of dispersion spectroscopy to tackle challenging analytical problems.

Experimental

Basic Principles of Mach–Zehnder Interferometer-Based Dispersion Spectroscopy

Generally, the intensity output I_{out} of a two-beam interferometer such as the MZI discussed herein can be expressed as

$$I_{\text{out}} = I_a + I_b + 2\sqrt{I_a I_b}\cos(\Delta\varphi) \tag{1}$$

where I_a and I_b are the intensities of the two interfering waves (measured at the detectors D1 and D2) and $\Delta\varphi$ is the phase shift between them. For the interferometric setup shown in Fig. 1, the interfering waves yielding the signal at detector 1 are characterized by the intensities and relative phase

$$I_{a,1} = I_0 T^2 10^{-A_0} \tag{2}$$

$$I_{b,1} = I_0 R^2 10^{-(A_0+A)} \tag{3}$$

$$\Delta\varphi_1 = \frac{2\pi}{\lambda}[\Delta l + (n - n_0)d] \tag{4}$$

Herein, I_0 is the laser intensity, T and R are the transmittance and reflectivity of the beam splitters (assumed equal), 10^{-A_0} denotes the attenuation of the reference liquid in flow cell FC1, and A is the absorption of the sample in flow cell FC2 with respect to the reference. Furthermore, λ indicates
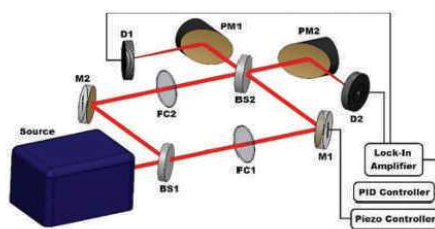
Figure 1. Schematic of the developed experimental setup. BS1, BS2 are ZnSe beam splitters and M1, M2 protected gold mirrors, which form the Mach–Zehnder interferometer. M2 is attached to a piezo drive to adjust the path lengths of the two-part beams. FC1 and FC2 are the BaF₂ liquid flow cells with 50 μm thickness. The parabolic focusing mirrors PM1 and PM2 are employed to focus the beams on the pyroelectric detectors D1 and D2, respectively.

the wavelength, Δl is the geometric path length difference between the two interferometer arms, n and n_0 are the refractive indices of the sample (FC2) and reference (FC1) cell and d is the equal film thickness of the two flow cells.

For detector D2, the interfering waves are described by

$$I_{a,2} = I_0 R T 10^{-A_0} \tag{5}$$

$$I_{b,2} = I_0 R T 10^{-(A_0+A)} \tag{6}$$

$$\Delta\varphi_2 = \Delta\varphi_1 - \pi \tag{7}$$

The difference of π between $\Delta\varphi_1$ and $\Delta\varphi_2$ originates from the different numbers of reflections (see Fig. 1: D1 receives beams with even numbers of reflections, D2 with odd numbers of reflections, yielding a phase difference of π due to the fact that every reflection causes a phase shift of π) and yields the antisymmetric behavior of the two interferometer outputs with respect to phase. Inserting Eqs. 2 to 7 in Eq. 1 yields

$$I_{\text{out},1} = I_0 10^{-A_0}$$
$$\cdot \left[T^2 + R^2 10^{-A} + 2RT 10^{-\frac{A}{2}} \right.$$
$$\left. \cdot \cos\left(\frac{2\pi}{\lambda}[\Delta l + (n-n_0)d] \right) \right] \tag{8}$$

$$I_{\text{out},2} = I_0 10^{-A_0}$$
$$\cdot \left[RT(1 + 10^{-A}) - 2RT 10^{-\frac{A}{2}} \right.$$
$$\left. \cdot \cos\left(\frac{2\pi}{\lambda}[\Delta l + (n-n_0)d] \right) \right] \tag{9}$$

Assuming $R = T = 0.5$, which is valid for beam splitters with sufficiently good performance of a 50:50 splitting ratio, delivers for the normalized differential detector signal

$$\Delta I_{\text{rel}} := \frac{I_{\text{out},1} - I_{\text{out},2}}{I_{\text{out},1} + I_{\text{out},2}} = \frac{\cos\left(\frac{2\pi}{\lambda}[\Delta l + (n-n_0)d] \right)}{\frac{1}{2}\left(10^{\frac{A}{2}} + 10^{-\frac{A}{2}} \right)} \tag{10}$$

With $\Delta l = \frac{\lambda}{4}$, which is fulfilled experimentally by holding mirror M1 in this position with a piezo drive, the expression for ΔI_{rel} can be further simplified to receive

$$\Delta I_{\text{rel}} \approx \frac{2}{10^{\frac{A}{2}} + 10^{-\frac{A}{2}}} \sin\left(\frac{2\pi d}{\lambda}(n-n_0) \right) \tag{11}$$

Furthermore, this expression can be approximated by

$$\Delta I_{\text{rel}} \approx \frac{2\pi d}{\lambda}(n-n_0) \tag{12}$$

when assuming small values for the absorption $A \approx 0$ and small differences in refractive index $n-n_0$, since $\sin x \approx x$

for small values of x. Both approximations are valid for low analyte concentrations. This delivers a linear dependence of the measured signal from the refractive index, which is the basis for one of the two methods we developed (see Fig. 2). In order to obtain signals that scale linearly with phase shift and hence concentration, the interferometer was operated at or around the indicated working point in Fig. 2, corresponding to a phase of $\frac{\pi}{2}$.

Experimental Setup

The experimental setup is depicted schematically in Fig. 1. It consists of a Mach–Zehnder type interferometer with a flow cell integrated in each of the beam paths. The laser beam emitted by a thermoelectrically-cooled external cavity quantum cascade laser (Daylight Solutions Inc.; Model No. 11088, laser head: 1240–890 cm^{-1}, laser Driver 1001-TLC) was split at a ratio of R:T = 48:52 by a ZnSe beam splitter (Thorlabs BSW710). Both, the reflected and transmitted beam, pass 50 μm liquid flow cells (1″ wedged BaF$_2$ windows with PTFE spacer, Korth Kristalle GmbH), and are recombined with another beam splitter (identical to first beam splitter) and mirror before getting focused on two pyroelectric detectors (Infratec LME-336, detectivity $4.0 \cdot 10^8$ cm$\sqrt{Hz}/W$ at 500 K, aperture size 5 mm diameter) by two parabolic gold mirrors (Thorlabs MPD229M01). To minimize fringing, the detectors were mounted in an angle of approximately 30° to the beam. One of the mirrors in the interferometer is glued to
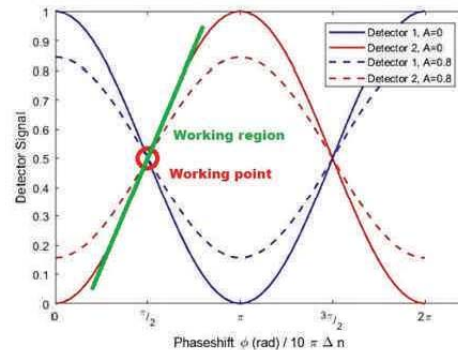

Figure 2. Visualization of the measurement principles for recording dispersion spectra. The figure shows the behavior of the normalized detector signals corresponding to $I_{\text{out},1}$ and $I_{\text{out},2}$ (compare Eqs. 8 and 9), normalized by the sum of $I_{\text{out},1}$ and $I_{\text{out},2}$ with phase shift $\phi = \frac{2\pi}{\lambda}(n-n_0)d$. With the used cell thickness of 50 μm and an average wavelength of 10 μm, this phase shift represents the difference in refractive index $\Delta n = n - n_0$ times 10π. The detector signals are plotted for $A = 0$ and $A = 0.8$, respectively. The red circle and the green line illustrate working regions of the two different measurement methods (moving and fixed-piezo method).

a piezo actuator (3.6 µm maximum displacement) connected to a commercial piezo controller (Thorlabs MDT644A) The laser was operated at a repetition rate of 100 kHz with a duty cycle of 5% and an over modulated square wave with a frequency of 100 Hz (train of pulses). The recorded detector signals were amplified and filtered with a custom-built lock-in amplifier synchronized to the 100 Hz modulation of the laser before being digitized by a NI DAQ-ADC (Model 9205, National Instruments Corp.).

Recording of Dispersion Spectra

Dispersion spectra are recorded based on analyzing the differential detector signal ΔI_{rel} while scanning the laser wavelength. As outlined above (compare Eqs. 10 to 12), ΔI_{rel} scales linearly with the sample's refractive index for sufficiently diluted samples. Therefore, ΔI_{rel} immediately yields dispersion spectra if the interferometric phase is kept close to $\frac{\pi}{2}$ (moving-piezo method). To record dispersion spectra independent from the small signal approximation (compare Eq. 11), an alternative approach, coined the "fixed-piezo method", was investigated.

Moving-Piezo Method. Using this method, the relative phase between the two interferometric arms is actively compensated by the piezo-positioned mirror. To achieve this, the differential detector signal ΔI_{rel} is digitized and supplied to a LabView internal PID-controller. The PID-controller keeps $\Delta I_{rel} = 0$ by acting on the piezo element attached to mirror M1 via the piezo-controller. The working point of this measurement principle is indicated by the red circle in Fig. 2. As the sample-induced phase shift is continuously compensated by the piezo drive while scanning the laser wavelength, the corresponding piezo voltage is a direct measure of mirror displacement δ and hence also of the sample's refractive index. To record dispersion spectra of a sample, a background spectrum $\delta_0(\tilde{\nu})$, obtained for both flow cells filled with the solvent, must be subtracted from the sample spectrum. The non-zero background originates from the interferometric phase differing from $\frac{\pi}{2}$ (see Eq. 10 and Fig. 2) for all wavelengths except the center wavelength since $\Delta l \neq \frac{\lambda}{4}$, as well as from small deviations of the interferometer from perfect symmetry. All spectra, including dispersion spectra using the fixed-piezo method (see below) and absorption spectra, were recorded at wavenumber steps of 1 cm^{-1} and an averaging time of 1 s per step. After subtraction of $\delta_0(\tilde{\nu})$ from the sample spectrum $\delta_{spl}(\tilde{\nu})$, the refractive index difference Δn between sample and solvent is calculated from the background-free mirror displacement $\delta(\tilde{\nu}) = \delta_{spl}(\tilde{\nu}) - \delta_0(\tilde{\nu})$ and the known film thickness d as (compare Eq. 4)

$$\Delta n(\tilde{\nu}) := n - n_0 = \frac{\delta(\tilde{\nu}) \cdot \sqrt{2}}{d} \tag{13}$$

The factor of $\sqrt{2}$ appears due to geometric considerations, because the mirror travel is along the diagonal line between the mirrors M1 and M2. In case of known refractive index n_0 of the reference solution in the wavenumber region of interest, an absolute refractive index spectrum can be determined. The main limitation of this approach in the current setup was the hysteresis effects of the piezo crystal, which limited the quality of the recorded piezo voltage as a measure of mirror displacement and limits the reproducibility of measurements. For this reason, quantitative measurements were performed using the differential signal ΔI_{rel} directly as a dispersion spectrum at a fixed mirror position.

Fixed-Piezo Method. When employing this method, the mirror displacement δ is fixed to $\frac{\lambda}{4}$ for the center wavelength throughout the measurement. To this end, the mirror displacement is adjusted until $\Delta I_{rel} = 0$ while both flow cells are filled with the solvent. Next, a background spectrum $\Delta I_{rel,0}(\tilde{\nu})$ and sample spectrum are recorded as described above, but with fixed piezo position. From both spectra, a spectrum of displacement is calculated using Eq. 14

$$\delta(\tilde{\nu}) = \frac{\lambda}{2\pi} \sin^{-1} \Delta I_{rel}(\tilde{\nu}) \tag{14}$$

which is derived from Eq. 11 by assuming A $\approx$ 0 (see Supplemental Material, Figure S2). The resulting spectra of displacement are treated as described above to derive a spectrum of the refractive index $\Delta n(\tilde{\nu})$ of the sample.

Besides overcoming the adverse hysteresis effects of the piezo crystal, this approach also allows increasing the scan speed. However, the spectrum of ΔI_{rel} is recorded for an interferometric phase other than $\frac{\pi}{2}$ for all wavelengths except the center wavelength since $\delta \neq \frac{\lambda}{4}$. This yields a non-zero background that depends also on the sample's absorption and makes measurements susceptible to laser intensity noise. Within the tuning range of the EC-QCL (1200 cm^{-1} to 950 cm^{-1}), the phase varies by approximately $\frac{\pi}{10}$ around 0. For high concentrations (large Δn and A), this yields significant contributions from absorption to the recorded spectrum of ΔI_{rel} and hence deviation from linearity of the obtained value with concentration.

Absorption Spectroscopy. For recording absorption spectra, the beam path in one of the two arms of the interferometer (here, the path passing FC1, Fig. 1) is blocked so that no interference occurs. Reference and sample spectra $I_0^A(\tilde{\nu})$ and $I^A(\tilde{\nu})$ are measured by consecutively injecting the reference and the sample in FC2 and recording the sum of both detector signals. Absorption spectra are calculated as

$$A(\tilde{\nu}) = \log_{10}\left(\frac{I_0^A(\tilde{\nu})}{I^A(\tilde{\nu})}\right) \tag{15}$$

Reagents and Samples

Sodium fluoride 99%, anhydrous and glucose, were purchased from Sigma Aldrich. Fructose 99%, sucrose 99%, and ethanol abs. were purchased from Merck. All samples were prepared in a 1% NaF solution to avoid corrosion of the BaF_2-windows (Korth Kristalle GmbH) in contact with solvent caused by the small solubility of BaF_2 in water.

Results and Discussion

Qualitative Evaluation of the Recorded Spectra

For qualitative evaluation of dispersion spectra recorded with the described setup, ethanol was chosen as an analyte. Ethanol features two separated and characteristic bands in the spectral emission region of the employed EC-QCL. The measured absorption and dispersion spectra of 5%v/v ethanol in water are shown in Fig. 3b. For comparison, a FT-IR absorption spectrum was recorded, and a refractive index spectrum was calculated by the Kramers–Kronig transformation (Fig. 3a). The absorption spectra show IR bands at 1046 and 1086 cm^{-1} that are attributed to the asymmetric C–C–O stretching modes of the gauche and anti-conformers of ethanol.[17,18] The absorption spectrum recorded with the MZI setup agrees well with the FT-IR spectrum. Regarding the dispersion spectra recorded with the MZI, the general shape of the dispersion spectra agrees well with the Kramers–Kronig transformed FT-IR absorption spectra. Dispersion spectra show the characteristic shape of the refractive index close to an absorption band including a region of anomalous dispersion $\left(\frac{dn}{d\lambda} > 0\right)$ around the band center (see Fig. 3b). Differences between the calculated spectrum and the dispersion spectrum recorded with fixed piezo

position are expected since the strong absorption yields significant errors when using the approximation, $A \approx 0$ (compare Eq. 12), as discussed above. The effect of this approximation on the retrieved dispersion spectrum is discussed in the supporting information (Figure S2). The slightly smaller excursion around resonance in the dispersion spectrum measured with moving-piezo method as compared to the calculated spectrum might point to an insufficient speed of the feedback loop and will be investigated in the future. For both methods, two kinds of deviation of optical components from assumptions taken above can affect the measurements. Firstly, the reflectivity and transmission of the beam splitters is not $R = T = 0.5$ as assumed in Eq. 10 for the whole spectral range (see datasheet of the used ThorLabs ZnSe beam splitter BSW710). Secondly, the response of the two detectors must be equal to justify the insertion of the detector signal for $I_{out,1}$ and $I_{out,2}$ in the equations above without scaling. Differences in detector response may arise during amplification of detector signals and from the optical alignment of the beams on the detectors. Differences might also be associated with insufficient temperature stabilization of the current setup. Assuming a temperature change of 1 K and a diameter of the interferometer of 0.25 m, the linear heat expansion coefficient of the aluminum breadboard results in a change of the overall diameter of around 5 μm,[19] which is much larger than the sample-induced displacements $\delta(\tilde{v})$.

Quantitative Analysis of the Acquired Spectra

Experimentally, an offset between consecutively recorded dispersion spectra was observed, most likely due to temperature instabilities and heat expansion of the used optical components. Thus, for obtaining calibration curves, the slopes of the dispersion spectrum in the points of inflection were used, as
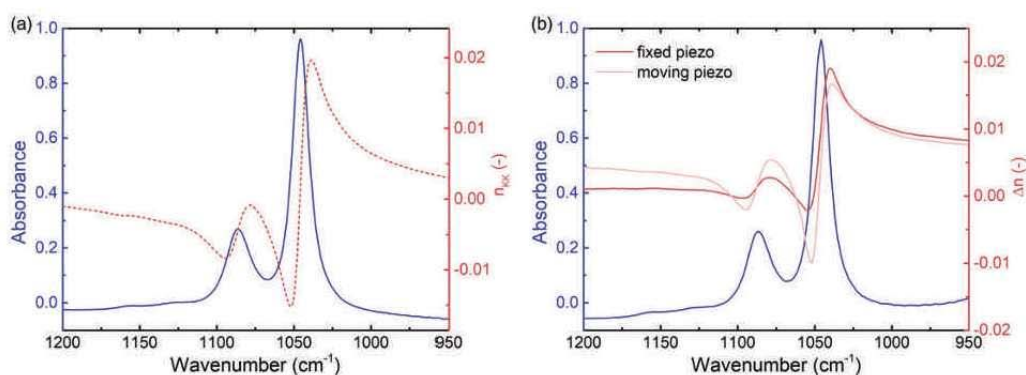

Figure 3. (a) Absorption spectrum (blue) of 5% ethanol recorded using FT-IR spectroscopy. The refractive index spectrum (red dashed) was calculated by Kramers–Kronig transformation. (b) Absorption (blue) and refractive index spectra of 5% ethanol recorded by the moving-piezo (light red) and fixed-piezo (red) method with the developed Mach–Zehnder interferometer setup.

144

illustrated in Figure S1. These points coincide with the band maxima in the corresponding absorption spectra. For evaluation of the slopes, a custom-made Matlab routine was programed. The routine uses the known wavenumber values of the absorption band and calculates an average slope using the four data points next to these wavenumber values. The slope values found in this way were finally averaged to obtain the slope values used for calibration.

Univariate Quantification Employing Absorption and Dispersion Spectra

In order to evaluate the capabilities of the MZI setup for quantification purposes, absorption and dispersion measurements were performed. To this end, glucose solutions were prepared with concentrations ranging between 2 and $10\,\mathrm{g\,L^{-1}}$. The recorded absorption spectra used as a reference for the dispersion spectroscopy measurements are shown in Fig. 4a. Characteristic IR bands at 994, 1036, 1081, 1108, and $1153\,\mathrm{cm^{-1}}$ can be assigned to C–O stretching, C–C stretching as well as C–O–H bending modes of the glucose molecule.[20] For quantitative analysis, the band height was evaluated at the most prominent IR absorption band at $1036\,\mathrm{cm^{-1}}$. The calibration curve (inset in Fig. 4a) indicates that the experimental data fit well to a linear regression line. By evaluation of the slope

$$\frac{\mathrm{d}A\left(1036\,\mathrm{cm^{-1}}\right)}{\mathrm{d}c}$$

and the root mean square noise level σ_{RMS} in the relevant spectral region, the limit of detection was calculated as $c_{\mathrm{LOD,A}} = 3\frac{\sigma_{RMS}}{\mathrm{d}A/\mathrm{d}c} = 0.19\,\mathrm{g\,L^{-1}}$. Quantitative measurements using dispersion spectroscopy were exclusively performed

employing the fixed-piezo method, due to aberrations introduced by hysteresis effects of the piezo element when using the moving-piezo method, as outlined in the experimental section. For quantitative evaluation of the dispersion spectra, the slopes of the tangents at the inflection points were evaluated (Figure S1). The obtained calibration curve (Fig. 4b, inset) confirms the expected linearity with concentration. For dispersion spectra, the limit of detection was evaluated to be $0.53\,\mathrm{g\,L^{-1}}$. These measurements and quantitative analysis demonstrate that both absorption and dispersion spectra can be employed for quantitative measurements and that the recorded dispersion spectra show the expected linear behavior with concentration. The higher limit of detection obtained for dispersion measurements most likely is explained by the limited thermal and mechanical stability of the current setup.

Multivariate Quantification of Glucose, Fructose and Sucrose Employing Absorption and Dispersion Spectra

In order to test the capabilities of the developed setup for quantification of complex analyte mixtures, ternary solutions containing glucose, fructose and sucrose were analyzed. Simultaneous quantification of these sugars in different matrices (e.g., fruit juices, honey) is routinely performed using FT-IR spectroscopy,[21–24] thus it poses an excellent problem to benchmark the performance of the developed method. A calibration data set comprising 17 solutions was prepared with individual sugar concentrations ranging between 1 and $10\,\mathrm{g\,L^{-1}}$ (Table S1) and absorption as well as dispersion spectra were recorded. Within the observed spectral region, the absorption bands of glucose, fructose and sucrose strongly overlap. To tackle quantification in this multicomponent system, multivariate partial
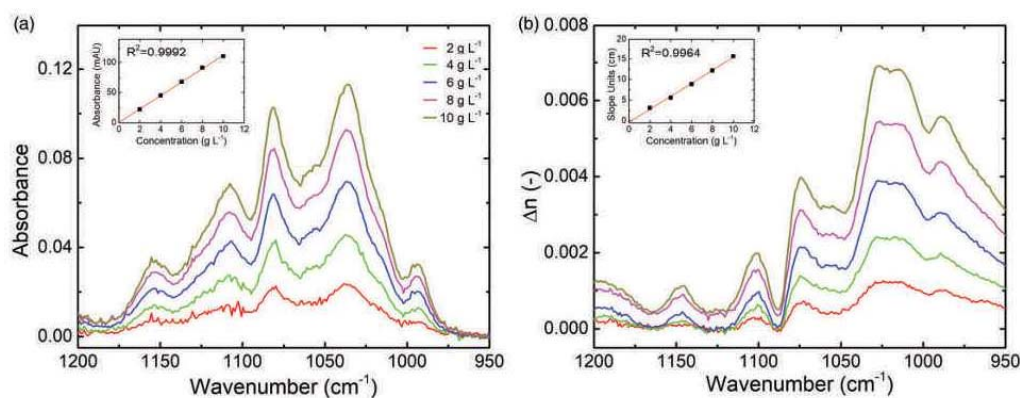

Figure 4. (a) Absorption spectra of glucose recorded with the MZI. Inset shows univariate calibration evaluated at $1036\,\mathrm{cm^{-1}}$. (b) Refractive index spectra of glucose recorded with fixed-piezo method using the MZI. Inset shows univariate calibration by evaluation of the slopes at the points of inflection.

Table I. PLS calibration parameters and internal figures of merit.

	Absorption spectra			Dispersion spectra		
	Fructose	Glucose	Sucrose	Fructose	Glucose	Sucrose
Spectral region (cm^{-1})	959–1209	947–1180	968–1185	958–1025, 1052–1121	917–1130	917–1151
Preprocessing	1st der. + MC	MC	1st der. + MC	2nd der. + MC	1st der. + MC	1st der. + MC
RMSEC (g L^{-1})	0.05	0.04	0.04	0.11	0.09	0.06
RMSECV (g L^{-1})	0.07	0.05	0.05	0.22	0.17	0.08
R^2 Cal	0.9995	0.9998	0.9997	0.998	0.998	0.9993
R^2 CV	0.9991	0.9995	0.9995	0.992	0.995	0.9990
CV bias	0.002	−0.001	0.0005	−0.037	−0.004	0.010

MC: mean centering; 1st der.: first derivative calculated using the Savitzky–Golay filter (order: 3, window: 15 points); 2nd der.: second derivative calculated using the Savitzky–Golay filter (order: 3, window: 15 points); R^2: coefficient of determination; Cal: calibration; CV: cross validation; RMSEC: root mean square error of calibration; RMSECV: root mean square error of cross-validation.

least squares (PLS) regression models were optimized for each analyte (PLS Toolbox 8.0, Eigenvector Research Inc.). The PLS calibration parameters and internal figures of merit are summarized in Table I. For all PLS models, three latent variables were used, reflecting the three components in the solution. Coefficients of determination (R^2) of calibration and leave-one-out cross-validation are >0.999 and >0.998 for absorption and dispersion spectra, respectively, for all three sugars. The root mean square error of calibration (RMSEC) and cross-validation (RMSECV) range between 0.04 and 0.05 g L^{-1} and 0.05 and 0.07 g L^{-1}, for absorption and between 0.06 and 0.11 g L^{-1} and 0.08 and 0.22 g L^{-1} for dispersion spectra, respectively, while the bias of cross validation (CV bias) as a measure of accuracy range between −0.037 and 0.01 g L^{-1}, respectively. Overall, both absorption and dispersion spectroscopy allow simultaneous quantification of the three sugars at few percent accuracy as determined from the cross-validation. The slightly, but actual better figures of merit found for absorption spectra most likely originate from the higher experimental sensitivity of dispersion spectroscopy with the current implementation to external, environmental fluctuations, as described in the previous sections.

Conclusion

In this work, a Mach–Zehnder interferometry setup was introduced for recording mid-IR dispersion spectra of liquid samples using an EC-QCL. After a thorough discussion of the theoretical basis and principles of signal generation, two methods were introduced for the acquisition of dispersion spectra. The spectra obtained with the moving-piezo method agree very well with theory, while spectra recorded with fixed-piezo method have the advantage of higher reproducibility. Qualitative comparison of the shape of the measured dispersion spectra delivered comparable results with state-of-the-art FT-IR measurements concerning absorption and Kramers–Kronig transformed refractive index spectra. Quantitative analysis was performed employing dispersion spectra for univariate calibration of glucose in water and results were compared with conventional absorption spectroscopy. The calibration results confirm the expected linearity of dispersion spectra with concentration and compare well with calibration based on absorption spectroscopy. PLS-based multivariate calibration of solutions containing three different sugars were performed based on dispersion spectra and referenced against results obtained from absorption spectroscopy. The RMSECV of only a few percent of the actual concentrations as well as other figures of merit are very similar to absorption spectroscopic results and demonstrate the potential of mid-IR dispersion spectroscopy for solving complex analytical problems at high accuracy based on the rich spectroscopic information of this spectral region.

In conclusion, this work demonstrates that mid-IR dispersion spectroscopy is an interesting alternative to state-of-the-art absorption spectroscopy not only for gases,[1,13] but also for liquid samples. Experimental drawbacks identified during this proof-of-concept work were the high susceptibility of the interferometric approach to temperature fluctuations of the optical components. Planned measures to overcome these issues include the implementation of an improved temperature stabilization of the interferometer to avoid temperature drifts and decrease phase noise of the interferometer. This is crucial to obtain consistent dispersion spectra. Also, further miniaturizations of the setup are planned. While the linearity of recorded signals with concentration in dispersion spectroscopy could already be successfully demonstrated, further improvements of the experimental setup promise to also harness dispersion spectroscopy's robustness against laser intensity noise and to increase sensitivity.

Declaration of Conflicting Interests

The author(s) declared no potential conflicts of interest with respect to the research, authorship, and/or publication of this article.

Funding

ORCID iDs

Stefan Lindner ● https://orcid.org/0000-0002-3451-7011

Bernhard Lendl ● https://orcid.org/0000-0003-3838-5842

Supplemental Material

All supplemental material mentioned in the text, consisting of figures and a table, is available in the online version of the journal.

References

1. M. Nikodem, G. Wysocki. "Molecular Dispersion Spectroscopy—New Capabilities in Laser Chemical Sensing". Ann. N.Y. Acad. Sci. 2012. 1260(1): 101–111.

2. P. Hoffmann, E. Knoezinger. "Dynamic Range Problems in Fourier Transform IR and Far-IR Spectroscopy". Appl. Spectrosc. 1987. 41(8): 1303–1306.

3. D.B. Chase. "Nonlinear Detector Response in FT-IR". Appl. Spectrosc. 1984. 38(4): 491–494.

4. M.J. Weida, B. Yee. "Quantum Cascade Laser-Based Replacement for FT-IR Microscopy". Proc. SPIE 7902, Imaging, Manipulation, and Analysis of Biomolecules, Cells, and Tissues IX, 79021C. 2011. https://doi.org/10.1117/12.873954 [accessed Nov 22 2019].

5. A. Schwaighofer, M. Brandstetter, B. Lendl. "Quantum Cascade Lasers (QCLs) in Biomedical Spectroscopy". Chem. Soc. Rev. 2017. 46(19): 5903–5924.

6. B. Lendl, J. Frank, R. Schindler, et al. "Mid-Infrared Quantum Cascade Lasers for Flow Injection Analysis". Anal. Chem. 2000. 72(7): 1645–1648.

7. M. Brandstetter, A. Genner, K. Anic, et al. "Tunable External Cavity Quantum Cascade Laser for the simultaneous Determination of Glucose and Lactate in Aqueous Phase". Analyst. 2010. 135(12): 3260–3265.

8. M.R. Alcaráz, A. Schwaighofer, C. Kristament, et al. "External-Cavity Quantum Cascade Laser Spectroscopy for Mid-IR Transmission Measurements of Proteins in Aqueous Solution". Anal. Chem. 2015. 87(13): 6980–6987.

9. A. Schwaighofer, M.R. Alcaráz, C. Araman, et al. "External Cavity-Quantum Cascade Laser Infrared Spectroscopy for Secondary Structure Analysis of Proteins at Low Concentrations". Sci. Rep. 2016. 6: 33556.

10. A. Schwaighofer, M. Montemurro, S. Freitag, et al. "Beyond Fourier Transform Infrared Spectroscopy: External Cavity Quantum Cascade Laser-Based Mid-Infrared Transmission Spectroscopy of Proteins in the Amide I and Amide II Region". Anal. Chem. 2018. 90(11): 7072–7079.

11. J. Hayden, S. Hugger, F. Fuchs, et al. "A Quantum Cascade Laser-Based Mach–Zehnder Interferometer for Chemical Sensing Employing Molecular Absorption and Dispersion". Appl. Phys. B: Lasers Opt. 2018. 124(2): 1–9.

12. G. Wysocki, D. Weidmann. "Molecular Dispersion Spectroscopy for Chemical Sensing Using Chirped Mid-Infrared Quantum Cascade Laser". Opt. Express. 2010. 18(25): 26123.

13. P. Martín-Mateos, J. Hayden, P. Acedo, et al. "Heterodyne Phase-Sensitive Dispersion Spectroscopy in the Mid-Infrared with a Quantum Cascade Laser". Anal. Chem. 2017. 89(11): 5916–5922.

14. P. Kozma, F. Kehl, E. Ehrentreich-Förster, et al. "Integrated Planar Optical Waveguide Interferometer Biosensors: A Comparative Review". Biosens. Bioelectron. 2014. 58: 287–307.

15. Q. Liu, X. Tu, K.W. Kim, et al. "Highly Sensitive Mach-Zehnder Interferometer Biosensor Based on Silicon Nitride Slot Waveguide". Sens. Actuators, B. 2013. 188: 681–688.

16. M. Sieger, F. Balluff, X. Wang, et al. "On-Chip Integrated Mid-Infrared GaAs/AlGaAs Mach-Zehnder Interferometer". Anal. Chem. 2013. 85(6): 3050–3052.

17. S. Corsetti, F.M. Zehentbauer, D. McGloin, et al. "Characterization of Gasoline/Ethanol Blends by Infrared and Excess Infrared Spectroscopy". Fuel. 2015. 141: 136–142.

18. M.K. Ahmed, S. Ali, E. Wojcik. "The C–O Stretching Infrared Band as a Probe of Hydrogen Bonding in Ethanol-Water and Methanol-Water Mixtures". Spectrosc. Lett. 2012. 45(6): 420–423.

19. A.J.-C. Wilson. "The Thermal Expansion of Aluminium from 0° to 650°C". Proc. Phys. Soc. 1941. 53(3): 235–244.

20. M. Kačuráková, M. Mathlouthi. "FT-IR and Laser-Raman Spectra of Oligosaccharides in Water: Characterization of the Glycosidic Bond". Carbohydr. Res. 1996. 284(2): 145–157.

21. L.F. Leopold, N. Leopold, H.A. Diehl, et al. "Quantification of Carbohydrates in Fruit Juices Using FT-IR Spectroscopy and Multivariate Analysis". Spectroscopy. 2011. 26(2): 93–104.

22. F. Cadet, C. Robert, B. Offmann. "Simultaneous Determination of Sugars by Multivariate Analysis Applied to Mid-Infrared Spectra of Biological Samples". Appl. Spectrosc. 1997. 51(3): 369–375.

23. I.F. Duarte, A. Barros, I. Delgadillo, et al. "Application of FT-IR Spectroscopy for the Quantification of Sugars in Mango Juice as a Function of Ripening". J. Agric. Food Chem. 2002. 50(11): 3104–3111.

24. J. Wang, M.M. Kliks, S. Jun, et al. "Rapid Analysis of Glucose, Fructose, Sucrose, and Maltose in Honeys from Different Geographic Regions Using Fourier Transform Infrared Spectroscopy and Multivariate Analysis". J. Food Sci. 2010. 75(2): C208–C214.

Theory, implementation and characterization of low-frequency Laser wavelength – Cavity resonance Locking Schemes for Cavity-enhanced spectroscopy

Stefan Lindner[1], Davide Pinto[1], Harald Moser[1], Johannes Paul Waclawek[1] and Bernhard Lendl[1*]

[1]Institute of Chemical Technologies and Analytics, Technische Universität Wien, Getreidemarkt 9/164-UPA, 1060 Vienna, Austria

[*] bernhard.lendl@tuwien.ac.at

ABSTRACT: Three technical implementations for locking a laser's wavelength to an inflection point of the periodic transfer function of a Fabry-Perot cavity are theoretically described, technically implemented and characterized. A proper implementation in terms of long-term stability, noise level and fast reaction to cavity transfer function (CTF) shifts in wavelength is crucial for cavity-enhanced spectroscopy such as Interferometric Cavity-Assisted Photothermal Spectroscopy (ICAPS) and has major influence on the performance of any implementation of cavity-enhanced spectroscopy. The first technique, called constant level locking scheme, fixes the CTF inflection point detector level by a feedback loop. The 2*f*-wavelength modulation technique directly approaches the CTF inflection point. The stochastic locking scheme also directly approaches the CTF inflection point and combines advantages of 2*f*- and constant level locking. Numerically simulated as well as experimentally achieved results confirm these predictions.

INDEX HEADINGS PHOTOTHERMAL SPECTROSCOPY; FABRY PEROT CAVITY; WAVELENGHT LOCKING; GAS SENSING

INTRODUCTION

Photothermal trace gas detection employing a Fabry-Pérot cavity was introduced by Campillo et.al. in 1981[1] and was further developed and coined as Interferometric Cavity-Assisted Photothermal Spectroscopy (ICAPS) by Waclawek

et.al. from 2016 on.[2–4]. A laser with narrow emission wavelength range (quantum cascade laser, QCL) and small wavelength-modulation is focussed between the semi-transparent mirrors of a Fabry-Pérot cavity to selectifely excite an analyte gas located there. This generates a photothermal wave and the refractive index of the locally heated gas changes, what can be sensed by a probe laser. This laser is guided through the cavity, perpendicular to the semi-transparent mirror surfaces and the excitation laser beam, which it crosses in its focus. The probe laser intensity reflected by the cavity[2] follows a periodic function of the probe laser wavelength. That function is called *Cavity Transfer Function* (CTF). Via a feedback loop, the emitted probe laser wavelength, which is itself a function of the probe laser injection current and temperature, is locked to one of the inflection points of the CTF. If a change in the refractive index of the analyte gas occurs, the CTF phase shifts and a detector signal change, proportional to the phase shift and to the slope of the CTF in the point of inflection is induced. This slope reaches its maximum value in the inflection points of the CTF, what corresponds to the point of highest sensor sensitivity. To keep the cavity-enhanced sensor at its highest possible sensitivity, the CTF phase is locked to one of that inflection points.
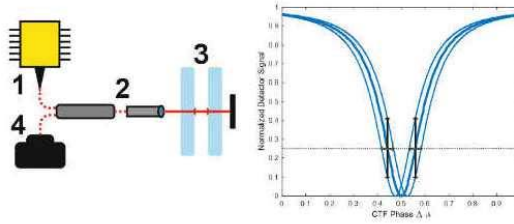

Figure 1. Left: Schematic of the LC-locking setup. 1 is the probe laser, 2 is the optical circulator and collimation lens, 3 the Fabry-Pérot cavity and 4 the detector. Right: Depiction of the effect of unwanted drifts of $\Delta\varphi$ (grey arrows) to the CTF and the sensor output signal (black arrows).

The refractive index of the analyte gas is not only dependent on the analyte gas concentration, but also on different system parameters like gas pressure and temperature[6]. Further, the phase of the CTF is not only dependent on the gas refractive index, but also on other parameters like the temperature distribution in the gas cell, the cavity is fixed into. To keep the system at highest sensitivity, the probe laser wavelength has to be constantly adjusted to correct for these unwanted drifts. This procedure, from now on it is called laser wavelength – cavity resonance locking (LC-locking), has to fulfil several requirements in terms of noise level and long-term stability. There have been published a wide range of laser frequency locking schemes like scanning transfer cavity lock methods[7,8] or the well-established Pound-Drever-Hall (PDH) technique[9], that is also used in infrared laser spectroscopy[10]. For some gas sensing techniques such as ICAPS, the LC-lock needs to have an update frequency in the

range of a few hundreds of Hz: The update frequency has to be below the double modulation frequency of the excitation laser, since otherwise the LC-lock would also compensate the wanted photothermal signal of the analyte gas. That frequency is very low compared to the frequency ranges of the LC locking techniques previously mentioned. In this work, different locking schemes were developed and characterized and compared in terms of accuracy and noise as well as long-term stability in the frequency range used in ICAPS. The setup used for those developments, is depicted in

Figure 1. The goal of LC locking in an ICAPS system is, to hold the probe laser wavelength at a value that corresponds to one inflection point of the CTF. This function describes the fraction of laser intensity, transmitted through the cavity, I_T, as a function of the phase shift $\Delta\varphi$:

$$I_T = \frac{1}{1 + \left(\frac{2F}{\pi}\right)^2 \sin^2 \frac{\Delta\varphi}{2}} \qquad (1)$$

F denotes the cavity's finesse, which is a function of the mirror reflectivity (reflectivity finesse[18]) and a shape parameter of the CTF (lorentzian finesse[18]). It is a device constant of the cavity. The actual form of the intensity measured by the detector is the product of I_T and the laser characteristics function I_0, shown in Figure 13. Further, the reflected beam, whichs intensity can be written as $I_R = 1 - I_T$ can be used for LC locking in

the same way. The phase shift $\Delta\varphi$ can be written as

$$\Delta\varphi = \frac{4\pi}{\lambda_0} nd \cos\theta \qquad (2)$$

It is a function of the refractive index n, the probe laser wavelength λ_0, which is itself a function of the laser temperature and the laser injection current as Figure 13 shows, the mirror spacing d and the angle of incidence θ, which is 0 in the employed setup. Further, the spectral distance between two peaks of the CTF is called *free spectral range* (FSR). The FSR of the cavity in the system developed in this work was experimentally determined by 1.2 nm. When a lock of the laser's wavelength to an inflection point of the CTF has to be performed, the minimum wavelength range the laser has to be able to be tuned is one FSR. Only if this is the case, the phase shift $\Delta\varphi$ of the CTF can be adjusted in a way, so that one CTF inflection point can be always accessed.

Parameter	d and θ	n and λ_0
Controlled via	Cavity temperature	Laser injection current
Tuning Speed	below 0.01 nm sec^{-1}	up to 10 nm sec^{-1}
Tuning Range	> 2 nm (1.7 FSR)	< 0.7 nm (0.6 FSR)
Application	Wide range tuning	Locking schemes

Table 1. Tuning capabilities of different parameters of the CTF phase according to equation (2).

Summarized, the CTF phase is dependent on the parameters n, λ_0, d and θ. While n carries (at a given frequency) the wanted chemical information, the other parameters have to be properly controlled to ensure stability. Long time scale and wide range drifts of $\Delta\varphi$ are mainly caused by

drifts of d and θ and are controllable by cavity temperature control. Short time scale and narrow range drifts of $\Delta\varphi$ are mainly caused by drifts of λ_0 and unwanted short-term fluctuations of n caused for instance by pressure or matrix changes in the cavity gas volume. These drifts are controlled by different LC-locking schemes, that change λ_0 via the laser injection current. The tuning capabilities of all parameters are summarized in Table 1 and discussed one by one in the following sections.

THEORETICAL SECTION

Wide range CTF phase tuning via cavity temperature control. As can be read from Figure 13, the probe laser wavelength λ_0 is not only dependent on the laser injection current, but also on the laser temperature. This property offers an easy way to tune the laser wavelength in over wide range – the tuning capability was found to be in the order of 0.1 nm per K. However, the laser chip is very small and therefor represents a very small heat reservoir. Additionally, all ohmic heat arising from the laser emission process is coming from that chip. As a consequence, a system that constantly changes the laser temperature is hard to implement in a stable way. This is the reason why the laser temperature is kept constant, what is a far easier task to fulfill in a stable way. Nevertheless, as mentioned in the introduction, a

way to perform wide-range tuning at least over one FSR (1.2 nm) is required to operate a cavity based sensor. In the system depicted in

Figure 1, this is done via temperature control of the cavity and its housing. If the temperature of the housing and the cavity is changed, micro-deformations of these components occur due to heat expansion of the material. This influences d and θ in equation (2), what further provides a way to tune $\Delta\varphi$. The cavity and its housing have a far bigger heat capacity than the laser chip, what means that their temperature is far easier to stabilize. On the other hand, this fact makes the tuning very slow. This means that the full requirements for the tuning capabilities for $\Delta\varphi$ (fast tuning AND a range covering at least one FSR) are to be met by two separate control systems: The fast, narrow range tuning is performed by LC-locking schemes that employ change of λ_0 by laser injection current control. These schemes are presented in the following section.

The influence of the cavity and housing temperature to d and θ to perform slow, wide range tuning of $\Delta\varphi$ can be understood as follows: Change of temperature causes heat expansion of the material. This leads, on the one hand, to direct change of d, and on the other hand, to change of xx due to trigonometric considerations: The cavity and its housing can only be cooled or heated from a surface. Actually, in the setup depicted in

Figure 1, this is performed by a Peltier element underneath the cavity housing. This means, in a simple model, that the heat expansion takes place on just one side while the other side is not at the same temperature. As a consequence, a tilt occurs what is equivalent to a change of θ. In reality, there is a highly complicated combination of those two effects, combined with additional effects arising from the elasticity of the glue that is used to fix and seal the cavity in the housing. Further, the heat distribution is not uniform, what makes it even more complicated to give an analytical expression of the dependence of d and θ from the cavity and housing temperature.
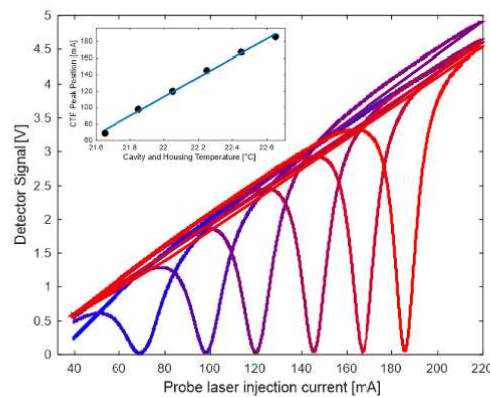

Figure 2. Temperature dependence of the CTF phase, shown by shift of the peak value. From left to right (blue to red), the CTF was recorded at temperatures from 21.45 °C to 22.65 °C in 0.2 °C steps. A slope of 116.53 mA laser injection current per K or 0.26 nm laser wavelength per K cavity temperature change has been observed.

However, it was experimentally found that this dependence is nearly linear (actually, a small second order term is recognisable), as shown in Figure 2. The tuning capability was found to be 0.26 nm per K, what means that one FSR can be covered by a cavity and housing temperature change of 4.62 K.

LC-locking via constant level scheme. The simplest LC-locking scheme is, to measure the reflected laser intensity and feed this value to a feedback loop, with the ordinate of the CTF inflection point as setpoint. In this feedback loop the laser injection current is controlled to shift the CTF phase. For that, the CTF pattern or at least the ordinate value of its inflection point has to be known. This means that this method needs to be constantly recalibrated by scanning the CTF peak, since the inflection point ordinate level will shift when the CTF phase changes (see

Figure 1, right). Nevertheless, in a system that is stabilized in terms of temperature, gas pressure and matrix composition, those phase changes are very small. They CTF phase stays in a narrow neighbourhood of the CTF inflection point, what is the linear range of the CTF. Due to its low complexity, intuitive underlying theory and because it was used in previous publications introducing ICAPS[2–4], this locking scheme serves as a benchmark.

To model this process, the wavelength characteristic of the probe laser (see Figure 13) is first approximated by a linear function

5

$$x(i) = k_\lambda \cdot i \tag{3}$$

that describes the linear dependence of the (dimensionless) laser wavelength $x(i)$ from the injection current i. In addition, the laser power, and with that, the measured detector intensity, is also dependent on the injection current. Also this dependence can be approximated with a linear function $P(i) = p \cdot i$ with proportional factor p. Linearity of both functions can be assumed, because the operation range of the LC-locking scheme is, practically limited to approximately the half width of half maximum of the CTF peak. This value is, as it can be recognised from

Figure 2, around 5 mA. The dependence of the laser wavelength from the injection current only shows negligible deviation from linearity (see Figure 13). The laser power vs. injection current function is even more linear.

Since the laser wavelength as well as the laser power can be considered as linear, the (dimensionless) laser power is proportional to the dimensionless laser wavelength x that was introduced before in equation (3):

$$P = p \cdot i = p \cdot \frac{x}{k_\lambda} =: k_P \cdot x =: P(x) \tag{4}$$

with the redefined proportional factor k_P.

For a model of the CTF, equation (1) has to be considered as follows: As described in the introduction, the laser wavelength is stabilized in the CTF's inflection point. Since the finesse F of the

cavity used in this work is 20 (and it is even higher in other published setups[3,4]), it is found $s := \left(\frac{2F}{\pi}\right)^2 \cong 162$. Employing equation (1) and setting $I_T = \frac{1}{2}$ delivers for the half width of half maximum (HWHM), and therefore for the linear range of the CTF peak in terms of φ

$$\Delta\varphi_{HWHM} = 2\sin^{-1}\frac{1}{\sqrt{s}} = 0.15 \tag{5}$$

That means, that the approximation

$$\sin x \cong x \tag{6}$$

can be used by acceptance of an error of below 0.4 %. Further, a shifting factor c is introduced to be able to analyse the CTF, without restriction of generality, in the interval [0,1]. c represents the peak position of the CTF. To sum up, under the condition that the CTF is not shifted far away from its peak value, what is fulfilled intrinsically because of the LC-lock, a reduced expression $L(x)$ for the CTF can be introduced. It is defined on the interval $[0, 1]$ and tells the fraction of light passing the cavity:

$$L(x) = \frac{1}{1 + s(x - c)^2} \tag{7}$$

With the functions P and L now the reflected probe laser detector response around the CTF peak $D_{Ref}(x)$ can be modelled as the product of the functions $P(x)$ and $1 - L(x)$[19]:

$$D_{Ref}(\mathrm{x}) := P(x) \cdot (1 - L(x)) \qquad (8)$$

For the transmitted intensity, $1 - L(x)$ is replaced by $L(x)$. The CTF peak for the cavity used in the employed setup is very narrow (around 60 pm of HWHM). This leads to a second approximation that can be done: In a close neighbourhood of the peak, the laser power vs injection current function $P(x)$ is nearly a constant (linearity, see Figure 11). Using this fact allows to replace $P(x)$ in equation (8) by the proportional factor k_P introduced in equation (4), so that the detector response can be simplified to

$$\widehat{D_{Ref}}(\mathrm{x}) := k_P(1 - L(x)) \qquad (9)$$

To calculate the position of the inflection points the second derivative of $\widehat{D_{Ref}}$ is found by

$$\frac{\partial^2}{\partial x^2}\widehat{D_{Ref}}(\mathrm{x}) = 2sk_P\left(\frac{1}{(1 + s(x - c)^2)^2} - \frac{4s(x - c)^2}{(1 + s(x - c)^2)^3}\right) \qquad (10)$$

Since the slope factor $s = \left(\frac{2F}{\pi}\right)^2$ is always positive and because the finesse is a positive quantity, it can be seen, that all denominators in this expression are bigger than zero at any time. That means, that the equation $\frac{d^2}{dx^2}\widehat{D_{Ref}} = 0$ can be multiplied by $\frac{(1 + s(x-c)^2)^3}{2sk_P}$ and finally, for x it is found

$$x = c \pm \frac{1}{\sqrt{3s}} \qquad (11)$$

This matches to previously published results of analysing lorentzian signals, where the case $c = 0$ and $s = 1$ was considered[20].

LC-locking via 2f-WM scheme. More difficult is the 2f-WM approach. The basic principle is to add a small sinusoidal modulation to the probe laser injection current and demodulate the detector signal at the second harmonic. This signal is zero (for small modulation amplitudes, as will be shown later), if the DC value of the laser injection current corresponds to the abscissa value of the CTF inflection point. This is a big advantage of the 2f-WM technique compared to the constant level locking scheme. This zero-condition is not dependent on any quantity that cannot be accessed during locking scheme runtime, as it is the case for the CTF inflection point ordinate value when employing the constant level lock.

For definition of a function that describes the modulation, the circular frequency $\omega = 2\pi f$ with the modulation frequency f, and the modulation depth m is introduced. With this, it can be defined in terms of the already introduced dimensionless wavelength x (equation (3)):

$$M(x) := m \sin \omega x \qquad (12)$$

A general expression for describing the modulation is the modulation index

$$m_i = \frac{x_m}{x_{HWHM}} \qquad (13)$$

with x_{HWHM} the HWHM of the CTF peak. x_m denotes the modulation amplitude m projected on the x axis. m_i is a dimensionless quantity describing the modulation independent from the form of the CTF peak.

The measurement of mi is done by measurement of the injection current over a small period of time (1000 periods – 0.25s). While x_{HWHM} is determined by direct measurement of the unmodulated reflection peak width (x_{HWHM} was found by 4.78 mA in the used setup), x_m is determined by

$$x_m = \sigma_x \cdot \sqrt{2} \qquad (14)$$

what follows from the general relationship between amplitude and mean value of a sine function. σ_x can be measured by the current monitor output of the laser.

To find an expression for the position of the CTF inflection point, again the reflected detector intensity function on the interval $[0, 1]$ is modelled. Therefore, equations (8) and (12) are combined and for the modulated probe laser detector response $D_{Ref,M}(x)$ it is found

$$D_{Ref,M}(\mathrm{x}) := (P(x) + M(x)) \\ \cdot \big(1 - L(P(x) + M(x))\big) \qquad (15)$$

Again, this expression is simplified by approximations. Additionally to the approximations done in the constant level lock section, the fact, that the applied modulation only has an effect around the CTF peak is used. This means, that for the power-term (first bracket in equation (15)) the modulation term can be neglected and as simplified detector response function $\widehat{D_{Ref,M}}(x)$ it is found

$$\widehat{D_{Ref,M}}(x) \\ = 1 - \frac{1}{1 + s(x + m\sin\omega x - c)^2} \qquad (16)$$

The demodulation process done by an Lock-In-amplifier has been modeled analytically already by Arndt[20] and Kluczinski[19]. An easier way to model this process is, to multiply the detector signal by a sine (X-value) or cosine (Y-Value) of the desired frequency (2*f*) and average this product over one period, which implements a simple low-pass-filter. This process was simulated in MATLAB. This simple model could reproduce the known fact, that with increasing modulation depth, the 2*f* peak broadens. In Figure 3, simulated results for different modulation indices m_i are shown. The inflection point distance has been calculated by use of equation (11) by $x_{Inf} = \pm 2 \cdot \frac{1}{\sqrt{3s}} = \pm 0.0365$, what is in good agreement with the simulations – the maxima of the first derivative of the unmodulated CTF, shown also in Figure 3 are at that position.

The 2*f*-WM locking scheme offers an universal set point in the following sense: The condition of the 2*f* amplitude being zero at the inflection point

of the CTF is, under the assumptions made before, independent on the probe laser operating parameters, especially on the injection current. The only limiting factor is, that the modulation index has not to be too high in order to keep the error between the $2f$ zero crossing and the actual inflection point of the underlying CTF low enough, so that the wavelength is locked to a point within the linear range of the CTF. Since the $2f$ zero crossing – inflection point error follows a defined behavior (see Figure 10 C), a correction model can be implemented that is only dependent on the (known) modulation index. If the CTF phase shifts during runtime of the setup, the $2f$ locking scheme corrects this shifts automatically, since the condition of a $2f$ amplitude of zero is universal. This self-calibrating property of the $2f$ locking scheme is a big advantage compared to the Constant Level locking scheme, where shifts of the CTF have to be corrected by (the measurement interrupting) recalibrations.
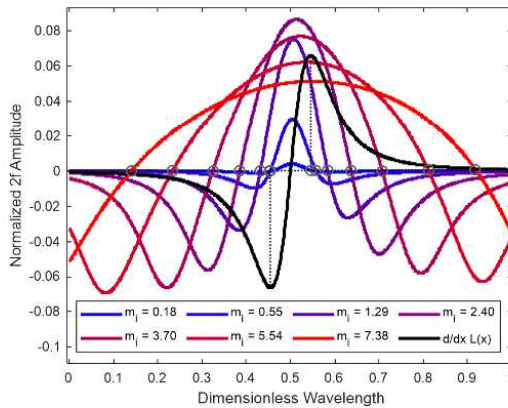

Figure 3. Simulated $2f$ amplitude spectra with different modulation indices m_i, in comparison with the second derivative of the CTF. The specific values of m_i were chosen in order to use the same values as found in the experiment (Figure 11).

LC-locking via stochastic scheme. For derivation of this scheme, it is started again with the detector signal response from a detector measuring the reflected beam of a modulated probe laser, which is given in equation (15). The mean of measured detector signal over a constant period of time (that piece of raw signal is called "block") follows the cavity transfer function while the standard deviation of this block follows the absolute value of the $2f$ output. This behavior was the motivation to investigate also higher moments of the deviation of these blocks. It was found, that the zero crossing of the block's 3rd moment (skewness, γ) values also indicates the CTF inflection point and, for that reason, can be used as a process variable of a feedback loop to lock the laser to the CTF inflection point.

This can be understood as follows: The skewness γ of a dataset is the third moment of the underlying distribution:

$$\gamma = E\left(\left(\frac{X - \mu}{\sigma}\right)^3\right) \tag{17}$$

where X is a stochastic variable. In the present case, X represents the CTF ordinate values of a set of values of dimensionless wavelength x distributed symmetrically around a center value μ

with standard deviation σ. Since just the zero crossing is from interest, the (normalizing) influence of σ can be neglected. As a first step, in the sense of an inductive proof, one set of 3 values for x is considered. The validity of the statement will be extended to a countable infinite number of such sets in a second step. Since the values of the considered set are symmetric, they can be defined by

$$x_1 = u - \varepsilon; \quad x_2 = u; \quad x_3 = u + \varepsilon \qquad (18)$$

with $\varepsilon > 0$. According to the definition of the stochastic variable X given before, the values of X are the CTF values $L(x_1)$, $L(x_2)$ and $L(x_3)$. The skewness defined in equation (17), is zero, if the underlying set of values is symmetric (what corresponds to the intuitive interpretation of "skewness" – skewness of zero means symmetry). In the case of three points, this is fulfilled, if the center value is the mean of the three values:

$$\mu = \frac{1}{3}\left(L(x_1) + L(x_2) + L(x_3)\right) = L(u) \qquad (19)$$

To find such a value u, the equation

$$L(x_1) - L(u) = L(u) - L(x_3) \qquad (20)$$

has to be solved. By solving equation (20) it is found for u

$$u = \pm \frac{\sqrt{s\varepsilon^2 + 1}}{\sqrt{3s}} \qquad (21)$$

Since ε was just the (small) distance between the chosen values for x, for small values of ε, it is found $u = \pm \frac{1}{\sqrt{3s}}$, what was found to be the x-value of the inflection point of the CTF in equation (11). Figure 4 A shows a graphic depiction of this situation.
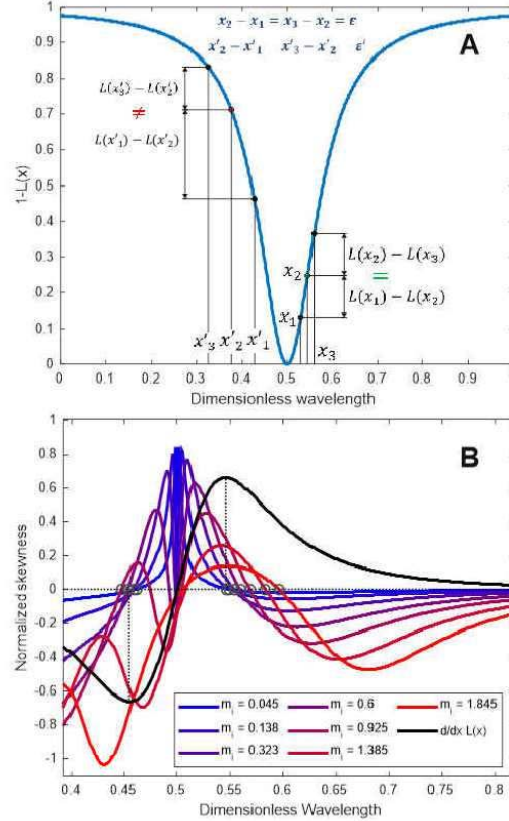

Figure 4. A: Graphic depiction of the inflection point defining condition (20). On the left flank, it is fulfilled and x_2 is the inflection point. On the left flank, it is not fulfilled, x'_2 is no inflection point. B: Simulated skewness amplitude spectra with different modulation indices m_i.

In the second step it has to be proven, that the result holds not only for a single triplet of points, but also for a countably infinite number of triples $\left(x_i^1, u, x_i^3\right) = (x_i + \varepsilon_i, u, x_i - \varepsilon_i)$ with $\varepsilon_i > 0$ small $\forall\, i \in \{1, \dots, n+1\}$. In the sense of an inductive proof, it remains to show, that if for a number of n of these triples the derivation of equations (19) to (21) holds, it does so also for a number of $n+1$ triplets. This is actually true: Since every single of the $n+1$ triples holds equation (19), also the mean of all $n+1$ triples is $L(u)$. The equation to solve is now

$$\sum_{i=1}^{n+1} L\left(x_i^1\right) - L(u) = \sum_{i=1}^{n+1} L\left(x_i^3\right) - L(u) \quad (22)$$

Since we know from the inductive assumption, that this equation fulfills $u = \pm\dfrac{\sqrt{s\varepsilon^2+1}}{\sqrt{3s}}$ because of the properties of the ε_i, it remains to show this fact for $L\left((x_{n+1}^1\right) - L(u) = L\left(x_{n+1}^3\right) - L(u)$, what is the case because of $u = \pm\dfrac{\sqrt{s\varepsilon_{n+1}^2+1}}{\sqrt{3s}}$.

In Figure 4 B a MATLAB simulation of the skewness as function of the generalized wavelength x is depicted. The result can also be found by using an integral over a range of values of x instead of a countably infinite number of triples. The approach is sketched in the appendix. When taking into account that an ICAPS system operates digitally by finite sampling frequency of the utilized DAQ-devices it is clear, that the countably infinite case is enough to describe the prob-

lem. Since just symmetry of the values of x was used, the use of the skewness as process variable for a locking scheme is not restricted to sinusoidal modulation as long as symmetric distribution around the modulation interval center is kept.

Similar to the 2f locking scheme, the condition of a skewness of zero that indicates the CTF inflection point, is universal. It is independent on the probe laser injection current and makes the stochastic locking scheme in this sense self-calibrating. One advantage of the stochastic locking scheme compared to the 2f-WM scheme is, that additionally to that, the skewness condition is not dependent on phase variations. This would also be the case if the total amplitude (R-value) of the LIA would be used for 2f-WM locking as a process variable, but this quantity does not show a zero crossing of uneven parity.
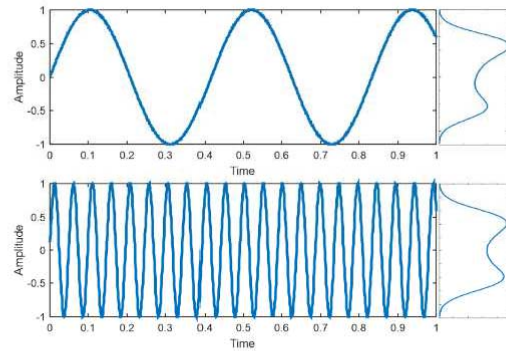

Figure 5. Effect of higher frequency on dataset symmetry. The flipped graph left of each sine is the empirical density function of the Amplitude values – the higher the frequency is, the more symmetric it is. As long as the frequency is high enough and the underlying waveform is symmetric,

also the amplitude values are symmetric and therefor meet the requirements for stochastic locking scheme.

In a practical implementation, high frequency modulation with a frequency just slightly below the Nyquist limit of the used DAC and ADC devices meets this requirements best. This becomes clear by a simple statistical consideration: While dividing a low-frequency (periodic) discrete waveform in parts of equal size, the symmetry of data points in these blocks is heavily dependent on the starting and ending point of the block. This is not the case for a high-frequency waveform: if the block length is far bigger than one period of the modulation waveform, the influence of the starting and ending position gets negligibly small. The situation is depicted in Figure 5.

This means that the modulation frequency of the stochastic LC-locking scheme can be pushed very close to the Nyquist limit, since only symmetry is required. This is an advantage of the stochastic locking scheme compared to the 2*f*-WM locking scheme: Since there a sinusoidal (harmonic) waveform has to be properly sampled by the digital-analog-converter (DAC), the maximum frequency that can be used for modulation is far below the Nyquist limit.

The fact, that the stochastic locking scheme requires only symmetry leads to a further advantage compared to the 2*f*-WM locking scheme: The modulation is not limited to harmonic (single frequency sinusoidal) waveform. This leads to

the following consideration: Due to the previously discussed nature of the skewness function, its "Quality" in the sense of big amplitude and low noise is higher, the higher the variance of the wavelength points within one period of the modulation waveform is. This means, that the ideal case would be, if half of the points are in a finite interval on the right, and the other half in a finite interval on the left edge of the modulation interval. Further, also a Gaussian distribution fulfills the requirement of symmetry – besides the fact, that a gaussian distributed stochastic variable has its majority of values around the center value. This is exactly contrary to the discussed ideal case, but in principle this means, that even (gaussian distributed) noise can be used as modulation waveform. Figure 6 shows simulated skewness amplitude spectra for different waveforms of modulation index $m_i = 0.2$.
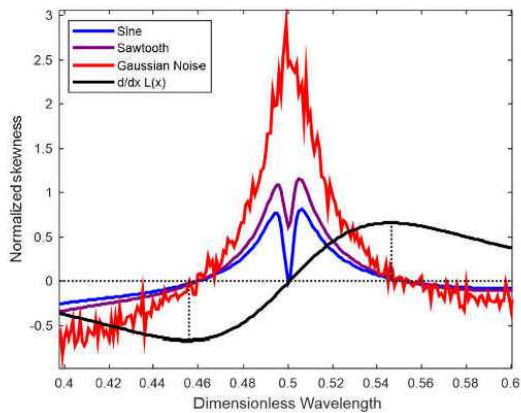

Figure 6. Skewness functions resulting from different modulation waveforms

Another interesting, but in the current paper technically not exploited feature of the skewness function is, that also the minimum of the CTF can be recognized by the condition of a skewness of zero. This becomes clear, when again considering symmetry: also any (gaussian or lorentzian) peak is (locally) symmetric, what corresponds to a skewness of zero. As it can be recognized from Figure 4, the peak of the skewness function not only decreases in width for decreasing modulation depths, but is for small modulation depths far narrower than the peak of the CTF itself. This means, that the skewness function can, besides the feature of finding the CTF's inflection points, be used for a very precise and accurate recognition of the CTF peak position.

EXPERIMENTAL SECTION

Instrumentation and Materials. The Setup including the ICAPS part is depicted in Figure 7. The instruments used in the Setup are listed in Table 2. Nitrogen in 5.0 purity level was purchased from Messer Industriegase GmbH, 65812 Bad Soden, Germany. 1000 ppm and 10000 ppm CO_2 in nitrogen 5.0 test gas mixtures for ICAPS were purchased from Air Liquide Austria GmbH, 2320 Schwechat, Austria.
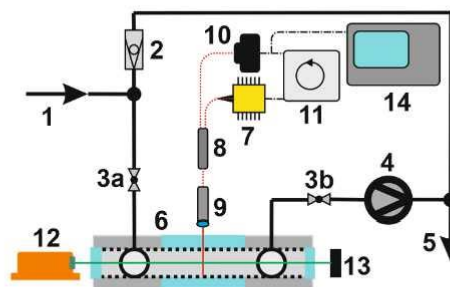

Figure 7. Schematic of the entire setup, including ICAPS spectrometer beam path. The dashed red lines depict fiber optics, the solid red and green lines free space laser beams. The solid black lines depict gas tubings, the dashed black line electronic connections. All instruments are listed in Table 2.

No.	Instrument	Manufacturer	Type/Model
1	Gas inlet	Parker	PU Tubing
2	Overpressure valve	Parker	1 bar
3	Pressision valves	Hoke	Needle valve
4	Scroll Vacuum Pump	Scroll labs	Miniature Scroll pump
5	Gas outlet	Parker	PU Tubing
6	Gas cell with cavity	custom	Aluminium housing, cavity SLS optics, F = 20
7	Probe Laser	Emcore	1782B-NM-050-34-FC-PM; fiber coupled butterfly packaged, 1550nm
8	Optical circulator	Thorlabs	CIR1550PM-EC; PM-fiber coupled, FP/APC connector
9	NIR detector	Thorlabs	PDA-10CS; preamplified InGaAs photodetector
10	GRIN collimator	Thorlabs	15-1550-PM-APC; PM-fiber coupled
11	Feedback loop	custom	custom electronics and LabView based software
12	ICAPS Excitation laser	Alpes Lasers	QCl, 4363.95 nm center-wavelength, 100mW
13	Beam dump	custom	eloxated aluminium
14	Spectrum Analyser	Rohde & Schwarz	FSC-4; 10 Hz to 4 GHz frequency range
x	FTIR-Spectrometer	Bruker	Vertex 80V
x	Laser power meter	gentec-eo	Solo 2 laser power meter

Table 2. List of Instruments. The numbers in the first column refer to Figure 7. The last two instruments were not used in the setup, but for acquisition of the data for Figure 13.

Characterization of LC-locking schemes by process variable signal to noise ratio. All three introduced locking schemes have in common, that they are based on a proportional control feedback loop. A process variable is measured and afterwards subtracted from a setpoint. This value is multiplied by a proportional factor P that has to be calibrated (the optima are listed besides other parameters in Table 3). The probe laser in-

13

jection current DC component is then corrected by this product. The update frequency of this feedback loop can be freely chosen, theoretically limited only by the computer hardware. A technical limitation is, that the update frequency must not be in the range of the excitation laser frequency, what would lead to cross talking effects. Since the update frequency of the feedback loop is very low (10 to 30 Hz), this is not a practical problem.

Property	Constant Level	2f-WM	Stochastic
Calibration	periodic recalibration	self-calibrating	self-calibrating
Process variable	Detector DC level	2f amplitude	skewness
Setpoint	relative, 1/4 of CTF peak height	absolute, $X(2f) = 0$	absolute, $\gamma = 0$
Modulation frequency	none	$f \ll f_{Nyquist}$	$f < f_{Nyquist}$
Modulation waveform	not applicable	harmonic (sin)	symmetric
Phase dependency	not applicable	yes	no
Value of P	0.1	2	0.2

Table 3. Overview of the introduced locking schemes and their operating parameters

Detector DC level (Constant Level Lock), $2f$ amplitude ($2f$-Lock) and skewness (Stochastic Lock) were measured, while the injection current was slowly tuned over the Fabry-Pérot reflection profile. Additionally, the injection current was modulated sinusoidally with a frequency of 4463 Hz. As Figure 8 shows and it is expected from theory, the position of the skewness and $2f$ zero crossings match with the positions of the CTF inflection points.
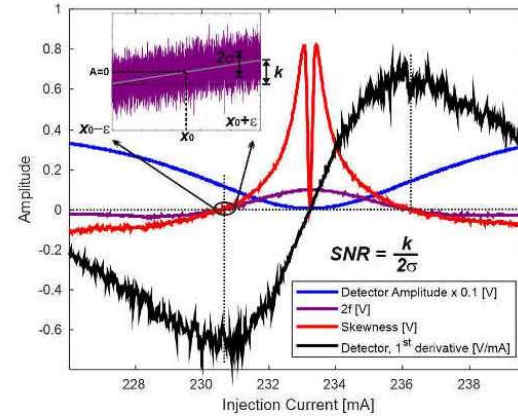

Figure 8. Injection current scan over one reflection mode of the Fabry-Pérot cavity in the setup. All relevant LC-locking process variables recorded simultaneous (modulation index $m_i = 1.29$). For getting the unmodulated Detector voltage in the same measurement, the Detector amplitude values were averaged over 1000 datapoints (see Figure 5 for explanation)

To compare the two process variables in terms of suitability for the locking process, the signal to noise ratio (SNR) in the locking position has to be defined and compared. The SNR for the locking procedure can be defined as depicted in Figure 8: in a neighborhood of the locking position, corresponding to one modulation amplitude in terms of injection current, the local process variable is fitted by a linear function. The residuals of that function can be understood as noise, while the slope of the function can be interpreted as signal (the higher the slope of the process variable in the locking position, the more precise it can be locked). Division of both quantities lead to the SNR, what is summarized in Table 4.

Process Variable	2σ	k	SNR
Detector Amplitude	0.2213	0.6528	2.95
$2f$-Amplitude	0.0034	0.0306	9.11
Skewness	0.0062	0.0581	9.36

Table 4. Comparison of LC-locking process variables

The SNR of both techniques is in the same order of magnitude. For the skewness is slightly better. What is also to mention, is that the SNR reaches its maximum at the zero crossing position for the $2f$ function. This is actually not true for the skewness function – The maximum SNR for the skewness is reached closer to the center peak. It reaches a value of 57.0, what means that by implementing a corresponding correction algorithm, the skewness function offers a precision level one order of magnitude higher than the $2f$ function.

Characterization of LC-locking schemes by noise power density spectra. For characterization of the developed implementations of the different locking schemes, a nitrogen flow of 200 ml min^{-1} and a pressure of 200 mbar in the gas cell was set. The setup is depicted in Figure 7. The most important characterization is the noise behavior in locked condition. Therefore, noise spectra in a frequency range of 0 to 1 and 10 kHz were recorded while the lock was active and the gas cell was under constant pressure and gas flow. To be able to compare these results to a measurement, where no lock was active, also noise spectra of the unlocked system were recorded. Therefore, the laser injection current was tuned off the cavity resonance profile and was

kept constant at this value. Just the modulation of the $2f$ locking scheme has been added to show also the behavior of in the range of the modulation frequency peak. Figure 9 shows the noise power density spectra in two relevant frequency ranges. Frequencies below 1 kHz are used for ICAPS excitation laser modulation, such below 10 kHz are used for probe laser modulation employing the $2f$ locking scheme.

In order to minimize cross talking effects between probe laser and excitation laser modulation, those two frequencies have to be as far away from each other as possible and, additionally, be relatively prime to each other.

In order to keep the setup simple und small, a software-based LIA with a partially in-house developed LabVIEW based code has been employed. In case of the device used in this setup, a limit of usable probe laser frequency was found around 5 kHz and was actually chosen by 4463 Hz. For the stochastic locking scheme, the modulation frequency can be choosen even higher – here, the limit can be pushed close to the Nyquist limit of the ADC without further restrictions, as described in the theory section.
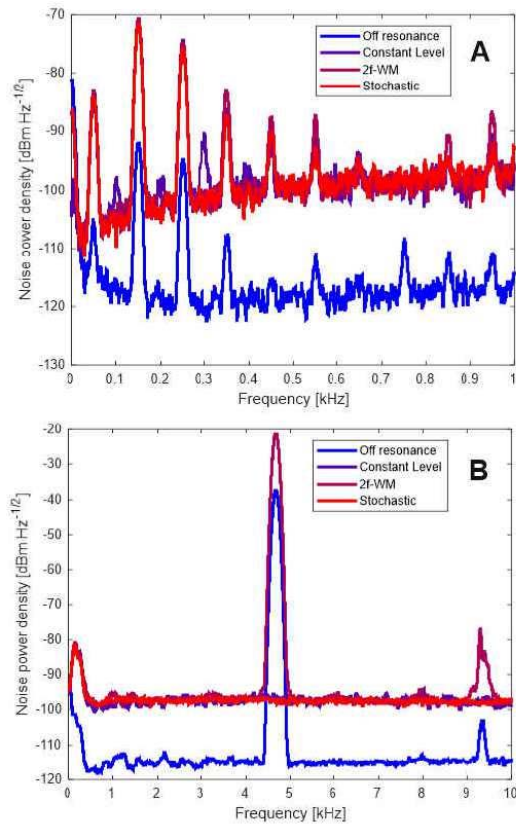
Figure 9. Experimental results for noise power density spectra. A Frequency range 0 to 1 kHz, 10 Hz Bandwidth. B Frequency range 0 to 10 kHz, 100 Hz Bandwidth.

This offers a wider range of possible modulation frequencies and therefore a bigger distance between probe and excitation laser frequency. The frequency for the stochastic lock was actually chosen by 10673 Hz.

The peaks around 50, 150 and 250 Hz in Figure 9 A are intrinsically coming from the laser driver – they remain observable when the laser is operated without any digital control – but do not represent an impact on the ICAPS measurement, since the excitation frequency can be chosen between these unwanted frequencies.

The observed difference in noise of 20 dBmHz$^{-1/2}$ between locked and unlocked condition matches with the factor of slope increase between the injection current – detector intensity function of the laser characteristics and the CTF in the inflection point, what is a factor of around 10.

The noise power density level of all developed LC-locking schemes, is comparable. To quantificate the differences between the developed schemes, we calculated mean and standard deviation of the noise power density in frequency ranges of 1 to 4 kHz and 70 to 120 Hz. The results are given in Table 5.

Scheme	70...120 Hz		1...4 kHz	
	Mean	Std. Deviation	Mean	Std. Deviation
Laser direct	-116.84	1.17	-114.93	0.96
Constant Level	-103.44	2.67	-97.58	0.86
2*f*-WM	-104.83	1.17	-96.75	0.67
Stochastic	-105.63	1.19	-96.57	0.75

Table 5. Noise power density levels of the three developed LC-locking schemes

Characterization of LC-locking schemes by set point accuracy and dynamic behavior. To measure the tuning capabilities in terms of set point accuracy and the dynamic operation, if any environmental change of the CTF phase occurs, the gas flow in the cell was changed from 200 to 1000 ml min^{-1} and vice versa. This was done while all three process variables (Detector DC, 2*f* amplitude and skewness) were recorded but only one LC-locking scheme was active. The gas flow

change causes a small pressure change in the gas cell which itself causes a small change in refractive index and therefor, in the CTF phase. This simulates an environmental change of the CTF phase, as it can be caused for instance by an unexpected change of the gas matrix in an ICAPS measurement. The reaction of any locking scheme to that "impact" has to be analyzed in order to describe its dynamic behavior and in order to show, that the set point is able to be stabilized.

In principle, also the tuning the speed of the locking scheme could be analyzed in this way by measuring the time it takes, until the process variable is back at the set point after an impact. Since this speed can be freely adjusted by the P values described in Table 3, there is no characterization necessary. In Figure 10 , three of the previously described measurements are shown: in A, the Constant Level locking scheme was active, in B the $2f$-WM scheme and in C the stochastic scheme. Additionally to all three process variables (Detector DC level, $2f$-amplitude and skewness), the laser injection current was recorded. Since the laser temperature is constant, this quantity is proportional to the laser wavelength. In order to analyze the dynamic behavior, all quantities were normalized by division by the standard deviation of the corresponding timeline. Additionally, since those two quantities are not zero, the injection current and the detector DC level

timelines are centered by subtraction of the mean. The results demonstrate the features of the different locking schemes described in the theory section as follows:

In Figure 10 A, where the Constant Level locking scheme is active, the 2f and the skewness amplitude have no meaning, since there is no modulation. They follow a standard gaussian distribution. The detector DC level and the injection current shows the biggest weakness of the Constant Level Locking scheme: While the detector DC level reaches the same level after the impact as it hat before, this is not true for the injection current and therefor for the laser wavelength. This means, that the CTF has (slightly) shifted in phase, what was the locking scheme is not able to recognize. Since the laser wavelength is the only accessible quantity for this scheme, all the CTF phase shift, independent from its contributing origins, is corrected just by the laser injection current. The situation is different for the self-calibrating schemes ($2f$-WM and Stochastic scheme, Figure 10 B and C). Here, the 2f and the skewness amplitude represent the shift of the CTF from its inflection point. Both quantities therefore are a direct measure of the CTF phase shift. The locking scheme keeps this phase shift at zero – it stabilizes the CTF inflection point.
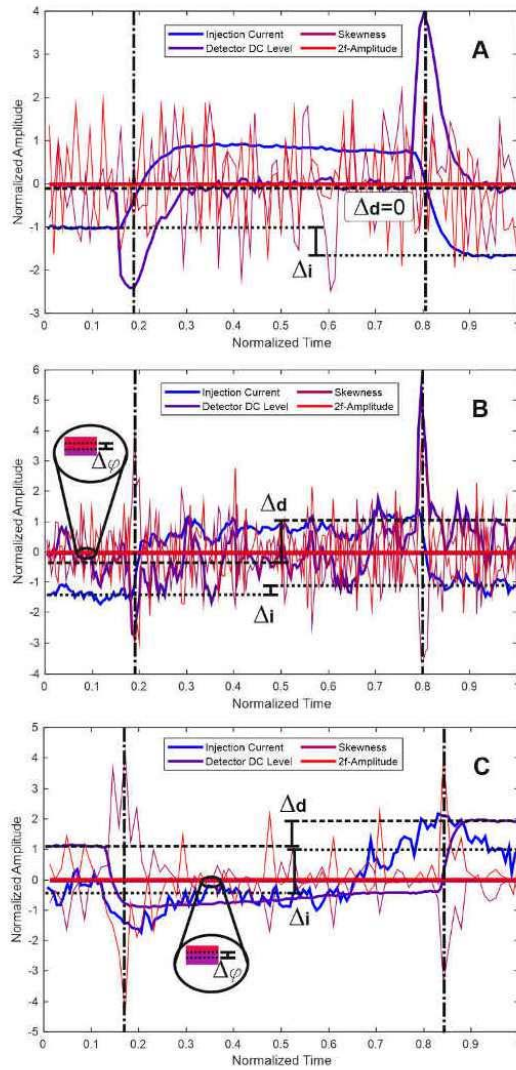
Figure 10. Experimental results for the dynamic behavior characterization. The LC-locking was performed by one specific locking scheme: **A** Constant Level scheme, **B** $2f$-WM scheme, **C** Stochastic scheme.

In contrast to the Constant Level locking scheme, the $2f$- and the stochastic scheme indirectly also recognize the changing laser power, if the laser wavelength is tuned in order to keep the system at the CTF inflection point. The "load" of CTF phase correction is now divided between the detector DC level (corresponding to the laser power) and the laser wavelength (represented by the injection current). Another detail is the mean of the $2f$ and the skewness amplitude. Since the $2f$ amplitude is dependent on the Lock-In-amplifier reference phase, and this can also change, there is a small difference in the mean of the $2f$ and the skewness amplitude. While the skewness amplitude is stabilized to zero in the stochastic locking scheme, the $2f$ amplitude can be slightly off zero and vice versa for the $2f$-locking scheme.

RESULTS AND DISCUSSION

Experimental Determination and comparison of the zero crossing position of $2f$ and skewness functions. The results of the simulation described in the theory section (Figure 3 and Figure 4 B) were experimentally confirmed. Therefore, the probe laser was modulated by different modulation indices and the 2f- as well as the skewness amplitude was measured. To get a high data resolution, what is important especially for the skewness data in the range of the narrow center peak, the corresponding injection current ramps were performed very slow (1 mHz).
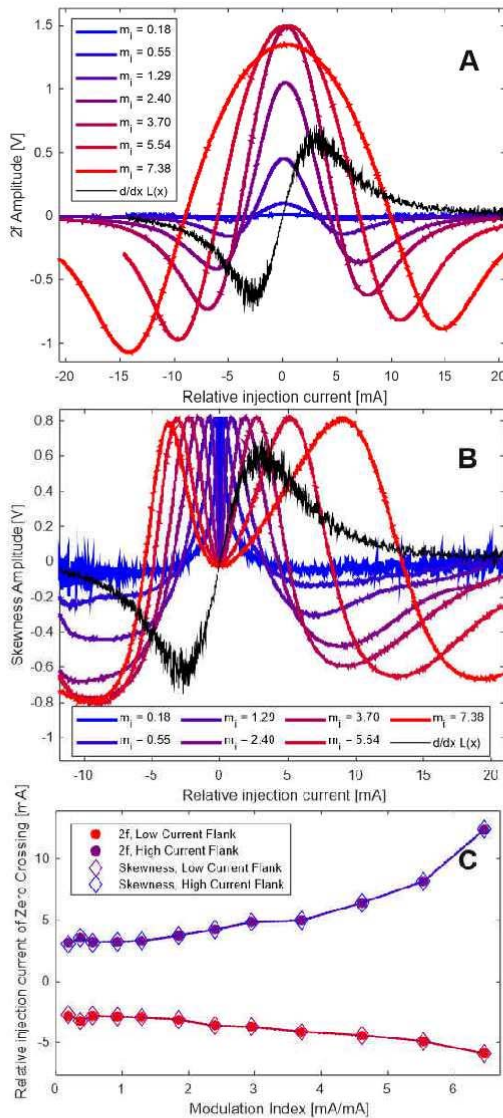
Figure 11. Measured $2f$-WM (A) and skewness (B) patterns with different modulation indices m_i. C Behavior of the zero crossing position of the measured $2f$ and skewness functions.

The time required for all measurements therefor is so long, that long-term drifts of the CTF phase occur.

This practical problem can be resolved by post-processing alignment of the center peaks of the $2f$ and skewness functions, since the (relative) zero crossing position and not the absolute CTF phase is from interest. The results for the $2f$-amplitude vs. injection current functions are depicted in Figure 11 A. Figure 11 B shows the results for the skewness vs. injection current functions.

It can be recognized, that the zero crossing positions, both on the left as well as on the right flank of both functions follow a defined trend. Figure 11 C shows this trend for the measured data at practical relevant low modulation indices. It can be recognised, that the trend for both variables very well overlapping. The asymmetry of the zero crossing position between left and right flank can be explained by the real form of the CTF pattern, recognizable from Figure 2. Because of the linear power-current characteristics of the laser, shown in Figure 13, there is a local maximum left to the Fabry-Pérot minimum.

Knowledge about the modulation index vs. zero crossing position trend can be used for implementation of a correction model for the zero crossing position to ensure, that inflection point of the CTF is approached also for higher modulation depths.

Recording of an ICAPS spectrum. Sensing of carbon dioxide, especially the ability of discriminating ^{12}C and ^{13}C carbon dioxide is from high interest for breath gas analysis[11] or monitoring of atmospheric CO_2[12]. Several methods for sensing ^{12}C and ^{13}C carbon dioxide in the field of mid-infrared spectroscopy have been published[13–15]. In our work we employ the $\Sigma_u^+ \leftarrow \Sigma_g^+$ transition of $^{12}C^{16}O_2$ (00^10-00^00) at 2291.5445 cm^{-1} [16] and the $\Pi_g \leftarrow \Pi_u$ Transition of $^{13}C^{16}O_2$ (01^11-01^10) at 2291.6712 cm^{-1} [17] for ICAPS measurements to demonstrate the performance of the system we developed.

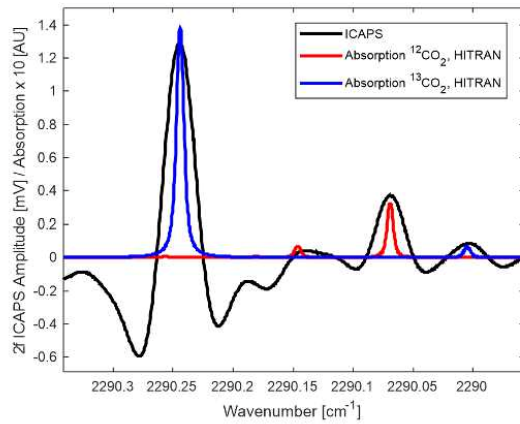**Figure 12.** $^{12}CO_2$ and $^{13}CO_2$ ICAPS spectrum around 2290.15 cm^{-1} in comparison with an absorption spectrum of the same molecules (HITRAN)

To record an ICAPS spectrum, the emitted wavelength of the excitation laser is slowly tuned (mHz range) by letting the injection current follow a low-frequency saw tooth wave. Additionally, to apply the 2f-wavelength modulation (2f-WM) technique, the probe laser wavlength is modulated with a higher frequency (typically few hundreds of Hz) sine wave of low amplitude. The detected probe laser signal is afterwards demodulated at the second harmonic of this modulation frequency[5] to extract the ICAPS signal. The ICAPS Setup used in this paper is depicted in Figure 7. As a showcase, $^{12}CO_2$ and $^{13}CO_2$ in a wavenumber regime between 2290 and 2290.3 cm^{-1} was measured. Figure 12 shows a typical ICAPS spectrum, measured by 2f-locked cavity in comparison with a HITRAN-Database absorbance spectrum. For the ICAPS demodulation, a time constant of 3 seconds was used. The QCL was modulated by 1.2 mA injection current modulation depth, what corresponds to a wavenumber modulation depth of 0.048cm^{-1}.

CONCLUSIONS AND OUTLOOK

In this paper, a theoretical background of a laser wavelength-cavity-locking schemes in the low frequency range was presented. The performance, the potential and the limits of constant transfer function level locking and 2f-WM locking was discussed. Further, a novel LC locking scheme, employing generalized modulation and higher stochastic moments, was presented. Its theoretical background was described simulated and and underlayed with real-world measured data confirming its competitive performance. All discussed locking schemes were compared in terms

of accuracy, noise and tuning speed. As a showcase, a $^{13}CO_2$ ICAPS spectrum was presented and compared to a HITRAN database spectrum.

The generalization of $2f$ modulation technique described in this paper offers some further options that can be investigated in the future. One of them is, to consider different distribution functions for modulation and to take advantage on their special form. One approach is, to measure the noise characteristics of the system and afterwards implement an inverse noise characteristic as modulation function to perform a new approach to active noise cancelling. Also, in analogy to the use of higher harmonics in wavelength modulation spectroscopy, the potential of higher stochastic moments for demodulation can be investigated. The results achieved with the 3rd moment as demodulation operator compare well to $2f$-WM results.

APPENDIX

Characterization of the probe laser emission. The probe laser shows, in first approximation, linear dependence of the emitted wavelength and power from the laser injection current. The CTF peak is very narrow (HWHM of 4.78 mA), so that this linear approximation is fulfilled locally (+/- 12.5 mA) in a range of two times the HWHM by an error of just 0.35 mW (0.51 %) for the power and 0.0022 nm ($1.4 \cdot 10^{-4}$ %) for the

wavelength.
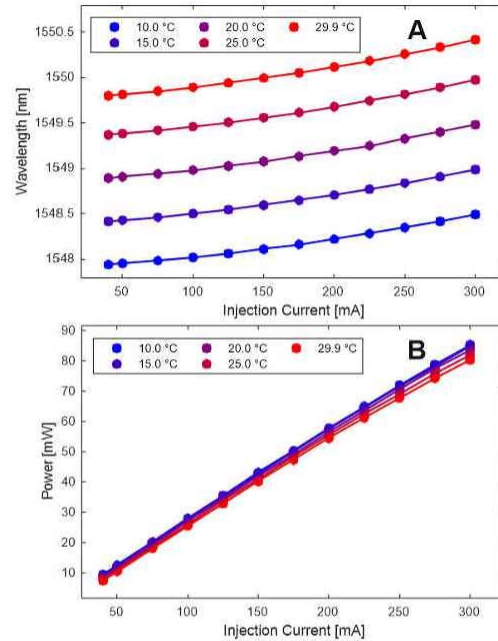
Figure 13. Measured wavelength (**A**) and power (**B**) emission spectra of the probe laser at different laser temperatures.

Figure 13 shows the measured data. By fitting the laser wavelength and power in dependence of the laser injection current and power with a bilinear function, slope factors of 0.0022 nm mA^{-1} and 0.0953 nm K^{-1} were found.

Integral version of skewness condition for inflection point identification. Instead of defining three points as done in equation (18), also the area under the CTF can be considered, what corresponds to a consideration of an infinite number of points. A symmetric interval of x values with

length 2ε surrounding a given value u is considered. Then for the mean of this interval it is found

$$\mu = \frac{1}{2\varepsilon} \int_{u-\varepsilon}^{u+\varepsilon} L(x)g(x)dx \qquad (23)$$

The function $g(x)$ is a weight function that describes the distribution of underlying x values. Since this distribution has to be uniform, $g(x)$ is a constant function and $g(x) = 1$ can be chosen without restriction of generality, since just the zero crossing is interesting. This leads to

$$\mu = \frac{1}{2\varepsilon} \int_{u-\varepsilon}^{u+\varepsilon} \frac{1}{1+sx^2} dx$$
$$= \left[\frac{1}{2\varepsilon\sqrt{s}} \tan^{-1}(x\sqrt{s}) \right]_{u-\varepsilon}^{u+\varepsilon} \qquad (24)$$

Since $s(u^2 - \varepsilon^2) > -1$ is fulfilled for a sufficiently small value of ε, $\tan^{-1} a - \tan^{-1} b = \tan^{-1}\frac{a-b}{1+ab}$ can be used and with $\tan^{-1} x \approx x$ it follows

$$\mu \approx \frac{1}{1+s(u^2-\varepsilon^2)} \qquad (25)$$

For the (unnormalized) skewness, it is found

$$\gamma = \frac{1}{2\varepsilon} \int_{u-\varepsilon}^{u+\varepsilon} \left(\frac{1}{1+sx^2} - \mu \right)^3 dx \overset{!}{=} 0 \qquad (26)$$

This leads to bulky algebraic expressions which can be, by use of the fact that ε is small and for small arguments of the inverse tangent function it holds $\tan^{-1} a - \tan^{-1} b = \tan^{-1}\frac{a-b}{1+ab}$, reduced to an algebraic equation for μ:

$$-\mu^3 + \frac{3}{8}(8\mu^3 - 4\mu + 1) = 0 \qquad (27)$$

if complexity is further reduced by consideration of the case s = 1. This equation has the non-trivial solution

$$\mu = \frac{3}{4} = L\left(\frac{1}{\sqrt{3}}\right) \qquad (28)$$

what corresponds, according to equation (11) to the inflection point of the CTF.

Higher momentum functions. Also the 4$^{\text{th}}$ moment (Kurtosis) was considered for being employed in an locking algorithm. There was found no direct use for the 4$^{\text{th}}$ moment, since it delivers even powers of the residuals, but the use of higher odd moment functions may be used for locking purposes in the future. Further, the maximum of the standard deviation (2$^{\text{nd}}$ moment) also corresponds to the CTF inflection point.
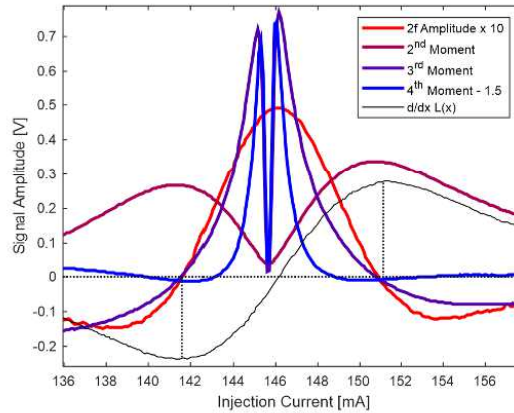
Figure 14. Injection current scan over CTF peak while measuring $2f$ amplitude, standard deviation (2nd moment), skewness (3rd moment), and kurtosis (4th moment)

AUTHOR INFORMATION
Corresponding Author
*E-mail: Bernhard.lendl@tuwien.ac.at
Notes
The authors declare no competing interest.

REFERENCES

1. Campillo, A. J., Davis, C. C. & Lin, H. Fabry – Perot photothermal trace detection. *Appl. Phys. Lett.* **41**, 327 (1982).

2. Waclawek, J. P., Bauer, V. C., Moser, H. & Lendl, B. 2f-wavelength modulation Fabry-Perot photothermal interferometry. *Opt. Express* (2016). doi:10.1364/OE.24.028958

3. Waclawek, J. P., Kristament, C., Moser, H. & Lendl, B. Balanced-detection interferometric cavity- assisted photothermal spectroscopy. *Opt. Express* **27**, (2019).

4. Waclawek, J. P., Moser, H. & Lendl, B. Balanced-detection interferometric cavity-assisted photothermal spectroscopy employing an all-fiber-coupled probe laser configuration. *Opt. Express* **29**, 7794 (2021).

5. Schilt, S. & Thévenaz, L. Wavelength modulation photoacoustic spectroscopy: Theoretical description and experimental results. *Infrared Phys. Technol.* **48**, 154– 162 (2006).

6. Jaeschke, M., Hinze, H. M., Achtermann, H. J. & Magnus, G. PVT data from burnett and refractive index measurements for the nitrogen-hydrogen system from 270 to 353 K and pressures to 30 MPa. *Fluid Phase Equilib.* **62**, 115–139 (1991).

7. Burke, J. H. T., Garcia, O., Hughes, K. J., Livedalen, B. & Sackett, C. A. Compact implementation of a scanning transfer cavity lock. *Rev. Sci. Instrum.* **76**, 1–3 (2005).

8. Seymour-Smith, N., Blythe, P., Keller, M. & Lange, W. Fast scanning cavity offset lock for laser frequency drift stabilization. *Rev. Sci. Instrum.* **81**, (2010).

9. Drever, R. W. P. *et al.* Laser phase and frequency stabilization using an optical resonator. *Appl. Phys. B Photophysics Laser Chem.* **31**, (1983).

10. Cygan, A. *et al.* Pound-drever-hall-locked,

frequency-stabilized cavity ring-down spectrometer. *Rev. Sci. Instrum.* **82**, (2011).

11. Dong, W., Keibler, M. A. & Stephanopoulos, G. Review of metabolic pathways activated in cancer cells as determined through isotopic labeling and network analysis. *Metab. Eng.* **43**, 113–124 (2017).

12. Zimnoch, M. *et al.* Partitioning of atmospheric carbon dioxide over Central Europe: Insights from combined measurements of CO_2 mixing ratios and their carbon isotope composition. *Isotopes Environ. Health Stud.* **48**, 421–433 (2012).

13. Wörle, K. *et al.* Breath analysis with broadly tunable quantum cascade lasers. *Anal. Chem.* **85**, 2697–2702 (2013).

14. Wang, Z. *et al.* A portable low-power QEPAS-based CO2 isotope sensor using a fiber-coupled interband cascade laser. *Sensors Actuators, B Chem.* **246**, 710–715 (2017).

15. Crosson, E. R. *et al.* Stable isotope ratios using cavity ring-down spectroscopy: Determination of 13C/12C for carbon dioxide in human breath. *Anal. Chem.* **74**, 2003–2007 (2002).

16. Baldacci, A., Devi, M., Narahari Rao, K., Chen, D.-W. & Fridovich, B. Absorption Spectrum of Carbon Dioxide at 4.3 µm. *J. Mol. Spectrosc.* **70**, 143–159 (1978).

17. Baldacci, A., Linden, L., Devi, M., Narahari Rao, K. & Fridovich, B. Interpretation of the 13C1602 Spectrum at 4.4 µm. **72**, 135–142 (1978).

18. Ismail, N., Kores, C. C., Geskus, D. & Pollnau, M. Fabry-Pérot resonator: spectral line shapes, generic and related Airy distributions, linewidths, finesses, and performance at low or frequency-dependent reflectivity. *Opt. Express* **24**, 16366 (2016).

19. Kluczynski, P. & Axner, O. Theoretical description based on Fourier analysis of wavelength-modulation spectrometry in terms of analytical and background signals. *Appl. Opt.* **38**, 5803 (1999).

20. Arndt, R. Analytical line shapes for Lorentzian signals broadened by modulation. *J. Appl. Phys.* **36**, 2522–2524 (1965).

Noise suppression and 1f - Quadrature Point signal readout technique for cavity-enhanced spectroscopy

Stefan Lindner[1], Davide Pinto[1], Harald Moser[1], Johannes Paul Waclawek[1] and Bernhard Lendl[1*]

[1]Institute of Chemical Technologies and Analytics, Technische Universität Wien, Getreidemarkt 9/164-UPA, 1060 Vienna, Austria

[*] bernhard.lendl@tuwien.ac.at

ABSTRACT: An overview of noise suppression techniques for sub-kHz cavity-enhanced optical dispersion spectroscopy is presented. Low noise level in all stages of signal generation and processing is crucial for a stable sensing system. Technical descriptions and experimental results of characterisation of the developed noise suppression techniques are given. Especially, theory, implementation and experimental results showing the performance of a signal readout technique called 1f - quadrature point balanced detection are described and compared to the well-established 2f-wavelength modulation (2f-WM) technique. To demonstrate functionality and application possibilities of the developed technique, the sensor is used as a microphone recording a 440 Hz tone.

INDEX HEADINGS DISPERSION SPECTROSCOPY; FABRY PEROT CAVITY; NOISE-SUPPRESSION; BALANCED DETECTION; WAVELENGTH MODULATION

INTRODUCTION

Fabry-Pérot interferometers are a widely used tool to implement various techniques for refractive index sensing of gasses. It has been shown to be a promising technique of chemical trace gas sensing[1–3] or has been used as transducer for an optical microphone[4]. A change of the refractive index of a gas volume located between the mirrors of a Fabry-Pérot interferometer can be sensed by a probe laser shining on that cavity. The cavity enhances this signal by the factor of the slope of its (periodic) cavity transfer function (CTF), which has its highest value in its inflection point. To keep the system at this highest sensitivity, the probe laser wavelength is locked to a value that corresponds to an inflection point of the CTF. The enhancement of the refractive index signal by the CTF principally is also performed for the noise, the probe laser carries. The

performance of a refractive index sensor is mainly influenced by the strength of the dispersion signal and the noise level of the probe laser beam, expressed by the quantity of signal-to-noise ratio (SNR).

$$SNR = \frac{S}{\bigcup_i N_i} \qquad (1)$$

$\bigcup_i N_i$ denotes the unification of all noise sources, measured by the overall noise amplitude. This cannot be expressed as sum of the different noise contributions N_i, since they don't add linearly. The signal strength S is usually limited by technical properties of the source that causes the refractive index change that has to be measured. This means that, to improve the SNR, the noise level has to be brought to as low levels as possible.

In this work, passive (parameter stabilisation, filtering) and active (balanced detection) techniques for noise level reduction in a cavity-enhanced dispersion sensing system were developed to improve the SNR. Further, a technique for the probe laser readout is introduced, that offers an intrinsic noise suppression. This technique is coined $1f$ - quadrature point readout.

The transmission trough a Fabry-Pérot cavity can be described with the cavity transfer function (CTF), which shows periodic peaks of lorentzian form. The graph is plotted in Figure 1 and mathematically expressed in equation (2).

$$\frac{I_T}{I_0} = \frac{1}{1 + \left(\frac{2F}{\pi}\right)^2 \sin^2\frac{\Delta\varphi}{2}} \qquad (2)$$

I_T denotes the laser intensity transmitted through a Fabry-Pérot cavity and I_0 the initial laser intensity, measured (by a monitor-photodiode of the probe laser) before being coupled into the cavity. This quantity is, if not stated differently, assumed to be 1, what gives I_T a relative meaning. F is the cavity's finesse and

$$\Delta\varphi = \frac{4\pi}{\lambda_0} nd \cos\theta \qquad (3)$$

is the CTF phase shift, which itself is a function of the refractive index n, the mirror spacing d and the angle of incidence θ, which is 0 in our setup. The setup is depicted in Figure 6. When a change of the refractive index n occurs between the mirrors of the cavity, the CTF peak is slightly shifted along the wavelength axis. This causes, according to the initial slope of the CTF, an change in the measured detector signal. If this change in refractive index is induced periodically also the enhanced detector signal change occurs periodically and can be retrieved by demodulation at the 2nd harmonic of the inducing (modulation) frequency.

Change of the CTF phase $\Delta\varphi$ is not only induced by changes in refractive index, but also by environmental influences such as fluctuations in the gas cell pressure (influencing n in an unwanted way), gas cell and cavity temperature (influenc-

ing the geometric parameters θ and d) or probe laser wavelength (λ_0) fluctuations. Further, the CTF slope and therefor the signal enhancement, is highest in the CTF inflection point. These two facts make it mandatory, that a laser wavelength-cavity locking algorithm is implemented, that holds the probe laser wavelength (by adjusting the corresponding injection current) at a value, that corresponds to an inflection point of the CTF. Generally speaking, this is nothing else than a feedback loop, although the specific implementation is not trivial. In this work, we apply a locking technique, that is based on $2f$-wavelength modulation ($2f$-WM) of the probe laser. By use of small modulation depths (amplitude of the modulation sine), the zero crossing of the detector signal demodulated at the second harmonic ($2f$ signal) marks the inflection point of the underlying CTF.
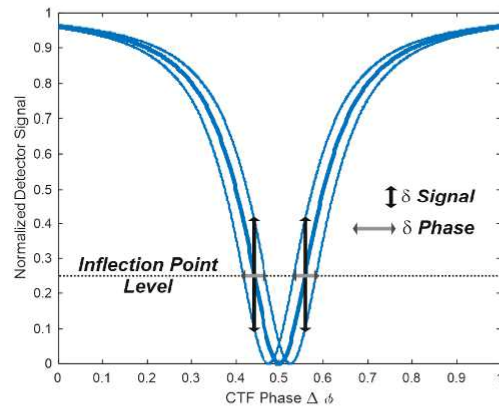

Figure 1. Phase-shifting CTF reflection peak and its effect on detector intensity

THEORETICAL SECTION

Noise reduction by cavity temperature stabilisation. According to equation (3), there are two parameters having influence to the CTF phase $\Delta\varphi$, that depend on the temperature of the cavity and its housing. These are the mirror spacing d and the angle of incidence θ. To understand this, we consider a temperature change of the cavity of 1°C.

Assuming, the gas volume in the cavity is filled with pure nitrogen, this gas temperature change causes a change of n in the order of[5] 10^{-6}, what causes, according to equation (3) a change of the CTF phase in the same order of magnitude. The change of the CTF phase caused by thermal expansion of the cavity's aluminium housing is far bigger. Assuming, that the change of $\Delta\varphi$ is caused only by a change of d, it follows that this influence is one order of magnitude higher, since aluminium shows a linear heat expansion coefficient of[6] $23 \cdot 10^{-6}$ K^{-1}.

If it is assumed, that the change of $\Delta\varphi$ is caused only by the angle of incidence, the following simplified model of the gas cell has to be used: Since temperature stabilisation of the gas cell is performed by a Peltier element placed underneath the gas cell, it is assumed, that only on this surface heat expansion takes place. The aluminium housing has an outer dimension of 20 mm along the probe laser beam direction and a height of

40mm. Using the previously mentioned linear heat expansion coefficient of aluminium and simplified triangular geometry, the change in the angle of incidence is in the order of $10 \cdot 10^{-6}$ K^{-1}. This is in the same order of magnitude as the influence by change of d.

In reality, there is a combined effect of heat expansion and cavity tilt, also because the cavity has to be glued in the aluminium housing and this glue has again different thermal properties. This leads to complicated relations between gas cell temperature and its influence to $\Delta\varphi$. For technical purposes it is sufficient to know the CTF peak laser wavelength vs. cavity temperature function, which was measured to be linear with a slope of 0.26 nm K^{-1}. For deeper understanding of the thermal effects on the CTF, further studies like tilting effects on aberrations from parallelism of the cavity have to be done.

Summarized, this means, that the effects on $\Delta\varphi$ caused by temperature fluctuations of the gas cell are around 10 times higher than the influence caused by gas temperature change. In terms of suppressing unwanted changes of $\Delta\varphi$ this means, that the gas cell temperature has to be stabilized. By use of a thermoelectric cooler, the temperature could be stabilized to sub mK range, compared to fluctuations in the range of tens of mK without stabilization. According to equation (3), the influence of d and $\cos\theta$ to $\Delta\varphi$ is linear. If the system is operated in the linear range of the CTF,

this means, that the probe laser detector noise is expected to be suppressed in the same order of magnitude. Figure 2 confirms that by experimental data: Stabilizing the gas cell temperature results in a noise reduction of a factor of 10 in terms of noise amplitude standard deviation.
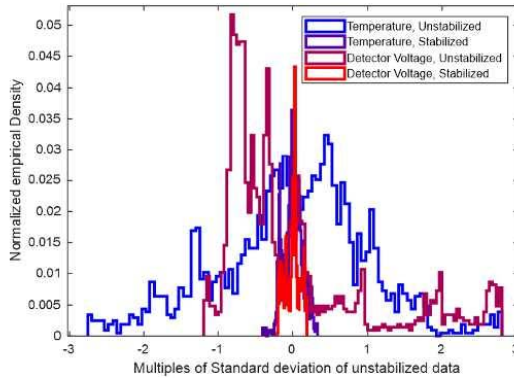

Figure 2. Empirical density of gas cell temperature and probe laser detector voltage before and after temperature stabilization.

Noise reduction by electronic filtering. Since a frequency dependent detection and locking scheme is implemented, electronic pre-filtering of the raw signal was found to lead to significantly lower noise levels at the sensor output. For that reason, several electronic filters were implemented. The probe laser control voltage generated in a DAQ device is filtered by a low-pass-filter with 10 kHz cut-off-frequency for anti-aliasing and a band-stop-filter at the desired detection frequency. The probe laser detector output is splitted in two channels. One channel, the probe laser locking channel, is filtered by a low-pass-filter with

10 kHz cut-off to avoid aliasing. On the other channel, the sensor signal output channel, the signal is filtered by a band-pass-filter with same cut-off-frequencies as the band-stop-filter of the probe laser control voltage. Additionally, a switchable preamplifier with 0, 10 or 20 dB is implemented. Figure 3 shows the measured characteristics of the different filter stages as Bode-diagrams.
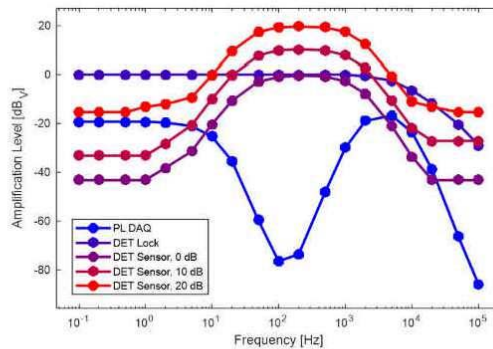

Figure 3. Measured Bode Diagrams of the implemented filters. PL DAQ...Probe laser control voltage. DET Lock...Probe laser detector, lock channel. PL Sensor...Probe laser detector, sensor channel with 0, 10 or 20 dB (adjustable) pre-amplifier gain.

Active Noise Suppression I - Electronic Balanced Detection. The idea of this method is, to find a compromise between full optical balancing as it is already reported for Interferometric cavity-assisted photothermal spectroscopy[2,3] and the significantly lower system complexity of a single-probe-beam setup. Therefore, a feature offered by the fiber-coupled probe laser is used:

The laser has an in-package monitor photodiode, that can be read out by an external transimpedance amplifier (TIA), which is in-house-built. The TIA output then delivers a signal, proportional to the initial probe laser intensity I_0 from equation (2). The signal amplitude has to be matched to the detector signal amplitude by adjusting the TIA total resistance to a value, so that the output amplitude matches the detector photodiode amplitude. To correct for possible phase shifts, an in-house-built all-pass filter is installed after the TIA. Those shifts arise from different electro-optic response times of monitor and detector photodiode. The aligned signals are then fed to a differential amplifier. This configuration realizes a balancing method, that cancels out noise contributions arising from electronic noise sources. These are the digital-analog conversion of the probe laser driving current control voltage, the laser driver and the laser itself. Optical noise contributions, coming from disturbing effects in the laser fiber and focusing optics or the cavity itself, are not canceled out. This would be the case, if instead of the monitor photodiode readout, a beam splitter after the probe laser output is used and two beams are coupled into the cavity and detected by two different photodetectors. With this, also any pressure fluctuations or disturbing acoustic noise in the cavity can be cancelled out. A noise reduction of 20.8 dBm at the excitation laser modulation frequency (597

Hz), compared to the unbalanced ICAPS setup is reported[3]. The setup therefore is significantly more complex than a single probe beam system. When the monitor photodiode of the probe laser is used for balancing purposes – the technique is called Electronic Balanced Detection, EBD – a noise reduction of 11.5 dBm $Hz^{-1/2}$ at the same frequency could be reached, as shown in Figure 4.
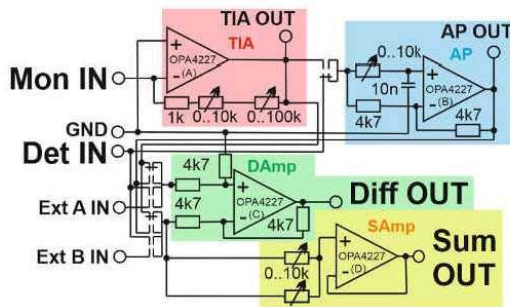

Figure 4. Circuitry of the in-house developed electronic balancing board. The red part represents the transimpedance amplifier (TIA) for the monitor photodiode, the blue part the all-pass-filter (AP) for phase shifting, the green part the differential amplifier (Damp) and the yellow part the summing amplifier (SAmp). GND is the ground connection, Mon IN the monitor photodiode input, Det IN the (amplified) photodetector input, Diff OUT the differential amplifier output and Sum OUT the adding amplifier output. AP OUT, the all-pass-filter output, TIA OUT, and Ext A and B, two external inputs, are used for developing and verification purposes.

Active Noise Suppression II - 1f Quadrature Point Balanced Detection. This technique was inspired by a Mach-Zehnder interferometer based technique for refractive index sending of liquids that uses specific properties of the quadrature point of two sinusoidal signals shifted in phase[7–9].

The idea is, to make use of the phase dependence of the amplitude of the sum signal, if monitor and detector photodiode signal are added and one of them is inverted. At this point, it is important to note, that the signal inverted in an ex-ante sense. That means, that the inverting input of the operational amplifier has to be used to invert the signal and no phaseshift of π is applied with all-pass-filters. Contrary to the fact, that it holds $\sin(\varphi + \pi) = -\sin\varphi$, a phaseshift of π is not equivalent to an inversion, because the noise would also be shifted and the noise cancellation by adding would fail.

The principle is depicted in Figure 5: Monitor (blue sine curve) and detector (orange sine curve) photodiode signal of the modulated probe laser are phase-aligned and one of them, in the depicted case the detector signal, is inverted (or, in other words, the quadrature point is shifted to zero) and added afterwards. This results – in the case, the probe laser beam is not anyhow disturbed on its pathway through the interaction volume – in a sum signal being constantly zero (purple straight line). As soon as a very little phase shift occurs

(yellow), the sum signal changes to a sinusoidal signal with the same frequency as the modulation frequency ($1f$) of the probe laser. The sum signal is then demodulated at the first harmonic of the probe laser modulation frequency, what delivers a signal amplitude proportional to the phase shift introduced in the gas cell.

To understand this, two sinusoidal signals of equal amplitude (ensured by choosing the TIA resistor of the monitor photodiode correctly) are considered: $M(t)$, describing the monitor photodiode signal and $D(t)$, describing the detector photodiode):

$$M(t) = A \sin \omega t \qquad (4)$$

and

$$D(t) = -A \sin(\omega t + \hat{\varphi}) \qquad (5)$$

t denotes the time, $\omega = 2\pi f$ the angular frequency with f the probe laser modulation frequency and

$$\hat{\varphi} = \varphi_{AP} + \Delta\varphi \qquad (6)$$

the total phase shift, which is a sum of the instrument phase shift φ_{AP}, applied by purpose via the all-pass-filter (see Figure 4) and the interaction phase shift $\Delta\varphi$ defined in equation (3). Initially, the system is tuned to a total phase shift of $\hat{\varphi} = 0$ with the all-pass-filter. The sum signal can be written as

$$M(t) + D(t) = A[\sin \omega t - \sin(\omega t + \hat{\varphi})] \qquad (7)$$

By using the trigonometric summation theorem, the second sine can be written as

$$\sin \omega t \cos \hat{\varphi} + \cos \omega t \sin \hat{\varphi} \qquad (8)$$

Since $\hat{\varphi}$ is near zero, the approximations $\cos \hat{\varphi} \cong 1$ and $\sin \hat{\varphi} \cong \hat{\varphi}$ can be used and finally it is found

$$M(t) + D(t) \cong -A\hat{\varphi} \cos \omega t =: S(t) \qquad (9)$$

what means, that the sum signal $S(t)$ keeps the frequency of the probe laser modulation and has an amplitude proportional to the total phase shift $\hat{\varphi}$.

Because of $-\cos x = \cos(x - \pi)$ and $\cos x = \sin\left(x + \frac{\pi}{2}\right)$ this can be written as

$$S(t) = A\hat{\varphi} \sin\left(\omega t - \frac{\pi}{2}\right) \qquad (10)$$

Demodulation at the first harmonic and applying a phase shift of $\frac{\pi}{2}$ at the corresponding Lock-In-Amplifier (LIA) delivers a $1f$ signal amplitude of

$$S_{1f} = A\hat{\varphi} = A\varphi_{AP} + A\Delta\varphi \qquad (11)$$

This signal, S_{1f}, is directly proportional to the phase shift $\Delta\varphi$ from equation (3), introduced by refractive index change of the sample gas volume.

Further, it has to be mentioned, that the modula-

tion amplitude A is the proportionality factor of this relation – that means, that the slope of this transfer function can in principle be varied (especially: increased) via the probe laser modulation amplitude. This is only limited by the CTF of the employed cavity: The modulation of the probe laser has to be performed within the linear range of the CTF, which is the region around the CTF inflection point that shows sufficient linearity (see Figure 1).
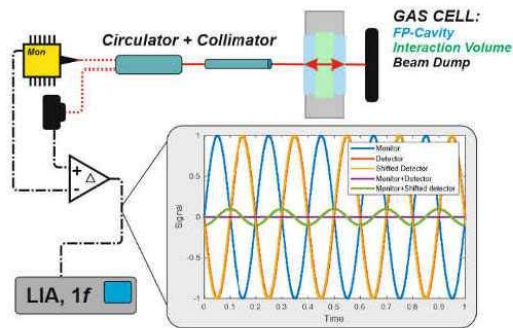

Figure 5. Principle of $1f$ Quadrature Point Balanced Detection

Analyzing the 1f LIA output, what is the carrier of the 1f-Quadrature point Balanced Detection (1f-QBD) signal, a significant noise reduction could be reached, as shown in Figure 6. The 1f signal of the demodulated probe laser has a zero crossing at the CTF peak minimum. This condition is used for laser-cavity locking for this technology. The critical parameter is the time constant. To ensure, that the system is able to recognize changes in refractive index by a source with a given frequency, the time constant of the 1f-

demodulation has to be at least lower than the reciprocal of this frequency.

EXPERIMENTAL SECTION

Instrumentation and Materials. The setup and the in-house developed electronics board is depicted in Figure 6. Nitrogen in 5.0 purity level was purchased from Messer Industriegase GmbH, 65812 Bad Soden, Germany. 1000 ppm and 10000 ppm CO_2 in nitrogen 5.0 test gas mixtures for ICAPS were purchased from Air Liquide Austria GmbH, 2320 Schwechat, Austria.
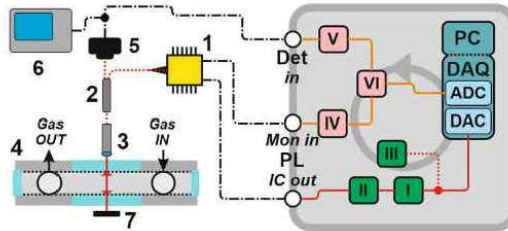

Figure 6. Schematic of optical and electronic compartment of the experimental setup. The instruments, in arabic numbers, are listed in Table 1. The components of the electronic compartment, in roman numbers, are described in Table 2.

No.	Instrument	Manufacturer	Type/Model
1	Probe Laser	Emcore	1782B-NM-050-34-FC-PM; fiber coupled butterfly packaged, 1550nm
2	Optical circulator	Thorlabs	CIR1550PM-EC; PM-fiber coupled, FP/APC connector
3	GRIN collimator	Thorlabs	15-1550-PM-APC; PM-fiber coupled
4	Gas cell with cavity	custom	Aluminium housing, cavity SLS optics, F = 20
5	NIR detector	Thorlabs	PDA-10CS; preamplified InGaAs photodetector
6	Spectrum Analyser	Rohde & Schwarz	FSC-4; 10 Hz to 4 GHz frequency range
7	Beam dump	custom	eloxated aluminium

Table 1. List of instruments, Arabic numbers in Figure 6

No.	Description
I	Electronic filter stage
II	Laser driver (Commercial model: Koheron CTL 101 B-400)
III	Analog Sine wave generator
IV	Transimpedance amplifier
V	All-Pass Filter
VI	Differential amplifier

Table 2. Description of the sub-compartments of the in-house developed electronic board, Roman numbers in Figure 6

Comparison of the developed noise suppression techniques. The measure to take, to characterize the performance of the developed noise suppression techniques, are noise power density spectra and the comparison of the measured noise level to the fundamental limit of shot noise. Two frequency ranges were investigated: The core range, frequencies, from DC to 1 kHz, that are target frequencies of the sensor and the range including the next decade, from 0 to 10 kHz. This range is from interest, since there the probe laser modulation frequencies required for laser wavelength-cavity locking with the 2f-WM technique (in the current setup: 4463 Hz) are located.

The measurements shown in Figure 7 (Graph 0 and 1) show the spectrum analyzer instrument noise floor (what represents the measured noise level of a 50 Ohm endcap at the instrument input and therefor the lowest measurable noise level with this instrument) and the noise level of the photodetector without any laser shining on it (Dark photodetector). Graphs No. 2 and 3 show the noise level of the unlocked system (pure nitrogen, 200 mL min^{-1}, 200 mbar) with and without the electronic filters characterized in Figure 3. Graph 4 shows the noise level of the 2f-WM-locked cavity. The probe laser modulation frequency of 4463 Hz is clearly recognizable. Also

the second harmonic of this frequency can be recognized but is already suppressed by the electronic filters applied. Graphs 5 and 6 represent
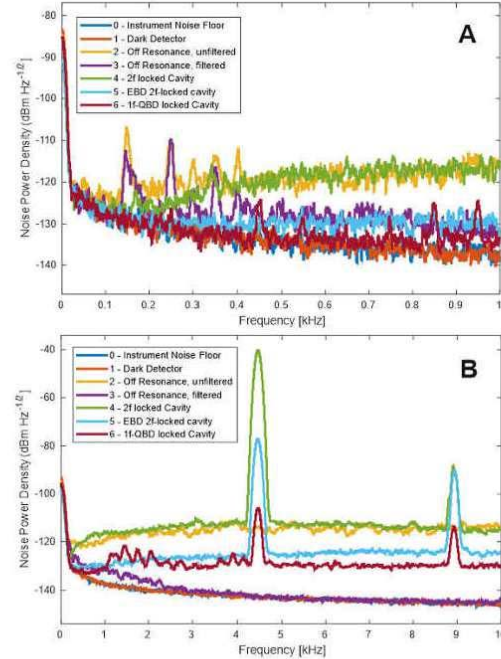
Figure 7. Measured noise power spectra of the output of different noise suppression techniques in the range of (**A**) 0 to 1 kHz and (**B**) 0 to 10 kHz. Different System conditions: 0 – Instrument noise floor (Spectrum analyzer, input 50 Ohm closed), 1 – Dark photodetector, 2 – Off cavity resonance (no cavity enhancement), unfiltered signal, 3 – Off cavity resonance, electronic filter board applied, 4 – 2f-WM-locked cavity, 5 – Electronic balanced detection, 2f-WM-locked cavity, 6 – 1f-Quadrature point locked cavity

the noise level of the EBD and the 1f-QBD technique. Employment of electronic filters shows a frequency dependent noise suppression effect of up to -30 dBm Hz$^{-1/2}$ (at 5 kHz) in noise power

9

density, compared to the unfiltered off-resonant signal. This high value cannot be fully exploited since it is reached only at high frequencies. Nevertheless, a contribution in terms of anti-aliasing is reached. The EBD and the $1f$-QBD techniques show a noise suppression performance of 11.5 and 16.6 dBm Hz$^{-1/2}$ (at 5 kHz) compared to the unfiltered off-resonant signal. This is poorer noise suppression compared to the noise suppression by electronic filters, but the noise suppression performance is reached in the whole frequency range. Especially this is the case at low frequency, where the sensor is operated. At this point it is also to mention, that the $1f$-QBD technique has, besides the already described balancing effect, the advantage, that it uses the $1f$ signal of the probe laser detector. That means, that the noise suppression capabilities of a LIA is employed already before a possible demodulation of a modulated refractive index change is performed by a second LIA. This results in additional noise suppression compared to the EBD technique. Further, intrinsic electronic noise sources having their origin most probably in the laser control system (NI DAQ System and laser driver) – recognizable as maxima in the noise power density spectrum – are fully compressed with both of these balancing techniques.

Comparison of process variables. The $1f$-QBD technology uses a two-stage Lock-In-

amplification: The differential signal of probe laser photodiode and monitor photodiode is demodulated at the first harmonic of the probe laser modulation frequency with a low time constant (sub-millisecond).
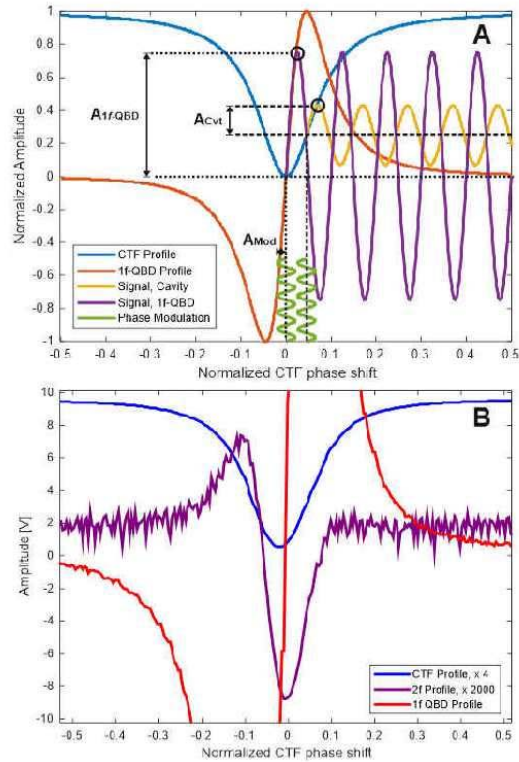
Figure 8. Signal enhancement by cavity and $1f$ probe laser demodulation. (**A**) Schematic of the principal. Both, the CTF and the $1f$-QBD amplitude are normalized. In practical operation, the $1f$-QBD amplitude can be adjusted by modulation depth of the probe laser. (**B**) Measurement of photodetector DC level, $2f$- and skewness amplitude of the demodulated photodetector signal and $1f$-QBD signal with different scaling factors. The $1f$-QBD signal is reaching saturation of the LIA when using same parameters as for 2f-demodulation.

This means, that the 1f-profile, which's amplitude is, according to equation (11), proportional to the phase shift introduced by refractive index changes due to excitation laser modulation, is modulated in phase. This has the consequence, that the modulation introduced by the excitation laser is not only enhanced by the CTF, but also by the 1f-demodulation of the probe laser signal.

RESULTS AND DISCUSSION

1f-Quadrature point readout technique as enhanced optical microphone. For this possible application of the 1f-QBD technique, the gas cell was opened by disconnecting the gas supply tubes. A sound source (440 Hz, a[1]) is placed in the optical compartment and the probe laser detector signal is demodulated at increasing frequency.
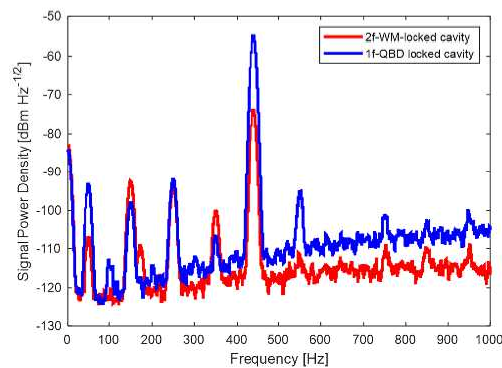

Figure 9. 1f-QBD for measuring sound frequency spectra (Blue) compared to same measurement performed by non-balanced 2f-wavelength modulation locked cavity (Red)

Two measurements are performed: First, the probe laser wavelength was locked to the CTF inflection point (2f-wavelength modulation lock). Then, the probe laser wavelength was locked to the quadrature point of detector and monitor photodiode signal (1f-QBD readout). Figure 9 shows the results. With this measurement, a further advantage of the 1f-QBD technique could be shown: The absolute detector signal of the quadrature point is theoretically zero, since the reflection CTF reaches its minimum. If a CTF phaseshift is applied, this signal changes from an absolute value of nearly zero to a finite absolute value. If the cavity is locked to the CTF inflection point, the absolute value is not zero and changes just to higher and lower levels, generating a demodulable oscillation. The absolute level of the locked system, if no phase shift due to sound is applied, is not zero in this case. This means, that the difference between signal and no signal is easier to recognize with 1f-QBD technique.

CONCLUSIONS AND OUTLOOK

Conclusions of the current work. In this work, the effect different noise sources in a cavity-based refraction index sensing system was demonstrated. Starting with temperature stabilization and electronic filtering, two balanced de-

11

tection techniques called EBD and $1f$-QBD were introduced. The effect of electronic filtering is an established technique of noise reduction and was characterized for a specific sensing system. A noise suppression of up to - 30 dBm Hz$^{-1/2}$ could be achieved with an in-house-developed filter board. The balanced detection techniques developed in this work show, while having different underlying principles, a comparable capability of noise suppression of -11.5 and -16.6 dBm Hz$^{-1/2}$. This is lower than the already published balanced detection technique of BICAPS, based on optical balancing, which reaches a noise reduction of 20.8 dBm Hz$^{-1/2}$. The developed techniques therefor are based on purely electronic principles. This brings the big advantage of lower complexity and therefore potentially higher sensor robustness.

$1f$-QBD active phase shift control as laser wavelength – cavity locking fine tuning feature. As mentioned in the introduction, a laser wavelength – cavity lock has to be implemented to keep the sensing system in its highest sensitive operating condition, the inflection point of the cavity's CTF. This lock, whatever locking scheme is applied, can be extended by making use of a property of the instrument phase shift $\boldsymbol{\varphi_{AP}}$. It can be split in a sum of two instrument phase shift contributions applied by the all-pass-filter:

$$\varphi_{AP} = \varphi_{AP}^0 + \varphi_{AP}^{lock} \tag{12}$$

The principal instrument phase shift $\boldsymbol{\varphi_{AP}^0}$ here overtakes the role of the previously discussed instrument phase shift $\boldsymbol{\varphi_{AP}}$, introduced in equation (6) – it arises from different (electronic and optic) signal forming and processing times in the monitor and the detector photodiode and is constant over time since those parameters are not changing. If the potentiometer in the AP-part of Figure 4 is replaced by a voltage dependent variable resistor (VDR, varistor), the phase alignment between monitor and detector photodiode can also be actively controlled by a control voltage for the phase $\boldsymbol{U_\varphi}$, resulting in a second contribution to $\boldsymbol{\varphi_{AP}}$, the locking instrument phase shift $\boldsymbol{\varphi_{AP}^{lock}} = \boldsymbol{\varphi_{AP}^{lock}}(\boldsymbol{U_\varphi})$. This can deliver valuable contribution to further stabilization of a $1f$-QBD system, besides a stable and reliable laser wavelength – cavity locking scheme. On the other hand, the active controlling is an additional noise source in the system and further research has to be done find an equilibrium between the advantages arising from active phase control and the disadvantage of introducing that additional noise source.

AUTHOR INFORMATION

Corresponding Author

*E-mail: Bernhard.lendl@tuwien.ac.at

Notes

The authors declare no competing interest.

REFERENCES

1. Waclawek, J. P., Bauer, V. C., Moser, H. & Lendl, B. 2f-wavelength modulation Fabry-Perot photothermal interferometry. *Opt. Express* (2016). doi:10.1364/OE.24.028958

2. Waclawek, J. P., Kristament, C., Moser, H. & Lendl, B. Balanced-detection interferometric cavity-assisted photothermal spectroscopy. *Opt. Express* **27**, (2019).

3. Waclawek, J. P., Moser, H. & Lendl, B. Balanced-detection interferometric cavity-assisted photothermal spectroscopy employing an all-fiber-coupled probe laser configuration. *Opt. Express* **29**, 7794 (2021).

4. Fischer, B. Optical microphone hears ultrasound. *Nat. Photonics* **10**, 356–358 (2016).

5. Peck, E. R. & Khanna, B. N. Dispersion of Nitrogen*. *J. Opt. Soc. Am.* **56**, 1059 (1966).

6. Wilson, A. J. C. The thermal expansion of aluminium from 0° to 650°C. *Proc. Phys. Soc.* (1941). doi:10.1088/0959-5309/53/3/305

7. Hayden, J., Hugger, S., Fuchs, F. & Lendl, B. A quantum cascade laser-based Mach–Zehnder interferometer for chemical sensing employing molecular absorption and dispersion. *Appl. Phys. B Lasers Opt.* **124**, 1–9 (2018).

8. Lindner, S. *et al.* External Cavity Quantum Cascade Laser-Based Mid-Infrared Dispersion Spectroscopy for Qualitative and Quantitative Analysis of Liquid-Phase Samples. *Appl. Spectrosc.* **74**, 452–459 (2020).

9. Dabrowska, A., Schwaighofer, A., Lindner, S. & Lendl, B. Mid-IR refractive index sensor for detecting proteins employing an external cavity quantum cascade laser-based Mach-Zehnder interferometer. *Opt. Express* **28**, 36632 (2020).

B. Additional Concepts

B.1. Autocorrelation

Autocorrelation is a powerful algorithmic tool to detect periodicities in extremely noisy signals. During the investigation of the applicability of autocorrelation to spectral data in this thesis, it turned out that, although some first promising results could be achieved, the method is not reliable enough for the planned application. Nevertheless, the principle ideas and the achieved results are presented at this point.

B.1.1. Motivation

When working on the increase of the signal amplitude of the interferometric cavity-assisted photothermal spectroscopy (ICAPS)[8,36] setup, several problems were encountered, and the signal strength was not able to increase to satisfyingly high levels. The idea was, to exploit a periodicity in the signal that has not been used so far: In ICAPS, the excitation signal for the employed Quantum cascade laser (see section 3.5.1) is built up from of two contributions:
A ramp (sawtooth or triangle function) of low frequency and high amplitude
A sinusoidal modulation of high frequency and low amplitude
The second part, the modulation, is used to implement a 2f-WM detection scheme (see section 2.4.2.1). The first part, the ramp, is just used to record one spectrum after the other and then average the results. The periodicity of this signal contribution was not exploited so far. The idea was, to record the ICAPS signal for some periods of the ramp - and not separate the gained signal period per period to get single ICAPS spectra that can be averaged afterwards – and apply autocorrelation to that (long term) signal.
From another, more technical point of view, the final averaging of multiple spectra was planned to be replaced by autocorrelation of the entire, multiple spectra containing, signal and exploit the feature, that periodicities get amplified by autocorrelation while non-periodic parts to the signal get suppressed. Autocorrelation was, in that interpretation, expected to serve as a more effective, nonlinear, alternative to averaging.

B.1.2. Theory of Autocorrelation

Autocorrelation is a technique, which allows amplification of periodic components of a signal while a non-periodic component, such as noise, is attenuated. The technique has been used in certain sensing methods in different fields like principle research such as the analysis of diffuse surfaces where it was shown that the autocorrelation function of the speckle pattern of reflected laser light is proportional to the diffraction pattern of the surface[95], or signal postprocessing of modern diagnostic methods in medicine such as optical coherence tomography (OCT)[96]. Autocorrelation in the frequency- and spatial domain has been used also for QCL characterisation[97] as well as the potential of application in spectroscopy was investigated from a theoretical point of view[98]. Improvement of trace gas sensors in the presence of disturbing effects such as optical fringes and atmospheric turbulence with autocorrelation functions has been investigated theoretically[99] and applications of the technique to infrared and Raman spectroscopy still exist[100,101].
It appears likely, to use an autocorrelation function for amplifying the periodic signal components caused by the (strictly constant) repetition rate of the excitation laser injection current ramp

which is used for wavelength tuning in ICAPS. When using autocorrelation, several spectra have to be recorded to generate a sufficiently long sequence of spectra. A sequence of around 10 spectra with sufficiently high spectral resolution and, even more important, temporal equidistantly recorded datapoints, are crucial for an effective use auf autocorrelation functions.

To define an autocorrelation function, consider a time-dependent signal $x(t)$, starting at $t = 0$. The autocorrelation function of $x(t)$ is defined as the cross-correlation function of the signal with itself[102].

$$\psi_{xx}(\tau) = \lim_{T \to \infty} \frac{1}{T} \int_0^\infty x(t) \cdot x(t + \tau) \ dt$$

(0.166)

To analyse time-discrete data, as it is the case when considering digitalized spectral data, a discretised form of the autocorrelation function is needed. This function can be defined as

$$\varphi_{xx}(j) = \frac{1}{t_0} \sum_{i=0}^{\frac{N}{2}} x_i \cdot x_{i+j} \qquad i, j \epsilon \left[1, \frac{N}{2} \right] \cap \mathbb{N}$$

(0.167)

where N is the data vector length and t_0 is the time difference between two digitalisation steps. It can be replaced by $\frac{N}{2}$, when considering dimensionless time steps (like an indexed data vector without corresponding timestamps). The discrete autocorrelation function in equation (0.167) was implemented in MATLAB code, presented in the appendix.
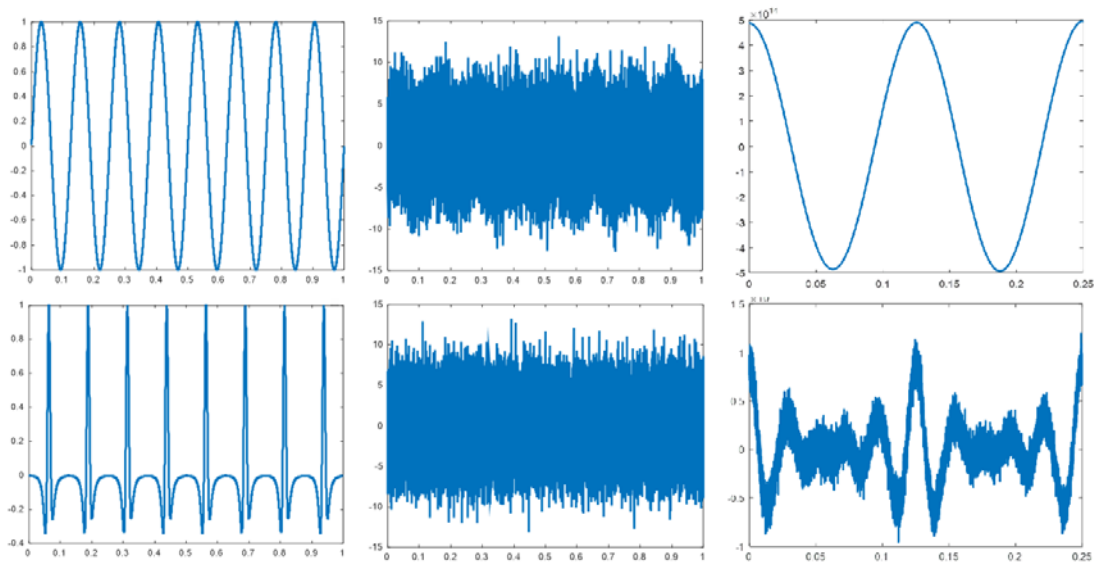
Figure A.1: Effect of the discrete autocorrelation function to sinusoidal and 2f-WM data with high noise. Left: pure signal, Middle: Noisy signal, Right: signal reconstructed by autocorrelation

To demonstrate the capability of the autocorrelation function, two model datasets have been generated: 8 periods each of a sine function and a 2f-WM pattern of normalized amplitude 1. Additionally, Gaussian distributed noise (random numbers with $\mu = 0$ and $\sigma = 3$) is added. Afterwards, the discrete autocorrelation function is applied to that dataset. The result is shown in Figure A.**1**: The closer the signal is to a sinusoidal signal, the better autocorrelation performs.

The discrete autocorrelation function can also be applied iteratively – the only thing that has to be kept in mind is, that by every application of the discrete autocorrelation function, the signal length gets halved as can be seen from equation (0.167).

If the results of (multiple) application of the autocorrelation function is now compared to ordinary averaging, it can be observed that the noise (measured by the sum of squared residuals to the initial, unnoisy signal) is going down much faster as it is the case for ordinary averaging. The situation depicted in Figure A.**2**. To a sequence of 128 $2f$-WM patterns again, gaussian noise of 9σ was added. A number of 2^n periods have then been averaged as well as autocorrelated and the sum of squared residuals has been calculated each. While this value increases linearly with n for the averaging as expected, the value is highly significantly lower from low values of n on for the autocorrelation.
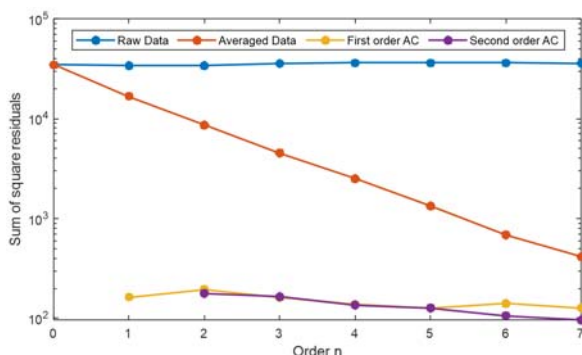

Figure A.2: Comparison of the noise of averaged and autocorrelated $2f$-WM signals

B.1.3. Application to periodic spectroscopy data

Finally, some results for the application of the discrete autocorrelation to spectral data are shown in Figure A.**3**. Linearity of the peak height with increasing analyte concentration is given for the raw spectral data as well as for the autocorrelated spectral data.

Nevertheless, the exact way of spectral transformation by autocorrelation could not be satisfyingly explained. Especially, due to the nature of autocorrelation there is no back-transformation from autocorrelated spectra to the initial spectrum. Because of that reason, the focus of research was put to other techniques and autocorrelation of spectral signals was not further investigated.
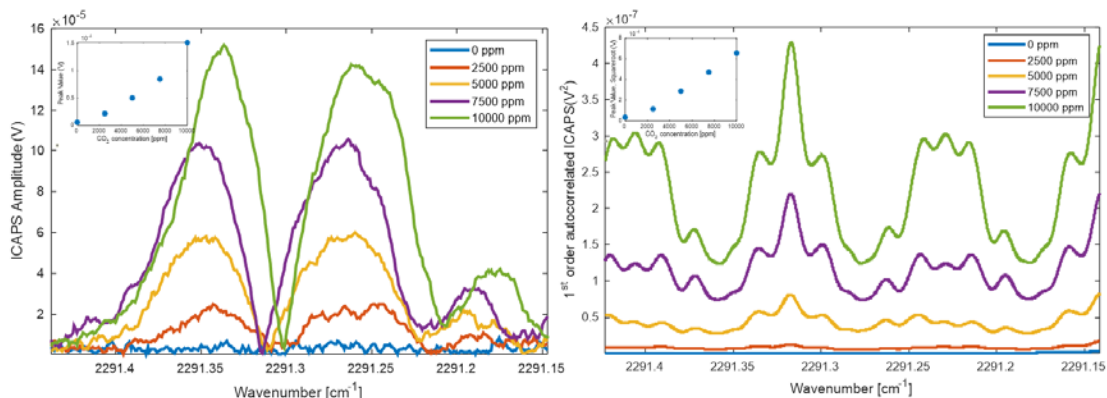

Figure A.3: Autocorrelation for CO_2 ICAPS data. Left: measured ICAPS spectra (R-amplitude) for CO_2, right: autocorrelated spectra

C. MATLAB Functions

C.1 Kramers-Kronig-Transformation

Absorption Spectrum to Dispersion Spectrum

Filename: kramerskronigAtoD.m

```matlab
function [ nspec ] = kramerskronigAtoD( absspec, WNumb )
%Kramers Kronig Transformation Diffraction -> Absorption
%    according to formula 40b from Ramer,Lendl: Attenuated Total Re?ection
%    Fourier Transform Infrared Spectroscopy, Encyclopedia of Analytical
%    Chemistry, 2013, DOI 10.1002/9780470027318.a9287
% k=-E ln(10)/d denotes imaginary part of complex ref index = Absorption
% coefficient
% Units: nspec dimensionless ref index; WNumb in cm^-1; absspec in AU

wnSI=WNumb*100;
nInfty=1;
thickness=0.00005;
numsteps=length(absspec);
nspec=zeros(numsteps,1);

%transformation AU to k
kspec=absspec*(-1)*log(10)/thickness;

for ii=1:numsteps
    inttmp=zeros(numsteps,1);
    for jj=1:numsteps
        if jj~=ii
            inttmp(jj)=wnSI(jj)*kspec(jj)/((wnSI(jj))^2+(wnSI(ii))^2);
        end
    end
    for jj=1:(numsteps-1)
        nspec(ii)=nspec(ii)+(inttmp(jj)+inttmp(jj+1))*(wnSI(jj+1)-
wnSI(jj))/2;
    end
    nspec(ii)=nspec(ii)*2/pi+nInfty;
end

end
```

Dispersion to Absorption Spectrum

Filename: kramerskronigDtoA.m

```matlab
function [ absspec ] = kramerskronigDtoA( shiftspec, WNumb )
%Kramers Kronig Transformation Diffraction -> Absorption
%    according to formula 40b from Ramer,Lendl: Attenuated Total Re?ection
%    Fourier Transform Infrared Spectroscopy, Encyclopedia of Analytical
%    Chemistry, 2013, DOI 10.1002/9780470027318.a9287
% k=-E ln(10)/d denotes imaginary part of complex ref index = Absorption
% coefficient
% Units: difspec in microns pathlengthshift; WNumb in cm^-1; absspec in
AU

wnSI=WNumb*100;
wL=(WNumb*100).^(-1);
nInfty=1;
nSurrnd=1; % TO THINK ABOUT!
thickness=0.00005;
numsteps=length(shiftspec);
nspec=zeros(numsteps,1);
absspec=zeros(numsteps,1);

%creating refractive index spectrum
for i=1:numsteps
    nspec(i)=shiftspec(i)*wL(i)/(2*pi*thickness)+nSurrnd;
end

%performing kramers kronig transformation to absorbance coefficient (k)
spectrum
for ii=1:numsteps
    tmpInt=zeros(numsteps,1);
    for jj=1:(numsteps)
        if jj~=ii
            tmpInt(jj)=(nspec(jj)-nInfty)/(wnSI(jj)^2-wnSI(ii)^2);
        end
    end
    for jj=1:numsteps-1
        absspec(ii)=absspec(ii)+(tmpInt(jj)+tmpInt(jj+1))*(wnSI(jj+1)-
wnSI(jj))/2;
    end
    absspec(ii)=absspec(ii)*wnSI(ii)*(-2)/pi;
end

absspec=absspec*(-1)*thickness/log(10);

%linear Scaling with fitted parameters - TO THINK ABOUT!
KScale=200000;
DScale=0.055;
absspec=KScale*absspec+DScale;

end
```

C.2 Allan-Werle-Plot

Filename: allanxyAlltau.m

```
function [allandata] = allanxyAlltau(data)
%calculates and plots Allan-Werle plot out of x=time and y=Signal
dataset:
%Fs is data sampling time in seconds, qtau is factor between tau-points
signal=data(:,2);
Fs=1/(data(2,1)-data(1,1));
tau=(1:floor(0.5*length(signal)))';
allandata=allanvar(signal,tau);
allandata=sqrt(allandata(:,1));
tau=(1/Fs)*tau;
loglog(tau, allandata,'.','MarkerSize',14);
xlabel('Tau (s)');
ylabel('\sigma_{Allan}');
grid on;
allandata=[tau,allandata];
end
```

C.3. Discrete Autocorrelation

Filename: discreteautokorrelationTime.m

```
function [AKvect] =
discreteautokorrelationTime(datavect,timevect,NPeriod)
%Calculates the autokorrelated function vector to a given input vector
%IMPORTANT: Corresponding timesteps (x-axis) have to be equidistant! ->
%"wait to next millisecond multiple" to be used in Labview

Nak=floor(length(datavect)/2);
AKvect=(1:Nak)';
for i=1:Nak
    sum=0;
    for j=1:Nak
        sum=sum+(datavect(j)*datavect(j+i))/(timevect(j+1)-timevect(j));
    end
    AKvect(i)=2*sum/Nak;
end
clear i
clear j
clear sum
AKvect=AKvect*NPeriod;
end
```

C.4 Sine – Line – Correction

Filename: sinelincorr.m

```matlab
function [ sincorr ] = sinelincorr( diff, diffzero )
%corrects the detsig/piezo error from sine approximation

diffcorr=diff;
diffzerocorr=diffzero;
ampl=1;

for i=1:length(diffcorr)
    diffcorr(i)=2*ampl*asin(diff(i)/(2*ampl));
    diffzerocorr(i)=2*ampl*asin(diffzero(i)/(2*ampl));
end
sincorr=diffcorr-diffzerocorr;
end
```

C.5 Find Ramp Start

Filename: findramp.m

```matlab
function [rspdramp] = findramp(data,h,cut)
%   Detailed explanation goes here
current=data(:,2);
cbool=(1:length(current))';
for i=1:length(cbool)
    cbool(i)=NaN;
end
for i=1:(length(current)-1)
    if current(i)-current(i+1)>h
        cbool(i)=i;
    end
end
cbool=cbool(not(isnan(cbool)));
startidx=cbool(1)+cut;
stopidx=cbool(2)-cut;
rspdramp=data(startidx:stopidx,:);
rspdramp(:,1)=(data(2,1)-data(1,1))*(0:(stopidx-startidx))';
plot(rspdramp(:,1),rspdramp(:,2),'.',rspdramp(:,1),rspdramp(:,3),'.',rspd
ramp(:,1),rspdramp(:,4),'.');
xlabel('Time (s)');
ylabel('Voltage (V)');
legend('Injection Current (60 mA/V)','Detector Voltage, Transmission
(V)','Detector Voltage, Reflection (V)');
end
```

D. LabVIEW Codes

D.1 Software Lock-In-Amplifier
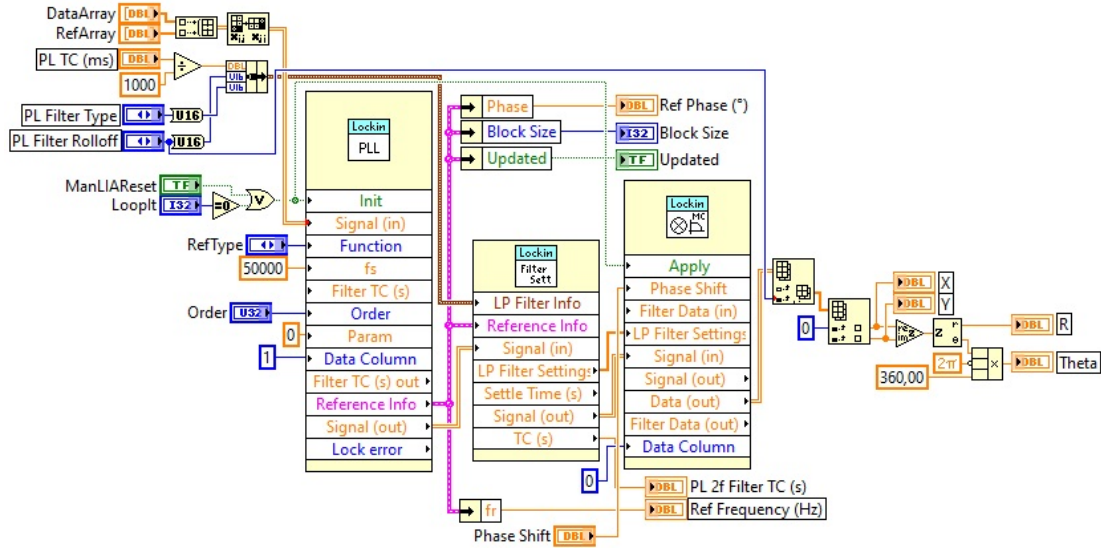
D.2 FT-IR Laser Characterization Peak Finder
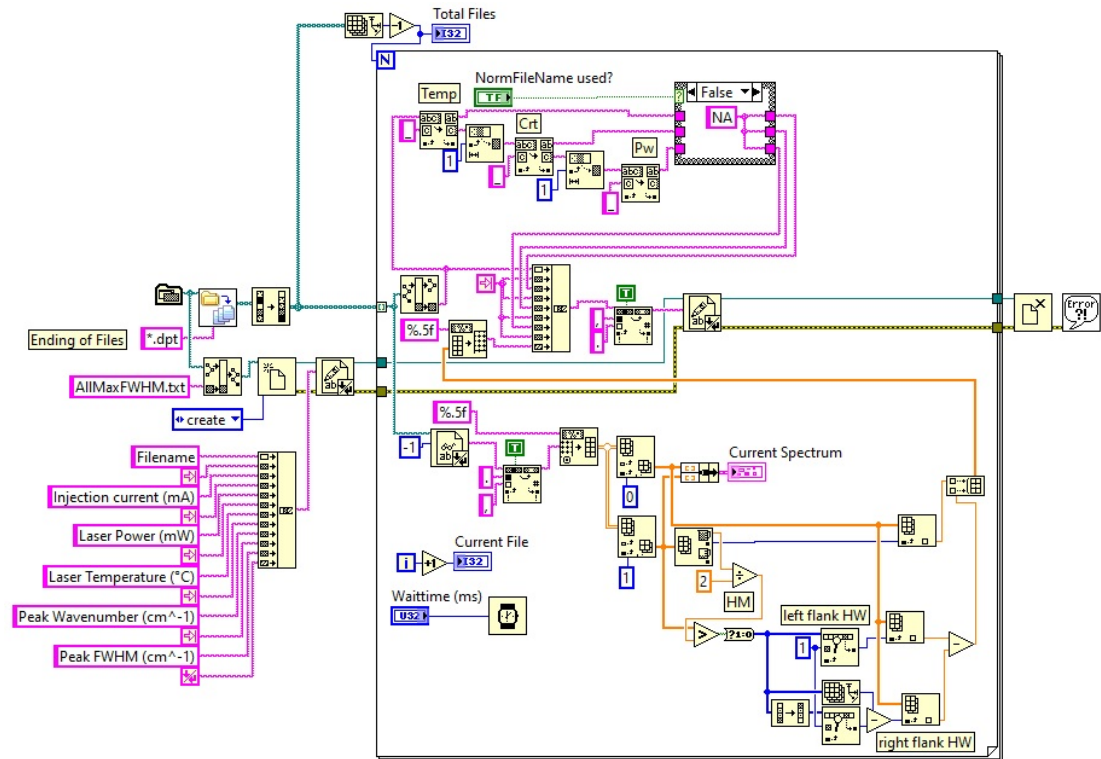
D.3 Laser-Wavelength-Cavity Locking

Data Acquisition

Calculation of Locking Process Variables

Feedback Loop

E. Circuitry of Developed Electronics

E.1. Electronic Filter Board

E.2. Electronic Balanced Detection Board

F. List of Figures – MATLAB source code

```matlab
%Figure 0.1
    % CorelDRAW only

%Figure 1.1
    %Im and Re of driven damped harmonic oscillator
    %w0=pi, gamma=0.1
    Fig1d1_w=(0:10000)'/10000*2*pi;
    Fig1d1_A=Fig1d1_w; for i=1:10001 Fig1d1_A(i)=1/sqrt((pi^2-
Fig1d1_w(i)^2)^2+(2*0.1*Fig1d1_w(i))^2); end
    Fig1d1_P=Fig1d1_w; for i=1:10001 Fig1d1_P(i)=acot(-
2*0.1*(Fig1d1_w(i))/(pi^2-Fig1d1_w(i)^2)); end
    Fig1d1_I=-Fig1d1_A.*sin(Fig1d1_P);
    Fig1d1_R=Fig1d1_A.*cos(Fig1d1_P);
    plot(Fig1d1_w/pi,Fig1d1_A,Fig1d1_w/pi,Fig1d1_P,'LineWidth',2);
    xlabel('Relative angular frequency \omega_E/\omega_0');
    ylabel('Stationary Amplitude A_S / Phase Shift \phi_S');
    legend('Stationary Amplitude A_S','Phase Shift \phi_S');
    plot(Fig1d1_w/pi,Fig1d1_I,Fig1d1_w/pi,Fig1d1_R,'LineWidth',2);
    xlabel('Relative angular frequency \omega_E/\omega_0');
    ylabel('Real / Imaginary Part of Complex Stationary Amplitude A_S');
    legend('Real Part Re(A_S)','Imaginary Part Im(A_S)');

%Figure 1.2
    %standing waves
    Fig1d2_p=(0:10000)'/10000*2*pi;
    Fig1d2_a1=Fig1d2_p; for i=1:10001 Fig1d2_a1(i)=sin(0.5*Fig1d2_p(i));
end
    Fig1d2_a2=Fig1d2_p; for i=1:10001 Fig1d2_a2(i)=sin(1*Fig1d2_p(i));
end
    Fig1d2_a3=Fig1d2_p; for i=1:10001 Fig1d2_a3(i)=sin(1.5*Fig1d2_p(i));
end
    Fig1d2_a4=Fig1d2_p; for i=1:10001 Fig1d2_a4(i)=sin(2*Fig1d2_p(i));
end
    Fig1d2_a5=Fig1d2_p; for i=1:10001 Fig1d2_a5(i)=sin(2.5*Fig1d2_p(i));
end

plot(Fig1d2_p/(2*pi),Fig1d2_a1,Fig1d2_p/(2*pi),Fig1d2_a2,Fig1d2_p/(2*pi),
Fig1d2_a3,Fig1d2_p/(2*pi),Fig1d2_a4,Fig1d2_p/(2*pi),Fig1d2_a5,'LineWidth'
,2);
    xlabel('Unit Volume');ylabel('Amplitude');
    legend('\omega = 1/2','\omega = 2/2','\omega = 3/2','\omega =
4/2','\omega = 5/2');

%Figure 1.3
    %Eigenstates of Harmonic Oscillator; normalized
    Fig1d3_x=(0:10000)'*10/10000-5;
    n=0; Fig1d3_y0=(2^n*factorial(n))^(-0.5).*hermiteH(n,Fig1d3_x).*exp(-
(0.5*Fig1d3_x.^2))+0.5;
    n=1; Fig1d3_y1=(2^n*factorial(n))^(-0.5).*hermiteH(n,Fig1d3_x).*exp(-
(0.5*Fig1d3_x.^2))+1.5;
    n=2; Fig1d3_y2=(2^n*factorial(n))^(-0.5).*hermiteH(n,Fig1d3_x).*exp(-
(0.5*Fig1d3_x.^2))+2.5;
    n=3; Fig1d3_y3=(2^n*factorial(n))^(-0.5).*hermiteH(n,Fig1d3_x).*exp(-
(0.5*Fig1d3_x.^2))+3.5;
    n=5; Fig1d3_y5=(2^n*factorial(n))^(-0.5).*hermiteH(n,Fig1d3_x).*exp(-
(0.5*Fig1d3_x.^2))+5.5;
    n=7; Fig1d3_y7=(2^n*factorial(n))^(-0.5).*hermiteH(n,Fig1d3_x).*exp(-
(0.5*Fig1d3_x.^2))+7.5;
    n=10; Fig1d3_y10=(2^n*factorial(n))^(-
0.5).*hermiteH(n,Fig1d3_x).*exp(-(0.5*Fig1d3_x.^2))+10.5;
```
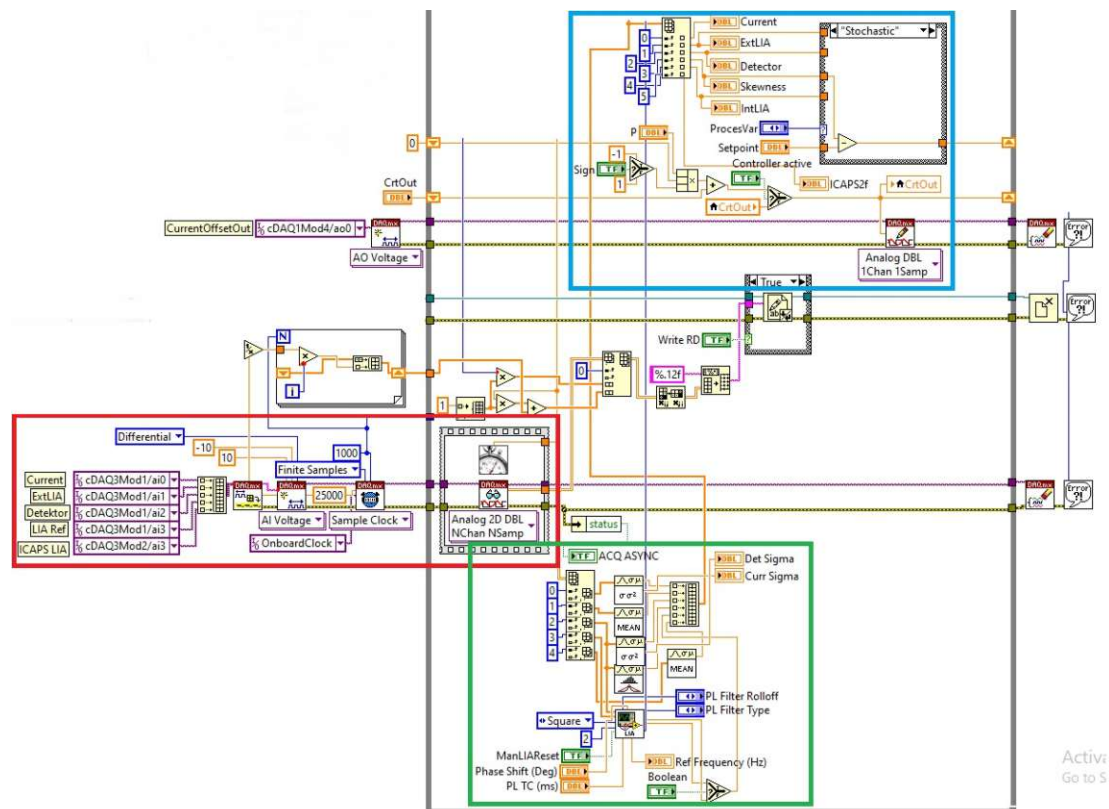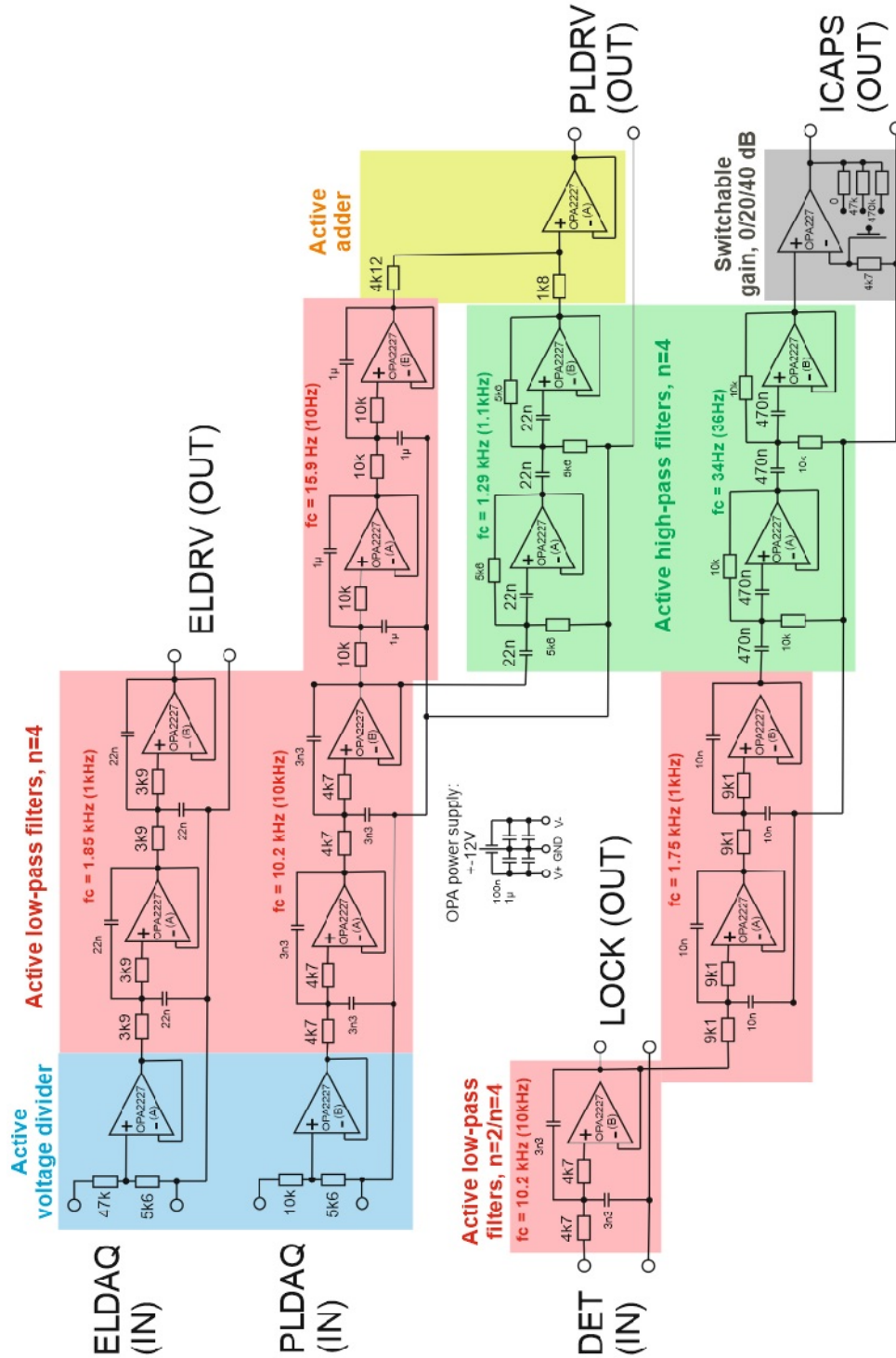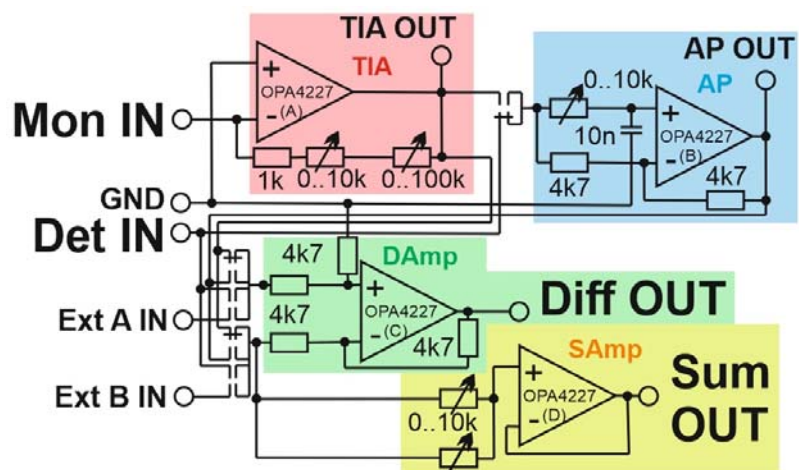
```matlab
    Fig1d3_pot=0.5*Fig1d3_x.^2;

plot(Fig1d3_x,Fig1d3_y0,Fig1d3_x,Fig1d3_y1,Fig1d3_x,Fig1d3_y2,Fig1d3_x,Fi
g1d3_y3,Fig1d3_x,Fig1d3_y5,Fig1d3_x,Fig1d3_y7,Fig1d3_x,Fig1d3_y10,'LineWi
dth',2);hold on;
    plot(Fig1d3_x,Fig1d3_pot,'LineWidth',3,'color',[0 0 0]);hold on;
    xlabel('Position x / (m \omega / h)^{1/2}');ylabel('Wavefunction
\psi_n(x) / h \omega_0');hold on;
    legend('n=0','n=1','n=2','n=3','n=5','n=7','n=10','Potential
V(x)');hold on;
    lgd=legend;lgd.NumColumns=4;hold off;

%Figure 1.4
    %Different important potentials
    Fig1d4_x=(0:10000)'/4000;
    Fig1d4_harm=40*(Fig1d4_x-1.1225).^2-1;for i=1:3950
Fig1d4_harm(i)=NaN; end;
    Fig1d4_PT=Fig1d4_x; for i=1:4200 Fig1d4_PT(i)=0;end;for i=4201:4800
Fig1d4_PT(i)=-1;end;for i=4801:10001 Fig1d4_PT(i)=0;end;
    Fig1d4_LJ=4*1*((1./Fig1d4_x).^12-(1./Fig1d4_x).^6);for i=1:3950
Fig1d4_LJ(i)=NaN; end;
    Fig1d4_Morse=1*(1-exp(-4*(Fig1d4_x-1.1225))).^2-1;;for i=1:3950
Fig1d4_Morse(i)=NaN; end;
    plot(Fig1d4_x-0.1225,Fig1d4_harm,Fig1d4_x-0.1225,Fig1d4_PT,Fig1d4_x-
0.1225,Fig1d4_LJ,Fig1d4_x-0.1225,Fig1d4_Morse,'LineWidth',2);
    xlabel('Dimensionless Distance x');ylabel('Dimensionless potential
AMplitude V(x)');
    legend('Harmonic potential','Finite potential well','Lennard-Jones
potential','Morse potential');

%Figure 1.5
    %Morse vs harmonic potential
    Fig1d5_x=(0:10000)'/4000;
    Fig1d5_harm=15*(Fig1d5_x-1).^2-1;for i=1:2000  Fig1d5_harm(i)=NaN;
end;
    Fig1d5_Morse=1*(1-exp(-4*(Fig1d5_x-1))).^2-1;for i=1:2000
Fig1d5_Morse(i)=NaN; end;
    plot(Fig1d5_x,Fig1d5_harm,Fig1d5_x,Fig1d5_Morse,'LineWidth',2);
    xlabel('Dimensionless Distance x');ylabel('Dimensionless potential
Amplitude V(x)');
    legend('Harmonic potential V(x)','Anharmonic (Morse) potential
V_A(x)');
    %Delta level
    Fig1d5_deltx=[0;1;2;3;4;5;6];
    Fig1d5_deltH=[1;1;1;1;1;1;1];
    Fig1d5_deltM=[1;0.9;0.8;0.7;0.6;0.5;0.4];
    plot(Fig1d5_deltx,Fig1d5_deltH,'.-',Fig1d5_deltx,Fig1d5_deltM,'.-
','MarkerSize',25, 'Linewidth',2);
    xlabel('n'); ylabel('\Delta E_n')

%Figure 1.6
    %CorelDraw and AutoCad 123Design

%Figure 1.7 to 1.12
    %CorelDraw only

%Figure 2.1 to 2.3
    %CorelDraw only

%Figure 2.4
    %QCL Profile; MEASURED
```

```matlab
    %Data: area of 6.8x6.8mm, 68x68 pixel with 100?m per pixel
Fig2d04_xy=(1:68)'/10;
surf(Fig2d04_xy,Fig2d04_xy,Fig2d04_QCLProfileMeasured);
xlabel('x Width [mm]');ylabel('y Width [mm]');zlabel('Detector Counts');
colorbar;


%Figure 2.5 to 2.8
    %CorelDraw only


%Figure 2.9
 %Quadrature Point MZI
Fig3d28_x=(1:10000)'*0.0001*2*pi;
plot(Fig3d28_x,cos(Fig3d28_x),'LineWidth',2);hold on;
plot(Fig3d28_x,-cos(Fig3d28_x),'LineWidth',2);hold on;
plot(Fig3d28_x,0.84*cos(Fig3d28_x),'--','LineWidth',2,'Color',[0 0.4470
0.7410]);hold on;
plot(Fig3d28_x,-0.84*cos(Fig3d28_x),'--','LineWidth',2,'Color',[0.8500
0.3250 0.0980]);hold on;
xlabel('Phase shift \phi [rad]');ylabel ('Detector Signal');hold on;
legend('Detector 1, A = 0','Detector 2, A = 0','Detector 1, A =
0.8','Detector 2, A = 0.8');hold off;
set(gca,'XTick',0:pi/2:2*pi);
set(gca,'XTickLabel',{'0','\pi/2','\pi','3\pi/2','2\pi'});


%Figure 2.10
    %CorelDraw only


%Figure 2.11
    % Transmission Airy Functions
Fig2d10_x=(1:10000)'./500-10;
Fig2d10_F1=1./(1+1*sin(Fig2d10_x./2).*sin(Fig2d10_x./2));
Fig2d10_F10=1./(1+10*sin(Fig2d10_x./2).*sin(Fig2d10_x./2));
Fig2d10_F20=1./(1+20*sin(Fig2d10_x./2).*sin(Fig2d10_x./2));
Fig2d10_F50=1./(1+50*sin(Fig2d10_x./2).*sin(Fig2d10_x./2));
Fig2d10_F100=1./(1+100*sin(Fig2d10_x./2).*sin(Fig2d10_x./2));
Fig2d10_F1000=1./(1+1000*sin(Fig2d10_x./2).*sin(Fig2d10_x./2));
plot(Fig2d10_x,Fig2d10_F1,Fig2d10_x,Fig2d10_F10,Fig2d10_x,Fig2d10_F20,Fig
2d10_x,Fig2d10_F50,Fig2d10_x,Fig2d10_F100,Fig2d10_x,Fig2d10_F1000,'LineWi
dth',2);hold on;
xlabel('Phase Shift \Delta\phi'); ylabel('Transmitted Intensity
I_T');hold on;
legend('F = 1','F = 10','F = 20','F = 50','F = 100','F = 1000');hold on;
lgd=legend;lgd.NumColumns=4;hold off;


%Figure 2.12
    %Principle of Cavity enhancement
    %left:
Fig2d11_x=(1:10000)'./5000-1;
Fig2d11_xs=(1:10000)'/10000*1.129-0.129; %-0.129..x-value of inflection
point
Fig2d11_y=(1:10000)'/10000;
Fig2d11_Lor=1./(1+20*Fig2d11_x.*Fig2d11_x);
Fig2d11_sin=0.08*sin(100*Fig2d11_y)-0.129; %-0.129..x-value of inflection
point
Fig2d11_sinamp=0.21*sin(100*Fig2d11_xs)+0.75;
plot(Fig2d11_x,Fig2d11_Lor,'LineWidth',3);hold on;
plot(Fig2d11_sin,Fig2d11_y,Fig2d11_xs,Fig2d11_sinamp,'LineWidth',2);hold
on;
xlabel('Phase Shift \Delta\phi'); ylabel('Transmitted Intensity
I_T');hold on;
legend('Transmission Profile', 'Initial Signal','Cavity Enhanced
Signal');hold off;
```

```matlab
%right:
Fig2d11_LorL=1./(1+20*(Fig2d11_x-0.04).*(Fig2d11_x-0.04));
Fig2d11_LorR=1./(1+20*(Fig2d11_x+0.04).*(Fig2d11_x+0.04));
plot(Fig2d11_x,Fig2d11_Lor,'LineWidth',3, 'Color', [0 0.4470
0.7410]);hold on;
plot(Fig2d11_x,Fig2d11_LorL,'LineWidth',1.5, 'Color', [0 0.4470
0.7410]);hold on;
plot(Fig2d11_x,Fig2d11_LorR,'LineWidth',1.5, 'Color', [0 0.4470
0.7410]);hold off;
Fig2d11_LorR=1./(1+20*(Fig2d11_x+0.03).*(Fig2d11_x-0.03));


%Figure 2.13
    %CorelDraw only


%Figure 2.14
    %Sampling Problem - Curve; rest CorelDraw
plot(Fig2d11_x,Fig2d11_Lor,'LineWidth',2, 'Color', [0 0 0]);
xlabel('Time axis'); ylabel('Signal axis');


%Figure 2.15
    %CorelDraw only


%Figure 2.16
    %Frequency doubling at absolute value function
Fig2d15_x=(1:10000)'/5000-1;
Fig2d15_Tfct=abs(Fig2d15_x);
Fig2d15_xv1=(1:10000)'/20000+0.5;
Fig2d15_sv1=0.05*sin(50*Fig2d15_xv1)-0.5;
Fig2d15_xv2=(1:10000)'/10000;
Fig2d15_sv2=0.05*sin(50*Fig2d15_xv2);
Fig2d15_xh1=(1:15000)'/10000-0.5;
Fig2d15_sh1=0.05*sin(50*Fig2d15_xh1)+0.5;
Fig2d15_xh2=(1:10000)'/10000;
Fig2d15_sh2=0.05*abs(sin(50*Fig2d15_xh2));
plot(Fig2d15_x,Fig2d15_Tfct,'LineWidth',3,'Color', [0 0 0]);hold on
plot(Fig2d15_sv1,Fig2d15_xv1,'LineWidth',2,'Color', [0.8500 0.3250
0.0980]);hold on
plot(Fig2d15_sv2,Fig2d15_xv2,'LineWidth',2,'Color', [0.8500 0.3250
0.0980]);hold on
plot(Fig2d15_xh1,Fig2d15_sh1,'LineWidth',2,'Color', [0 0.4470
0.7410]);hold on
plot(Fig2d15_xh2,Fig2d15_sh2,'LineWidth',2,'Color', [0 0.4470
0.7410]);hold on
xlabel('Normalized Frequency');ylabel('Normalized transduced Amplitude')
hold off;
% Lorentz and 2f Lorentz
Fig2d16_Lor=Fig2d11_Lor;
Fig2d16_xLor=Fig2d11_x;
Fig2d16_DxLor=Fig2d11_x*0;
Fig2d16_DxxLor=Fig2d11_x*0;
for i=5:9995 Fig2d16_DxLor(i)=Fig2d16_Lor(i+4)-Fig2d16_Lor(i-4); end
for i=5:9995 Fig2d16_DxxLor(i)=Fig2d16_DxLor(i+4)-Fig2d16_DxLor(i-4); end
Fig2d16_DxxLor(1:10)=0;Fig2d16_DxxLor(9990:10000)=0;
Fig2d16_DxxLor=-Fig2d16_DxxLor/max(Fig2d16_DxxLor);
plot(Fig2d16_xLor,Fig2d16_Lor,'LineWidth',2);
xlabel('Normalized Frequency');ylabel('Normalized transduced Amplitude');
plot(Fig2d16_xLor,Fig2d16_DxxLor,'LineWidth',2);
xlabel('Normalized Frequency');ylabel('Normalized transduced Amplitude');


%Figure 2.17
    %2f signal generation
Fig2d16_x=(1:100000)'/100000;
```

```matlab
Fig2d16_yG1=Fig2d16_x./(1+162*(Fig2d16_x-0.5).*(Fig2d16_x-0.5));
plot(Fig2d16_x,Fig2d16_yG1,'LineWidth',2);
xlabel('Normalized Frequency');ylabel('Normalized Detector Amplitude');
Fig2d16_yG2=0.05*sin(2*pi*1000*Fig2d16_x);
plot(Fig2d16_x(1:1000),Fig2d16_yG2(1:1000),'LineWidth',2);
xlabel('Normalized Frequency');ylabel('Normalized Detector Amplitude');
Fig2d16_yG3=(Fig2d16_x+Fig2d16_yG2)./(1+162*(Fig2d16_x+Fig2d16_yG2-
0.5).*(Fig2d16_x+Fig2d16_yG2-0.5));
plot(Fig2d16_x,Fig2d16_yG3,'LineWidth',1);
xlabel('Normalized Frequency');ylabel('Normalized Detector Amplitude');
Fig2d16_yG3DMsin=cos(2*2*pi*1000*Fig2d16_x);
Fig2d16_yG3DM=Fig2d16_yG3.*Fig2d16_yG3DMsin;
plot(Fig2d16_x,Fig2d16_yG3DM,'LineWidth',1);
xlabel('Normalized Frequency');ylabel('Normalized Detector Amplitude');
Fig2d16_x2=(1:1000)'/1000;
Fig2d16_G4=Fig2d16_x2;
for i=1:1000 Fig2d16_yG4(i)=mean(Fig2d16_yG3DM((i-1)*100+1:i*100)); end
plot(Fig2d16_x2,Fig2d16_yG4,'LineWidth',2);
xlabel('Normalized Frequency');ylabel('Normalized 2f Amplitude');


%Figure 2.18
    %Skewness principle and example
plot(Fig2d16_x,Fig2d16_yG1,'LineWidth',2); %Lorentzian taken from figure
2.16
xlabel('Normalized Frequency');ylabel('Normalized Detector Amplitude');
Fig2d17_skw=(1:1000)'/1000;
for i=1:1000 Fig2d17_skw(i)=-0.1*skewness(Fig2d16_yG3((i-
1)*100+1:i*100)); end
Fig2d17_x=(1:1000)'/500-1;
plot(Fig2d17_x,Fig2d16_yG4,Fig2d17_x,Fig2d17_skw,'LineWidth',2);
xlabel('Normalized Frequency');ylabel('Normalized 2f and Skewness
Amplitude');
legend('2f-WM Amplitude','Skewness Amplitude')


%Figure 2.19
    %CorelDraw only


%Figure 2.20
    %Setup Sketch CorelDraw only
    %Graph:
Fig2d22_x=(1:10000)'/10000;
Fig2d22_sin=sin(2*pi*2*Fig2d22_x);
plot(Fig2d22_x,Fig2d22_sin,'LineWidth',2);
Fig2d22_Nse=(1:10000)'/10000; for i=1:10000
Fig2d22_Nse(i)=normrnd(0,0.5);end;
plot(Fig2d22_x,Fig2d22_Nse,'LineWidth',2);
plot(Fig2d22_x,Fig2d22_sin+Fig2d22_Nse,'LineWidth',2);


%Figure 2.21
%Left part:
Fig2d23_x=(1:10000)'/10000;
Fig2d23_y1=sin(Fig2d23_x.*(2*pi*5));
Fig2d23_y2=sin(Fig2d23_x.*(2*pi*5)+pi);
Fig2d23_y3=sin(Fig2d23_x.*(2*pi*5)+pi+0.1);
plot(Fig2d23_x,Fig2d23_y1,Fig2d23_x,Fig2d23_y2,Fig2d23_x,Fig2d23_y3,Fig2d
23_x,Fig2d23_y1+Fig2d23_y2,Fig2d23_x,Fig2d23_y1+Fig2d23_y3,'LineWidth',2)
xlabel('Time');ylabel('Signal');
legend('Monitor','Detector','Shifted
Detector','Monitor+Detector','Monitor+Shifted detector');
%Right part:
Fig2d23_x=(1:10000)'/5000-1;
tmp=1./(1+162*Fig2d23_x.*Fig2d23_x);
```

```matlab
Fig2d23_1f=Fig2d23_x*0; for i=1:9999 Fig2d23_1f(i)=tmp(i+1)-tmp(i);end;
Fig2d23_1f=Fig2d23_1f/max(Fig2d23_1f);
Fig2d23_sinx=(1:5000)'/10000;
Fig2d23_Cavsiny=0.18*sin(2*pi*10*(Fig2d23_sinx))+0.25;
Fig2d23_siny=0.02*sin(2*pi*10*Fig2d23_sinx);
Fig2d23_1fsiny=0.72*sin(2*pi*10*(Fig2d23_sinx));
plot(Fig2d23_x,Fig2d23_1f,'Linewidth',2);hold on;
plot(Fig2d23_sinx+0.5-0.5,Fig2d23_1fsiny,'Linewidth',2);hold on;
plot(Fig2d23_siny+0.5-0.5, Fig2d23_sinx-1,'Linewidth',2);hold on;
xlabel('Normalized CTF phase shift');ylabel('Normalized Amplitude');hold
on;
legend('1f-QBD Profile','Signal, 1f-QBD','Phase Modulation');hold off;

%Figure 3.1 to 3.3
    %CorelDraw only

%Figure 3.4
    %Filter Bode diagrams, measured
semilogx(Fig3d4_data(:,1),Fig3d4_data(:,2),'.-
','MarkerSize',25,'LineWidth',2);hold on;
semilogx(Fig3d4_data(:,1),Fig3d4_data(:,3),'.-
','MarkerSize',25,'LineWidth',2);hold on;
semilogx(Fig3d4_data(:,1),Fig3d4_data(:,4),'.-
','MarkerSize',25,'LineWidth',2);hold on;
semilogx(Fig3d4_data(:,1),Fig3d4_data(:,5),'.-
','MarkerSize',25,'LineWidth',2);hold on;
xlabel('Frequency [Hz]');ylabel('Amplification Level [dB_V]');hold on;
legend('Channel 1','Channel 2','Channel 3','Channel 4');hold off;

%Figure 3.5 to 3.11
    %CorelDraw only

%Figure 3.12
    %Comparison SRS vs LabView LIA, measured data
    %1..Wavenumber, 2..LabView LIA, 3..SRS LIA
    plot(Fig3d12_data(:,1)+0.594,-
Fig3d12_data(:,2)*1000,'LineWidth',2);hold on;
    plot(Fig3d12_data(:,1)+0.594,-
Fig3d12_data(:,3)*1000,'LineWidth',2);hold on;
    xlabel('Wavenumber [cm^{-1}]');ylabel('2f signal amplitude
[mV]');hold on;
    legend('LabView based LIA','Stanford SRS 860');hold on;
    lgd=legend;lgd.NumColumns=2;hold off;
    set(gca,'Xdir','reverse');
    plot(Fig3d20_Hitran(:,2),Fig3d20_Hitran(:,3)*1000,'Linewidth',2);hold
on;
    plot(Fig3d20_Hitran(:,2),Fig3d20_Hitran(:,1)*1000,'Linewidth',2);hold
on;
    xlabel('Wavenumber [cm^{-1}]');ylabel('Absorption units [mAU]');hold
on;
    legend('Absorption ^{12}CO_2, HITRAN','Absorption ^{13}CO_2,
HITRAN');hold on;
    lgd=legend;lgd.NumColumns=2;hold off;
    set(gca,'Xdir','reverse');

%Figure 3.13
    %Power-and wavelength spectra Alpes QCL; measured Data
    %1..Injection current, 2..Amplitude 10?C 3..Amplitude 15?C,
4..Amplitude 20?C, 5..Amplitude 25?C, 6..Amplitude 30?C
    plot(Fig3d13_PWdata(:,1),Fig3d13_PWdata(:,2),'.-
','LineWidth',2,'MarkerSize', 25);hold on;
```

```matlab
    plot(Fig3d13_PWdata(:,1),Fig3d13_PWdata(:,3),'.-
','LineWidth',2,'MarkerSize', 25);hold on;
    plot(Fig3d13_PWdata(:,1),Fig3d13_PWdata(:,4),'.-
','LineWidth',2,'MarkerSize', 25);hold on;
    plot(Fig3d13_PWdata(:,1),Fig3d13_PWdata(:,5),'.-
','LineWidth',2,'MarkerSize', 25);hold on;
    plot(Fig3d13_PWdata(:,1),Fig3d13_PWdata(:,6),'.-
','LineWidth',2,'MarkerSize', 25);hold on;
    xlabel('Injection current [mA]');ylabel('Laser power [mW]');hold on;
    legend('10?C','15?C','20?C','25?C','30?C');hold off;
    plot(Fig3d13_WNdata(:,1),Fig3d13_WNdata(:,2),'.-
','LineWidth',2,'MarkerSize', 25);hold on;
    plot(Fig3d13_WNdata(:,1),Fig3d13_WNdata(:,3),'.-
','LineWidth',2,'MarkerSize', 25);hold on;
    plot(Fig3d13_WNdata(:,1),Fig3d13_WNdata(:,4),'.-
','LineWidth',2,'MarkerSize', 25);hold on;
    plot(Fig3d13_WNdata(:,1),Fig3d13_WNdata(:,5),'.-
','LineWidth',2,'MarkerSize', 25);hold on;
    plot(Fig3d13_WNdata(:,1),Fig3d13_WNdata(:,6),'.-
','LineWidth',2,'MarkerSize', 25);hold on;
    xlabel('Injection current [mA]');ylabel('Laser wavenumber [cm^{-
1}]');hold on;
    legend('10?C','15?C','20?C','25?C','30?C');hold off;

%Figure 3.14
    %Power-and wavelength spectra Emcore fibre laser; measured Data
    %1..Injection current, 2..Amplitude 10?C 3..Amplitude 15?C,
4..Amplitude 20?C, 5..Amplitude 25?C, 6..Amplitude 29.9?C
    plot(Fig3d14_PWdata(:,1),Fig3d14_PWdata(:,2),'.-
','LineWidth',2,'MarkerSize', 25);hold on;
    plot(Fig3d14_PWdata(:,1),Fig3d14_PWdata(:,3),'.-
','LineWidth',2,'MarkerSize', 25);hold on;
    plot(Fig3d14_PWdata(:,1),Fig3d14_PWdata(:,4),'.-
','LineWidth',2,'MarkerSize', 25);hold on;
    plot(Fig3d14_PWdata(:,1),Fig3d14_PWdata(:,5),'.-
','LineWidth',2,'MarkerSize', 25);hold on;
    plot(Fig3d14_PWdata(:,1),Fig3d14_PWdata(:,6),'.-
','LineWidth',2,'MarkerSize', 25);hold on;
    xlabel('Injection current [mA]');ylabel('Laser power [mW]');hold on;
    legend('10?C','15?C','20?C','25?C','29.9?C');hold off;
    plot(Fig3d14_WLdata(:,1),Fig3d14_WLdata(:,2),'.-
','LineWidth',2,'MarkerSize', 25);hold on;
    plot(Fig3d14_WLdata(:,1),Fig3d14_WLdata(:,3),'.-
','LineWidth',2,'MarkerSize', 25);hold on;
    plot(Fig3d14_WLdata(:,1),Fig3d14_WLdata(:,4),'.-
','LineWidth',2,'MarkerSize', 25);hold on;
    plot(Fig3d14_WLdata(:,1),Fig3d14_WLdata(:,5),'.-
','LineWidth',2,'MarkerSize', 25);hold on;
    plot(Fig3d14_WLdata(:,1),Fig3d14_WLdata(:,6),'.-
','LineWidth',2,'MarkerSize', 25);hold on;
    xlabel('Injection current [mA]');ylabel('Laser wavenumber [cm^{-
1}]');hold on;
    legend('10?C','15?C','20?C','25?C','29.9?C');hold off;

%Figure 3.15
    %CorelDraw only

%Figure 3.16
%Alpes DFB-QCL
plot(Fig3d15a_DFB(:,1),Fig3d15a_DFB(:,2)/max(Fig3d15a_DFB(:,2)),'LineWidt
h',2);
xlabel('Wavenumber [cm^{-1}]');ylabel('Normalized ADC Counts');
```

```matlab
set(gca,'Xdir','reverse');
%Daylight EC-QCL
plot(Fig3d15a_EC(:,1),Fig3d15a_EC(:,2)/max(Fig3d15a_EC(:,2)),'LineWidth',
2);
xlabel('Wavenumber [cm^{-1}]');ylabel('Normalized ADC Counts');
set(gca,'Xdir','reverse');
%Emcore NIR
plot(Fig3d15a_NIR(:,1),Fig3d15a_NIR(:,2)/max(Fig3d15a_NIR(:,2)),'LineWidt
h',2);
xlabel('Wavenumber [cm^{-1}]');ylabel('Normalized ADC Counts');
set(gca,'Xdir','reverse');

%Figure 3.17
%GasZelleCO2
plot(Fig3d15b_RefCell(:,1),Fig3d15b_RefCell(:,2));
xlabel('Wavenumber [cm^{-1}]');ylabel('Transmission');
set(gca,'Xdir','reverse');
%Ethanol
plot(Fig3d15b_EtOH(:,1),Fig3d15b_EtOH(:,2),'LineWidth',2);
xlabel('Wavenumber [cm^{-1}]');ylabel('Absorption [AU]');
set(gca,'Xdir','reverse');
%Glucose
plot(Fig3d15b_Gluc(:,1),Fig3d15b_Gluc(:,2),'LineWidth',2);
xlabel('Wavenumber [cm^{-1}]');ylabel('Absorption [AU]');
set(gca,'Xdir','reverse');

%Figure 3.18
    %CorelDraw only

%Figure 3.19
    %Sine-Line-extrapolation
Fig3d29_x=(1:10000)'*0.0001*pi;
plot(Fig3d29_x,cos(Fig3d29_x),'LineWidth',2);hold on;
plot(Fig3d29_x,-cos(Fig3d29_x),'LineWidth',2);hold on;
plot(Fig3d29_x,Fig3d29_x-pi/2,'LineWidth',2,'Color',[0.4660 0.6740
0.1880]);hold on;
xlabel('Phase shift \phi [rad]');ylabel ('Detector Signal');hold on;
legend('Detector 1, D_1(\phi)','Detector 2, D_2(\phi)','Linear
Approximation, L(\phi)');hold off;
set(gca,'XTick',0:pi/4:pi);
set(gca,'XTickLabel',{'0','\pi/4','\pi/2','3\pi/2','\pi'});
lgd=legend;lgd.NumColumns=2;hold off;

%Figure 3.20
    %Ethanol spectra - measured data
plot(Fig3d30_AbsFTIR(:,1),Fig3d30_AbsFTIR(:,2),'LineWidth',2);hold on;
plot(Fig3d30_AbsMZI(:,1),Fig3d30_AbsMZI(:,2),'LineWidth',2);hold on;
xlabel('Wavenumber [cm^{-1}]');ylabel('Absorbance [AU]');hold on;
legend('Absorption, FTIR','Absorption, MZI-Setup');hold off
set(gca,'XDir','reverse');
plot(Fig3d30_DispMv(:,1),Fig3d30_DispMv(:,2),'LineWidth',2);hold on;
plot(Fig3d30_DispFx(:,1),Fig3d30_DispFx(:,2),'LineWidth',2);hold on;
plot(Fig3d30_KKAbs(:,1),Fig3d30_KKAbs(:,2),'LineWidth',2);hold on;
xlabel('Wavenumber [cm^{-1}]');ylabel('Dispersion []');hold on;
legend('Dispersion, Moving Piezo','Dispersion, Fixed Piezo','Kramers-
Kronig transformed Absorption');hold off
set(gca,'XDir','reverse');

%Figure 3.21
    %CorelDraw only
```

```matlab
%Figure 3.22
    %CTF peaks at different temperatures and Linear regression of peak
    %values; Measured Data
plot(Fig3d21_21d45C(:,1),Fig3d21_21d45C(:,2),'Linewidth',2);hold on;
plot(Fig3d21_21d65C(:,1),Fig3d21_21d65C(:,2),'Linewidth',2);hold on;
plot(Fig3d21_21d85C(:,1),Fig3d21_21d85C(:,2),'Linewidth',2);hold on;
plot(Fig3d21_22d05C(:,1),Fig3d21_22d05C(:,2),'Linewidth',2);hold on;
plot(Fig3d21_22d25C(:,1),Fig3d21_22d25C(:,2),'Linewidth',2);hold on;
plot(Fig3d21_22d45C(:,1),Fig3d21_22d45C(:,2),'Linewidth',2);hold on;
plot(Fig3d21_22d65C(:,1),Fig3d21_22d65C(:,2),'Linewidth',2);hold on;
xlabel('Probe laser injection current [mA]');ylabel('Detector Signal
[V]');hold on;
legend('21.45 ?C','21.65 ?C','21.85 ?C','22.05 ?C','22.25 ?C','22.45
?C','22.65 ?C');hold off;
%ivsT
tmp=(1:6)';Fig3d21_IvsT=[tmp,tmp];
Fig3d21_IvsT(:,1)=[21.65;21.85;22.05;22.25;22.45;22.65];
Fig3d21_IvsT(:,2)=[68.97;98.04;119.9;145.3;166.95;185.69]; %peak Values
read from Graph
Fig3d21_IvsT(:,3)=[72.47;95.78;119.09;142.39;165.7;189]; %CalibLine
plot(Fig3d21_IvsT(:,1),Fig3d21_IvsT(:,2),'.','MarkerSize',30,'Color',[0 0
0]);hold on;
plot(Fig3d21_IvsT(:,1),Fig3d21_IvsT(:,3),'Linewidth',2,'Color',[0 0.4470
0.7410]);hold on;
xlabel('Cavity and Housing Temperature [?C]');ylabel('CTF Peak Position
[mA]');hold off;


%Figure 3.23
    %CorelDraw only


%Figure 3.24
     %Different modulation frequencies
Fig3d23_x=(1:1000)'/1000;
Fig3d23_LFsine=sin(2.4*2*pi*Fig3d23_x);
Fig3d23_HFsine=sin(20.4*2*pi*Fig3d23_x);
plot(Fig3d23_x, Fig3d23_LFsine,'Linewidth',2);hold on;
plot(Fig3d23_x, Fig3d23_HFsine,'Linewidth',1.5);hold on;
xlabel ('Time');ylabel('Amplitude');hold off;
plot(ksdensity(Fig3d23_LFsine),'Linewidth',2);
plot(ksdensity(Fig3d23_HFsine),'Linewidth',2,'Color',[0.8500 0.3250
0.0980]);


%Figure 3.25
    %Different modulation waveforms
Fig3d24_x=(1:1000000)'/1000000;
Fig3d24_MSine=Fig3d24_x; Mx=0.2*0.08*sin(2000*pi*Fig3d24_x); for
i=1:1000000 Fig3d24_MSine(i)=(Fig3d24_x(i)+Mx(i))*(1-
1/(1+162*(Fig3d24_x(i)+Mx(i)-0.5)^2));end
Fig3d24_MSwt=Fig3d24_x; Mx=0.2*0.08*sawtooth(2000*pi*Fig3d24_x); for
i=1:1000000 Fig3d24_MSwt(i)=(Fig3d24_x(i)+Mx(i))*(1-
1/(1+162*(Fig3d24_x(i)+Mx(i)-0.5)^2));end
Fig3d24_MNse=Fig3d24_x; for i=1:1000000 Mx=normrnd(0,0.5*0.2*0.08);
Fig3d24_MNse(i)=(Fig3d24_x(i)+Mx)*(1-1/(1+162*(Fig3d24_x(i)+Mx-
0.5)^2));end
Fig3d24_DMSine=(1:1000)'; for i=1:1000
Fig3d24_DMSine(i)=skewness(Fig3d24_MSine((i-1)*1000+1:i*1000));end
Fig3d24_DMSwt=(1:1000)'; for i=1:1000
Fig3d24_DMSwt(i)=skewness(Fig3d24_MSwt((i-1)*1000+1:i*1000));end
Fig3d24_DMNse=(1:1000)'; for i=1:1000
Fig3d24_DMNse(i)=skewness(Fig3d24_MNse((i-1)*1000+1:i*1000));end
plot((1:1000)'/1000,Fig3d24_DMSine,'Linewidth',2);hold on;
plot((1:1000)'/1000,Fig3d24_DMSwt,'Linewidth',2);hold on;
```

```matlab
plot((1:1000)'/1000,Fig3d24_DMNse,'Linewidth',2);hold on;
xlabel('Dimensionless Wavelength');ylabel('Normalized skewness');hold on;
legend('Sine','Sawtooth','Gaussian Noise');hold off;


%Figure 3.26 to 3.28
    %CorelDraw only


%Figure 3.29
    %reflected vs. transmitted probe laser beam
%Left:Transmitted vs. reflected
plot(Fig3d19_dataScan(:,1),Fig3d19_dataScan(:,2),'LineWidth',2);hold on;
plot(Fig3d19_dataScan(:,1),Fig3d19_dataScan(:,3),'LineWidth',2);hold on;
plot(Fig3d19_dataScan(:,1),0.8*Fig3d19_dataScan(:,2)+Fig3d19_dataScan(:,3
),'LineWidth',2);hold on;
xlabel('Normalized Injection Current');ylabel('Probe Laser Detector
Voltage');hold on;
legend('Transmitted','Reflected','Sum');hold off;
%Right: Transmission and Monitor PD
plot(Fig3d19_dataDM(:,1),(Fig3d19_dataDM(:,2)-
mean(Fig3d19_dataDM(:,2)))/std(Fig3d19_dataDM(:,2)),'LineWidth',2);hold
on;
plot(Fig3d19_dataDM(:,1),(Fig3d19_dataDM(:,3)-
mean(Fig3d19_dataDM(:,3)))/std(Fig3d19_dataDM(:,3)),'LineWidth',2);hold
on;
xlabel('Normalized Injection Current');ylabel('Normalized Voltage');hold
on;
legend('Transmission Signal','Monitor Photodiode Signal');hold off;


%Figure 3.30
    %ICAPS spectra CO2
%Spectra
plot(Fig3d20_Hitran(:,2),Fig3d20_Hitran(:,3)*10,'Linewidth',2);hold on;
plot(Fig3d20_Hitran(:,2),Fig3d20_Hitran(:,1)*10,'Linewidth',2);hold on;
plot(Fig3d20_icaps(:,1),Fig3d20_icaps(:,2),'Linewidth',2);hold on;
xlabel('Wavenumber [cm^{-1}]');ylabel('2f ICAPS Amplitude [mV] /
Absorption x 10 [AU]');hold on;
legend('Absorption ^{12}CO_2, HITRAN','Absorption ^{13}CO_2,
HITRAN','ICAPS');hold off;
set(gca,'XDir','reverse');
%CalibLine Steps
Fig3d20_CstepsC12(2050:2140)=0.4;
Fig3d20_CstepsC13(1780:1840)=0.64;
Fig3d20_x=(1:3000)'/3000;
plot(Fig3d20_x,Fig3d20_CstepsC12(1:3000),'Linewidth',2);hold on;
plot(Fig3d20_x,Fig3d20_CstepsC13(1:3000),'Linewidth',2);hold on;
xlabel('Normalized Time');ylabel('2f ICAPS Amplitude [mV]');hold on;
legend('ICAPS ^{12}CO_2','ICAPS ^{13}CO_2');hold off;
%CalibLine
plot(Fig3d20_calibdata(:,1)*0.01,Fig3d20_calibdata(:,3),'.','MarkerSize',
25);hold on;
plot(Fig3d20_calibdata(:,2),Fig3d20_calibdata(:,4),'.','MarkerSize',25);h
old on;
xlabel('Concentration, ^{12}CO_2 [100ppm], ^{13}CO_2
[ppm]');ylabel('ICAPS 2f Amplitude [mV]');hold on;
legend('ICAPS ^{12}CO_2','ICAPS ^{13}CO_2');hold off;


%Figure 3.31
    %2f and skewness peak broadening
    %simulated data:
Fig3d17_x=(1:1000000)'/1000000;
%generating (pure) Lorentz profile (-> HWHM = 0.08) and first derivative
```

```matlab
Fig3d17_Lx=Fig3d17_x; for i=1:1000000 Fig3d17_Lx(i)=1-
1/(1+162*(Fig3d17_x(i)-0.5)^2); end;
Fig3d17_dLx=Fig3d17_Lx; for i=5:999995 Fig3d17_dLx(i)=(Fig3d17_Lx(i+4)-
Fig3d17_Lx(i-4))*1000; end;
Fig3d17_dLx(1:5)=0;Fig3d17_dLx(999995:1000000)=0;
Fig3d17_sdLx=(1:1000)';
for i=1:1000 Fig3d17_sdLx(i)=mean(Fig3d17_dLx((i-1)*1000+1:i*1000));end
%generating modulated profiles
Fig3d17_MLx000=Fig3d17_x; Mx=0.00*0.08*sin(2000*pi*Fig3d17_x); for
i=1:1000000 Fig3d17_MLx000(i)=(Fig3d17_x(i)+Mx(i))*(1-
1/(1+162*(Fig3d17_x(i)+Mx(i)-0.5)^2));end
Fig2d17_MLx018=Fig3d17_x; Mx=0.18*0.08*sin(2000*pi*Fig3d17_x); for
i=1:1000000 Fig2d17_MLx018(i)=(Fig3d17_x(i)+Mx(i))*(1-
1/(1+162*(Fig3d17_x(i)+Mx(i)-0.5)^2));end
Fig3d17_MLx055=Fig3d17_x; Mx=0.55*0.08*sin(2000*pi*Fig3d17_x); for
i=1:1000000 Fig3d17_MLx055(i)=(Fig3d17_x(i)+Mx(i))*(1-
1/(1+162*(Fig3d17_x(i)+Mx(i)-0.5)^2));end
Fig3d17_MLx129=Fig3d17_x; Mx=1.29*0.08*sin(2000*pi*Fig3d17_x); for
i=1:1000000 Fig3d17_MLx129(i)=(Fig3d17_x(i)+Mx(i))*(1-
1/(1+162*(Fig3d17_x(i)+Mx(i)-0.5)^2));end
Fig3d17_MLx240=Fig3d17_x; Mx=2.40*0.08*sin(2000*pi*Fig3d17_x); for
i=1:1000000 Fig3d17_MLx240(i)=(Fig3d17_x(i)+Mx(i))*(1-
1/(1+162*(Fig3d17_x(i)+Mx(i)-0.5)^2));end
Fig3d17_MLx370=Fig3d17_x; Mx=3.70*0.08*sin(2000*pi*Fig3d17_x); for
i=1:1000000 Fig3d17_MLx370(i)=(Fig3d17_x(i)+Mx(i))*(1-
1/(1+162*(Fig3d17_x(i)+Mx(i)-0.5)^2));end
Fig3d17_MLx554=Fig3d17_x; Mx=5.54*0.08*sin(2000*pi*Fig3d17_x); for
i=1:1000000 Fig3d17_MLx554(i)=(Fig3d17_x(i)+Mx(i))*(1-
1/(1+162*(Fig3d17_x(i)+Mx(i)-0.5)^2));end
Fig3d17_MLx738=Fig3d17_x; Mx=7.38*0.08*sin(2000*pi*Fig3d17_x); for
i=1:1000000 Fig3d17_MLx738(i)=(Fig3d17_x(i)+Mx(i))*(1-
1/(1+162*(Fig3d17_x(i)+Mx(i)-0.5)^2));end
%demodulating
Fig3d17_Refcos=cos(4000*pi*Fig3d17_x);
Fig3d17_DMx=(1:1000)'/1000;
Fig3d17_DMLx000=(1:1000)';tmp=Fig3d17_MLx000.*Fig3d17_Refcos; for
i=1:1000 Fig3d17_DMLx000(i)=(-1)*mean(tmp((i-1)*1000+1:i*1000));end
Fig3d17_DMLx018=(1:1000)';tmp=Fig2d17_MLx018.*Fig3d17_Refcos; for
i=1:1000 Fig3d17_DMLx018(i)=(-1)*mean(tmp((i-1)*1000+1:i*1000));end
Fig3d17_DMLx055=(1:1000)';tmp=Fig3d17_MLx055.*Fig3d17_Refcos; for
i=1:1000 Fig3d17_DMLx055(i)=(-1)*mean(tmp((i-1)*1000+1:i*1000));end
Fig3d17_DMLx129=(1:1000)';tmp=Fig3d17_MLx129.*Fig3d17_Refcos; for
i=1:1000 Fig3d17_DMLx129(i)=(-1)*mean(tmp((i-1)*1000+1:i*1000));end
Fig3d17_DMLx240=(1:1000)';tmp=Fig3d17_MLx240.*Fig3d17_Refcos; for
i=1:1000 Fig3d17_DMLx240(i)=(-1)*mean(tmp((i-1)*1000+1:i*1000));end
Fig3d17_DMLx370=(1:1000)';tmp=Fig3d17_MLx370.*Fig3d17_Refcos; for
i=1:1000 Fig3d17_DMLx370(i)=(-1)*mean(tmp((i-1)*1000+1:i*1000));end
Fig3d17_DMLx554=(1:1000)';tmp=Fig3d17_MLx554.*Fig3d17_Refcos; for
i=1:1000 Fig3d17_DMLx554(i)=(-1)*mean(tmp((i-1)*1000+1:i*1000));end
Fig3d17_DMLx738=(1:1000)';tmp=Fig3d17_MLx738.*Fig3d17_Refcos; for
i=1:1000 Fig3d17_DMLx738(i)=(-1)*mean(tmp((i-1)*1000+1:i*1000));end
%Generating Figure 3d17
plot(Fig3d17_DMx,Fig3d17_DMLx018,'Linewidth',2);hold on;
plot(Fig3d17_DMx,Fig3d17_DMLx055,'Linewidth',2);hold on;
plot(Fig3d17_DMx,Fig3d17_DMLx129,'Linewidth',2);hold on;
plot(Fig3d17_DMx,Fig3d17_DMLx240,'Linewidth',2);hold on;
plot(Fig3d17_DMx,Fig3d17_DMLx370,'Linewidth',2);hold on;
plot(Fig3d17_DMx,Fig3d17_DMLx554,'Linewidth',2);hold on;
plot(Fig3d17_DMx,Fig3d17_DMLx738,'Linewidth',2);hold on;
plot(Fig3d17_DMx,Fig3d17_sdLx,'Linewidth',2);hold on;
xlabel('Dimensionless Wavelength');ylabel('Normalized 2f Amplitude');hold
on;
```

```matlab
legend('m_i = 0.18','m_i = 0.55','m_i = 1.29','m_i = 2.40','m_i =
3.70','m_i = 5.54','m_i = 7.38','d/dx L(x)');
lgd=legend;lgd.NumColumns=4;hold off;
%generating modulated profiles for skewness (0.25fold mi)
Fig3d17_MLx000=Fig3d17_x; Mx=0.25*0.00*0.08*sin(2000*pi*Fig3d17_x); for
i=1:1000000 Fig3d17_MLx000(i)=(Fig3d17_x(i)+Mx(i))*(1-
1/(1+162*(Fig3d17_x(i)+Mx(i)-0.5)^2));end
Fig3d17_MLx018=Fig3d17_x; Mx=0.25*0.18*0.08*sin(2000*pi*Fig3d17_x); for
i=1:1000000 Fig3d17_MLx018(i)=(Fig3d17_x(i)+Mx(i))*(1-
1/(1+162*(Fig3d17_x(i)+Mx(i)-0.5)^2));end
Fig3d17_MLx055=Fig3d17_x; Mx=0.25*0.55*0.08*sin(2000*pi*Fig3d17_x); for
i=1:1000000 Fig3d17_MLx055(i)=(Fig3d17_x(i)+Mx(i))*(1-
1/(1+162*(Fig3d17_x(i)+Mx(i)-0.5)^2));end
Fig3d17_MLx129=Fig3d17_x; Mx=0.25*1.29*0.08*sin(2000*pi*Fig3d17_x); for
i=1:1000000 Fig3d17_MLx129(i)=(Fig3d17_x(i)+Mx(i))*(1-
1/(1+162*(Fig3d17_x(i)+Mx(i)-0.5)^2));end
Fig3d17_MLx240=Fig3d17_x; Mx=0.25*2.40*0.08*sin(2000*pi*Fig3d17_x); for
i=1:1000000 Fig3d17_MLx240(i)=(Fig3d17_x(i)+Mx(i))*(1-
1/(1+162*(Fig3d17_x(i)+Mx(i)-0.5)^2));end
Fig3d17_MLx370=Fig3d17_x; Mx=0.25*3.70*0.08*sin(2000*pi*Fig3d17_x); for
i=1:1000000 Fig3d17_MLx370(i)=(Fig3d17_x(i)+Mx(i))*(1-
1/(1+162*(Fig3d17_x(i)+Mx(i)-0.5)^2));end
Fig3d17_MLx554=Fig3d17_x; Mx=0.25*5.54*0.08*sin(2000*pi*Fig3d17_x); for
i=1:1000000 Fig3d17_MLx554(i)=(Fig3d17_x(i)+Mx(i))*(1-
1/(1+162*(Fig3d17_x(i)+Mx(i)-0.5)^2));end
Fig3d17_MLx738=Fig3d17_x; Mx=0.25*7.38*0.08*sin(2000*pi*Fig3d17_x); for
i=1:1000000 Fig3d17_MLx738(i)=(Fig3d17_x(i)+Mx(i))*(1-
1/(1+162*(Fig3d17_x(i)+Mx(i)-0.5)^2));end
%demodulating with skewness
Fig3d17_DMLx000=(1:1000)'; for i=1:1000
Fig3d17_DMLx000(i)=skewness(Fig3d17_MLx000((i-1)*1000+1:i*1000));end
Fig3d17_DMLx018=(1:1000)'; for i=1:1000
Fig3d17_DMLx018(i)=skewness(Fig3d17_MLx018((i-1)*1000+1:i*1000));end
Fig3d17_DMLx055=(1:1000)'; for i=1:1000
Fig3d17_DMLx055(i)=skewness(Fig3d17_MLx055((i-1)*1000+1:i*1000));end
Fig3d17_DMLx129=(1:1000)'; for i=1:1000
Fig3d17_DMLx129(i)=skewness(Fig3d17_MLx129((i-1)*1000+1:i*1000));end
Fig3d17_DMLx240=(1:1000)'; for i=1:1000
Fig3d17_DMLx240(i)=skewness(Fig3d17_MLx240((i-1)*1000+1:i*1000));end
Fig3d17_DMLx370=(1:1000)'; for i=1:1000
Fig3d17_DMLx370(i)=skewness(Fig3d17_MLx370((i-1)*1000+1:i*1000));end
Fig3d17_DMLx554=(1:1000)'; for i=1:1000
Fig3d17_DMLx554(i)=skewness(Fig3d17_MLx554((i-1)*1000+1:i*1000));end
Fig3d17_DMLx738=(1:1000)'; for i=1:1000
Fig3d17_DMLx738(i)=skewness(Fig3d17_MLx738((i-1)*1000+1:i*1000));end
%Generating Figure 3d17
plot(Fig3d17_DMx,Fig3d17_DMLx018,'Linewidth',2);hold on;
plot(Fig3d17_DMx,Fig3d17_DMLx055,'Linewidth',2);hold on;
plot(Fig3d17_DMx,Fig3d17_DMLx129,'Linewidth',2);hold on;
plot(Fig3d17_DMx,Fig3d17_DMLx240,'Linewidth',2);hold on;
plot(Fig3d17_DMx,Fig3d17_DMLx370,'Linewidth',2);hold on;
plot(Fig3d17_DMx,Fig3d17_DMLx554,'Linewidth',2);hold on;
plot(Fig3d17_DMx,Fig3d17_DMLx738,'Linewidth',2);hold on;
plot(Fig3d17_DMx,10*Fig3d17_sdLx,'Linewidth',2);hold on;
xlabel('Dimensionless Wavelength');ylabel('Normalized Skewness');hold on;
legend('m_i = 0.045','m_i = 0.138','m_i = 0.323','m_i = 0.6','m_i =
0.925','m_i = 1.385','m_i = 1.845','d/dx L(x)');
lgd=legend;lgd.NumColumns=4;hold off;
%MeasuredData
%data: 1..current, 2..skewness, 3..2f, 4..relcurrent
%d/dx:1..current,2..detector,3..d/dx detector, 4..relcurrent
%Current normalization - last number=peakposition; 100->mA
Fig3d17_Ma(:,4)=Fig3d17_Ma(:,1)*100-217.16;
```

```matlab
Fig3d17_Mb(:,4)=Fig3d17_Mb(:,1)*100-218.5;
Fig3d17_Mc(:,4)=Fig3d17_Mc(:,1)*100-224.2;
Fig3d17_Md(:,4)=Fig3d17_Md(:,1)*100-220.37;
Fig3d17_Me(:,4)=Fig3d17_Me(:,1)*100-239.96;
Fig3d17_Mf(:,4)=Fig3d17_Mf(:,1)*100-226.65;
Fig3d17_Mg(:,4)=Fig3d17_Mg(:,1)*100-220.54;
%Figure2f
plot(Fig3d17_Ma(:,4),-Fig3d17_Ma(:,3),'Linewidth',2);hold on;
plot(Fig3d17_Mb(:,4),-Fig3d17_Mb(:,3),'Linewidth',2);hold on;
plot(Fig3d17_Mc(:,4),-Fig3d17_Mc(:,3),'Linewidth',2);hold on;
plot(Fig3d17_Md(:,4),-Fig3d17_Md(:,3),'Linewidth',2);hold on;
plot(Fig3d17_Me(:,4),-Fig3d17_Me(:,3),'Linewidth',2);hold on;
plot(Fig3d17_Mf(:,4),-Fig3d17_Mf(:,3),'Linewidth',2);hold on;
plot(Fig3d17_Mg(:,4),-Fig3d17_Mg(:,3),'Linewidth',2);hold on;
xlabel('Relative Injection Current [mA]');ylabel('2f Amplitude [V]');hold
on;
legend('m_i = 0.18','m_i = 0.55','m_i = 1.29','m_i = 2.40','m_i =
3.70','m_i = 5.54','m_i = 7.38');
lgd=legend;lgd.NumColumns=1;hold off;
%FigureSkew
plot(Fig3d17_Ma(:,4),Fig3d17_Ma(:,2),'Linewidth',2);hold on;
plot(Fig3d17_Mb(:,4),Fig3d17_Mb(:,2),'Linewidth',2);hold on;
plot(Fig3d17_Mc(:,4),Fig3d17_Mc(:,2),'Linewidth',2);hold on;
plot(Fig3d17_Md(:,4),Fig3d17_Md(:,2),'Linewidth',2);hold on;
plot(Fig3d17_Me(:,4),Fig3d17_Me(:,2),'Linewidth',2);hold on;
plot(Fig3d17_Mf(:,4)+1.1,Fig3d17_Mf(:,2),'Linewidth',2);hold on;
plot(Fig3d17_Mg(:,4)+3.48,Fig3d17_Mg(:,2),'Linewidth',2);hold on;
xlabel('Relative Injection Current [mA]');ylabel('Skewness Amplitude
[V]');hold on;
legend('m_i = 0.18','m_i = 0.55','m_i = 1.29','m_i = 2.40','m_i =
3.70','m_i = 5.54','m_i = 7.38');
lgd=legend;lgd.NumColumns=4;hold off;


%Figure 3.32
%2f-WMS spectra CO2, ICL
plot(Fig3d16_specdata(:,1),Fig3d16_specdata(:,2)*50,'LineWidth',2);hold
on;
plot(Fig3d16_specdata(:,1),Fig3d16_specdata(:,3)*50,'LineWidth',2);hold
on;
plot(Fig3d16_specdata(:,1),Fig3d16_specdata(:,4)*50,'LineWidth',2);hold
on;
plot(Fig3d16_specdata(:,1),Fig3d16_specdata(:,5)*50,'LineWidth',2);hold
on;
plot(Fig3d16_specdata(:,1),Fig3d16_specdata(:,6)*50,'LineWidth',2);hold
on;
plot(Fig3d16_specdata(:,1),Fig3d16_specdata(:,7)*50,'LineWidth',2);hold
on;
plot(Fig3d16_specdata(:,1),Fig3d16_specdata(:,8)*50,'LineWidth',2);hold
on;
plot(Fig3d16_specdata(:,1),Fig3d16_specdata(:,9)*50,'LineWidth',2);hold
on;
plot(Fig3d16_specdata(:,1),Fig3d16_specdata(:,10)*50,'LineWidth',2);hold
on;
xlabel('Excitation Laser Wavenumber [cm^{-1}]');ylabel('2f-Amplitude
[mV]');hold on;
legend('0 ppm','10 ppm','25 ppm','50 ppm','100 ppm','250 ppm','500
ppm','750 ppm','1000 ppm');hold off;
plot(Fig3d16_calibdata(1:10,1),Fig3d16_calibdata(1:10,2)*50,'.-
','LineWidth',2,'MarkerSize',25);
xlabel('CO_2 Concentration [ppm]');ylabel('2f-Amplitude [mV]');

%Figure 4.1
```

```matlab
    %CorelDraw only

%Figure Appendix B1
    %Autocorrelation
Fig2d18_x=(1:80000)'/80000;
Fig2d18_sin=sin(2*pi*8*Fig2d18_x);
%2f-pattern generation
Fig2d18_2f=(1:80000)'/80000;
tmp=(1:1000000)'/1000000;
tmp1=tmp./(1+162*(tmp-0.5).*(tmp-0.5));
tmp2=0.05*sin(2*pi*10000*tmp);
tmp3=(tmp+tmp2)./(1+162*(tmp+tmp2-0.5).*(tmp+tmp2-0.5));
tmp4=cos(2*2*pi*10000*tmp);
tmp5=tmp3.*tmp4;
for i=1:10000 Fig2d18_2fsgl(i)=mean(tmp5((i-1)*100+1:i*100)); end
for i=1:8 Fig2d18_2f((i-1)*10000+1:i*10000)=Fig2d18_2fsgl; end
Fig2d18_2f=Fig2d18_2f/max(Fig2d18_2f);
plot(Fig2d18_x, Fig2d18_sin,'LineWidth',2);
plot(Fig2d18_x, Fig2d18_2f,'LineWidth',2);
for i=1:80000 Fig2d18_Nsin(i)=Fig2d18_sin(i)+normrnd(0,3); end
for i=1:80000 Fig2d18_N2f(i)=Fig2d18_2f(i)+normrnd(0,3); end
plot(Fig2d18_x, Fig2d18_Nsin,'LineWidth',2);
plot(Fig2d18_x, Fig2d18_N2f,'LineWidth',2);
Fig2d18_AKsin=discreteautokorrelation(Fig2d18_Nsin,1/80000);
Fig2d18_AAKsin=discreteautokorrelation(Fig2d18_AKsin,1/80000);
Fig2d18_AK2f=discreteautokorrelation(Fig2d18_N2f,1/80000);
Fig2d18_AAK2f=discreteautokorrelation(Fig2d18_AK2f,1/80000);
plot(Fig2d18_x(1:20000), Fig2d18_AAKsin,'LineWidth',2);
plot(Fig2d18_x(1:20000), Fig2d18_AAK2f,'LineWidth',2);


%Figure Appendix B2
    %Autocorrelation vs averaging
    %MeasuredData: 1..n, 2..periods, 3..RawData, 4..Averaged,
5..AC,1order,
    %6..AC,2order
semilogy(Fig2d19_data(:,1),Fig2d19_data(:,3),'.-
','LineWidth',1.5,'MarkerSize',20); hold on;
semilogy(Fig2d19_data(:,1),Fig2d19_data(:,4),'.-
','LineWidth',1.5,'MarkerSize',20); hold on;
semilogy(Fig2d19_data(:,1),Fig2d19_data(:,5),'.-
','LineWidth',1.5,'MarkerSize',20); hold on;
semilogy(Fig2d19_data(:,1),Fig2d19_data(:,6),'.-
','LineWidth',1.5,'MarkerSize',20); hold on;
xlabel('Order n');ylabel('Sum of square residuals'); hold on;
legend('Raw Data', 'Averaged Data', 'First order AC', 'Second order AC');
hold on;
lgd=legend;lgd.NumColumns=4;hold off;


%Figure Appendix B3
    %Autocorrelation ICAPS
    %MeasuredData, data and ACdata: 1..Wavelength,nm, 2..0ppm,
3..2500ppm,
    %4..5000ppm, 5..7500ppm, 6..10000ppm
    %MeasuredData, MaxVals: 1..Concentration,ppm, 2..MaxICAPS, 3..MaxAC
%ICAPS spectra:
plot(10000000./Fig2d20_data(1:450,1),Fig2d20_data(1:450,2),'LineWidth',2)
;hold on;
plot(10000000./Fig2d20_data(1:450,1),Fig2d20_data(1:450,3),'LineWidth',2)
;hold on;
plot(10000000./Fig2d20_data(1:450,1),Fig2d20_data(1:450,4),'LineWidth',2)
;hold on;
```

```matlab
plot(10000000./Fig2d20_data(1:450,1),Fig2d20_data(1:450,5),'LineWidth',2)
;hold on;
plot(10000000./Fig2d20_data(1:450,1),Fig2d20_data(1:450,6),'LineWidth',2)
;hold on;
xlabel('Wavenumber [cm^{-1}]');ylabel('ICAPS Amplitude (V)');
set(gca,'Xdir','reverse');
legend('0 ppm','2500 ppm','5000 ppm','7500 ppm','10000 ppm');hold off;
%Autocorrelated ICAPS spectra:
tmp=max(10000000./Fig2d20_AKdata(:,1))-
min(10000000./Fig2d20_AKdata(:,1));
tmp2=min(10000000./Fig2d20_AKdata(:,1));
Fig2d20_WN=((1:2079)'/2079).*tmp+tmp2;
plot(Fig2d20_WN,Fig2d20_AKdata(:,2),'LineWidth',2);hold on;
plot(Fig2d20_WN,Fig2d20_AKdata(:,3),'LineWidth',2);hold on;
plot(Fig2d20_WN,Fig2d20_AKdata(:,4),'LineWidth',2);hold on;
plot(Fig2d20_WN,Fig2d20_AKdata(:,5),'LineWidth',2);hold on;
plot(Fig2d20_WN,Fig2d20_AKdata(:,6),'LineWidth',2);hold on;
xlabel('Wavenumber [cm^{-1}]');ylabel('1^{st} order autocorrelated
ICAPS(V^2)');
set(gca,'Xdir','reverse');
legend('0 ppm','2500 ppm','5000 ppm','7500 ppm','10000 ppm');hold off;
%Max peak heights
plot(Fig2d20_MaxVals(:,1),Fig2d20_MaxVals(:,2),'.','MarkerSize',30);
xlabel('CO_2 concentration [ppm]');ylabel('Peak Value (V)');
plot(Fig2d20_MaxVals(:,1),sqrt(Fig2d20_MaxVals(:,3)),'.','MarkerSize',30)
xlabel('CO_2 concentration [ppm]');ylabel('Peak Value, Squareroot (V)');

%Figure Appendix D1 to D3
    %Screenshot LabView Block Diagrams

%Figure Appendix E1, E2
    %Circuitry, CorelDraw only
```

G. Curriculum Vitae

Name

Dipl.-Ing. Ing. Stefan LINDNER, BSc

Citizenship

Austria

Date and place of birth

18.12.1990, Vienna

Education

2018-2022	PhD-studies in technical sciences at the Technical University of Vienna, expected completion end of 2022
Since 2022	Diploma studies in law at the Johannes Kepler University Linz
Dec. 2017	Graduation in Physical Energy and Measurement Engineering with the thesis „Delayed choice in a quantum cheshire cat experiment"
2009 -2018	Technical University of Vienna, undergraduate studies Technical Physics and Technical Mathematics

- 2015: Bachelor's Degree in Applied Mathematics
- 2017: Master's Degree in Physical Energy and Measurement Engineering

2015 -2017	Teaching Studies Physics and Mathematics at University of Vienna
2005 - 2009	HBLVA Rosensteingasse, Technical college of chemical engineering

- 2006: 2nd form skipped
- From 2007 Department of Biochemistry, Biotechnology and Genetics
- 2009 university entrance diploma, summa cum laude

2001 - 2005	Secondary school Bundesgymnasium und Bundesrealgymnasium Bruck an der Leitha, science department

Languages

German, English fluently
French beginner

Job experience

2018-2022	Project assistant at TU Wien, research group Process analytics
2017-2019	College Member at School Board Vienna
02/2017-03/2017	Research assistent at the Institut Laue-Langevin, Grenoble, France
2013 - 2017	Student assistant at Atomintitut, TU Wien
2012-2018	Self-employment, Lindner Nachhilfe OG, Senior-Partner lecturer for Mathematics, Physics and Chemistry
July 2011	Community worker Enzersdorf an der Fischa
Aug. 2008	Institute of Applied Synthetic Chemistry, Technical University Vienna; Performance of Diploma Thesis „Glucuronyldonors in the synthesis of glycoconjugates and metabolites"
June 2007	Laboratory assistent, Quality Assurance at Brauerei Schwechat, Brauunion AG

Additional Qualifications

- Certified Quality Coach (SystemCert)
- Driving Licence classes A, B
- February 2010: Publication of the lyrical drama „Der Ringfürst" at Wagner Verlag, ISBN 978-3-86683-604-4
- Austrian national firearms license

Peer reviewed publications

ORCID-ID: 0000-0002-3451-7011

5. <u>Stefan Lindner</u>, Jakob Hayden, Andreas Schwaighofer, Tobias Wolflehner, Christian Kristament, María Gonzáles-Cabrera, Stefan Zlabinger and Bernhard Lendl: *External Cavity Quantum Cascade Laser-Based Mid-Infrared Dispersion Spectroscopy for Qualitative and Quantitative Analysis of Liquid-Phase Samples*, Appl. Spectrosc. **74** (4) 452-459 (2020)

6. <u>Stefan Lindner</u>, Davide Pinto, Harald Moser, Johannes P. Waclawek and Bernhard Lendl: *Theory, implementation and characterization of low-frequency Laser-Cavity-Locking schemes for Interferometric Cavity-Assisted Photothermal Spectroscopy (ICAPS)*, Ready for submission

7. <u>Stefan Lindner</u>, Davide Pinto, Harald Moser, Johannes P. Waclawek and Bernhard Lendl: *Noise suppression and 1f - Quadrature point signal readout technique for cavity-enhanced optical dispersion spectroscopy*, Ready for submission

8. <u>Davide Pinto</u>, Johannes P. Waclawek, Stefan Lindner, Harald Moser, Giovanna Ricchiuti and Bernhard Lendl: *Wavelength Modulated Diode Probe Laser for an Interferometric Cavity-Assisted Photothermal Spectroscopy Gas Sensor*, SSRN Electronic Journal (2022), doi:10.2139/ssrn.4210238

9. <u>Alicja Dabrowska</u>, Andreas Schwaighofer, Stefan Lindner, and Bernhard Lendl: *Mid-IR refractive index sensor for detecting proteins employing an external cavity quantum cascade laser-based Mach-Zehnder interferometer*, Optics Express, **28** (24) 36632-36642 (2020)

10. <u>Alicja Dabrowska</u>, Stefan Lindner, Andreas Schwaighofer, and Bernhard Lendl: *Mid-IR dispersion spectroscopy – A new Avenue for liquid phase analysis*, Spectrochimica Acta Part A: Molecular and Biomolecular Spectroscopy (2023), doi: 10.1016/j.saa.2022.122014

11. <u>Hedwig Knötig</u>, Borislav Hinkov, Robert Weih, Benedikt Schwarz, Stefan Lindner, Johannes P. Waclawek, Bernhard Lendl, Sven Höfling, Johannes Koeth and Gottfried Strasser: *Vertically emitting ring interband cascade lasers*, Proc. SPIE 11705, Novel In-Plane Semiconductor Lasers XX, 1170517 (5 March 2021)

Conference contributions

1. <u>Stefan Lindner</u>, Harald Moser and Bernhard Lendl: *$^{12}CO_2$ and $^{13}CO_2$ detection at 2291 cm^{-1} by interferometric cavity-assisted photothermal spectroscopy (ICAPS)*, ICAVS11 Conference, Krakow, Poland (online, flash presentation), August 23rd to August 26th, 2021.

2. <u>Stefan Lindner</u>, Andreas Schwaighofer, Jakob Hayden, Bernhard Lendl: *A new approach to QCL-based Mid-Infrared Refractive Index Spectroscopy*; FLAIR, Assisi, Italy October 10th to 14th, 2018.

3. <u>Stefan Lindner</u>, Harald Moser and Bernhard Lendl: *Fabry-Perot cavity probe laser transmission line locking strategies for photothermal spectroscopy*, IRDG-Meeting 2019, Imperial College of London, London, United Kingdom, December 19th, 2019.

4. <u>Stefan Lindner</u> and Bernhard Lendl: *Advances in Dispersion Spectroscopy of Liquids and Photothermal Gas Sensing*, IRDG-Meeting 2022, Imperial College of London, London, United Kingdom, December 19th, 2022.

5. <u>Hedwig Knötig</u>, Borislav Hinkov, Robert Weih, Benedikt Schwarz, Stefan Lindner, Johannes P. Waclawek, Bernhard Lendl, Sven Höfling, Johannes Koeth and Gottfried Strasser: *Vertically emitting ring interband cascade lasers*, Novel In-Plane Semiconductor Lasers XX (Photonics West), online conference (formerly planned in San Francisco, USA), March 6th to 11th, 2021.

6. <u>Borislav Hinkov</u>, Hedwig Knötig, Stefan Lindner, Hermann Detz, Robert Weih, Sven Höfling, Werner Schrenk, Johannes Koeth, Johannes P. Waclawek, Bernhard Lendl, and Gottfried Strasser: *Optoelectronic devices for sensing applications in the mid-infrared*, 1st Laser Components (LC) Talks (formerly 6th International WORKshop on Infrared Technologies), online workshop (formerly planned in Olching, Germany), December 1st and 2nd 2020 & January 19th and 20th 2021.

7. <u>Bernhard Lendl</u>, Jakob Hayden, Stefan Lindner, Andreas Schwaighofer, Milaglos Montemurro, Johannes P. Waclawek, Andreas Genner, Harald Moser: *Recent Advances in QCL Based Sensing of Gases and Liquids,* 14th International Conference on Mid-IR Optoelectronics: Materials and Devices MIOMD, Flagstaff, Arizona October 7th to 10th, 2018

8. <u>Davide Pinto</u>, Johannes P. Waclawek, Stefan Lindner, Harald Moser and Bernhard Lendl: *2f zero-crossing locked Interferometric Cavity-Assisted Photothermal Spectroscopy system for trace gas sensing,* International School of Quantum Electronics – 64th Course: Progress in Photoacoustic and Photothermal Phenomena, Erice, Italy; October 16th to 23rd , 2021

9. <u>Hedwig Knötig</u>, Borislav Hinkov, Robert Weih, Sven Höfling, Werner Schrenk, Johannes Koeth, Johannes P. Waclawek, Stefan Lindner, Bernhard Lendl and Gottfried Strasser: *Ring interband cascade lasers emitting in continuous-wave mode at room temperature*, 20th International Winterschool on New Developments in Solid State Physics, Mauterndorf, Austria, February 25th to March 2nd, 2020.

10. <u>Davide Pinto</u>, Stefan Lindner, Johannes P. Waclawek, Harald Moser, Bernhard Lendl: *2f zero-crossing locked Interferometric Cavity-Assisted Photothermal Spectroscopy system for NO sensing,* ICAVS11 Conference, Krakow, Poland (online, flash presentation), August 23rd to August 26th, 2021